Brine and pressure dynamics in growing sea ice: measurements and modelling in the Roland von Glasow air-sea-ice chamber

by

Max Thomas

A thesis submitted to the School of Environmental Sciences of the University of East Anglia in partial fulfilment of the requirements of the degree of Doctor of Philosophy.

School of Environmental Sciences
University of East Anglia

Abstract

I investigate two physical processes in growing sea ice using a new experimental facility, the Roland von Glasow air-sea-ice chamber, which I helped develop. I also write two numerical models to simulate the facility and support the experimental results. The processes investigated are 1) the redistribution of solutes within sea ice by gravity drainage, and 2) the build up and release of pressure within sea ice.

Measurements of salt and a tracer during a sea-ice growth experiment are used to evaluate four gravity drainage parameterisations. I have coded these parameterisations in a halo-dynamic model that can predict the evolution of solute concentrations in sea ice. Two parameterisations based on brine convection outperform empirical and enhanced diffusivity schemes. These results 1) confirm that convective parameterisations are a powerful tool for predicting the salinity evolution of sea ice, 2) show that these tools can be extended to any solute, and 3) add a novel line of evidence that gravity drainage is a convective process.

Pressure is measured during a suite of sea-ice growth experiments. Pressure build up, of up to 33 kPa, and relaxation are observed during initial sea-ice formation, or when sea ice is warmed. I write a thermal stress model that qualitatively reproduces observations, and aids interpretation of the pressure signals. The pressure build up during initial growth may be caused by a combination of the expansion of water upon freezing and thermal stress, while the build up during warming is caused by thermal stress. The observed signals may have significant consequences for sea-ice gas dynamics, and for setting the stress state of sea ice.

The results from this thesis provide a strong foundation for future studies in the Roland von Glasow air-sea-ice chamber, and inform the numerical modelling of sea-ice physics and biogeochemistry.

Contents

This thesis, and the facility it's built on, is dedicated to Prof. Roland von Glasow.

Roland sadly died early on in my PhD. He was a lovely person and a great example. I'm grateful for the year we worked together.

Acknowledgements

After Roland passed, I received overwhelming support from friends, colleagues, and the wider cryospheric community. I was touched by their willingness to give up their valuable time to help fill the void left by Roland's death.

In particular, thanks to James France. We spent several years working together in the Roland von Glasow air-sea-ice chamber. The facility, my scientific output, and my PhD experience would've be immeasurably poorer without James.

And thanks to my other supervisors. After Roland passed Bill Sturges, Dorothee Bakker, Martin Vancoppenolle, and Sebastien Moreau all took extra responsibility for my supervision. I was lucky to find such a generous team, and couldn't have done it without them.

Thanks to Jan Kaiser for taking responsibility for the Chamber, and helping to secure its future. He did an amazing job. Thanks also to the Ollies, Legge and Lambert, and Josue Bock for many stimulating discussions.

Dirk Notz and Leif Riemenschneider were extremely generous with their time and advice on key instrumentation. Bruno Delille, Jean-Louis Tison, Ellen Damm, Marie Kotovitch, Crispin Halsall, and Jack Garnett all came to work in the facility during my PhD, and were generous with their support. Thanks to all of them. Thanks also to Inga Smith, who emailed out of the blue with some kind thoughts and an offer of support.

The facility was made possible by the skill and dedication of the technical staff here at UEA. Dave Blomfield, Nick Griffin, Stuart Rix, and Gareth Flowerdue all contributed significant equipment to the project. Thanks to them, and to Andy Macdonald, for all the help along the way.

And, finally, thanks to my friends and family for your love and support.

This thesis was made possible by funding from the European Research Council. After Roland died the school of Environmental Sciences at UEA very kindly paid my stipend.

List of Symbols

a	fitting parameter for dye rise experiments	[cm]
A_i	internal sea-ice surface area	[cm^2 kg^{-1}]
b	fitting parameter for dye rise experiments	[s^{-1}]
br_{down}	mass of brine from sea ice to ocean	[kg m^{-2}]
br_{up}	mass of brine from moving upwards through sea ice	[kg m^{-2}]
c_l	heat capacity of water	[J m^{-3} K^{-1}]
C_b	bulk concentration concentration of a chemical	[g kg^{-1}]
C_{br}	brine concentration of a chemical	[g kg^{-1}]
C_{SA}	concentration of a chemical adsorbed per surface area	[g cm^{-2}]
C_{ads}	bulk concentration of chemical adsorbed to internal surface	[g kg^{-1}]
D_e	effective diffusivity	[m^2 s^{-1}]
D_m	molecular diffusivity	[m^2 s^{-1}
D_{tur}	turbulent diffusivity	[m^2 s^{-1}]
E	elastic modulus	[GPa]
$E^{'}$	effective elastic modulus	[GPa]
F_c	conductive heat flux	[W m^{-2}]
F_w	ocean heat flux	[W m^{-2}]
g	acceleration due to gravity	[m s^{-2}]
h	sea-ice thickness	[m]
k_l	thermal conductivity	[J s^{-1} m^{-3} K^{-1}]
k_{eff}	salt segregation coefficient	
K_{br}	compressibility of brine	[Pa^{-1}]
K_i	compressibility of ice	[Pa^{-1}]
L	latent heat of fusion	[J m^{-3}]
m_o	mass of ocean	[kg]
m_{si}	mass of sea ice	[kg]

m_{sys}	mass of system	[kg]
$m_{s,o}$	mass of salt in ocean	[g]
$m_{s,si}$	mass of salt in sea ice	[g]
$m_{s,sys}$	mass of salt in system	[g]
M	predicted mirabilite precipitate from 1kg of standard seawater cooled to temperature T	[g kg^{-1}]
M_i	bulk mirabilite concentration in sea ice	[g kg^{-1}]
n	moles of gas	[mol]
n_r	moles of gas released	[mol]
N	fractional crack coverage	
P	pressure	[kPa]
P_{bub}	pressure of bubble	[kPa]
P_e	excess brine pressure	[kPa]
P_h	hydrostatic equilibrium pressure	[kPa]
P_{sur}	pressure of surroundings	[kPa]
R	ideal gas constant	[kPa m^3 mol^{-1} K^{-1}]
Ra	Rayleigh number	
Ra_c	critical Rayleigh number	
Ra_e	effective Rayleigh number	
S	salinity	[g kg^{-1}]
S_b	bulk salinity	[g kg^{-1}]
S_{br}	brine salinity	[g kg^{-1}]
S_o	ocean salinity	[g kg^{-1}]
T	temperature	[^{o}C]
T_b	basal sea-ice temperature	[^{o}C]
T_s	surface sea-ice temperature	[^{o}C]
t	time	[s]
t_A	timescale of advection	[s]
t_D	timescale of diffusion	[s]

V	volume	[m^3]
V_a	volume of gas	[m^3]
V_{br}	volume of brine	[m^3]
V_i	volume of ice	[m^3]
V_{ss}	volume of solid salts	[m^3]
w	upwards brine velocity	[m s^{-1}]
z	depth	[m]
z_c	convecting layer depth	[m]
z_d	height of dye front	[cm]
Z_0	resistance at start of freezing	[Ω]
Z_t	resistance at some time after start of freezing	[Ω]
α_{RJW}	prefactor used to calculate w (Rees Jones and Worster, 2014)	
α_{GN}	prefactor used to calculate w (Griewank and Notz, 2013)	[kg m^{-3} s^{-1}]
β_c	concentration expansion coefficient	[(g kg^{-1})$^{-1}$]
δ	tuning parameter for gravity drainage parameterisation	[g m kg^{-1} s^{-1} $^oC^{-1}$]
η	tuning parameter for gravity drainage parameterisation	
ε	strain	
ε_t	free thermal strain rate	[s^{-1}]
Γ_0	brine conductivity at start of freezing	[Ω^{-1}]
Γ_t	brine conductivity at some time after start of freezing	[Ω^{-1}]
γ	viscous creep strain rate	[s^{-1}]
κ	coefficient of linear expansion	[$^oC^{-1}$]
μ	constant in linear liquidus relationship	[^oC kg g^{-1}]
ν	kinematic viscosity	[m^2 s^{-1}]
ρ_{br}	density of brine	[kg m^{-3}]
ρ_i	density of ice	[kg m^{-3}]
Π	permeability	[m^2]

Π_0	reference permeability	[m^2]
Π_{HM}	harmonic mean permeability	[m^2]
ϕ	solid fraction	
Φ	porosity	
σ	stress	[GPa]
χ	function to switch between D_m and D_{tur}	
ζ_t	mechanical strain rate	[s^{-1}]

List of Figures

List of Tables

Overview

Each year vast areas of ocean water freeze as polar night envelopes the high latitudes. The resulting mixture of fresh ice and salty, liquid brine is sea ice. Much of this sea-ice layer melts away as air temperatures rise in summer. This seasonal expansion and contraction of sea ice is one of the defining characteristics of polar oceans. The area of ocean that is seasonally sea-ice covered is around 7 million km^2 in the Arctic and 15 million km^2 in the Southern Ocean (Strove and Meier, 2017). Around 10% of the worlds oceans are sea-ice covered for at least part of the year.

The importance of sea ice in climate physics has long been recognised. Budycko (1969), for example, discussed the importance of the ice albedo feedback on global temperatures. As well as radiation, sea ice mediates the exchange of heat, moisture, and momentum between ocean and atmosphere. A large fraction of the salt in sea ice is transferred to the underlying ocean, and the consequent increase in water density can drive deep water formation (Meredith and Brandon, 2017). The effects of sea ice on climate are therefore globally relevant.

And sea ice is biogeochemicaly active (Loose et al., 2011). Liquid inclusions, always present in sea ice, are an extensive and unique ecosystem. Algae and bacteria live in this porous microstructure, and are an important aspect of polar ecosystems (Vancoppenolle et al., 2013). Microbial and physico-chemical processes produce and consume climactically relevant gases (Tison et al., 2002), and these gases are key to polar biogeochemical cycles (Delille et al., 2014; Rysgaard et al., 2011). The drivers and magnitudes of most biogeochemical sea ice processes remain poorly understood.

The aim of this thesis is to improve our understanding of two important physical processes in sea ice: the transport of dissolved compounds by gravity drainage, and the build up and release of pressure. Gravity drainage is a well studied process so my goal is to compare and evaluate the performance of several existing parameterisations. Pressure in sea ice is poorly understood and studied, so my goal

is to take steps towards estimating the magnitudes and drivers of pressure events in sea ice. These physical processes underpin biogeochemical processes, and a goal of this thesis is to develop our ability to model sea-ice biogeochemistry.

In the Chapter 1 I present the background knowledge that is necessary to understand subsequent results chapters. I describe what sea ice is, how it grows, and how it evolves. Because gravity drainage and pressure build up are quite different processes, detailed information about them is presented in the relevant results chapters. I also discuss the role of sea ice in the climate so that I can present my results in a wider context.

All of the measurements presented in this thesis were made using a new facility, the Roland von Glasow air-sea-ice simulator. Chapter 2 describes the design of this facility. I also present a general experimental protocol to build a picture of how the facility has been used. Similar to Chapter 1, I leave detailed methodology to the relevant results chapters.

In Chapter 3 I formulate the one dimensional (1D) thermo/halo-dynamic sea-ice model that I use to evaluate gravity drainage parameterisations. The halo dynamics in this model can be evolved using four important gravity parameterisations. I also include a dissolved tracer that moves conservatively with salt, but can be decoupled from salt. Finally, I evaluate these parameterisations against the experiments of Eide and Martin (1975). While some differences between the parameterisations are apparent, these experiments are not suitable for quantitatively evaluating the parameterisations. I therefore perform an experiment in the Roland von Glasow air-sea-ice chamber that can can be used to evaluate the parameterisations. Chapter 4 presents results from this experiment, and the performance of the model developed in Chapter 3 against these results.

To investigate pressure in sea ice I use a novel sensor, developed for the facility. In Chapter 5 I describe the design, calibration, and deployment of this sensor. I then present data collected from a set of experiments covering different temperature regimes and modes of sea-ice growth. I finish this chapter by speculating on the drivers of measured pressure signals. One such driver is thermal stress. In Chapter

6, to investigate to what extent thermal stresses are driving pressure signals, I formulate a thermal stress model (Lewis, 1998). I then compare modelled stress to measured pressure.

Chapter 7 concludes this thesis. I reflect on the outcomes of this thesis, then describe what I believe are the next steps in this work. I also suggest some studies that could use either the facility or the models I have developed.

Chapter 1

Introduction

1.1 Composition of sea ice

What do we mean by 'sea ice'? Sea ice is not simply frozen ocean, because the frozen water in sea ice exists alongside liquid brine, salt precipitates, and gas bubbles. Sea ice is a collection of these phases. In this section I describe a parcel of freezing ocean (sea ice), focusing on these different phases and how they determine important properties of the sea ice.

Imagine a small parcel of ocean, a cubic centimetre say, that is cold enough for some ice to have formed in it. I will call this parcel 'sea ice'. A reasonable approximation for many applications is that this sea ice is a two component (water and salt), two phase (ice and brine) mixture. The fraction of ice relative to the total mass or volume is the the solid fraction, ϕ. In a two component mixture the liquid fraction is equal to $1-\phi$.

As this mixture of ice and brine cools, some of the liquid in the brine freezes, increasing ϕ. To an excellent approximation, all of the salt that was dissolved in the brine is expelled from the newly formed ice back into the brine (Weeks, 2010). Fresh water is frozen from the brine until the remaining brine is at its salinity dependent freezing point. The salinity of brine within sea ice, S_{br} (g kg^{-1}), is therefore only a function of the local sea ice temperature, T (^{o}C).

$$S_{br} = f(T) \tag{1.1}$$

Equation 1.1 is valid as long as the local solid and liquid fraction of sea ice remain in thermodynamic equilibrium. Feltham et al. (2006) show that this is indeed the case in sea ice, because thermodynamic equilibrium is achieved on timescales on the order of minutes, much faster than the rate of diurnal temperature variations within the sea ice.

The form of f depends on the composition of salts in the water from which the sea ice is forming. Notz (2005) derive f for seawater and sodium chloride (NaCl) solutions, based on the experimental work of Assur (1958) and Weast (1971), respectively. The detailed form of the function to calculate the freezing point used in this thesis is presented in Chapter 2. For the purposes of this introduction it is sufficient to note that brine salinity is only a function of temperature, and that brine salinity increases with decreasing temperature.

The bulk salinity, S_b (g kg^{-1}), of the sea ice is then given by

$$S_b = (1-\phi)S_{br} \tag{1.2}$$

and is equivalent to the salinity of some mass of fully melted sea ice. In this two component system, if any two of S_b, S_{br}, and ϕ are known then the third can then be calculated *via* Equation 1.2.

When conceptualised as a two component, two phase system, Feltham et al. (2006) show that sea ice is an example of a 'mushy layer'. In a mushy layer some solid matrix (ice) contains pockets of impurity (salt) rich liquid (water). Mushy layer theory provides a set of equations to describe sea ice based on the conservation of heat and salt.

However, ice and brine are not the only phases in sea ice. A variety of solid salts precipitate in high salinity, low temperature sea-ice brines (Assur, 1958). This precipitation is driven by the increasing concentrations and reduced solubilities of dissolved salts in the brine as it cools (Equation 1.1). In natural sea ice, ikaite (a form of calcium carbonate) starts to precipitate at around -2.2 ^{o}C (Dieckmann et al., 2008, 2010), and a series of other salts precipitate out as the temperature decreases. The temperature at which a salt precipitates is the 'eutectic' temperature. In sea ice

grown from aqueous sodium chloride the situation is more simple. Only sodium chloride, as hydrohalite, precipitates, beginning at around -21 ^{o}C (Weeks, 2010).

Bubbles of gas also exist in sea ice. These bubbles may be incorporated into growing or decaying sea ice, or may nucleate within sea-ice brines (Tison et al., 2017, and references therein). If bubbles are present in the water from which sea ice forms those bubbles may be trapped in the sea ice. Also, as brines cool, an increase in gas solubility from decreasing temperature is outweighed by a decrease in solubility from increasing brine salinity. The reduction in gas solubility in brine during sea ice cooling may cause bubbles to nucleate (Zhou et al., 2013).

To summarise, cooling a small parcel of ocean below its freezing point will increase its solid (ice) fraction. The remaining liquid fraction, known as 'brine', will become more saline as salt is excluded from the newly formed ice, and the salinity of this brine can be predicted from fits to experimental data (Equation 1.1). Decreases (increases) in temperature will cause the fraction of ice to rise (fall) and the salinity of the brine to increase (decrease). If the temperature falls below the eutectic temperatures of specific salts these salts will precipitate out of solution. Also, as brine cools, the net effect of the temperature and salinity changes causes the solubility of dissolved gases in the brine to decrease. These gases will be driven towards efflux from the brine and may form bubbles. 'Sea ice', as shown in Figure 1.1, is the collection of these phases.

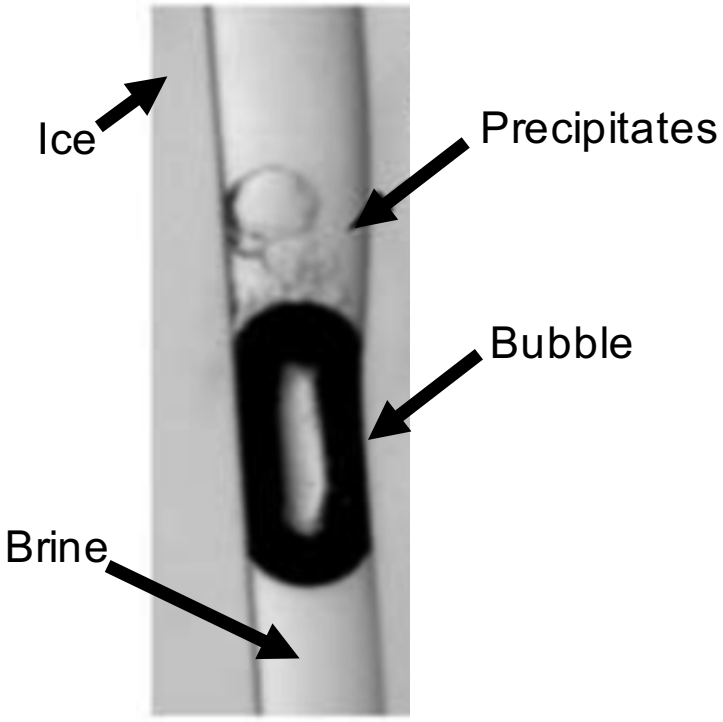

Figure 1.1: Photograph of a thin slice of sea ice, adapted from Light et al. (2003). The tube like area in the centre of the image is a brine inclusion, this brine inclusion is surrounded by ice. Mirabilite precipitates and a gas bubble exist in the brine inclusion. The width of the image is around 1 mm.

1.2 Evolution of sea ice

How does sea ice come about, and what happens to that sea ice? A given mass of sea ice, on the scale of a centimetre, is broadly similar across the globe. Sea ice from the central Arctic, like sea ice from the edge of the Southern Ocean marginal ice zone or a brackish lake, is a collection of fresh ice crystals, brine, bubbles, and solid salts. But this similarity does not necessarily hold on larger scales. The growth history of the sea ice critically determines the properties of sea ice on scales of, say, a meter.

How sea ice forms, and how sea ice evolves, under different environmental conditions is the focus of this section. I first describe by what processes sea ice grows, and how these processes lead to different types of sea ice (Section 1.2.1). Next, I describe the processes that affect the salinity of sea ice, and discuss their relative importance (Section 1.2.2). The salinity of sea ice determines the structure

of sea ice on the micro and macro scale. I then describe the porosity of sea ice, and how this porosity is determined by the history of the sea ice (Section 1.2.3). Next, I discuss how pressure may change in sea ice (Section 1.2.4). I finish this section by discussing how sea ice melts (Section 1.2.5).

1.2.1 Sea-ice growth

In the environment the growth of sea ice occurs under a wide range of conditions, and important characteristics of the resulting sea ice are determined by these conditions. Sea ice grown in a storm will differ from sea ice grown in calm waters. Sea ice thickened by dynamical processes will be more heterogeneous than sea ice grown by thermodynamic processes alone. Figure 1.2 gives some of the processes that can grow sea ice. In this section, growing specifically refers to the vertical thickening of sea ice. Internal freezing, within brine pockets, is discussed in Section 1.2.3.

The thermodynamic growth of sea ice is driven by heat transfer from the ocean to the atmosphere. Process 1 in Figure 1.2 shows the thermodynamic growth of sea ice from open water. If conditions are calm (1a), growth from open water starts when frazil ice crystals collect at the surface. These crystals grow laterally and quickly form a consolidated, elastic sheet of sea ice known as 'nilas'[1] (Naumann et al., 2012).

If conditions are turbulent (1b), the sea ice resulting from growth from open water is different. Frazil ice crystals nucleate throughout the upper water column. These rise up buoyantly and collect at the surface in a soupy layer, known as 'grease ice' (Naumann et al., 2012; De La Rosa et al., 2011). This layer would not retain its shape if extracted from the water, in contrast to nilas (Weeks, 2010). Eventually, after further cooling, grease ice consolidates into a sheet of sea ice. Frequently, under ocean swell, consolidated grease ice collects in disks, with a diameter on the order of a meter, known as 'pancake ice' (Doble et al., 2003; De La Rosa et al.,

[1]The elasticity of nilas is due to its high brine volume and elongated ice crystals (Weeks, 2010), and is discussed further in Chapter 5.

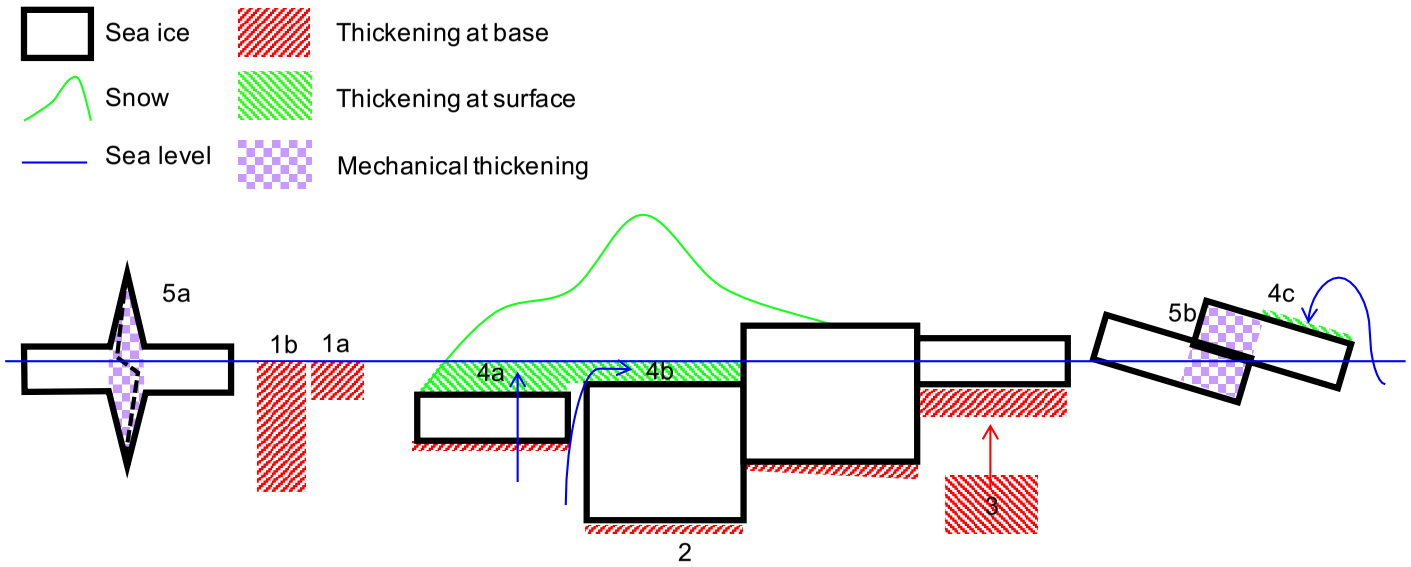

Figure 1.2: Schematic diagram of processes that thicken sea ice. 1a and 1b are the growth of sea ice from open water under calm and turbulent conditions, respectively. 2 is the growth of sea ice as heat is conducted upwards through an existing sea-ice cover. 3 shows platelet ice forming in the water column and floating to the sea-ice base. 4 shows the growth of sea ice at the surface. 4 shows the wetting and refreezing of snow through the porous sea ice (4a), and seawater rising up through cracks (4b). 4c shows the washing of seawater onto sea ice, and subsequent freezing. 5a shows ridging and 5b shows rafting.

2011).

After a consolidated layer of sea ice has been established, thermodynamic thickening of the sea ice may occur by growth at the base of the sea ice (2). Heat is conducted away from the ice/ocean interface towards the cold atmosphere. The balance of this upwards, conductive heat flux, F_c, and the heat flux to the sea ice from the ocean, F_w, drives thickening (or thinning) at the base of the sea ice according to

$$\rho_i L \frac{dh}{dt} = F_c - F_w \tag{1.3}$$

where L is the latent heat of fusion of water, $\frac{dh}{dt}$ is the rate of change of sea ice thickness over time, and ρ_i is the ice density (Maykut and Untersteiner, 1971). The conductive heat flux is greatest for thin, snow free sea ice, because icy layers insulate the ocean from the cold atmosphere. All else being equal, thin sea ice therefore grows more quickly than thicker sea ice.

Sea ice grown from the base is often called 'columnar ice' because of the orientation of the ice crystals that results from this mode of growth. The preferred growth direction of an ice crystal in sea ice is perpendicular to its c-axis (Weeks, 2010). Crystals with c-axes orientated horizontally therefore have a growth advantage and tend to cut crystals with different orientations off from the seawater below. The result of this geometric selection is sea ice with long crystals with horizontal c-axis orientation.

Another form of sea-ice thickening, particularly important in regions of the Southern Ocean in the vicinity of ice shelves, is the accumulation of small discs of ice at the base of sea ice (3). The sea ice formed in this way is often referred to as 'platelet ice' (e.g. Jeffries et al., 1993). Frazil ice crystals nucleate in the water column below sea ice and rise buoyantly to the surface. Layers of platelet ice on the order of meters thick have been observed. The mechanism for platelet ice formation is thought to involve supercooling in the vicinity of ice shelves (Weeks, 2010, and references therein).

Various processes thicken sea ice at the surface. If enough snow falls on sea ice to depress the sea ice below sea level, then liquid will flood the surface of the

sea ice. This liquid may percolate up through the sea ice (4a) (Golden et al., 1998), or may flow from the ocean through cracks (4b) (Maksym and Jeffries, 2000). This wetted snow forms a slushy layer and may re-freeze as snow ice (e.g. Maksym and Jeffries, 2000; Jutras et al., 2016). Ocean water may also wash onto the surface of floes under wave action, and the subsequent re-freezing of this liquid thickens the sea ice (4c) (Doble et al., 2003).

Two processes grow sea ice mechanically. When two floes are forced together they may form a pressure 'ridge' and 'keel' (Weeks, 2010, 5a). The ridge and keel refer to the thickened portion of the floe, with the ridge existing above the surface and the keel below. Alternatively, a floe may mount another floe under wave action, and if the interface of the two floes freezes, the sea ice in the region of overlap has essentially thickened (Dai et al., 2004, 5b).

A wide variety of processes thicken sea ice, and the relative importance of these processes varies between season and region. Sea ice thickens at the base as heat is conducted to the atmosphere, or at the surface as processes wet and refreeze snow. Mechanical processes can also thicken sea ice as floes collide. In this thesis I try to ensure only mechanisms 1 and 2 occur to simplify my experimental system as much as possible.

1.2.2 Redistribution of salt

The bulk salinity of sea ice, after some period of growth, is significantly lower than that of the ocean. Typical bulk salinities in the interior of first year sea ice are around 5 g kg^{-1} (e.g. Griewank and Notz, 2015). This loss of salt during sea-ice growth is driven by several processes. Salinity is then depleted further as sea ice begins to melt. The flux of salt between sea ice and ocean contributes to deep water formation and the formation of the Arctic halocline (Aagaard et al., 1981), both of which affect climate. In addition to its impact on sea ice/ocean coupling, the redistribution of salt within the sea ice affects important sea-ice characteristics such as the porosity and permeability (Section 1.2.3). In this section I describe the processes that affect salinity dynamics in sea ice (see also Notz and Worster, 2009,

for a review of desalination processes in sea ice).

In summer the dominant desalination process is known as 'flushing'. In essence, as overlying snow and surface sea ice melt, a hydraulic head forms on top of the sea ice. If the sea ice is permeable, this meltwater can flow through the porous microstructure, displacing brine and reducing the bulk salinity. When the meltwater reaches sea level it stops flushing the sea ice.

In winter, or when the sea ice is growing, several processes may desalinate sea ice or redistribute salt within it. Notz and Worster (2009) identify gravity drainage, brine expulsion, initial segregation, and brine pocket diffusion as such processes. I will also discuss molecular diffusion. Of all of these processes, gravity drainage is the dominant driver of desalination (Notz and Worster, 2009).

The driver of gravity drainage is the temperature profile in growing sea ice, where the coldest temperatures are nearest the cold atmosphere. Because brine salinity is only a function of temperature, with colder temperatures producing higher brine salinities (Equation 1.1), the brine salinity in growing sea ice increases towards the sea ice/atmosphere interface. Brine density increases with brine salinity (Cox and Weeks, 1983) so the brine density also increases towards the sea ice/atmosphere interface. This dense brine overlying less dense brine and ocean causes an instability. This instability causes brine to drain from the sea ice, and this desalination is gravity drainage.

There is strong evidence, from laboratory (Eide and Martin, 1975) and modelling studies (Oertling and Watts, 2004; Wells et al., 2010, 2011, 2013), that gravity drainage is a convective process. Brine that drains from the sea ice is replaced by upwelling brine and ocean. Because the upwelling brine and ocean are less saline than the downwelling brine, this convection causes a net desalination. The biogeochemical consequences of this return flow are discussed in Section 1.3.1.

Whether or not sea ice is convecting can be diagnosed using a Rayleigh number, Ra (Wells et al., 2011; Griewank and Notz, 2013; Worster and Rees Jones, 2015). The Rayleigh number represents the ratio of the the diffusive and advective timescales acting on sea ice brines, t_D and t_A, respectively (Griewank and Notz,

2013).

$$Ra = \frac{t_D}{t_A} \tag{1.4}$$

As brine flows downwards through the sea ice, on a timescale of t_A, energy is dissipated through thermal diffusion and viscosity, on a timescale of t_D. High Rayleigh numbers indicate that brine is flowing so fast that it cannot attain thermal equilibrium with its surroundings before reaching the ocean, and so flows into the ocean. When the Rayleigh number is sufficiently high, over some critical Rayleigh number, brine convection occurs.

There are several second order processes acting on the salinity profile in sea ice. 'Brine expulsion' is the movement of brine in response to the volume increase of freezing water (Cox and Weeks, 1986). Notz (2005) shows that brine expulsion cannot remove salt from the sea ice, and Notz and Worster (2009) find that the redistribution of salt within a depth of sea ice is on the order of 1% of the bulk salinity. 'Brine diffusion' is the migration of brine inclusions driven by the temperature gradient within the inclusion. The bottom of a brine pocket is warm relative to the top. Brine, at a given temperature, will therefore dissolve the ice at the base of the pocket, while the brine at the top of the pocket partially freezes. In this way, brine pockets can move downwards. However, the vertical distance travelled by a brine pocket during the growth season by brine diffusion is likely less than 2 cm (Notz and Worster, 2009, and references therein), so is almost always negligible. Salt may also be transported by molecular diffusion within and between brine inclusions. The effect of the molecular diffusion of salt is orders of magnitude weaker than gravity drainage, and cannot account for observed desalinations (Vancoppenolle et al., 2010).

A controversial desalination process is the initial segregation of salt at the advancing interface. During initial segregation, forming sea ice is assumed to have a bulk salinity that is lower than the ocean salinity, with the difference in salt rejected instantly to the ocean. The fraction of the ocean salinity remaining in the sea ice has been parameterised as a function of growth rate (Cox and Weeks, 1988, see also Chapter 3). Weeks (2010) assert that initial segregation 'is the aspect of the salinity

of sea ice where we have the best predictive capacity'.

However, using *in situ* measurements of bulk salinity, Notz and Worster (2008) show that the bulk salinity is continuous across the sea-ice/ocean interface, refuting initial segregation. Despite this result, initial segregation features in modelling studies by Saenz and Arrigo (2012); Vancoppenolle et al. (2007); Butler et al. (2016), and as recently as Butler et al. (2017).

Part of this conflict is due to a discrepancy in the definition of the sea-ice/ocean interface. Notz and Worster were interested in developing a model of sea ice as a mushy layer. In their proposed framework, the ocean is simply a region of sea ice with 0 solid fraction. The bulk salinity must be continuous across the interface, because the interface is defined as the depth where solid fraction becomes 0. Cox and Weeks were concerned with modelling the strength of sea ice, and to achieve this they needed to model the solid fraction *via* the salinity (Equation 1.2). Noting that the bottom portion of sea ice, the 'skeletal layer', was poorly understood and likely had no strength, they neglected it from their model. They constructed a model predicting bulk salinity (including an initial segregation scheme) that performed adequately for sea ice, providing sea ice was defined as the the region from the sea-ice/atmosphere interface to the top of the skeletal layer. Initial segregation, for Cox and Weeks (1988), is effectively a parameterisation of the desalination of the skeletal layer. For many applications, the study of sea ice algae for example, modelling the skeletal layer is critical. The empirical parameterisation of Cox and Weeks (1988) may not be useful for such problems.

Several modelling studies have attempted to capture the evolution of sea-ice salinity. The salinity of growing sea ice can be accurately modelled taking into account only gravity drainage (Rees Jones and Worster, 2014). To accurately model bulk salinity over a full growth/melt cycle in sea ice, flushing must be modelled alongside gravity drainage (Griewank and Notz, 2013). Depending on the region of interest, other processes such as salt entrapment with platelet ice, and snow ice formation (Maksym and Jeffries, 2000), may be necessary to accurately model bulk salinity.

In summary, when sea ice forms all of the salt that was present in the freezing ocean water is retained within the sea ice, partitioned to the liquid fraction. During the subsequent growth and evolution of the sea ice, salt is redistributed and the sea ice desalinates. Flushing and gravity drainage are the dominant processes redistributing and removing salt from the sea ice. The bulk salinity profiles of growing sea ice can be accurately modelled by considering desalination by gravity drainage only.

1.2.3 Evolving porosity

Sea ice is a porous matrix of ice crystals interspersed with fluid inclusions and salt precipitates (Section 1.1). The fraction of the total volume that these inclusions occupy is the porosity of the sea ice. The porosity determines important sea-ice properties, such as the albedo (Light et al., 2003) and and habitable volume (Krembs et al., 2000). The porosity also critically affects the permeability of sea ice, and as such controls the movement of fluids within it. The porosity changes, both in terms of the size and spatial distribution, as sea ice cools and desalinates. The evolution of porosity is critical for a wide range of sea-ice processes.

In this section I first define porosity for two phase sea ice (ice plus brine), and then for sea ice also including gas bubbles and solid salts. I then discuss the distribution of this porosity within sea ice. Finally, I discuss how porosity affects the permeability of sea ice.

Approximating sea ice as a two component mixture of ice and brine, the porosity, Φ, is simply the volume of brine, V_{br}, as a fraction of the total sea-ice volume, $V_{br} + V_i$.

$$\Phi = \frac{V_{br}}{V_{br} + V_i} \tag{1.5}$$

In a two component system Φ is simply the liquid fraction, $1 - \phi$.

The total brine volume of a section of sea ice will be distributed over many brine inclusions. Because these inclusions tend to form in the interstitial space between crystals, the inclusions tend to be roughly cylindrical (Eicken et al., 2000). The long axis of a brine inclusion lies perpendicular to the c-axis of adjacent ice

crystals, which tend to point horizontally (Weeks, 2010).

Changes in local temperature will change the size of brine inclusions (Eicken et al., 2000, Figure 1.3). The salinity of the brine within them remains at its salinity dependent freezing point because the amount of liquid water increases upon warming and decreases upon cooling. Cooling sea ice therefore reduces the size of brine inclusions, and so decreases the porosity. Cooling may also increase the number of brine inclusions as single inclusions may shrink so much that they neck and form multiple, smaller inclusions (Eicken et al., 2000).

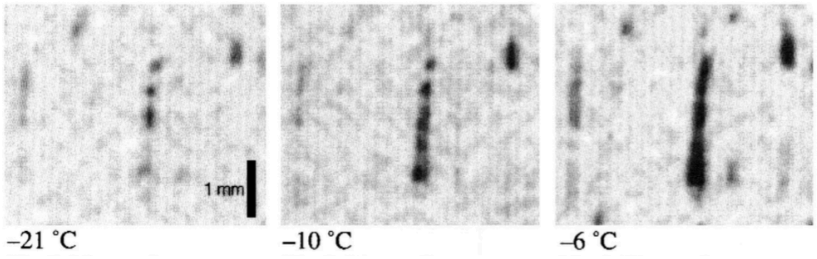

Figure 1.3: MRI of sea ice, adapted from Eicken et al. (2000). The dark areas are brine inclusions, and the light areas are ice. As the temperature is increased the brine inclusions expand and some merge together.

The distribution of brine inclusions is not homogeneous, vertically or horizontally. The convection of brine within growing sea ice tends to increase the brine volume fraction in areas of downwelling, and to decrease the brine volume fraction in areas of upwelling (Rees Jones and Worster, 2014). To see why, consider a parcel of downwelling brine. This brine must be colder, saltier, and denser than brine deeper in the sea ice, because the increased density is the driving force behind it downwelling. As the brine moves downwards it comes into contact with sea ice at a higher temperature. The brine pocket is now out of thermodynamic equilibrium, with a freezing point below the local temperature (Equation 1.1). The local liquid fraction increases to maintain thermodynamic equilibrium. The converse applies to the upward moving return flow.

The increase in liquid fraction in areas of downwelling creates macroscopic features in sea ice, know as ‘brine channels’. Figure 1.4 shows an MRI scan of a brine channel (Galley et al., 2015). The brine channel is approximately vertical, extending from the interior of the sea ice for around 8 cm to the ocean. Diagonal

branch like areas of high brine volume feed into the main brine channel. Brine channels have been observed in the laboratory (Eide and Martin, 1975; Niedrauer and Martin, 1979; Cottier et al., 1999; Middleton et al., 2016), in the field (Lake and Lewis, 1970), and have been simulated in two dimensional (2D) models (Oertling and Watts, 2004; Wells et al., 2011). Brine channels are ubiquitous in growing sea ice.

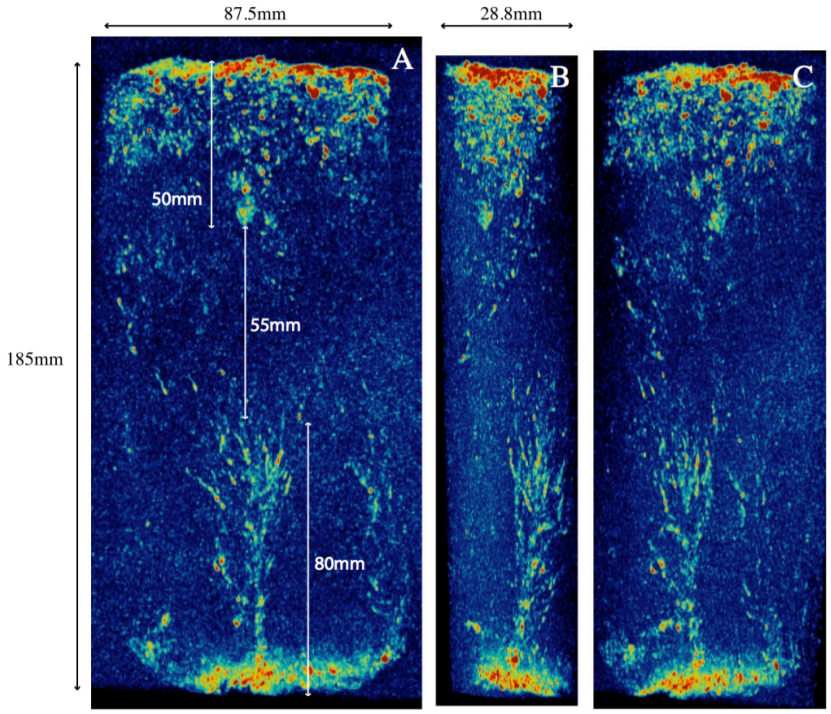

Figure 1.4: MRI of a vertical profile of sea ice, adapted from Galley et al. (2015). Brighter areas contain more brine. The vertical feature with high brine volume in the deepest 80 mm of sea ice is a brine channel. The three images show the same sea ice rotated around the vertical axis.

The brine volume fractions of nilas and grease ice are around 0.25 as they initially form (Naumann et al., 2012). The solid fraction of nilas rises during growth. The solid fraction of grease ice also rises until it begins to consolidate at a solid fraction of around 0.4 (De La Rosa et al., 2011). As young sea ice cools and desalinates the brine volume fraction will decrease. Depending on its history first year sea ice will have a brine volume fraction in the interior of around 0.05 after cooling and desalination. Flushing in summer will reduce the brine volume fraction, so multi year ice will often have a lower brine volume fraction. Towards

the base of the sea ice the brine volume fraction will transition towards 1.

In reality, the porosity of natural sea ice will contain the volume of gas and solid salts, though gases and precipitates likely exist in brine inclusions (Light et al., 2003). In this case, the porosity would be

$$\Phi = \frac{V_{br} + V_a + V_{ss}}{V_{br} + V_a + V_{ss} + V_i} \tag{1.6}$$

where V_a is the air volume, V_{ss} is the volume of solid salts, and the denominator is the volume of sea ice[2]. Estimates from Loose et al. (2011), Nakawo (1983), and Cox and Weeks (1983) give air volume fractions in first year sea ice of around 0.01. The air volume fraction in multi year ice may be larger because freeze/melt cycles may leave large voids in the sea ice.

The precipitation of ikaite at around -2 ^{o}C means solid salts are present even in young, relatively warm sea ice. As temperatures drop below this temperature more salts will precipitate out. This increase in precipitated salts with decreasing sea ice temperature is partially balanced by a decrease in the bulk salinity by desalination that reduces the pool of ions from which salts can precipitate. In extremely cold sea ice, where precipitate concentrations will be largest, precipitated salts are predicted to be around 10 g kg^{-1} by mass (Butler et al., 2016, 2017). Taking the density of salt to be around 1500 kg m^{-3}, the solid salt volume fraction is likely to reach a maximum at around 0.01.

The local permeability, Π, of young sea ice composed of ice and brine can be calculated from the local porosity using (Freitag, 1999)

$$\Pi = 10^{1.9953}(1-\phi)^{3.1} \tag{1.7}$$

The permeability increases exponentially as the solid fraction decreases. Other things being equal, warmer and saltier sea ice will tend to have higher permeabilities. The air and solid salt volume fraction may slightly increase the permeability

[2]I have included solid salts in this definition because even though they are solid they do not contribute to the ice matrix of sea ice that contains the porosity.

at a given solid fraction, because, when present, gas bubbles and solid salts will increase the porosity above $1 - \phi$.

Ono and Kasai (1985) measure the permeability of young sea ice at a series of surface temperatures, and find that the permeability increases sharply above around -5 ^{o}C. Motivated by this observation, Golden et al. (1998) apply a percolation theory model to sea ice, and propose that the permeability of sea ice suddenly and dramatically increases at a brine volume of around 5%[3]. They conclude that around 5% brine volume is the critical threshold at which the microstructure of sea ice becomes well connected, with brine free to flow between inclusions. A subsequent study by Pringle et al. (2009) calculated a similar threshold by measuring the pore space of a single ice crystal.

By studying argon dynamics in first year sea ice, Zhou et al. (2013) were able to estimate the brine volume fraction at which gas bubbles migrated upwards through sea ice. They find that bubbles escaped somewhere between 7.5 and 10% brine volume. This threshold is analogous to the 5% critical brine volume for brine connectivity (Golden et al., 1998). Zhou et al. (2013) calculated V_{br} using empirical relationships relating S_b to T (Cox and Weeks, 1983). They neglect the air volume in their calculations so the 7.5 to 10% brine volume threshold likely underestimates the total porosity needed for bubbles to migrate by around 1%. Solid salts may fall out of sea ice once it becomes sufficiently porous, but to the best of my knowledge no study has proposed a porosity threshold for solid salts.

In summary, the brine volume fraction of sea ice is determined by the amount of salt in the sea ice and the temperature, with decreasing temperature or bulk salinity leading to decreases in brine volume fraction. Porosity therefore tends to decrease during sea-ice growth, increase during melt, and increase towards the warmer base of the sea ice. The brine volume fraction is generally a close approximation of the porosity. Brine is not distributed evenly in the sea ice. Areas containing brine channels tend to have a higher brine fraction. The air volume contributes around 1% to the total porosity of young and first year sea ice, and

[3]Which corresponds to a temperature of around -5 ^{o}C and a bulk salinity of around 5, the so called 'rule of fives'. (Golden et al., 1998)

the volume of solid salts is even less. The permeability of sea ice is a function of porosity, with increases in porosity leading to exponential increases in permeability. For some applications it may be useful to specify around 5%, and 7.5 to 10%, as the thresholds at which brine and bubbles may migrate, respectively.

1.2.4 Pressure dynamics

There are several reasons to believe that pressure could rise or fall dramatically in sea ice. Sea ice is dynamic with regards to both the movement of floes, and changes in microstructure. Winds and waves interact with the sea ice. Such forcing may exert pressure on the sea ice. Internally, changes in temperature and salinity drive phase changes. Each of these phase changes is associated with a density change, and in enclosed brine pockets, these density changes could cause pressure effects. Pressure within brine inclusions could have important effects on processes such as gas dynamics (Section 1.3.3).

Despite the many possible drivers of pressure increases in sea ice, and the potential importance of pressure, little is known about the magnitudes of pressure in sea ice. In this section I describe what we know about sea-ice pressure, and how pressure might change in an evolving sea-ice cover.

Events, external to sea ice, may cause pressure events within sea ice. The collision of sea-ice floes, for example, often exerts enough pressure to deform and ridge sea ice (Richter-Menge and Elder, 1998). Internal sea-ice stresses of several hundred kPa have been measured, both compressive and tensile (Tucker and Perovich, 1992; Lewis et al., 1994). These stresses were caused by a combination of dynamic and thermal events. To what extent these stresses were experienced as pressures by brine inclusions was not considered, but the presence of these stresses provides a possible mechanism for pressure build up in sea ice.

Phase changes may also cause pressure build up within sea ice brine inclusions. Assuming constant pressure, when liquid brine freezes, or when dissolved gases efflux, there is a concurrent increase in volume. If either of these occurs in an enclosed environment, such as an isolated brine inclusion, then the volume cannot

change and there must be an increase in pressure.

Results from the experiments of Light et al. (2003) suggest that the pressure in brine inclusions may be variable. They photographed isolated brine inclusions in thin sections of sea ice during cooling and warming cycles. During cooling they observed decreases in the size of brine inclusions as fresh water freezes from the brine. Light et al. also observed shrinking, and sometimes total disappearance of gas bubbles within the shrinking brine inclusions. The gas in these bubbles may have been pressurised by the volume expansion of the now frozen water. This increased pressure had either driven the gas to partition to the dissolved phase, or somehow driven the gas from the brine inclusion. Note that this pressure effect must be dominating the decrease in gas solubility caused by the increase in brine salinity (Section 1.1).

Observations by Light et al. (2003) during warming also suggest that the pressure in brine inclusions may vary. They observed brine pockets expanding during warming, as the brine pocket walls melted. The corresponding increase in density within an enclosed volume did not lead to the formation of voids or gas inclusions. This surprising results suggests that either some unseen brine was flowing into the inclusions, or that the pressure in the inclusions had decreased significantly.

The study of Nakawo (1983) goes some way towards constraining the pressure of gaseous inclusions in sea ice. They compare measurements of gas volume to theoretical predictions of gas volume from measured sea-ice density. The two agree well when the bubbles are taken to be at atmospheric pressure, which suggests that the bubbles were at around atmospheric pressure *in situ*. However, Nakawo (1983) note that their results would be biased towards atmospheric pressure because of brine drainage during the extraction of their samples. Also, their results are relevant for an average pressure upon sampling and could mask local or transient pressure deviations from atmospheric. Given that the sensitivity of their measured pressure to assumed bubble pressure is not presented, these results cannot be used to quantitatively constrain bubble pressure in sea ice.

Little is known about pressure in sea ice and in sea-ice brines. Large stresses have been observed in sea ice, and these may pressurise brine inclusions. Phase changes are constantly occurring in sea ice and may pressurise isolated brine inclusions. Currently the sparse, indirect measurements and inferences of bubble pressure are not sufficient to constrain the range of bubble pressures in sea ice.

1.2.5 Sea-ice melt

Sea-ice melt may occur at the surface, base, or edge of sea ice. The way sea ice melts influences the rate of the melting and the state of the sea ice after melt. Surface melting, for example, may accelerate melt because of feedbacks. In this section I limit the discussion of melting to the external surfaces of the sea ice.

Sea-ice melt occurs at the base of the ice when more heat is input into the sea-ice/ocean interface by the ocean than is removed through the sea ice by conduction. This occurs when F_w is greater than F_c in Equation 1.3. Because F_c is affected by sea-ice thickness and the atmospheric temperature, the growth history of sea ice and the atmospheric temperature partially determine whether basal melting takes place.

Surface melting of sea ice is driven by warming atmospheric temperatures in spring and summer. Increased downwelling longwave and shortwave radiation increase the temperature of the near surface sea ice until it reaches its melting temperature, and this near surface sea ice begins to melt.

A prominent and climactically relevant consequence of surface melting is the formation of melt ponds. These form when melting sea ice or snow collects on the surface of sea ice. Meltponds may drain until they reach sea level, or may sit above sea level if the sea ice is impermeable (Polashenski et al., 2017). In the Arctic widespread ponding occurs at the sea-ice surface. The albedo of meltponds (0.15 to 0.4) is lower than the albedo of bare or snow covered sea ice (0.5 to 0.95) (Schröder et al., 2014). Ponded sea ice therefore absorbs more incoming radiation, and so warms quicker. This positive feedback accelerates the melting of ponded sea ice.

Meltponds also exist under sea ice (Notz et al., 2003; Eicken, 1994). Draining meltwater is fresher than the underlying seawater due to desalination of the sea

ice (Section 1.2.2) and so can collect at the underside of the sea ice. Because the collected meltwater is fresh, and so has a higher freezing point, the interface between the meltwater and the seawater may be below the freezing point of the meltwater. A lens of meltwater may then freeze and isolate the under ice meltpond from the ocean. These lenses may be a source of heat to the ocean, and may cause an overall thickening of the sea ice.

Sea ice may melt at the upper or lower interface, and this melt is driven by the balance of fluxes at that interface. Ponds of fresh water may form as sea ice melts. These ponds can be above or below the sea ice, and significantly affect subsequent sea ice melt.

1.3 Biogeochemical impacts of gravity drainage and pressure

As well as determining the porosity and permeability of sea ice (Section 1.2.3), gravity drainage affects any biogeochemical process in growing sea ice. Gravity drainage directly and obviously affects several processes by transporting dissolved, biogeochemically relevant tracers. Such a tracer could be dissolved nutrients, gases, or pollutants[4]. Algae rely on nutrient replenishment from gravity drainage (Fritsen et al., 1994), for example. Section 1.3.1 discusses how general dissolved tracers differ from salt, and how gravity drainage transports these general dissolved tracers. The convective nature of gravity drainage also has a subtle and disguised effect on processes where a compound is partitioned between a dissolved and non-dissolved phase. Sections 1.3.2 and 1.3.3 discus how gravity drainage may affect these processes in ways that are often neglected in the literature.

Pressure may also affect several biogeochemical processes in sea ice. The partitioning of gases within brine inclusions, for example, will depend on the local pressure. The transport of gases may also be partially driven by pressure. Section 1.3.3 discusses the role of pressure in sea-ice gas dynamics.

[4]I have used ‘tracer’ to describe these because later in this thesis I use measurements of salt and rhodamine to trace brine dynamics.

1.3.1 Transport of dissolved tracers

Salinity is one example of a dissolved tracer in sea ice, but there is a distinction between salinity and a general dissolved tracer. For example, the salinity of brine is only a function of temperature (Section 1.1). Because other tracers may be created, destroyed, or partitioned out of the dissolved phase in sea ice, the brine concentration of a general dissolved tracer is not a function of temperature. It is a function of the amount of tracer and the brine volume. Because brine salinity is a function of temperature, its profile through growing sea ice is monotonic and approximately linear with depth (Cox and Weeks, 1988). The profile of a general dissolver tracer may not be either.

The distinction between salt and general dissolved tracers is highlighted by the performance of a widely used gravity drainage parameterisation, presented originally in Cox and Weeks (1988). The details of this scheme are discussed in detail in Chapter 3. This scheme can adequately reproduce sea-ice salinity profiles during a growth season. However, it is unable to predict tracer concentrations because it relies on a monotonic and close to linear concentration profile, which may not be a valid assumption for a general dissolved tracer. Similar arguments could be made for the scheme of Turner et al. (2013). The constraints on the brine salinity of sea ice allow parameterisations to function well for salinity, but poorly for general dissolved tracers which are not subject to such constraints.

The processes that transport general dissolved tracers are the same as those that transport salt. Gravity drainage is therefore the dominant transport mechanism for general dissolved tracers in growing sea ice. However, the differences between salt and general dissolved tracers means that evaluating the performance of gravity drainage parameterisations against salinity is not sufficient if they are to be applied to general dissolved tracers.

1.3.2 Precipitation of salts

The albedo and chemical properties of sea ice are affected by salt precipitation. The precipitation of salts alters ionic ratios in sea-ice brines, and the exchange of these brines with the ocean and atmosphere has consequences for marine biogeochemical cycles (Rysgaard et al., 2012), atmospheric chemistry (Sander et al., 2006), and ice core proxies (Rankin et al., 2000). Ikaite, for example, has been observed in Arctic and Southern Ocean sea ice, and plays a role in polar carbon cycling (Rysgaard et al., 2011, 2012). Recently, modelling studies have predicted mirabilite and gypsum concentrations in first year sea ice (Butler et al., 2016, 2017).

The range of pressure within sea ice probably has a small or negligible effect on salt precipitation. Marion et al. (2005) use a salt precipitation model to calculate the effect of pressure on the eutectic temperature of various salts. Their scientific interest was one of Jupiter's moons, Europa, which is hypothesised to have and icy crust several kilometres thick. Marion et al. (2005) find that the effect of several hundred bars of pressure only decreases the eutectic temperature of various salts by around 1 K. The pressures in sea ice on the order of a meter thick are likely much less than those considered by Marion et al. (2005), so the effect of sea-ice pressures on salt precipitation is likely negligible.

Gravity drainage affects salt precipitation in two ways. First, salt is removed from the sea ice. The pool of ions is therefore reduced, and less salts can precipitate. This aspect of gravity drainage is captured by the studies of Butler et al. (2016, 2017). Second, convective overturning may replenish dissolved ions in brine that has undergone precipitation (Figure 1.5). This process is analogous to the often noted replenishment of nutrients after they have been eaten (e.g. Fritsen et al., 1994). Just as algae in sea ice would be less numerous of there was no nutrient re-supply from the ocean, precipitate mass may be reduced if there were no convective re-supply of dissolved ions. This re-supply is neglected by the studies of Butler et al. (2016, 2017), and as such these studies may underestimate the degree of salt precipitation (see also Chapter 7).

The separation of stationary, precipitated salts from the mobile, dissolved ions

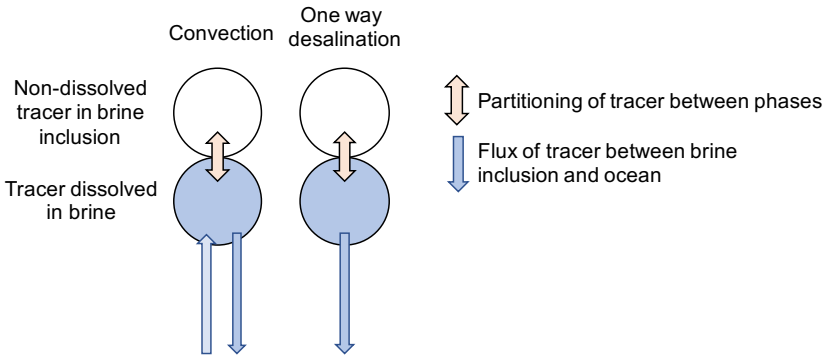

Figure 1.5: Diagram of the dynamics of some tracer in sea ice. The dissolved tracer (blue circles) is transported by gravity drainage. The blue arrows show fluxes of dissolved tracer or brine. If the dissolved tracer were salt, the downflow in the convective scheme would be more concentrated than the upflow. For a general dissolved tracer there is no such constraint. Some process, represented by the orange arrows, partitions tracer between the dissolved phase and some other phase (white circles). This process could be the precipitation of salts (Section 1.3.2), the nucleation of bubbles (Section 1.3.3), or some other process.

The effect of convection (left diagram) relative to one way desalination (right diagram) is discussed in Section 1.3.2. That even stationary bubbles control gas dynamics, illustrated by either diagram, is discussed in Section 1.3.3.

also has implications for bulk salinity measurements (Butler et al., 2016). If the ionic ratios in sea-ice brines deviate from the ionic ratios in seawater, then using conductivity to measure the bulk salinity may cause systematic errors.

When salt precipitation and brine convection have occurred in a brine inclusion, the ionic ratios in that inclusion will be distorted away from those in seawater frozen to that temperature. Distorted ionic ratios relative to seawater may lead to measurement errors in bulk salinity. These distorted ionic ratios may also affect the precipitation of further salts. The transport of dissolved compounds in general, rather than the salt alone, is what must be modelled to most accurately predict salt precipitation in sea ice. In growing sea ice this transport process is gravity drainage.

1.3.3 Transport of gases

Gases in sea ice are involved in biogeochemical cycling of climactically relevant compounds (Delille et al., 2014). CO_2, for example, may be produced or consumed, and transported within sea ice. This, and other, gases may be exchanged with the ocean and atmosphere (Gosink et al., 1976; Delille et al., 2014). Analogous to dissolved and precipitated salts (Section 1.3.2, Figure 1.5), gas dynamics in sea ice

are complicated by the partitioning of gases between dissolved and gaseous phases.

In this section I first review the literature on sea-ice gas dynamics. Then, building on the work of Crabeck et al. (2014), I propose a conceptual model of sea-ice gas dynamics. I then consider how gravity drainage and pressure may affect the various processes highlighted by the conceptual model.

The processes transporting dissolved gases in sea ice are the same as those for general dissolved compounds (Sections 1.2.2 and 1.3.1). However, gases are also transported by bubbles within the sea ice (e.g. Crabeck et al., 2014). To describe the transport of gases in sea ice, two additional processes are therefore required: bubble nucleation and bubble rise.

Bubble nucleation is the process by which bubbles form in sea-ice brine inclusions. Bubbles may also be incorporated into sea ice from the ocean and atmosphere, but gas dynamics within sea ice can be described without considering these, so I ignore them in this discussion. Measurements of argon in first year sea ice suggest that bubbles do indeed nucleate in brine inclusions (Zhou et al., 2013). Zhou et al. (2013) compare the total argon (gaseous and dissolved) present in an evolving first year sea ice cover to the theoretical maximum amount that could be dissolved in the brine. Early in the growth season the total argon was close to the theoretical dissolved maximum, indicating that most argon was dissolved. As the sea ice cooled the argon solubility in brine decreased, but the total gas did not. Eventually the argon far exceeded its theoretical dissolved maximum, indicating much of the argon existed in bubbles, or that the bubbles were at greater than atmospheric pressure.

Bubble rise, sometimes called ‘bubble migration’, is the process by which bubbles buoyantly rise upwards in the sea ice. Zhou et al. (2013) find evidence for bubble migration also. They observed the sea ice become more porous as it warmed. At some point during this increase in porosity, as the brine volume reached 7.5 to 10%, the total argon concentration decreased, and decreased to the theoretical dissolved maximum. Zhou et al. (2013) conclude that the argon bubbles that had built up during cooling were rapidly released to the atmosphere under buoyancy as

the sea ice became permeable enough to permit their rise.

I have taken several robust, qualitative statements from the research into gas dynamics (see also Crabeck et al. (2014)):

- Gasses are entrained, dissolved and in bubbles, during sea-ice growth (Tison et al., 2017)
- Gas bubbles are present in brine inclusions, and, probably, dominantly in brine inclusions (Light et al., 2003)
- Dissolved gasses may be transported by the same processes as salt
- The increasing salinity of cooling brine, and the consequent decrease in gas solubility, may cause dissolved gasses to efflux to bubbles (Tison et al., 2002)
- Cooling of brine, and the shrinking and pressurisation of isolated brine inclusions, may cause gases in bubbles to dissolve in brine (Light et al., 2003)
- In growing sea ice, gases may be far in excess of the amount that could theoretically be dissolved in the brine at atmospheric pressure (Zhou et al., 2013)
- Bubbles may rise buoyantly when the sea-ice brine volume is between 7.5 and 10% (Zhou et al., 2013).

Crabeck et al. (2014) propose a conceptual model of sea ice gas dynamics that goes some way to formalising such observations. They use permeability thresholds for brine (Golden et al., 1998, $V_{br} > 5\%$) and gas (Zhou et al., 2013, taken to be $V_{br} = 7\%$) to define the regions where these fluids can flow. They also use critical Raleigh number thresholds, $Ra_c = 5$ to 10, to define when gravity drainage is occurring. Their model defines three gas dynamics regimes:

C1: If $Ra < Ra_c$ or $V_{br} < 7\%$ then diffusion processes control the gas content.

C2: If $Ra > Ra_c$ and $V_{br} > 5\%$ then brine convection controls the gas content.

C3: If $V_{br} > 7\%$ and $Ra < Ra_c$ bubble migration and diffusion control the gas content.

However, these regimes must be revised in several ways if they are to be consistent with our understanding of bubble and brine dynamics. First, the use of a Rayleigh number and brine volume to define regions where the sea ice is convecting is unhelpful. The Rayleigh number takes porosity into account because it includes the permeability, and only the Rayleigh number should be used to define regions of convection (Worster and Rees Jones, 2015). Second, recent studies show that sea ice convects below the shallowest super critical Rayleigh number (Rees Jones and Worster, 2014; Worster and Rees Jones, 2015). Convection may therefore occur in a layer with a subcritical *Ra* if there is some shallower layer that is convecting. Whether or not a layer is convecting should be defined by it's existence within or outside of a convecting region of sea ice, rather than the local Rayleigh number.

My third criticism focuses on regime C2, which is defined incorrectly. Regime C2 states, implicitly, that bubbles can play no role in gas dynamics if sea ice is convecting. This statement is not obvious and is not justified, and must be revised. As an example, take sea ice that is permeable to bubble rise and convecting. Bubble rise should partially control gas dynamics in this case.

My fourth criticism applies to the model as a whole. Crabeck et al. (2014) assume that if bubbles are stationary ($V_{br} < 7\%$) they cannot control the gas dynamics. This assumption is not valid because bubbles are not the only mobile phase in sea ice. Bubble nucleation probably does occur in sea ice that is impermeable to bubble rise (Zhou et al., 2013). This bubble nucleation controls gas dynamics if there is a subsequent separation of the dissolved and gaseous phases. Even if the bubble remains stationary, convecting or diffusing brine will separate the phases. Gas may be transferred between the bubble and the brine, so the nucleation of the bubble exerts a part control on the gas dynamics. Figure 1.5 shows a brine pocket, where brine is advecting, in contact with a bubble (or any stationary phase), illustrating that the stationary bubble does control gas dynamics.

In light of these criticisms, I have revised the model proposed by Crabeck et al.

(2014) (regimes C1 to C3) to form a new conceptual model (G1:G4), which I use to discuss the effects of gravity drainage and pressure on gas dynamics. In my model I have, following, Crabeck et al. (2014), assumed that molecular diffusion is insignificant relative to convection in convecting sea ice. I use the phrase 'permeable (impermeable) to bubbles' to identify sea ice with a brine volume fraction of more (less) than $7.5 - 10\%$ (Zhou et al., 2013). I use the phrase 'is (is not) convecting' to indicate that some sea ice is within (outside of) the convecting layer. I also split the term 'bubble migration' used by Crabeck et al. (2014) into 'bubble nucleation' and 'bubble rise'. My revised regimes are:

G1 When sea ice is convecting and impermeable to bubbles, convection and bubble nucleation control the gas dynamics.

G2 When sea ice is convecting and permeable to bubbles, convection and bubble nucleation and rise control the gas dynamics.

G3 When sea ice is not convecting and is permeable to bubbles, bubble nucleation and rise control the gas dynamics.

G4 When sea ice is not convecting and is impermeable to bubbles, bubble nucleation and diffusion processes control the gas dynamics.

The numerical scheme in the modelling studies of Moreau et al. (2014), Moreau et al. (2015), and Kotovitch et al. (2016) is consistent with the revised conceptual model I have proposed. The scheme used in these studies is not consistent with the conceptual model of Crabeck et al. (2014).

Bubble nucleation features in every regime in the revised scheme, highlighting its importance. Despite the critical role bubble nucleation plays in gas dynamics, the processes controlling bubble nucleation in sea ice are poorly understood. This issue is highlighted by a discrepancy between the studies of Kotovitch et al. (2016) and Moreau et al. (2014). Both of these studies use a 1D biogeochemical sea-ice model (LIM1D) to study gas dynamics in sea ice. The model includes a bubble physics routine with a parameterisation for bubble nucleation, with a tunable bubble

nucleation timescale. To capture observations of gas fluxes over sea ice Kotovitch et al. (2016) are forced to use a bubble nucleation time scale an order of magnitude larger than Moreau et al. (2014), even though the physical parameterisations were the same for both studies. Important controls are likely captured poorly in the parameterisation of bubble nucleation in these studies.

Equation 1.8 is a reasonable starting point to explore the controls on bubble nucleation for a bubble in contact with brine, as it gives the equilibrium concentration of a gas dissolved in brine, C_{br} (Tison et al., 2017).

$$K_0 = \frac{C_{br}}{f_{bub}} \tag{1.8}$$

In Equation 1.8, K_0 is the equilibrium solubility of some gas and f_{bub} is the fugacity of gas in a bubble. K_0 is experimentally determined, and is a function of temperature and salinity (Weiss, 1974). In sea ice K_0 must often be extrapolated far outside the range of data, and so should be used with caution. However, for the purposes of this discussion it is sufficient to note that increasing brine salinity and decreasing brine temperature will decrease K_0, and that the net effect of cooling sea ice brines is to decrease K_0.

In growing sea ice, gravity drainage will control the transport of dissolved gases and so control C_{br} (Notz and Worster, 2009). If, for example, some gas was removed from the dissolved phase by bubble nucleation in the convecting region of sea ice, gravity drainage could replenish this dissolved this gas by drawing it up from deeper in the sea ice or the ocean (Figure 1.5). Assuming the partitioning of the gas followed its equilibrium value, K_0, some fraction of the replenished gas would be transferred to the bubble. Gravity drainage could therefore sustain bubble nucleation.

Pressure changes in isolated brine pockets could also control bubble nucleation. If the pressure of a brine inclusion changed, f_{bub} would be affected. Imagine an enclosed brine inclusion with a bubble in it. The pressure of the bubble, P, is given by the ideal gas law

$$P = \frac{nRT}{V} \tag{1.9}$$

where n, R, T, and V are the moles of gas in the bubble, the universal gas constant, the absolute temperature, and the volume of the bubble. Changes in T will be on the order of 1% so I neglect them in this discussion. Also, for this discussion it is sufficient to note that increasing P is positively correlated with f_{bub}, rather than rigorously defining the relationship between P and f_{bub}.

Now, if the brine in this enclosed inclusion is supersaturated relative to the equilibrium solubility, K_0, some gas will be driven out of the brine and into the bubble. In an enclosed brine inclusion increasing n would cause P to increase, because V must remain constant. This increase in P would cause f_{bub} to increase. Because of pressure effects in an enclosed brine inclusion, less gas must be transferred from the dissolved to gaseous phase to attain K_0. Bubble nucleation would be reduced. Kotovitch et al. (2016) suggest that this feedback between bubble nucleation and pressure may be an important missing process in their model.

The shrinking bubbles observed by Light et al. (2003) show that the effect of increasing pressure from freezing brine likely outweighs the effect of decreasing gas solubility on bubble nucleation in isolated brine inclusions. There is a conflict between this observation and the conclusions of Zhou et al. (2013), that gases effluxed from sea-ice brines to bubbles during cooling. Part of this conflict may be driven by the different temperature regimes in the two studies. The coldest temperatures in the study of Zhou et al. (2013) are roughly equal to the warmest temperatures in the experiments of Light et al. (2003). The porosity and permeability were therefore likely higher in the study of Zhou et al. (2013), which may have allowed the release of some pressure.

Pressure changes in an open brine inclusion would likely affect the transport of gas present in bubbles, rather than the partitioning of the gas. If an open brine inclusion was pressurised, fluid would move to relieve the pressure. Increasing the amount of gas, n, for example would cause V to expand, at constant pressure, into the surroundings. Pressurising open brine inclusions could therefore drive the migration of gas through sea ice.

In this section I first summarised the current state of understanding of gas

dynamics in sea ice by revising the conceptual model of Crabeck et al. (2014). I then discussed how gravity drainage and pressure could affect gas dynamics in sea ice. I showed that the convective resupply of dissolved gas by gravity drainage could positively feedback on bubble nucleation. I also showed that pressure effects would impede bubble nucleation in enclosed brine inclusions, and drive gas transfer in open brine inclusions. Quantifying the effects of gravity drainage and pressure in sea ice are therefore necessary to predict sea-ice gas dynamics.

1.4 Future changes to sea-ice extent

So far I have discussed what sea ice is (Section 1.1), and how sea ice evolves, physically, on the timescale of a season (Section 1.2). Then, in Section 1.3, I discussed three biogeochemical processes in sea ice that are of particular relevance to the physics studied in this thesis. But how is sea ice evolving on longer timescales? In this section I discuss how sea ice is changing in our warming climate, and how these changes might affect gravity drainage and pressure.

Sea-ice cover is decreasing dramatically in the Arctic and this decrease is dominantly driven by anthropogenic CO_2 emissions (Notz and Stroeve, 2016). The sensitivity of Arctic sea-ice cover to emitted CO_2, given by Notz and Stroeve (2016) (Figure 1.6), is such that the Artic is predicted to be largely sea ice free in September by the middle of this century for business as usual emissions. Such a profound change in the Arctic ice cover has never occurred in recorded history.

In the Southern Ocean the trend in circumpolar sea-ice area is on the order of $+1\%$ or insignificant. But this circumpolar average masks dramatic regional decreases in the Bellinghausen/Amundsen seas that are slightly outweighed by increases in the Ross and Weddell seas (Stammerjohn and Maksym, 2017). Southern Ocean sea ice is predicted to decrease in a warming climate (Collins et al., 2013).

The recent and predicted changes in sea-ice cover in the Arctic increase the global relevance of young and first year sea ice. Trends in Arctic summer sea-ice

cover are more negative than those in winter, so the area of new sea-ice growth has increased (Meier, 2017). If, as predicted, the Arctic Ocean becomes sea ice free in summer then all Arctic sea ice will be first year by definition. The Antarctic sea ice cover is, and seems likely to remain, dominantly seasonal (Stammerjohn and Maksym, 2017). First year sea ice is generally more porous and permeable than older, multi year ice, which may have implications for sea-ice biogeochemistry.

These changes in sea-ice cover, both in terms of the area and proportion of first year sea ice, will profoundly affect the high latitudes and Earth System in general. Quantifying the role of sea ice in the Earth System is therefore critical to a host of scientific questions. Of particular relevance to this thesis are the effects of changes in sea-ice cover on gravity drainage and pressure in sea ice. Most gravity drainage occurs during the first year of sea-ice growth, and particularly in its early stages (Worster and Rees Jones, 2015). Sea-ice gas dynamics, which may be affected by pressure, are also most active during the first year of sea-ice growth (Delille, 2006). Quantifying the role of gravity drainage and pressure in biogeochemical cycles is therefore of critical importance for the likely future sea-ice regimes.

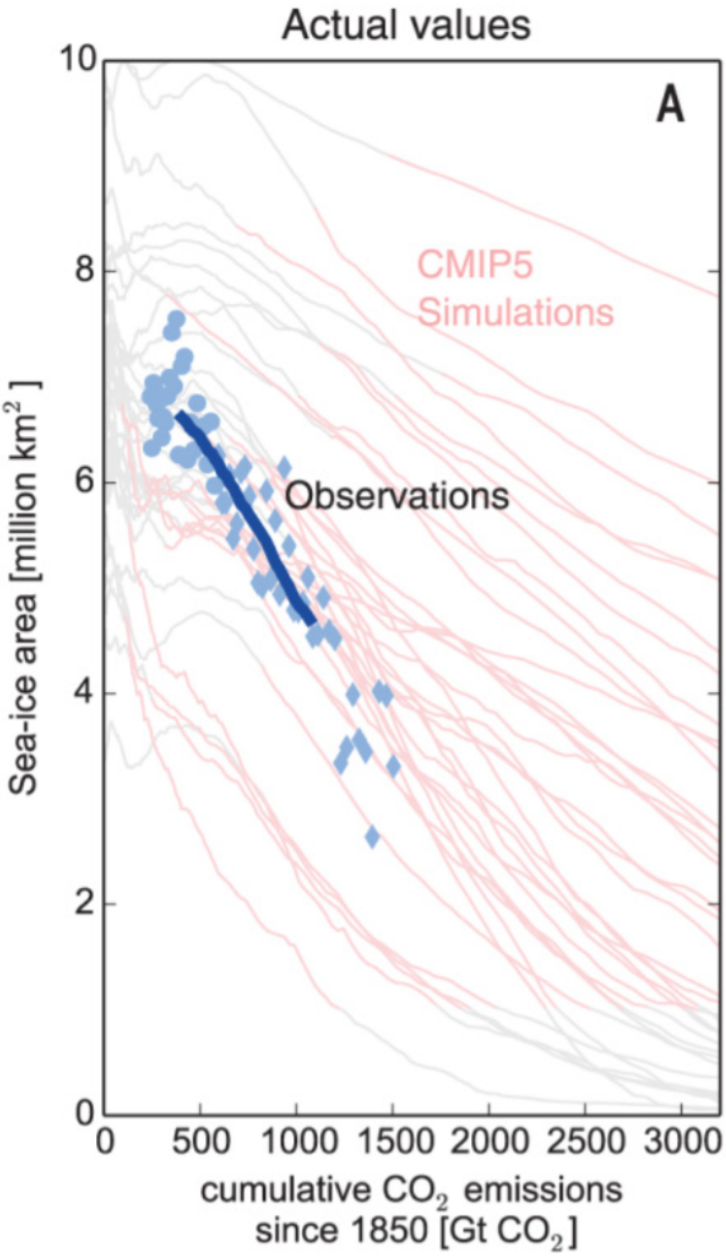

Figure 1.6: September Arctic sea-ice area against cumulative anthropogenic CO_2 emissions, adapted from Notz and Stroeve (2016).

1.5 Summary

In this chapter I first described sea ice on a small scale (Section 1.1) because the different phases of sea ice must be understood before meaningful conclusions can be

drawn about gravity drainage and pressure in sea ice. I then described the processes that thicken and melt sea ice in the environment, and that redistribute compounds within sea ice (Section 1.2). I described the wide range of environmental processes acting on sea ice so that I can place the sea ice in this thesis in context. In Section 1.3 I introduced three biogeochemical processes that are underpinned by the physical processes investigated in this thesis. The results presented in this thesis will help to improve our understanding of and ability to model these processes in particular. Finally, in Section 1.4, I described the dramatic changes that are occurring to the Earth's sea-ice cover so that I can later contextualise these results within our changing climate.

Despite the biogeochemical importance of sea ice, and the dramatic changes that are occurring to this unique biome, our understanding of many biogeochemical processes remains poor. Developing this understanding is hampered by uncertainties in the physics that underpin these processes. In this thesis I use experiments and modelling to investigate two key physical processes in sea ice. In doing so I hope to guide the use and development of numerical sea ice models so that the role of sea ice in the Earth System can be better quantified.

The first physical process I investigate is gravity drainage. The importance of gravity drainage to the desalination of sea ice has stimulated much work on the topic and a proliferations of gravity drainage parameterisations in the literature. In Chapters 3 and 4 I aim to 1) evaluate the performance of several gravity drainage parameterisations when predicting salt dynamics, and 2) evaluate the performance of those when predicting the dynamics of dissolved chemicals that move conservatively with brine but are decoupled, in terms of concentration, from the salinity. Achieving these aims will allow me to recommend which parameterisations should be used in future.

The second physical process I investigate is the build up and release of pressure in sea ice. Relatively little is know about sea-ice pressure, though we have reason to believe it could be important in biogeochemical processes (gas dynamics, for example). In Chapters 5 and 6 I aim to identify the likely magnitudes, drivers, and

implications of pressure in young sea ice. Doing so is an early step in developing an adequate understanding of sea-ice pressure.

Chapter 2

Facility description and experimental protocols

All of the data used in this thesis was collected using a unique facility, the Roland von Glasow air-sea-ice chamber. Roland conceived of the facility, and together with myself and James France created, from scratch, this powerful tool for polar research. Roland sadly died soon after the completion of the facility. With generous support from colleagues at the Environmental Sciences department at the University of East Anglia, and from the wider cryospheric science community, James and I have developed methodology to use the facility to its full potential, and completed a set of initial experiments. These experiments form the basis of this thesis. The facility is a tank housed in a coldroom and a suite of supporting instrumentation (Figure 2.1). So far the facility has been used to grow and melt artificial sea ice, simulating processes occurring in the surface polar oceans.

The purpose of the facility is to build a bridge between models, numerical or conceptual, and the environment. When the model is numerical, the facility can be used to create a simplified system against which to evaluate the model. Individual model parameterisations can be evaluated in isolation from other processes, and statements can be made about the skill of the model and the confidence in our understanding of the process. When the model is conceptual, experimental conditions may be varied to challenge our qualitative understanding of some process.

The facility is best used to test well defined hypotheses. The facility is only capable of producing artificial sea ice, which has limited relevance. Simply observing the system is therefore usually not sufficient. Users must carefully design experiments to test their hypotheses. To address important science questions using the facility inevitably requires compromise, because adequately representing the process of interest may preclude study of some other process. For example, free floating sea ice is incompatible with gas exchange experiments, because there is an unquantified gas exchange pathway at the edges of the sea ice.

The Roland von Glasow air-sea-ice chamber fills a niche between smaller sea-ice tanks that have been used to investigate physical processes (e.g. Wettlaufer et al., 1997; Eide and Martin, 1975), and larger tanks used as mesocosms (e.g. Rysgaard et al., 2014; Tison et al., 2002). The tank is small enough to tightly control the forcing, and to ensure experimental runs are affordable. The tank is large enough to be highly instrumented, and to minimise edge effects.

In this chapter I first describe the different components of the facility (Section 2.1). Next, I outline the core instrumentation (Section 2.2), and experimental methodology (Section 2.3) used in this thesis. Finally, I show how the sea-ice ocean system can be represented in numerical models (Section 2.4). The aim of this chapter is to build a picture of the facility and how it has been used. Detailed experimental methodologies are presented in the relevant results chapters.

2.1 Description of the facility

2.1.1 Sea-ice tank

A cuboid glass tank (2.4×1.4 m footprint, 1.2 m deep, 25 mm wall thickness) contains the experimental ocean, and is referred to in this thesis as the tank (Figure 2.1). Silicon resin binds the glass panels, and steel bars bracket the outside of the tank as reinforcement. The tank sits on around 4 cm of foam. The top of the tank is open. The dimensions of the tank were chosen so that the tank was as large as practically possible. The size of the coldroom limited the tank size, as it was

necessary to retain a comfortable space to work, maintain access to all sides, and to have a safe and practical waterline for accessing the ocean/sea-ice surface. When full to 1 m depth, the volume of the tank is 3170 l.

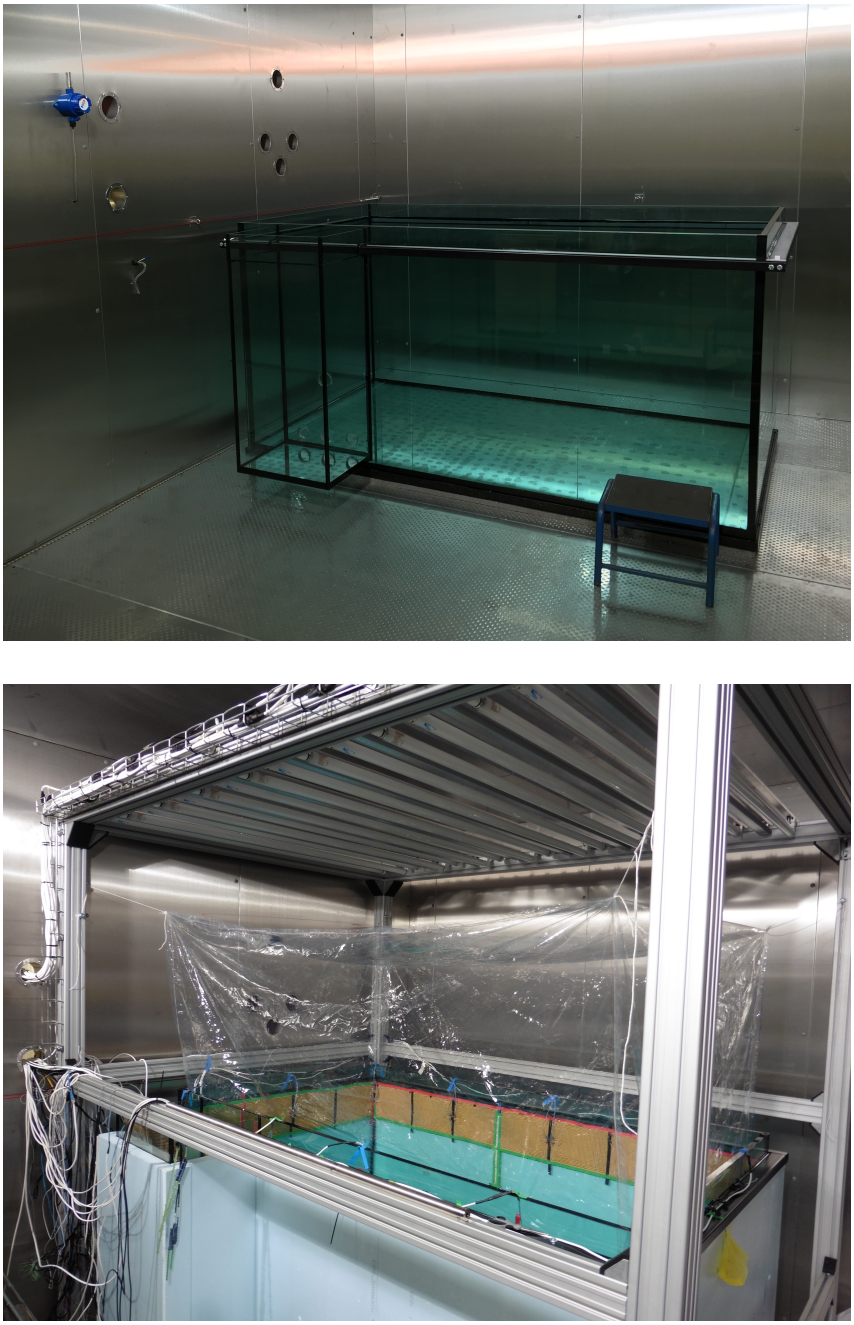

Figure 2.1: The **top** picture shows the tank just after installation. The **bottom** picture shows the tank a few months later, when all of the main elements were in place. Insulation clads the sides. A cuboid teflon atmosphere sits above the tank, and a set of lights sit above the atmosphere.

A cuboid side tank (0.5×0.4 m footprint, 1.12 m deep, 12 mm wall thickness)

is attached to the main tank by four open holes, and is never allowed to freeze entirely at the surface. The side tank has two functions. First, it provides an outlet for water displaced as ice growth increases the volume of the sea ice and ocean. Second, it allows sample lines and cables to run into the main tank without disturbing the ocean surface or the sea ice.

A lighting rack sits between 1 and 2 m above the ocean surface to facilitate photochemical, radiative and biological experiments. Solar spectrum LED (Fluence Solar Max), UVa (Cleo performance 100W) and UVb (Phillips broadband TL 100W) fluorescent bulbs are evenly spaced over the tank in sets of three, with 24 lights total (Figure 2.1). This gives the most uniform possible light field over the tank. The LED lights can be dimmed individually.

An atmosphere may be attached to the main tank, although the lighting must sit outside of the atmosphere. The atmosphere may be cuboid and raised well above the sea-ice surface (Figure 2.1), or may lay in a flat sheet on top of the main tank. At the time of writing, only 50 μm FEP teflon atmospheres have been attached to the tank, but a steel sheet is also available that can lay flat on the main tank. The choice of atmosphere should be tailored to individual experiments. FEP teflon, for example, is transparent in the visible and UV spectrum, and chemically inert, making it ideal for many photochemical experiments. However, it is highly permeable to CO_2, making it unsuitable for investigating CO_2 fluxes. The results in this thesis were all collected without an atmosphere. The coldroom itself can also act as a contained atmosphere, but in this case experimenters cannot enter the coldroom without disturbing an experiment. The side tank may be sealed off from the coldroom with a lid.

A variety of equipment supports the tank. Two pond pumps (TUNZE stream 6215) sit in the ocean and are used to mix the water. They also have potential to be used to generate currents or waves. A camera (Camsecure, underwater camera submarine style) also sits in the ocean and is used to monitor the progression of the sea ice from below. Above the main tank, low and high definition video cameras are used to monitor the sea ice from above. Heating pads (Heizfolip thermo 12V, 15W)

may be placed within the water, around the inside or outside of the tank, or in the side tank. The heating pads are always used to prevent the side tank from freezing, and in some capacity to prevent supercooling in the ocean which may damage instrumentation. They have also proved to be versatile tools in other respects, and are discussed further in Section 2.3.1. Insulation (FLOORMATE 500A and YSB superquilt multilayer) is used to clad the tank and minimise heat loss through the tank sides.

The final tank design is different to the original proposal in several respects (Figure 2.2). The most significant change in the revised design is that the top of the tank is uncapped by default. This allows for much greater versatility as the atmosphere can be capped by different materials to suit different experiments, or left uncapped. It also allows for easier access to sample the sea ice. Inbuilt cooling/heating in the contained atmosphere is replaced by control of the temperature of the atmosphere of the coldroom. A second significant change is the addition of a side tank. Functionally the side tank is similar to the water reservoir pictured in the original proposal. The side tank allows pressure relief, but does require any control systems. It also does not allow for dilution of the underlying water, or control of the water level in the system. The side tank therefore sacrifices some level of control to achieve ease of use. If a water reservoir is ever necessary for an experiment, it can be installed *via* the side tank.

2.1.2 Coldroom

The environmental chamber that houses the tank was designed and built by CLIMATEC, and has a footprint of 4.4×4.4 m. The internal floorspace of the coldroom is 18.5 m^2. The coldroom is constructed from Veissmann panels, and has stainless steel interior surfaces. A compressor sits outside of the building and recirculates air within the coldroom, heating/cooling to maintain a set temperature. Six fans circulate air from the compressor (Figure 2.3). The coldroom is connected to the laboratory by doubledoors, and six holes (10 cm diameter) for power leads and sample lines. These holes can be closed when not in use. Temperature

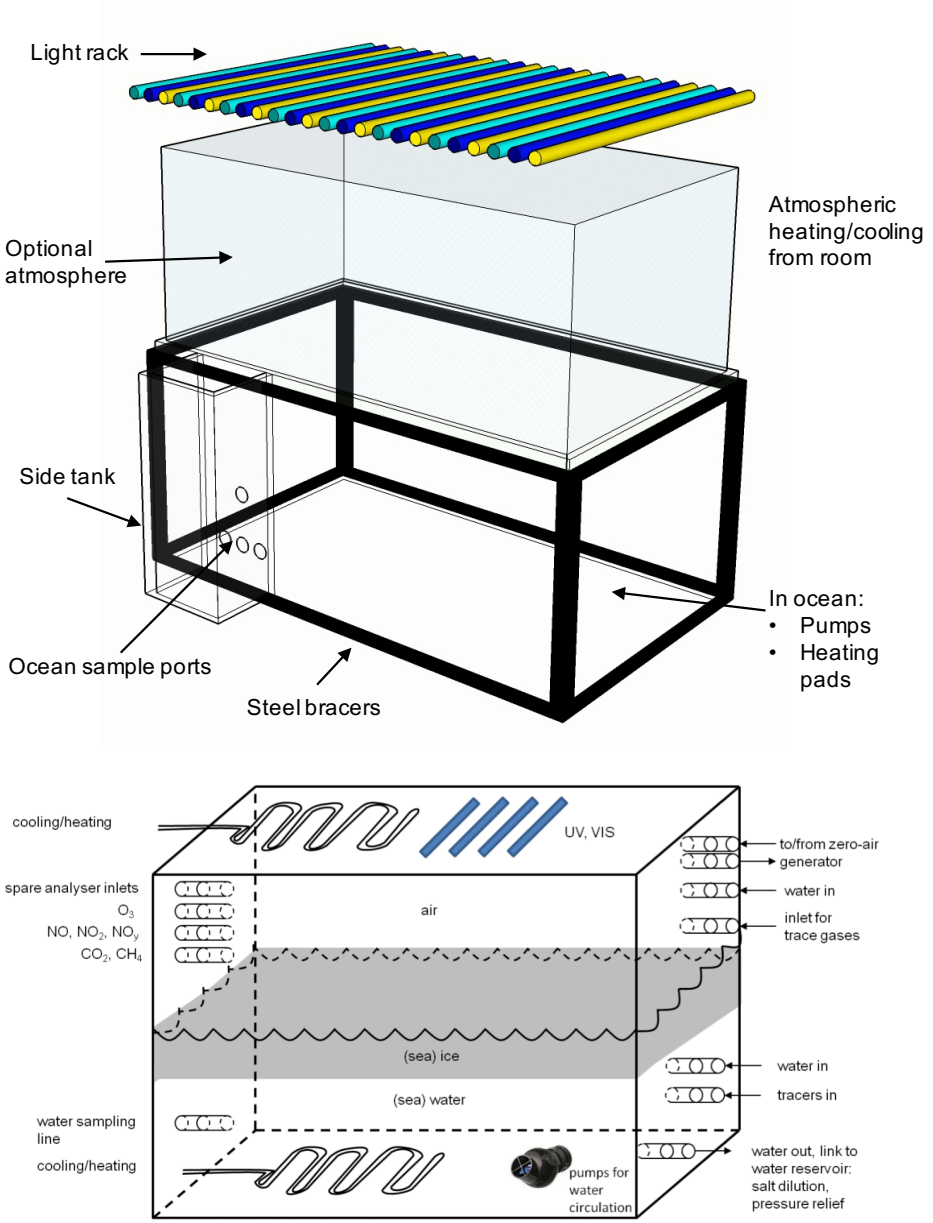

Figure 2.2: The **top** schematic drawing shows the realised tank, and the **bottom** schematic is from Roland's original funding proposal. The scale is similar for both schematics, and the length of the longest side of the realised tank is 2.4 m.

control and logging are facilitated by a control panel and can be accessed remotely (Nanadac Eurotherm). The temperature range of the coldroom is -50 to +30 ^{o}C, facilitating a wide range of experiments.

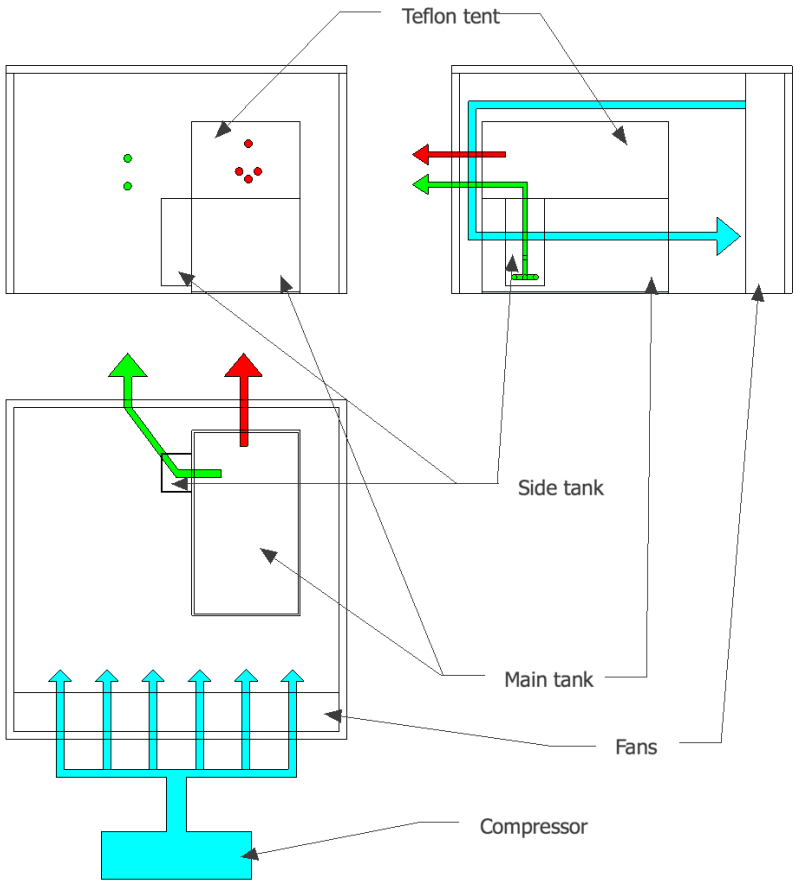

Figure 2.3: To scale schematic of the coldroom and tank from vantage points next to the fans (**top left**), the doorway (**top right**) and from above (**bottom**). For reference, the length of the longest main tank side is 2.4 m. Red and green arrows and circles indicate paths for gas and water sampling lines, respectively. Blue arrows indicate typical airflow through the coldroom.

2.1.3 External laboratory

An external laboratory houses the coldroom (Figure 2.4). The control boxes for all instrumentation, gas valves, heating pads, pumps and cameras sit in the external laboratory. A mains or ultra pure water supply (Centra R 200) is available for filling the tank. A chest freezer (Thermo Scientific, REVCO CXF) with a temperature range of -10 to -40 ^{o}C is used to compliment experiments, store samples, and test instruments. An acrylic tank (0.3$\times$0.45 m footprint, 0.4 m deep) can be used in the chest freezer to test the robustness of instruments and equipment, and adds versatility to the facility.

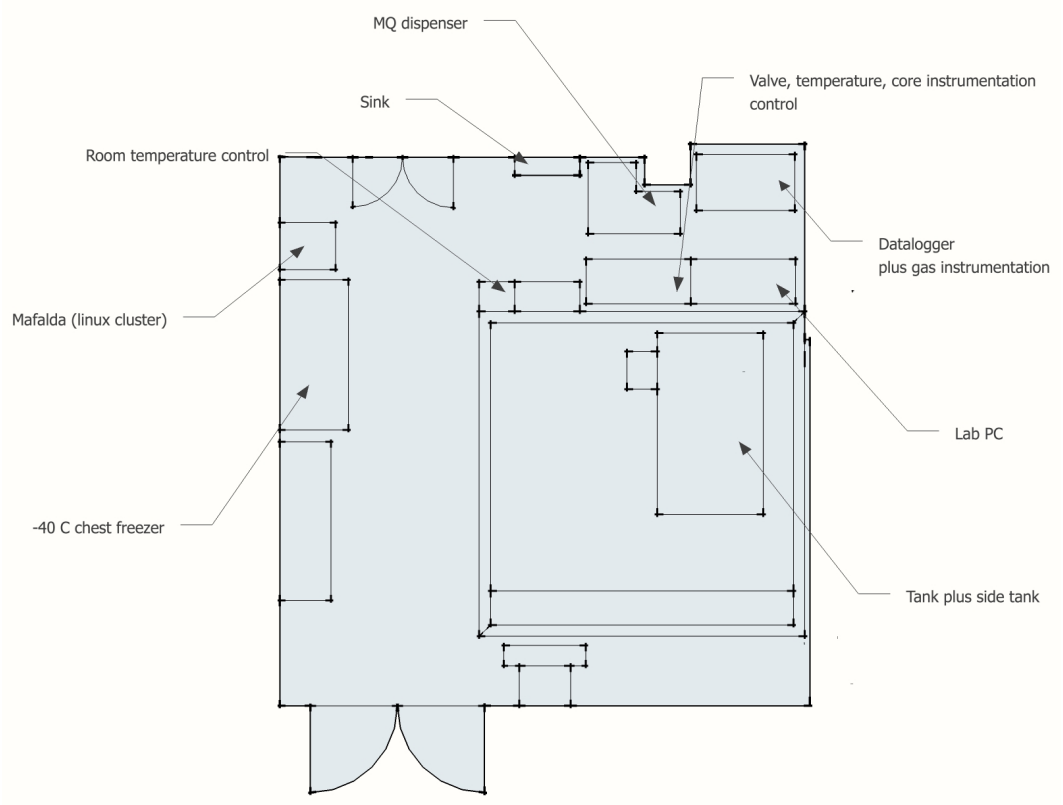

Figure 2.4: To scale schematic of the outer laboratory, containing the coldroom and tank, from above. For reference, the length of a coldroom side is 4.4 m.

2.2 Instrumentation for the facility

2.2.1 Ocean instrumentation

A SBE-37SIP Microcat CTD was used to measure the temperature and salinity of the main tank ocean in almost every experiment. This CTD is pumped. Two smaller CTDs (SeaStar DST CTD) were also used occasionally, but require offsetting to some reference salinity. In this thesis, ocean salinity is calculated from the CTD in two steps. First, a CTD salinity is calculated using empirical relationships relating conductivity and temperature to seawater salinity (Fofonoff and Millard, 1978). The CTD salinity ($S_{o,CTD}$) is not representative of the salinity of artificial NaCl sea water ($S_{o,NaCl}$ (g kg^{-1})) because the ionic composition differs significantly from natural sea water. To correct this I use Equation 2.1 (Naumann et al., 2012), where T_o is the ocean temperature (^{o}C). The accuracy and precision of the CTD (Table 2.1) translate to an error in salinity of less than 0.01 g kg^{-1}. This uncertainty is excellent in the

context of the sea ice simulator, where changes in salinity during an experiment are on the order of 5 g kg^{-1} and the precision of wireharp (see next section) and discrete bulk salinity measurements is relatively poor.

$$S_{o,NaCl} = S_{o,CTD} - 0.0517 S_{o,CTD} + 0.0079 T_o \tag{2.1}$$

2.2.2 Sea-ice instrumentation

Several pieces of instrumentation span the ocean, sea ice, and atmosphere, and I discuss these in this section (see also Table 2.1). Three types of temperature sensors are used in this thesis (DS28EA00, DS18B20U, TFPT0603L1001FV). These are deployed with between 1 and 4 cm vertical resolution in 'thermistor chains', and I use the highest resolution where possible. The thermistors are waterproofed using a conformal coating (HPA200H). However, even with the conformal coating the thermistor chains broke frequently and it is important to deploy the thermistors so that there is redundancy in case of failure. Zeroing all of the thermistors in an ice/water slurry, which will maintain constant temperature of 0 ^{o}C, improves the absolute accuracy of the thermistors, and I did this at least once a year.

Pressure was measured through the ocean, sea ice, and atmosphere by a set of ten piezo-resistive pressure sensors. The sensors were mounted in a PVC block, shown in Figure 2.5. The face of each sensor is 1.2 cm in diameter. Given that these sensors are discussed heavily in Chapter 5 and Chapter 6 I leave detailed discussion of the pressure sensors to those chapters.

Vertical profiles of solid fraction, ϕ, through sea ice into the ocean were measured using 'wireharps' similar to those developed in Notz et al. (2005), who build on the work of Shirtcliffe et al. (1991). The wireharps used were purchased from Dirk Notz's research group, and are shown in Figure 2.5. The measurement of solid fraction for a given depth is based on the resistance measured between two titanium wires (12 cm long, 1 mm diameter) mounted horizontally. Electrical current may pass easily through liquid, salty water (ocean and brine), but is well insulated by fresh, frozen water (ice). The resistance therefore increases as the sea

Table 2.1: Summary table of sensors used in this thesis.

Sensor	Parameter	Medium	Accuracy	Precision
Seabird microcat 37SIP	Conductivity Temperature	Ocean	0.003 mS cm^{-1} 0.002 ^{o}C	
ME506 piezo-resistive sensor	Pressure	Sea ice ocean atmosphere	1 kPa	
DS28EA00 digital thermometer	Temperature	Sea-ice ocean atmosphere	$< 0.5\ ^{o}$C	$\frac{1}{16}\ ^{o}$C
DS18B20U digital thermometer	Temperature	Sea-ice ocean atmosphere	$< 0.5\ ^{o}$C	$\frac{1}{8}\ ^{o}$C
TFPT0603L1001FV thermistor	Temperature	Sea-ice ocean atmosphere	1 %	1 %
Wireharps (Notz et al., 2005)	Bulk salinity	Sea ice	<5 g kg^{-1}	

ice initially forms, and as it solidifies, making resistance a strong function of the solid fraction (Notz et al., 2005),

$$\phi = 1 - \frac{\Gamma_0 Z_0}{\Gamma(T,S) Z_t} \tag{2.2}$$

The $\frac{Z_0}{Z_t}$ term is the ratio of the resistance at the beginning of sea-ice formation to the resistance at some later point in time. I manually define Z_0 by inspecting graphs of the resistance and noting the beginning of the first steep rise. I conservatively estimate that the error on my choice of Z_0 to be $< 5\%$ of the true Z_0. The $\frac{\Gamma_0}{\Gamma(T,S)}$ term is the ratio of the conductivity of the brine at the point of sea-ice formation to the conductivity of the brine at some later point. This term corrects for the change in conductivity due to the changes in brine salinity and temperature. However, this term is only a second order effect, and I ignore this term on the advice of Dirk Notz and Leif Riemenschnieder, who developed and built the instrument.

The wireharps tend to overestimate solid fractions at solid fractions greater than 0.8. This is likely because isolated brine pockets are not in the path of current flowing between the wirepairs, and so are not properly accounted for by Equation 2.2.

Also, the air volume fraction in growing sea ice is likely around 1%, and would be measured by the wireharps as solid fraction due to the low conductivity of air. I am not aware of any study considering the impact of air volume fraction on wireharp measurements. The air volume fraction will cause solid fraction to be overestimated, porosity to be underestimated, and have no effect on the calculated liquid fraction.

The *in situ* bulk sea-ice salinity can be calculated using co-located solid fraction and temperature data. To calculate *in situ* bulk salinity using the solid fraction from the wireharps, I first co-locate each solid fraction measurement with a measured temperature. I then retrieve the brine salinity using an appropriate inversion of the liquidus relationship. In the case of sea ice grown from artificial NaCl seawater I use Equation 2.3, which is a third order fit to the data of Weast

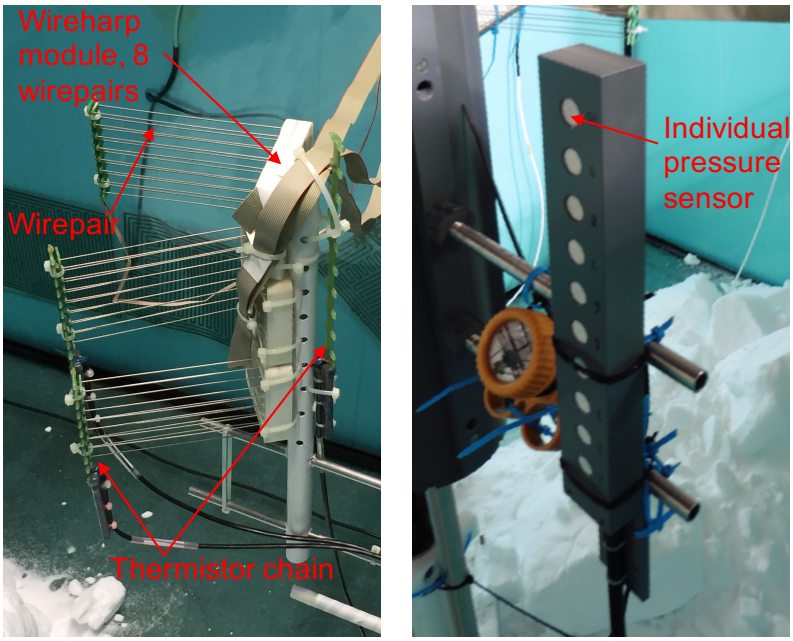

Figure 2.5: The picture on the **left** shows three wireharp modules in a depth profile. I have attached thermistor chains to each wireharp module so the solid fraction measurements can be co-located with temperature measurements. The picture on the **right** shows the pressure sensor bar, which is discussed in depth in Chapter 5.

(1971) for the freezing point of $NaCl_{aq}$ (Rees Jones and Worster, 2014).

$$S_{br} = -17.6T - 0.389T^2 - 0.00362T^3 \tag{2.3}$$

In Equation 2.3, T is the local sea-ice temperature (^{o}C). In situations with a natural, oceanic salt composition, which do not occur in this thesis, a fit to the data of Assur (1958) should be used instead of Equation 2.3 (Notz, 2005). Once I have calculated the brine salinity, I use Equation 2.4 to calculate the bulk salinity at each depth.

$$S_b = (1-\phi)S_{br} \tag{2.4}$$

Because wireharp resistance measurements rely on brine pathways between wires, the measured ϕ is most accurate when $\phi < 0.8$. Brine inclusions that are isolated from the path of current may not be properly accounted for in the measured resistance. Also, at high solid fractions, small absolute errors in solid fraction cause large relative errors in the bulk salinity. At $\phi = 0.95$, for example, a 3% error in ϕ mentioned above translates to around a 50% error in liquid fraction and bulk

salinity. Another source of error is the co-location of temperature and solid fraction, because the temperature sensors are larger than the wirepairs. Griewank and Notz (2013) suggest that absolute errors in bulk salinity are less than 5 g kg^{-1} when $\phi < 0.8$, and that relative errors rise with $(1-\phi)^{-1}$ as ϕ approaches 1. From my experience (again, Chapter 4 and other, not shown, data) measured and modelled bulk salinity agree to within 5 g kg^{-1} for solid fractions below around 0.9. While the model is not truth, it performs well against discreet salinity measurements, and agreement between measured wireharp salinity and modelled salinity increases my confidence in the wireharp performance. At higher solid fractions, greater than around 0.95, a bulk salinity error of around 300% may be required to bring measured wireharp salinity into agreement with discreet samples and modelled salinity. The suggestion of Griewank and Notz (2013), that relative error increases exponentially as solid fraction increase above 0.8, gives bulk salinity errors of around 1000% for solid fractions around 0.95, which is overly conservative. For lack of a better characterisation, I approximate the salinity error from the wireharps to be around 5 g kg^{-1} below around 0.8 solid fraction, and note that the bulk salinity error may be more significant, and biased towards underestimation, at higher solid fractions.

2.2.3 Atmospheric instrumentation

The atmospheric instrument used most heavily in this thesis is a weather station (WS600-UMB). The weather station provides a calibrated reference air temperature and pressure. I used the weather station to calibrate the thermistors used in Chapters 4 and 5. I also used the weather station, in combination with overhead water pressure, to calibrate the pressure sensors (Chapter 5).

The facility also contains several dedicated gas analysers. A Los Gatos greenhouse gas analyser (Los Gatos 30R-EP) measures CO_2, CH_4, and H_2O. A T200 UP Teledyne measures NO_x, a T200 U Teledyne measures NO_y, and there is an ozone analyser (T400 Teledyne) and generator. Each of these analysers has a dedicated suite of calibration gasses, and a zero-air generator (T701 H Teledyne)

can be used for dilutions. This gas phase instrumentation does not contribute data to this thesis, but is a core part of the facility.

2.3 Growing sea ice in the facility

Many methodologies were developed, and mistakes made, during the initial experiments in the Roland von Glasow air-sea-ice chamber. In this section I describe a general experiment, from set up to sampling, so that future users of the facility do not have to waste time on problems that have already been solved.

2.3.1 Set-up phase

The first stage of any experiment is to clean the tank and instrumentation. The level of cleanliness required is determined by the nature of the experiment. An experiment concerned with trace chemicals or biology requires greater levels of cleaning than an experiment concerned only with physical processes. In between each run I cleaned the wireharps with isopropanol, as bio-fouling increases the measured resistance.

The next step is to position the heating pads. Again, the nature of the experiment must be considered. The first consideration must be whether the sea ice will be fixed to the tank sides or free floating. Free floating sea ice has the advantage of maintaining a natural freeboard, but is undesirable for certain experiments. I spent significant time developing methodology to maintain a free floating slab. For my first attempt I taped heating pads around the sides of the tank at the level where sea ice would grow. By running these at high power I was able to maintain an open water gap around the heating pads. However, the sea ice in this instance was not free floating because sea ice fixed to the tank sides around the edges of the heating pads, and around the heating pad connectors. In Chapter 5 I say that the sea ice in these experiments had partially melted sides. My next attempt to maintain free floating sea ice involved fixing a sloping teflon skirt around the sides of the tank, and fixing heating pads to the teflon (Figure 2.6), the rational being the the sea ice

would not fix to the teflon, and would float upwards because of its wedge shape. Using this method I was able to maintain free floating sea ice, and this method was used to generate the free floating sea ice in Chapter 5.

But this methodology was time consuming and messy, so I also developed a lower maintenance way to maintain free floating sea ice. Placing heating pads between the tank and the insulation is sufficient to maintain a free floating slab up to a point. The sea ice appears to be fixed (there is no visible gap between the sea ice and glass) but the sea ice bobs when pushed, which indicates that it is free floating. I used this method to grow free floating sea ice in Chapter 4. During that experiment I could bob the sea ice up until the last day, and the freeboard at the end of the growth phase was natural (1.7 ± 0.1 cm for 16.5 ± 1 cm of sea ice). Placing heating pads around the outside of the tank therefore maintains free floating sea ice up to around 17 cm of sea ice.

Once the side heating pads are placed, further heating pads may be placed in the body of the main tank, and in the side tank. The heating pads in the main tank simulate an ocean heat flux and can be used to keep the ocean just above its freezing point. These pads should be fixed so that they float in the water and do not touch the glass. In this way all of the heat is transferred to the ocean and is quantifiable. A single heating pad in the side tank, straddling the ocean/atmosphere interface, is sufficient to maintain a water gap and keep the tank system open. Even so, multiple heating pads should always be used in the side tank in case one fails. The connectors of any heating pads in contact with salty water should be conformal coated and covered with duct tape. Where possible heating pads in water should be deployed with some redundancy, as they have a tendency to break. Even with coating and tape, I expect to lose around one in ten heating pads deployed in water per week. Heating pads can also be rolled up and wrapped around sample lines that are in contact with the atmosphere, and then insulated, to prevent freezing in the line. Adding a temperature probe to the sample line and side tank headspace aids in troubleshooting during experiments.

Once the heating pads are positioned, a central structure is placed in the tank

so that instrumentation can be fastened to it. The pumps and cameras should also be positioned at this stage. When the sea ice is free floating this central structure should be free to rise with the sea ice as it forms. I have achieved this by placing the central structure on a rigid greased pole, and seating the pole in a tube resting on the tank base (Figure 2.6). Instrumentation can also be hung from above the ocean, then cut away once it begins to freeze in. Instrumentation should be mounted near the centre of the tank to minimise edge effects and to best represent the average of the eventual sea-ice thickness, which may vary by around 10%, with the thickest sea ice nearest the fans. Instruments should be positioned close together so that they are measuring sea ice that is as similar as possible, but at least 30 cm should be left between any two instruments at a given depth, so that sea-ice growth is not disrupted. Individual wireharp modules are mounted in a depth profile, and thermistors are mounted such that they span at least the depth of the wireharps. The CTD is mounted deeper, well away from the predicted final sea-ice/atmosphere interface. The weather station and pressure sensor bar are also added.

If an atmosphere is require it should be attached at this stage. When an atmosphere is present, the temperature of the contained headspace will be higher than the coldroom, and relatively unresponsive to changes in coldroom temperature. In experimental runs with a contained atmosphere, temperatures in the headspace never fell below -8 ^{o}C, even with the coldroom at -35 ^{o}C. Loose et al. (2011) had similar issues.

If the experiment requires real sea water, the next step is have sea water delivered and pump it into the tank. If the experiment requires artificial sea water, the next step is to add either NaCl (AksoNobel Sanal-P >99.5% NaCl) or some more complex mix of salts to the tank. The added salt can be weighed in if a salt budget is required, or the salinity can be topped up to the desired value by using the CTD as a reference. Water is then pumped into the tank, either from the mains or deionised water supply. Filling takes approximately three days when using deionised water. During or after the fill the water is cooled down from around room temperature to around -1.5 ^{o}C. With the room at around -20 ^{o}C the water cools

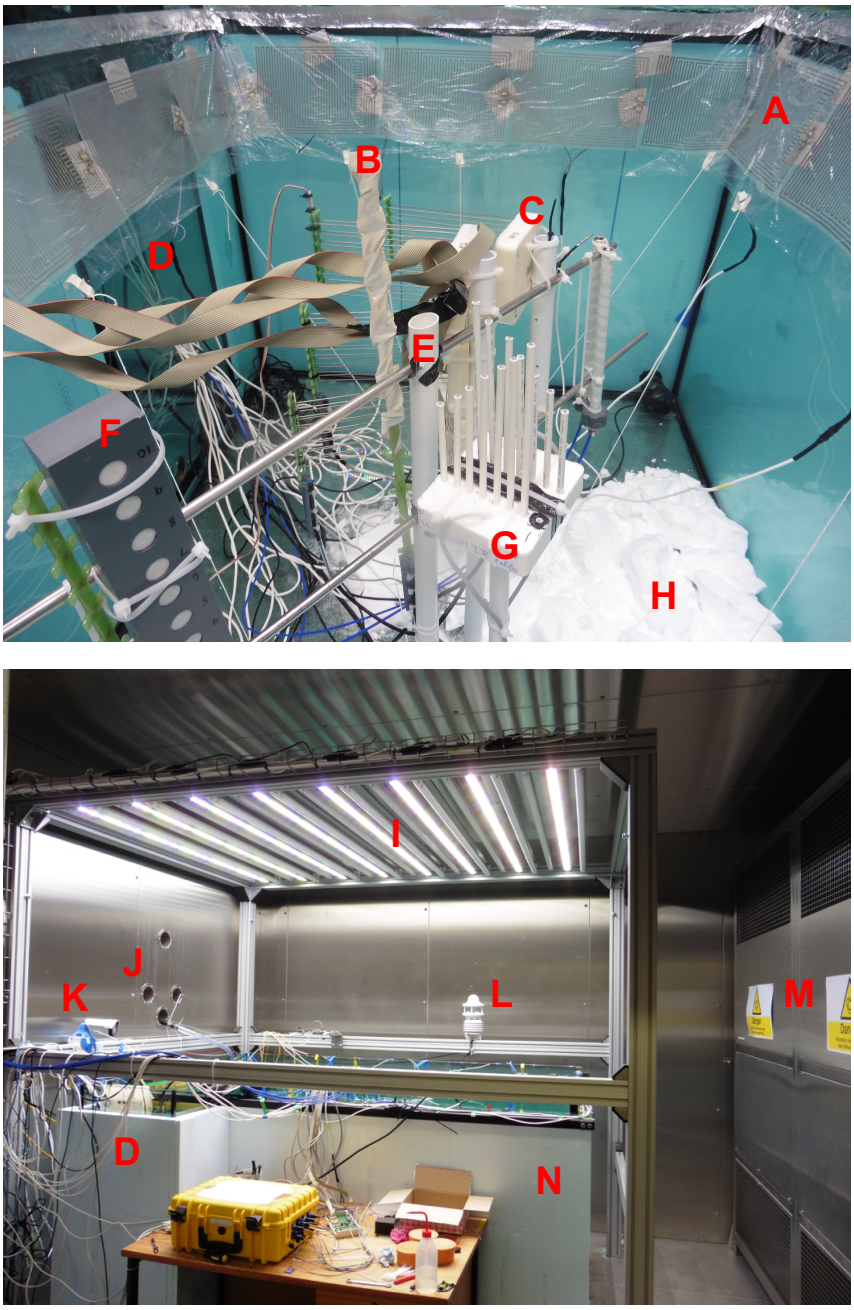

Figure 2.6: Both these pictures show the tank just before adding water. In the **top** picture I have mounted a teflon skirt with heating pads attached (A). The skirt allowed me to maintain a free floating sea-ice slab. The **bottom** picture was taken from the doorway of the coldroom.

The remaining labels show: a thermistor chain spanning the eventual atmosphere, sea ice, and ocean (B); wireharps with attached thermistors (C); the side tank (D); the central structure (E); the pressure sensor bar (F); an instrument to measure light intensity (G); NaCl salt (H); the light rack, with visible switched on (I); ports connecting the cold and outside room (J); a high definition video camera (K); the weather station (L); the coldroom fans (M); the insulation (N).

by around a degree every four hours. During this period of cooling, setting the pumps to maximum prevents frazil ice forming at the surface while the bulk water

is still relatively warm and helps dissolve the salt. If necessary, drift in the offset of thermistors can be corrected to each other or the CTD during the period where they sit in well mixed, cooling water.

A large amount of moisture condenses and freezes from the coldroom atmosphere as it is brought from room temperature to, say, -20 ^{o}C, and the coldroom can lose performance during this period as ice blocks air circulation. There is a manual defrost setting on the chamber that runs for 15 minutes to deal with this issue, but even multiple defrosts may not be sufficient. Before the start of an experiment, the easiest way to deal with ice build ups is to turn the chamber to 10 ^{o}C for around an hour, then back a desired sub zero temperature, whilst keeping the door closed.

2.3.2 Sea-ice growth phase

Sea-ice growth can be initiated by continuing to cool vigorously pumped water, or by switching the pumps off or to a low setting. With the pumps on, grease ice forms (Figure 2.7, top picture), and more vigorous pumping produces a thicker grease ice layer before consolidation. With the pumps off, nilas forms (Figure 2.7, bottom picture). Experiments were generally initiated by turning the pumps down or off.

The artificial sea ice best approximates congelation growth of natural sea ice when all of the heat is removed from the growing sea ice *via* the sea-ice/atmosphere interface. The edges of an area of sea ice in the environment are most likely to be in contact with similar sea ice, with a similar temperature, so removing heat from the sides or base of the growing artificial sea ice is not desirable. Other modes of growth occur in nature (Chapter 1, Figure 1.2), and are important, but are beyond the scope of the initial set of experiments presented in this thesis. Also, congelation sea-ice growth is the mode of growth most often incorporated into models (e.g. Maykut and Untersteiner, 1971).

If the insulation were removed, or the heating pads switched off, for an experimental run, then the water underlying the sea ice would supercool. Ice would nucleate at the cold glass interfaces, on instrumentation, and in the water column,

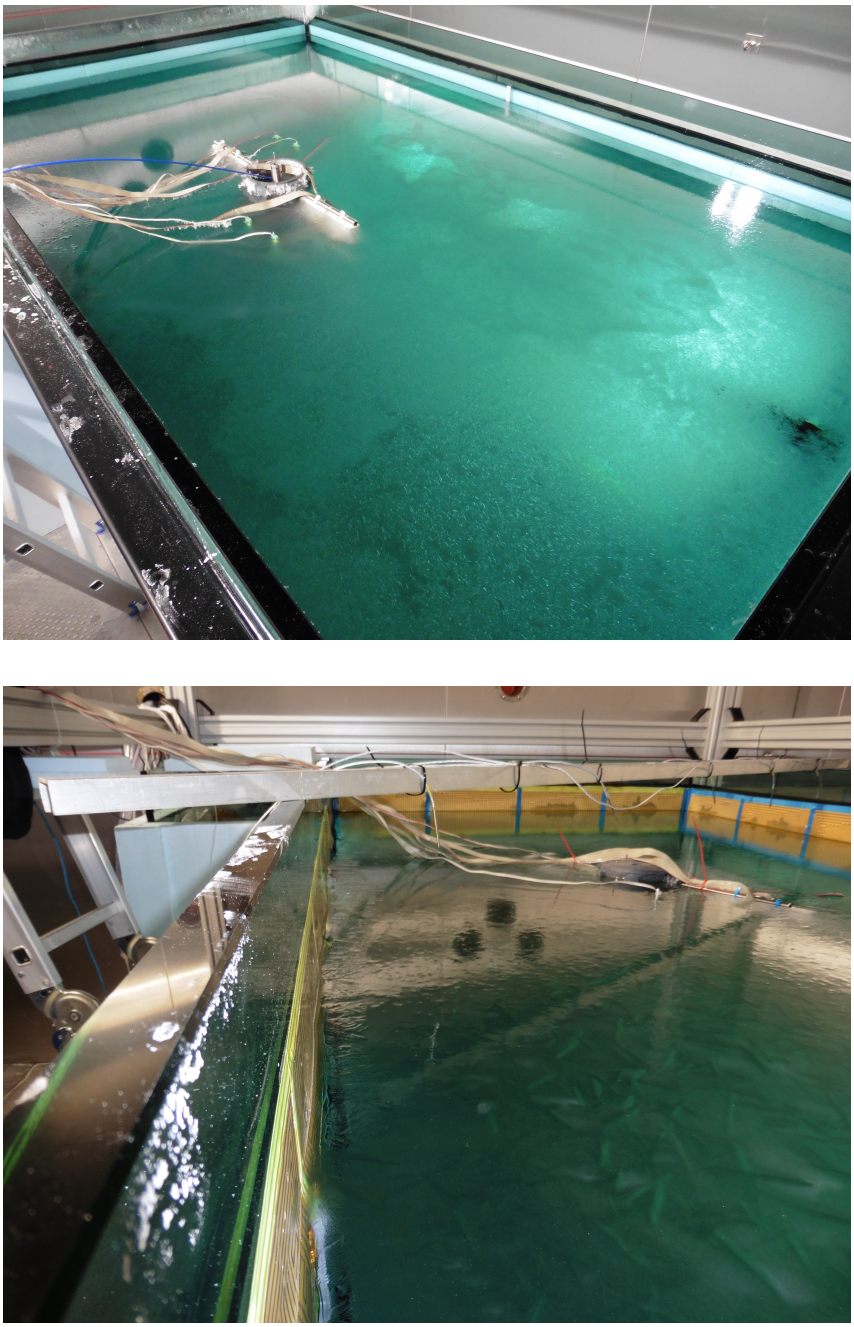

Figure 2.7: The **top** picture shows the early stages of sea-ice formation when the water was pumped. Grease ice is forming, and the initial layer of sea ice is patchy and unconsolidated. The **bottom** picture shows the early stages of sea-ice growth under quiescent conditions. Nilas is forming, and a single sheet of sea ice has formed across the entire tank

as is shown in Figure 2.8. In early experiments this occurred more than once. This mode of sea-ice growth approximates platelet sea-ice growth, which is areas of the Southern Ocean (Weeks, 2010), and may be useful for future studies. However, given the potential to damage the CTD, and the difficulties caused by nucleation of

ice on wireharp wirepairs ahead of the advancing sea-interface, I used the heating pads to maintain the water just above freezing in all experiments.

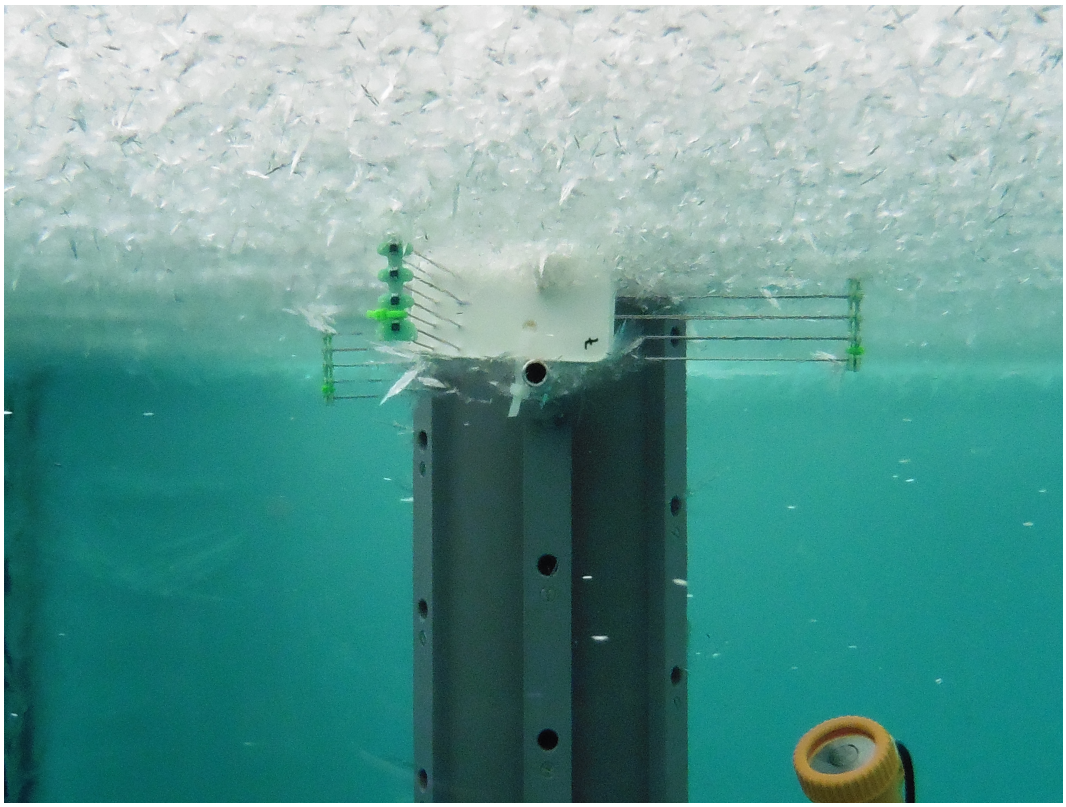

Figure 2.8: This picture was taken through the glass of the main tank, and shows sea ice growing from below in supercooled water. Note the ice that has nucleated on the wireharps ahead of the advancing sea-ice front. The white flecks in the water column are frazil ice crystals that are rising up. More heating was required for this run.

During sea-ice growth it is often best to not enter the coldroom as inflow of warm, humid air can add complexity to experiments. During a run I might never enter the coldroom, or I might enter once a day to check something specific (Figure 2.9). The sea-ice thickness can be estimated during the experiment, and without entering the coldroom, from the real time temperature profiles. Unfrozen thermistors will all read a similar temperature, and thermistors frozen into the sea ice will be colder. The side tank temperature should be checked periodically using an *in situ* thermistor, and if the temperature is lower than expected the tank should be visually inspected to make sure it is capable of relieving pressure (i.e. does not have a complete ice cover). If the coldroom is not able to maintain a stable air temperature it is likely that the fans have iced up, and unusually noisy readings

from the CTD may indicate that the water is supercooled. In the later case the temperature should be checked against the freezing temperature of the water, and the heating pad power should be increased if the water is supercooled.

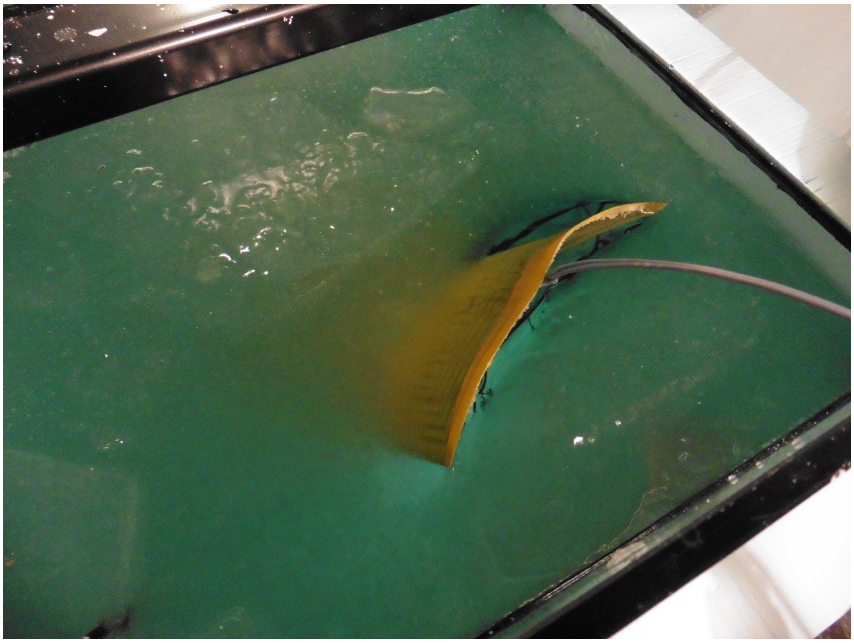

Figure 2.9: During an experiment I might enter the coldroom to check and/or photograph the the sea ice. This image shows the side tank during an experiment, where an area of open water is being maintained by a heating pad. When only one heating pad was used in the side tank I entered the room and checked it periodically, but in most experiments multiple heating pads were deployed for redundancy, and thermistors were deployed so that the temperature could be checked remotely. This picture shows the side tank with an unusually large and undesirable amount of ice growth.

Figure 2.10 shows some sea ice towards the end of an experiment. In the top picture, frost flowers have formed. Frost flowers grow on the surface of sea ice when the air temperature is less than around $-25\ ^{o}$C. The bottom picture shows the ocean under around 10 cm of sea ice.

2.3.3 Sampling protocols

Sampling sea ice is destructive, and for many scientific questions sea ice may only be sampled once, with this sampling ending the experiment. Holes left by sampling expose ocean directly to atmosphere, allow ocean to infiltrate the sides of the sea ice, and alters the freeboard when the sea ice is not free floating. Kotovitch et al. (2016), for example, sample sea ice through time in a laboratory study by separating their sea ice into several individual containers. Once the sea ice in a single container

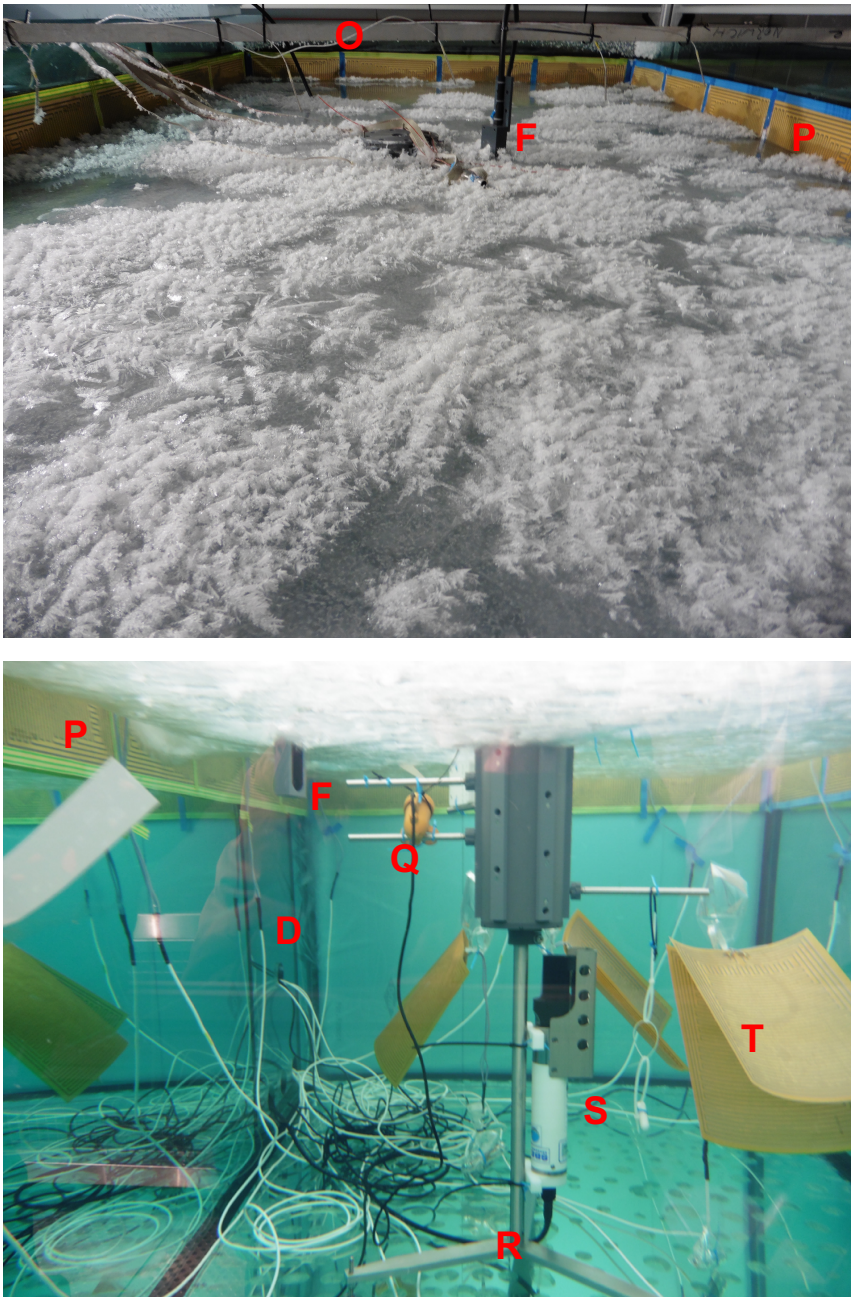

Figure 2.10: The **top** picture shows the sea-ice surface during an experiment where frost flowers were growing. The **bottom** picture shows the ocean photographed through the tank glass with overlying sea ice. These picture were not from the same experiment.

The labels show: A bar the instruments were hung from (O); the pressure sensor bar (F); heating pads taped to the inside of the glass (P); the underwater camera (Q); the side tank (D); instrumentation to measure ocean salinity and temperature (S), with the CTD and a DST to the left and right of S, respectively; a floating heating pad (T); the base of the central structure (R).

The sea ice to the right of P is creeping down the tank side because the adjacent heating pad is broken.

was sampled, it was assumed to be compromised. While separating the sea ice may be a promising route in future experiments, so far sea ice has been sampled only

once for each experimental run in the Roland von Glasow air-sea-ice chamber.

Coring sea ice causes the bulk salinity to be underestimated in the lower portions of the sea ice, because brine drains out of the permeable bottom portion of the sea ice upon removal (Notz and Worster, 2008). The permeable portion of young sea ice is large relative to its thickness, so brine loss during coring is a particularly severe problem in young sea ice. The method for sea-ice sampling I use primarily in the Roland von Glasow air-sea-ice chamber is that of Cottier et al. (1999). This method extracts sea ice, still floating on ocean, in a box. Anomalous brine drainage therefore does not occur. The sea ice and ocean are then shock frozen, together, to immobilise the brine within the sea ice and to freeze the ocean. The ocean can then be cut away, and the sea ice can be cut into layers. A detailed description of this process, and an assesment of errors induced by the re-freezing process, are given in Chapter 4. Core and slab sampling is shown in Figure 2.11.

Unlike the sea ice, the underlying water may be sampled through time without compromising the ocean. However, some care must be taken to not significantly alter the water level in the tank if the sea ice is not free floating. Every 10 litres removed from the tank alters the water level by around 3 mm. Taking tens of litres may therefore significantly alter the freeboard of fixed sea ice. Water used to replace volume should be salty, because fresh water may freeze at typical ocean temperatures and block the line used to repalce the water. The water sampling technique described in Chapter 4 represents the most up to date water sampling methodology at the time of writing.

Generally the sea ice was sampled at around 20 cm. The slab sampling technique of Cottier et al. becomes increasingly difficult as the sea ice thickens, and sampling $>$ 25 cm of sea ice using this method is very difficult. A vertical section of sea ice grown in the facility and sampled using the Cottier et al. methodology is shown in Figure 2.12. This particular sea ice was grown in one of the earliest experiments, and James France and I were encouraged by the prominent brine channel.

Figure 2.11: This picture shows me and a collaborator sampling sea ice. I am taking a core, and they are taking a (second) slab (Cottier et al., 1999). The ochre ring has been frozen onto the surface with de-ionised water to prevent brine from contaminating the surface of the next slab. This photo also highlights one of the issues with taking multiple samples from sea ice that is fixed to the tank walls. The extraction of several cores, and the sea ice removed to take the slab, has lowered the water level in the tank by around 5 cm below a natural freeboard. This likely had little effect over the hour or so it took to extract these samples, at which point the experiment was over, but could have caused brine drainage from the surface if the experiment had been continued.

2.3.4 Sea-ice melt phase

The sea-ice melt phase in the tank is harder to interpret than the growth phase. There are several reasons for this. First, when temperatures are greater than around 0 ^{o}C the sea ice at the surface melts, and this is the dominant processes thinning the sea ice. The position of the instrumentation relative to the sea-ice surface therefore

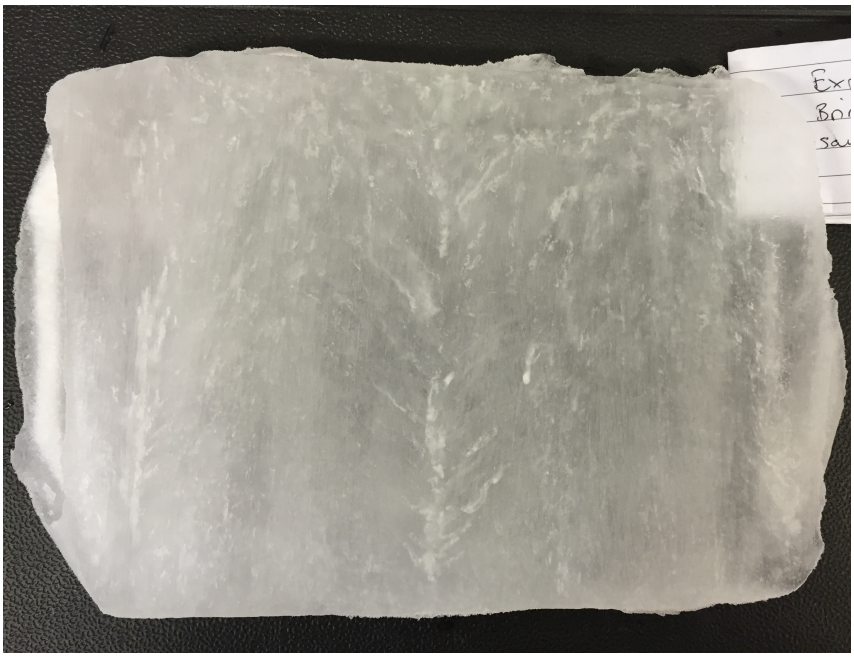

Figure 2.12: This picture shows a vertical slice of sea ice cut from a slab, around 15 cm thick, grown in the Roland von Glasow air-sea-ice chamber. The lighter area near that runs vertically through the sea ice is a brine channel.

changes through time. Second, the sea ice melts quickest around the edges of the tank, even when the heating pads are off. Open water is therefore exposed to the atmosphere, and meltwater runs off of the sea ice into the ocean. Finally, sampling warm sea ice is more difficult than sampling cold sea ice because the permeability is higher. Even using the Cottier et al. (1999) technique is problematic, because the sea ice must re-freeze more than colder sea ice, and so may undergo more significant post processing.

Setting the atmospheric temperature to -2 ^{o}C is the most controlled melt phase achievable in the facility. In this case, the sea ice retains its position and thickness relative to the end of the growth phase, but the microstructure opens up as significant internal melt occurs.

2.4 Modelling the sea-ice tank

2.4.1 Constructing tank models

The tank can be well approximated by 1D models. Chapters 3 and 6 detail the formulation of two such models, so here I only give a broad overview of the models I have developed. A model representing the facility will likely need, at most, three parts: ocean, sea ice, and atmosphere. Depending on the question of interest, any one of these parts could be the focus of a model, and in this thesis I always focus on the sea ice. Both of my models consider 1D vertical columns of sea ice, divided into several vertical layers, and key variables are computed by the models for each layer. These layers may change in size as sea-ice thickness changes (Chapter 3), or may have a fixed thickness (Chapter 6). Figure 2.13 shows, schematically, the two model grids used in this thesis.

The ocean may be of no concern to the modelling of the sea ice, and considered simply as a region of sea ice with zero solid fraction. This may be the case if budgeting of dissolved species in the sea ice and ocean is not required to address the scientific question (Chapter 6). Alternatively, the ocean can be represented as a box, containing a mass of water and, say, salt (Chapter 3). In this way the salinity of the ocean can change as sea ice grows and salt is rejected from the sea ice. Not only does this approach allow for budgeting of salt, it also allows the freezing temperature of the sea water, and so the basal sea-ice temperature, to change with the salinity. When salinity changes are small, the basal sea-ice temperature can be approximated as constant, but for the larger salinity changes observed in the sea ice tank experiments this assumption is not valid. In Chapter 4 I continuously mix the experimental ocean with pumps so that I can model the ocean as a well mixed box.

I have either neglected the atmosphere in my model formulations, or have treated it as simply a temperature that changes through time. The rational for this approach is that 1) I do not attempt to model volatile compounds in this thesis; 2) wind speed and ocean heat fluxes are poorly quantified in the facility, so sea-ice thickness must be tuned, even for realistic atmospheric forcing; and 3) I have

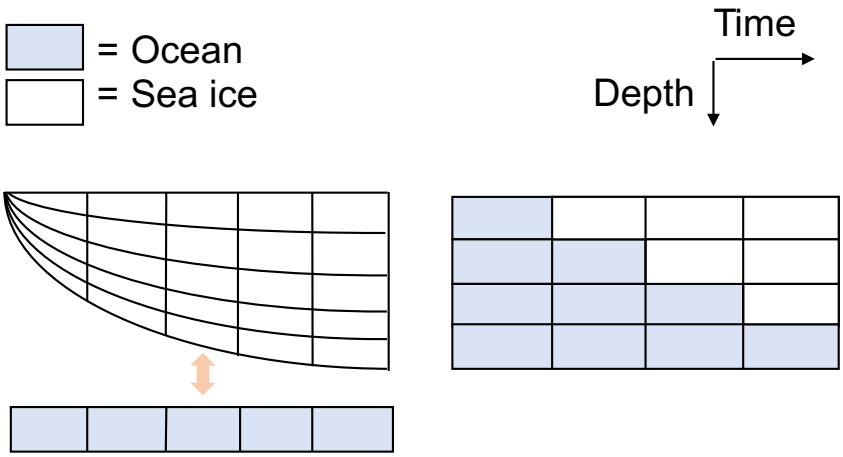

Figure 2.13: These are diagrams of the model grids used in this thesis to represent the facility. The schematic on the **left** represents the grid used in Chapter 4. The number of layers within the sea ice (white) is fixed, so the layers thicken in proportion to the sea ice. The orange arrow shows that water and dissolved compounds can be exchanged between the sea ice and an ocean (blue). The schematic on the **right** represents the grid used in Chapter 6. Here, the layers do not change in size. A layer freezes when the solid fraction becomes greater than 0.

the option to force the model with measured sea-ice properties, in which case atmospheric forcing is dealt with implicitly.

2.4.2 Forcing tank models

In this thesis I often use measured sea-ice temperature, solid fraction, and thickness in lieu of a thermodynamic model component[1]. I take this approach because I am investigating processes that are affected by sea-ice thermodynamics, but not thermodynamic processes themselves. By simply measuring the results of the thermodynamics, and using these to force the models, I minimise the error from the thermodynamics in the models, and I can study the processes of interest with reduced uncertainty.

In Chapter 6 I use temperature and solid fraction as forcing, and in Chapter 4 I use temperature and thickness. In both modelling studies I map the measured temperature (and solid fraction) onto a model grid. This step is necessary because 1) the 1 or 2 cm vertical resolution in measured temperature (and solid fraction) is undesirably coarse, particularly for the early stages of sea-ice growth; and 2) the thermistors used to measure temperature are stationary, and so cannot represent the

[1]The only exception is Chapter 3, when I model the experiments of Eide and Martin (1975).

varying layer size used in Chapter 4.

The first step in building model forcing is to define the sea-ice thickness. This step is necessary because while it is valid to interpolate between points of measurement in sea ice, it is not valid to interpolate between frozen and unfrozen sensors. There are two possible approaches to defining the thickness. The first is to find the points in time when wireharp wirepairs first become frozen. The depth of these wirepairs as they begin to freeze in is the position of the advancing sea-ice/ocean interface. This approach gives a measurement of sea-ice thickness for each wirepair that eventually freezes, and to build a continuous thickness I linearly interpolate between these measurements. This approach is difficult if ice nucleates on the wireharps ahead of the advancing front, and impossible if the wireharps are not used in a given experiment.

The second approach (Figure 2.14) exploits the fact that temperature profiles in growing sea ice are approximately linear (Notz and Worster, 2008), and that ocean temperature is independent of depth. I first define an approximate thickness, either by manually inspecting the temperature profiles, or by using the deepest point with non zero solid fraction. All thermistors shallower than this are taken to be frozen into sea ice. I then build a linear model of temperature against depth for the frozen thermistors for each time point. I calculate the thickness by finding the depth at which the model predicts the average ocean temperature. This approach provides a thickness 'measurement' for each timestep. The resulting thickness is noisy, and to make it suitable for use as forcing I smooth the thickness.

Once the thickness is defined for each time step, the steps to build the final forcing diverge depending on the required grid (Figure 2.13). For the dynamic grid in Chapter 4 I first define the number of layers. I then calculate the position of the time varying mid points and edges of each layer, assuming an even spacing over the thickness at each timestep. When the midpoint of a model layer is between two frozen temperature measurements I linearly interpolate the measured temperature to the model grid. When the mid point of a model layer is shallower than the near surface thermistor, or deeper than the deepest frozen thermistor, I linearly

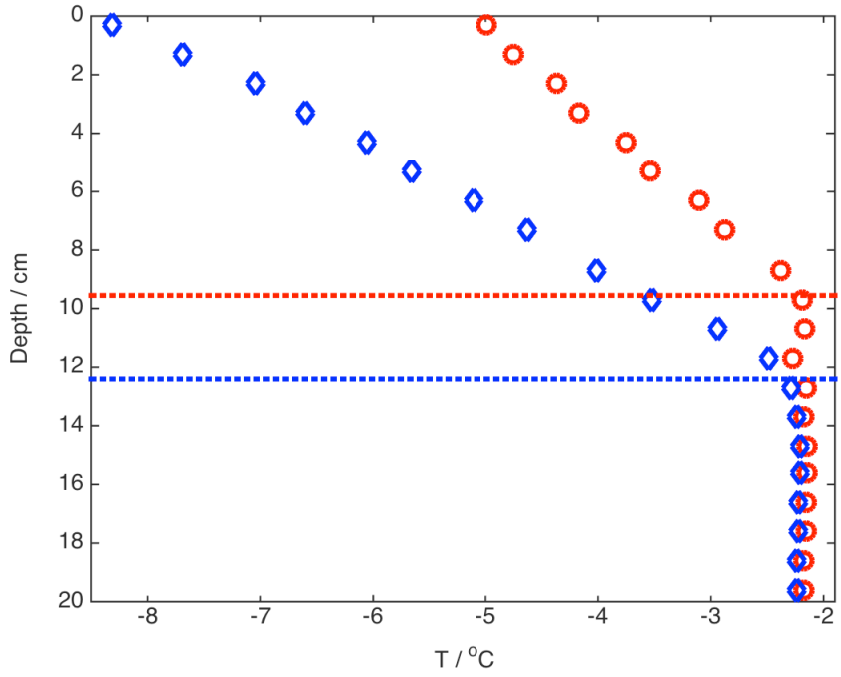

Figure 2.14: The data in this graph are from the experiment presented in Chapter 4, and show how I use temperature profiles to calculate sea-ice thickness. Each colour denotes a point in time, and the data shown by red circles come before the blue diamonds. For each point in time I have extrapolated a linear fit to the temperature profile back to the mean water temperature to calculate the thickness (dotted lines). The procedure is described in Section 2.4.2. The deviation from linearity near the surface in the blue data, which is around 0.5 ^{o}C lower than the extrapolation of the interior temperature profile to the surface, is caused by a cold bias, as heat is conducted along the body of the thermistor chain. In this case I have excluded the near surface data from the linear model used to calculate thickness.

extrapolate the measured temperature of the two nearest thermistors to the model grid. The edge points are defined in a similar way, but using the temperature at the mid points, rather than the measured temperature. After this the sea-ice thickness, and temperature profile through that thickness, is defined for each model timestep.

In Chapter 6 I map measured temperature and solid fraction to a stationary grid. To do this I first define a model grid with a total depth greater than the largest sea-ice thickness, divided evenly into the required number of layers. I then use a similar procedure to the above paragraph to map temperature and solid fraction to this grid. In this case, the model grid is a mixture of sea ice and ocean, with the ocean defined as a region with a solid fraction of 0. The ocean (and the most porous sea ice) do not factor into the model calculations due to my formulation of the model.

The result of these procedures is a specific forcing file for each experiment. This file takes into account all of the processes contributing to the sea-ice

thickness, temperature, and solid fraction. A trade off is made, however, in that perturbing this forcing is difficult and time consuming. The user must run another experiment! This tradeoff is justified by the increase in confidence that the underlying thermodynamics for a given model run are as accurate as possible.

2.5 Conclusions

I used the Roland von Glasow air-sea-ice chamber to generate data to address two scientific questions, and these questions form the basis of this thesis. In Chapter 4 I am able to evaluate gravity drainage parameterisations against data collected in the facility. In this experiment I exploit the tight control I had over the water composition in the facility to observe gravity drainage in a novel way. In Chapter 4 and Chapter 6 I use measured sea-ice properties as model forcing, minimising any error from modelled thermodynamics. In Chapter 5 I exploit the opportunity presented by the facility to systematically vary the atmospheric forcing, ocean conditions, and the state of the sea ice at the tank sides, allowing me to investigate the drivers of measured pressure signals. I also highlight some of the limitations of the facility in Chapter 6, where I show that the the confined tank environment cannot simultaneously satisfy all of the assumptions in a thermal stress model. The results in this thesis were made possible by the control, flexibility, and well defined boundary conditions provided by the facility.

The Roland von Glasow air-sea-ice chamber is a powerful tool for sea-ice research when used to address well defined scientific objectives. Tightly controlled experiments can be conducted to investigate polar processes, and to evaluate model parameterisations. The temperature range, size of tank, high level of instrumentation, and controllable visible and UV lighting make the range of possible experiments uniquely wide for a facility of this type. The results in this thesis are only a subset of the work that has been completed in the Roland von Glasow air-sea-ice chamber, which has now been used in physical, chemical and biological studies.

The scientific outcomes, to date, from the facility are reduced in scope from Roland's original vision, but two key objectives have been satisfied. First, Roland wanted to use the facility to bridge gaps between numerical models and the real world. I hope I further this goal in Chapter 6 and, in particular, in Chapter 4. Second, Roland wanted the facility to instigate collaborations and bring research groups together. Groups from across the UK and Europe have come together to use the facility, and at the time of writing researchers from all over the world are booked in for collaborative experiments. The wide range of users and new collaborations is a great success, and speaks to Roland's ambition and foresight, and the care he took when designing the facility.

Chapter 3

Using gravity drainage parameterisations to model general dissolved tracers

3.1 Summary

- I implement four gravity drainage parameterisations in a numerical model: Rees Jones and Worster (2014) (RJW14), Griewank and Notz (2013) (GN13), Vancoppenolle et al. (2010) (VC10), Cox and Weeks (1988) (CW88).
- A convective version of the scheme presented by Cox and Weeks (1988) (CWconv) is formulated.
- The convective gravity drainage parameterisations of RJW14, GN13, and CWconv are implemented using the same numerical framework.
- I describe how these schemes are used to model dissolved tracers that are decoupled from the salinity.
- I present a model that can evolve these schemes in a tank environment.
- A preliminarily evaluation of the performance of these schemes is performed against salinity measurements made in the Roland von Glasow air-sea-ice chamber.

- A preliminary evaluation of the performance of these schemes is performed against measurements of a general dissolved tracer, which is decoupled from the salinity. These measurements were made by Eide and Martin (1975).

- For both preliminary evaluations the convective parameterisations (RJW14, GN13) perform well. VC10 performs worst due to numerical instabilities. The performance of CWconv is intermediate between the other schemes when predicting bulk salinity.

- Further experiments are suggested to quantitatively evaluate the schemes for general dissolved tracers.

3.2 Background and objectives

Many observational and numerical studies have been conducted that provide a foundation for parameterising gravity drainage. Gravity drainage was observed in laboratory sea ice by Eide and Martin (1975), Niedrauer and Martin (1979), and in the field by Lake and Lewis (1970). All of theses studies suggested that some convective process drives gravity drainage, and that brine channels play key role in the desalination of sea ice. Recent instrumental developments (Notz et al., 2005) allowed Notz and Worster (2008) to measure the evolution of sea ice salinity *in situ* during the early stages of sea-ice growth in the Arctic. The measured salinity profile is continuous across the sea-ice/ocean interface, which refutes claims of initial segregation (Cox and Weeks, 1988; Weeks, 2010), and confirms that gravity drainage is the only important process desalinating growing sea ice. They interpret their results using a Rayleigh number (Equation 1.4) as an indicator of whether gravity drainage is occurring. Wells et al. (2011) perform two dimensional numerical simulations of growing sea ice. The salt flux, by gravity drainage, is shown to be linearly related to the Rayleigh number. Their modelled gravity drainage is convective, with brine flowing upwards over a broad region (called 'mush'), and downwards in a narrow region (called a 'brine channel').

Several one dimensional parameterisations of gravity drainage have been proposed that build on these suggestions that gravity drainage can be diagnosed and quantified using a Rayleigh number. These parameterisations improve on previous empirical parameterisations (Cox and Weeks, 1988) by better representing the physical mechanisms that underly gravity drainage, and by not requiring initial segregation. Vancoppenolle et al. (2010) parameterise gravity drainage as a diffusive process, with a diffusivity that is greatly increased when the Rayleigh number exceeds a certain threshold. Building the work of Wells et al. (2011), Griewank and Notz (2013), Turner et al. (2013), and Rees Jones and Worster (2014) parameterise gravity drainage as an advective process, based on convection, and calculate the velocity of moving brine using the Rayleigh number. Despite the proliferation of gravity drainage schemes in the literature, no quantitive comparison

of the schemes has been performed.

Another motivation for the development of these gravity drainage parameterisations was the need for a scheme that could predict the transport of dissolved tracers other than salt, so called 'general dissolved tracers' (Section 1.3). Modelling such tracers is an important step towards quantifying the role of sea ice in biogeochemical cycles of, for example, carbon. The most widely used gravity drainage parameterisation, proposed by Cox and Weeks (1988), cannot be applied to general dissolved tracers because it relies on assumptions that are specific to salinity. Vancoppenolle et al. (2010) was the first scheme to be applied to general dissolved tracers, and has been used subsequently in several studies, for a variety of biogeochemical tracers (Moreau et al., 2014, 2015; Kotovitch et al., 2016). Another, similar diffusive scheme is proposed by Jeffery et al. (2011) that transports general dissolved tracers, with additional options for parameterising the diffusivity. Convective schemes have so far not been applied to general dissolved tracers.

The transport of general dissolved tracers is governed by the same processes that transport salt, but it does not necessarily follow that parameterisations that perform well for salt perform well for general dissolved tracers. All of these parameterisations are approximate, representing a three dimensional process, convection in a mushy layer, in a one dimensional framework. The schemes are tools, developed using, tuned to, and evaluated against measurements of salinity. In order to use these tools confidently they must be evaluated against measurements of a general dissolved tracer, and against each other.

My overarching goals for this study, which spans this chapter and Chapter 4, are to:

1. Compare the performance of several important gravity drainage parameterisations when predicting the salinity profile of growing sea ice.

2. Evaluate how well these parameterisations perform when predicting the dynamics of general dissolved tracers.

To progress these goals, in this chapter I aim to:

- Formulate a model that can predict the salinity evolution of growing sea ice using several gravity drainage parameterisations, and that can do so in a tank environment.
- Extend this model so that it can predict the evolution of a general dissolved tracer, the concentration of which can be decoupled from the salinity.
- Perform a preliminary evaluation of the performance of these schemes against salinity data collected in the Roland von Glasow air-sea-ice chamber.
- Preform a preliminary evaluation of the performance of these schemes against the experiments of Eide and Martin (1975), where observations are made of a decoupled tracer.

In this chapter I first describe the various gravity drainage parameterisations in the literature, and justify the inclusion/omission of these schemes from the model I develop (Section 3.3). In Section 3.4 I describe the numerical implementation of the schemes in the model, as well as the model set up I use to simulate sea ice tanks. Then, in Section 3.5, I evaluate the chosen schemes against my own measurements of salinity, and the the experiments of Eide and Martin (1975). Finally, I conclude and suggest refinements to the experimental approach of Eide and Martin (1975) that allow me to qualitatively evaluate the schemes in Chapter 4.

3.3 Modelling gravity drainage as a one dimensional, vertical process

3.3.1 Parameterisations of salinity evolution

Empirical parameterisations

Cox and Weeks (1988) propose a parameterisation for the desalination of growing sea ice based on gravity drainage. Their scheme is derived from salinity measurements made by Cox and Weeks (1975). In their scheme, sea ice desalinates *via* two mechanisms, 1) a transfer of salt from the sea-ice interior to the ocean

(gravity drainage), and 2) a segregation of salt between newly forming sea ice and ocean (initial segregation).

Mechanism 1) proceeds *via* Equation 3.1, which is a simplified recasting of the equation presented in Cox and Weeks (1988)

$$\frac{\Delta S_b(z)}{\Delta t} = \delta(1-\eta(1-\phi(z)))\frac{\Delta T}{\Delta z} \tag{3.1}$$

The rate of change of sea-ice bulk salinity ($\frac{\Delta S_b(z)}{\Delta t}$) is related empirically to the temperature profile ($\frac{\Delta T}{\Delta z}$). δ is an empirical parameter used to tune the rate of desalination. η is chosen such that the rate of change of salinity becomes zero when the solid fraction, ϕ, reaches a certain threshold, at which point the sea ice is assumed to be so solid that no desalination occurs (i.e. becomes totally impermeable). Cox and Weeks (1988) choose this threshold as $\phi = 0.95$, which is consistent with other studies (Golden et al., 1998; Pringle et al., 2009). The form of Equation 3.1 is such that, other things being equal, less solid sea ice undergoes quicker desalination. Cox and Weeks (1988) assume that the temperature profile is always positive (warming with increasing depth), and is perfectly linear, both of which are reasonable assumptions in growing sea ice.

Mechanism 2) instantly desalinates any newly formed sea ice. In each mass of new sea ice, some salt is retained and some salt is transferred to the ocean. The fraction of retained salt, k_{eff}, is calculated using the basal growth rate of the sea ice, with faster growth retaining more salt.

$$k_{eff} = f\left(\frac{dh}{dt}\right) \tag{3.2}$$

The growth rate is the change in sea-ice thickness, h, over time. The functional form of f is not continuous, and is split into three growth rate regimes which can be found in Cox and Weeks (1988). As mentioned in Chapter 1, Cox and Weeks (1988) define sea ice as not including the bottommost portion. The region between ocean and 'sea ice' is treated as a boundary layer known as the skeletal layer. Equation 3.2 can be thought of as a parameterisation for the desalination of the skeletal layer.

The scheme presented by Cox and Weeks (1988), which from this point I refer to as CW88, has been used in several studies. The original Cox and Weeks (1988) paper investigates sea-ice strength using porosity as predicted by CW88. Vancoppenolle et al. (2006) and Saenz and Arrigo (2012) use CW88 to investigate the desalination of sea ice. The studies of Butler et al. (2016, 2017) use CW88 to predict the amount of precipitated salts in sea ice.

But CW88 is deficient in two ways. First, field measurements show that the salinity across the sea-ice/ocean interface is continuous (Notz and Worster, 2008). When using CW88, sea ice cannot be defined to include the skeletal layer without the initial segregation scheme conflicting with these measurements. Important biogeochemical processes, such as the growth of sea-ice algae, occur largely in the skeletal layer. CW88 is not appropriate for studying these processes.

Second, the empirical nature of Equation 3.1 make it difficult to model tracers other than salinity with CW88. Equation 3.1 assumes that the bulk salinity always decreases. This assumption is valid for salinity, but cannot be extended to a general tracer. Also, brine salinity is a function of temperature in sea ice. The temperature gradient in Equation 3.1 can therefore be interpreted as a brine salinity gradient, which drives desalination. The concentration of a general tracer is not a function of temperature, so the temperature gradient is not an appropriate way to parameterise the dynamics of such a tracer.

Because of these drawbacks CW88 cannot be evaluated in this study in its original form. However, given its widespread use and historical importance I have developed a version of CW88 that can deal with biogeochemical tracers, which is described in Section 3.3.1.

Diffusive parameterisations

Vancoppenolle et al. (2010) propose a diffusive gravity drainage parameterisation, from here called VC10 (Figure 3.1). Diffusive schemes are analogous to some ocean models, where a condition defines whether diffusion is molecular or turbulent. ‘Diffusive’ refers to the functional form of salt transfer in these schemes, and should not be confused with the true molecular diffusion of salt. In diffusive

parameterisations there is no need to segregate salt at the growing sea-ice/ocean interface. Also, diffusive schemes don't rely on prior assumptions about the form of the salinity profile, and so can readily be applied to general tracers.

In diffusive schemes, gravity drainage is simulated using

$$\frac{\partial S_b}{\partial t} = \frac{\partial}{\partial z}\Big((1-\phi)D_e\frac{\partial S_{br}}{\partial z}\Big) \tag{3.3}$$

where D_e is the effective diffusivity, and S_{br} is the brine salinity. Other things being equal, larger effective diffusivities cause more diffusion of salt. VC10 cannot capture observed desalination if the effective diffusivity is equal to the molecular diffusion of salt. Vancoppenolle et al. (2010) therefore define a condition whereby D_e switches from molecular to turbulent diffusion, and set turbulent diffusion, D_{tur}, to be three orders of magnitude larger than molecular diffusion, D_m. The effective diffusivity is then given by

$$D_e = \begin{cases} (1-\chi)D_m + \chi D_{tur} & \phi <= 0.95 \\ 0 & otherwise \end{cases} \tag{3.4}$$

When the solid fraction increases above 0.95 diffusion ceases completely, similar to CW88, as the sea ice is presumed to be impermeable. The function χ acts to switch between D_m and D_{tur}

$$\chi = \frac{tanh((Ra(z) - Ra_c)) + 1}{2} \tag{3.5}$$

When the local Rayleigh number, $Ra(z)$, is larger than Ra_c, χ approaches 1 and D_e is about equal to D_{tur}. When $Ra(z)$ is less than Ra_c, χ approached 0 and D_e is about equal to D_m. In this way VC10 seek to represent the onset of gravity drainage as some critical Rayleigh number is exceeded, as noted by (Notz and Worster, 2008).

So far, only diffusive schemes have been used to transport biogeochemical tracers in model studies. Vancoppenolle et al. (2010) focus on dissolved silicate, and on algal growth within sea ice. Subsequent studies, using the same parameterisation, used diffusive schemes to transport various dissolved gases and nutrients (Moreau et al., 2014, 2015; Kotovitch et al., 2016). Jeffery et al. (2011)

use two formulations of D_e to investigate the transport of salt within sea ice. One formulation is similar to Equation 3.4, and the other is based on a mixing length analogy. In their study, temperature and bulk salinity from a laboratory study (Cottier et al., 1999) are used as forcing. They then use their scheme to transport salt, treating this salt as a tracer. They are able to reproduce bulk salinity profiles well, and achieve reasonable agreement with brine salinities calculated from the local sea-ice temperature.

But there are important drawbacks to the diffusive schemes, regardless of the formulation of D_e. First, our best understanding of gravity drainage is that it is an advective process (Wells et al., 2011; Worster and Rees Jones, 2015). Parameterisations of salt transport in sea ice would therefore ideally transport brine, rather than diffusing salt between model layers. Second, diffusive schemes lead to anomalous salt depletion in near surface sea ice, as can be seen in Figures 5 and 7 in Jeffery et al. (2011). Finally, in VC10 the diffusivity drops to zero at the sea-ice/ocean interface because the Rayleigh number drops to zero here. In VC10 the diffusivity in the bottom layer is taken from the midpoint, rather than the edge, which gives VC10 an unwanted dependance on the model layer thickness.

I evaluate the parameterisation of Vancoppenolle et al. (2010), VC10, in this study because of its previous use in biogeochemical studies. I do not include the the scheme of Jeffery et al. (2011) because it is similar in form to VC10 and no framework is presented by Jeffery et al. to include it in a model that is not forced by salinity, which is a requirement for this study.

Convective parameterisations

Wells et al. (2011) model gravity drainage as a convective process, with a broad area of brine upflow and narrow downflow through a brine channel (Figure 3.1). They find that the magnitude of the salt flux form sea ice is linearly related to the Rayleigh number, when the Rayleigh number is above some critical value. Several gravity drainage parameterisations have been proposed that rely heavily on the results of Wells et al. (2011). These parameterisations derive 1D parameterisations based on

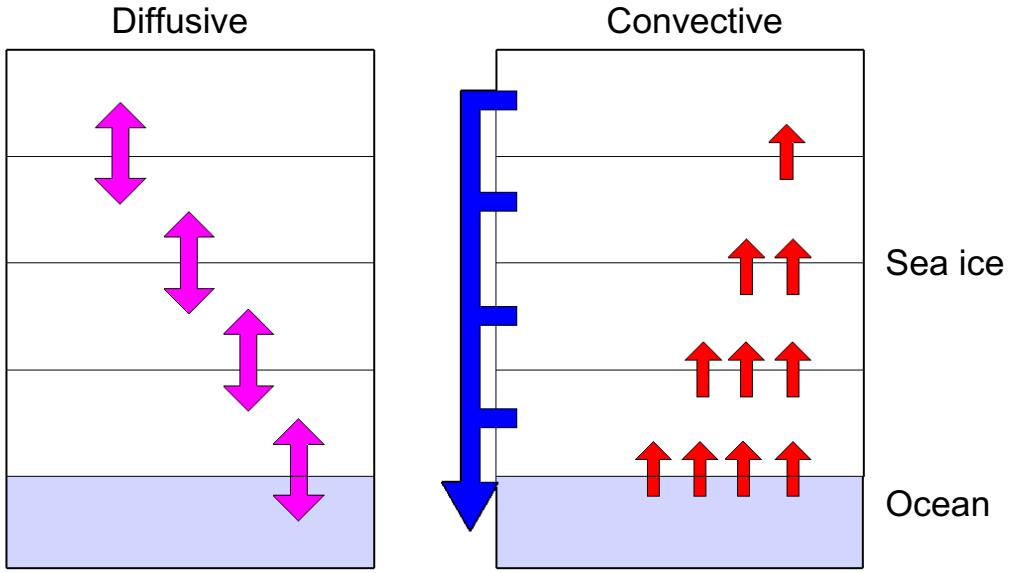

Figure 3.1: Schematic diagram of the transport of dissolved compounds in diffusive and convective gravity schemes. In the diffusive scheme compounds diffuse between sea-ice layers, and between the sea ice and the ocean. In the convective scheme, parcels of brine are moved from each layer directly into the ocean, and this brine is replaced by the adjacent underlying layer, or the ocean.

convection occurring in the sea ice (Rees Jones and Worster, 2014; Griewank and Notz, 2013; Turner et al., 2013).

Rees Jones and Worster (2014), from here referred to as RJW14, use local Rayleigh numbers to define a sea-ice layer over which convection is occurring by taking the shallowest depth where $Ra(z) > Ra_c$ to be the top of a convecting layer, and the base of the sea ice to be the bottom. They then calculate an effective Rayleigh number, Ra_e, that acts over the whole convecting layer, and use this to calculate the upwelling mush brine velocity, w_{RJW}, for each depth in the convecting layer

$$w_{RJW} = \begin{cases} -\alpha_{RJW} Ra_e \frac{k_l}{c_l} \frac{z-z_c}{(h-z_c)^2} & \text{if } z \geq z_c \\ 0 & \text{otherwise} \end{cases} \tag{3.6}$$

where α_{RJW} is a free tuning parameter, k_l and c_l are the thermal conductivity and volumetric heat capacity of brine, respectively, and z_c and z are the depth of the convecting layer and the depth of the model layer, respectively. h is the sea-ice thickness.

Their scheme then solves Equation 3.7 for each depth in the sea ice to evolve

the salinity. The salt lost from each sea-ice layer is assumed to be deposited directly into the underlying water *via* a brine channel.

$$\frac{\partial S_b}{\partial t} = -w\frac{\partial S_{br}}{\partial z} \tag{3.7}$$

Griewank and Notz (2013) derive a similar parameterisation of gravity drainage. Rather than diagnosing the upwelling brine velocity, they calculate the flux of downwelling brine into the ocean. The magnitude of the downwelling flux from a given model layer is linearly related to the local Rayleigh number at that depth *via* Equation 3.8.

$$br_{down} = \alpha_{GN}(Ra(z) - Ra_c)\Delta z.dt \tag{3.8}$$

In the above, br corresponds to a mass of brine, and α_{GN} is a free tuning parameter. The subscript $down$ indicates brine movement downwards, and can never be negative. The upwards brine flux, br_{up}, to each layer is calculated *via* mass conservation. The use of a local Rayleigh number contrasts with Rees Jones and Worster (2014), who use a local Rayleigh number to calculate the depth of the convecting layer, then calculate the upwelling brine velocity using the largest Rayleigh number in that region.

The change in salinity at each depth in the Griewank and Notz (2013) parameterisation is given by Equation 3.9

$$\Delta S_b = \frac{br_{up}}{\rho_{br}dz}(\Delta S_{br}) \tag{3.9}$$

where ρ_{br} is the density of brine. Griewank and Notz (2013) achieve impressive agreement with laboratory experiments (Notz, 2005), and Griewank and Notz (2015) apply a 1D model utilising this parameterisation, forced with reanalysis data, and successfully capture measured Arctic sea-ice salinities.

Two modes of gravity drainage are present in a scheme proposed by Turner et al. (2013). A rapid drainage mode acts in a region close to the ice-ocean interface, and a slow mode desalinates the full ice thickness. In their scheme, only the rapid mode is parameterised based on a Rayleigh number, while the slow mode is a

simple relaxation of the salinity profile (Vancoppenolle et al., 2009). The motivation for these two modes is an apparent step change in desalination rates at higher permeabilities, which occurs near the ice/ocean interface. Their scheme is capable of reproducing laboratory experiments (Notz, 2005), and has been incorporated into large scale, 3D models.

Worster and Rees Jones (2015) show that RJW14, GN13, and Turner et al. (2013) are theoretically similar. In this study I evaluate RJW14 and GN13. The scheme proposed by Turner et al. (2013) is not included because the slow desalination mode, where the salinity profile is simply relaxed, is not compatible with biogeochemical tracer transport because such tracers may not decrease in sea ice through time.

Equivalence of convective schemes

Before implementing RJW14 and GN13 numerically I show that both schemes can be solved using the same equation to evolve the salinity (Equation 3.7). I also formulate a convective version of CW88, called CWconv, that can be used to transfer salt and tracers between model layers. To include these schemes in the same numerical framework, I recast the GN13 (Equation 3.9) and CW88 (Equation 3.1), such that they can be expressed using Equation 3.7, which evolves salinity for RJW14.

Starting with GN13, I note that by dividing both sides by dt, Equation 3.9 can be recast as

$$\frac{\Delta S_b}{dt} = \frac{br_{up}}{\rho_{br} dt \Delta z}(\Delta S_{br}) \tag{3.10}$$

which is equivalent to Equation 3.7 when

$$w_{GN} = \frac{br_{up}}{\rho_{br} \Delta t} \tag{3.11}$$

Noting that $br_{up}(k) = \sum_{i=1}^{i=k} br_{down}(i)$, using Equation 3.8 I define

$$w_{GN} = \frac{\alpha}{\rho_{br}} \sum_{k=1}^{i=k} \alpha(Ra(z) - Ra_c)\Delta z.dt \tag{3.12}$$

Similarly, for CW88 I note that, to a good approximation, brine salinity is a linear function of temperature, such that $S_{br} = -\mu T_{br}$, where μ is a constant in the linear liquids relationship (Assur, 1958; Notz, 2005). I then recast Equation 3.1 as Equation 3.13

$$\frac{\Delta S_b(z)}{\Delta t} = -\delta\mu(1-\eta(1-\phi(z)))\frac{\Delta S_{br}}{\Delta z} \tag{3.13}$$

which is equivalent to Equation 3.7 when

$$w_{CW} = \begin{cases} \delta\mu(1-\eta(1-\phi(z))) & \text{if } \phi \leq 0.95 \\ 0 & \text{otherwise} \end{cases}$$

It is striking that the scheme of Cox and Weeks (1988) is similar to the convective schemes of Rees Jones and Worster (2013) and Griewank and Notz (2013). As S_{br} is a function of T, the change in salinity of each layer in the CW88 is driven by the decreasing brine salinity (and hence density) with depth. The magnitude of this salinity change is mediated by the porosity of the sea ice rather than some Rayleigh number, but Rayleigh numbers are mediated by permeability, which is in turn a function of porosity, and in this sense the schemes are again similar.

A significant difference between CWconv compared to the two convective parameterisations is the segregation of salt at the interface. To ensure the schemes are consistently implemented I am forced to remove initial segregation from CWconv. In a sense it is unfair to compare CWconv to more recently developed parameterisations, as Cox and Weeks (1988) explicitly ignore the skeletal layer in their scheme. However, CWconv is the best available option to evaluate this important scheme in this study.

Now, CWconv, RJW14 and GN13 can all be represented using Equation 3.7, and an appropriate formulation for the upwelling brine velocity, w.

3.3.2 Extending parameterisations to general dissolved tracers

A general dissolved tracer has been added to the model based on three assumptions:

1. The concentration of the tracer is so low that it is has no effect on the brine

dynamics.

2. The tracer is always perfectly dissolved.

3. The tracer has no sources/sinks such that the mass of tracer in the system is constant.

To evolve biogeochemical tracers, Vancoppenolle et al. (2010) simply replace the brine salinity in Equation 3.3 with the concentration of a given tracer in the brine to give Equation 3.14. The effective diffusivity, D_e, for tracer transport is taken to be equal to that of salt. This assumption is valid because brine dynamics drive the transport of dissolved compounds in general in sea ice.

$$\frac{\partial C_b}{\partial t} = \frac{\partial}{\partial z}\Big((1-\phi)D_e\frac{\partial C_{br}}{\partial z}\Big) \tag{3.14}$$

In the above, C_b and C_{br} are the bulk and brine concentrations of any given solute. As yet no studies have transported biogeochemical tracers using a convective scheme. I take a similar approach to Vancoppenolle et al. (2010) and simply replace the brine salinity by the brine tracer concentration in Equation 3.7, using the same w value that was used to transport salt, to give Equation 3.15. Convective schemes simulate the advection of parcels of brine. Using the same w value for salt and tracer is therefore valid, because the evolution of salinity and tracer is driven by the movement of the same parcel of brine.

$$\frac{\partial C_b}{\partial t} = -w\frac{\partial C_{br}}{\partial z} \tag{3.15}$$

With this implementation of diffusive and convective schemes, if tracer is well mixed with the initial salinity then the tracer and salinity concentration evolve identically. However, tracer can be added to the ocean underlying sea ice at any timestep, so that the tracer concentration can be decoupled from the salinity.

Table 3.1: 1D gravity drainage parameterisations that are evaluated in this study.

Abbreviation	References	Mechanism
CW88/ CWconv	Cox and Weeks (1988) Vancoppenolle et al. (2006) Saenz and Arrigo (2012) Butler et al. (2016, 2017)	Empirical / Convective
VC10	Vancoppenolle et al. (2010) Moreau et al. (2014) Moreau et al. (2015) Kotovitch et al. (2016)	Diffusive
RJW14	Rees Jones and Worster (2013) Rees Jones and Worster (2014)	Convective
GN13	Griewank and Notz (2013) Griewank and Notz (2015)	Convective

3.4 Modelling gravity drainage in laboratory experiments

3.4.1 Numerical implementation of parameterisations

I have implemented the schemes presented in Table 3.1 into a numerical model written in Matlab. In this section I describe this model, and how I have applied it to sea-ice tank studies.

The steps required to evolve the bulk salinity are shown in Figure 3.2. The steps to evolve tracer are similar, except that the brine tracer concentration is a function of the bulk concentration at the previous timestep and the brine volume, whereas the brine salinity is a function of temperature.

The thickness, h, surface temperature, T_s, basal temperature, T_b, and interior temperature, T_i, of the model sea ice can all be read from a forcing file. The procedures I use to produce this forcing file are described in Section 3.4.2. Alternatively, the model can calculate these parameters, and in this section I describe the calculated, rather than the prescribed, forcing.

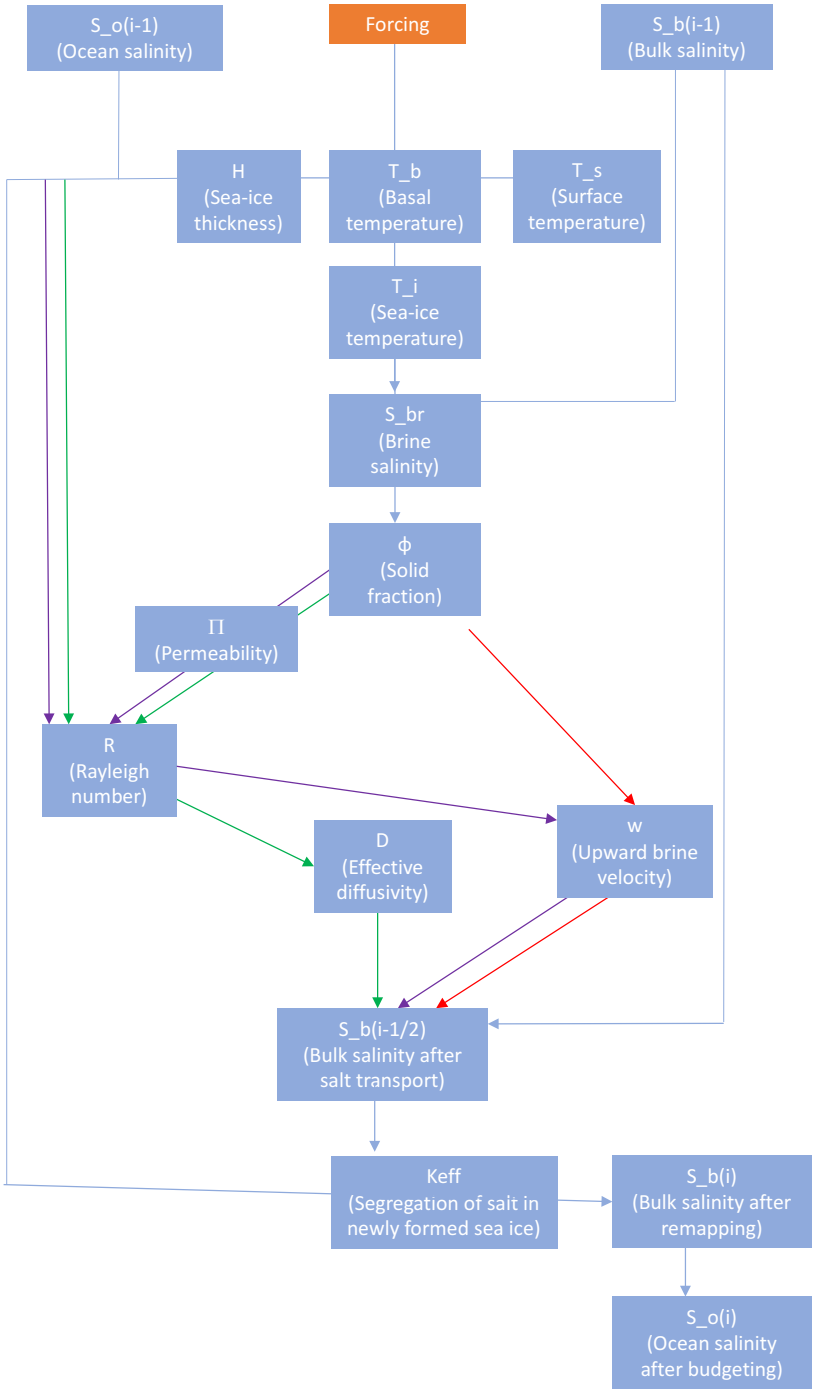

Figure 3.2: Steps involved in the calculation of the bulk sea-ice salinity, S_b, for timestep i. Arrows show the progression of the model through the intermediate parameters. Blue (all schemes), purple (convective schemes, RJW14 and GN13), red (CWconv and CW88) and green (VC10) arrows correspond to processes specific to certain schemes. Blue boxes contain model variables, and the orange box represents the forcing used.

An initial ocean and sea-ice salinity, and sea-ice thickness, is user defined for the first timestep. For each timestep I then define a temperature profile through the

sea ice using T_b, T_s, and h.

The ocean is assumed to be at its freezing point, such that the temperature at the sea-ice/ocean interface is given by

$$T_b = f(S_o) \tag{3.16}$$

where f is an appropriate liquidus that calculates the salinity dependent freezing point of the ocean (Notz, 2005). For NaCl, Notz (2005) give the following fit to the data of Weast (1971)

$$T_b = -0.0592 S_o - 9.37 \times 10^{-6} S_o^2 - 5.33 \times 10^{-7} S_o^3 \tag{3.17}$$

When T_s is prescribed, the model simulates experiments where sea ice is grown from a cold plate, such that the surface sea-ice temperature is constant (Eide and Martin, 1975; Wettlaufer et al., 1997; Notz, 2005). When computed, an air temperature and ocean heat flux is input, and a surface heat flux equation is solved numerically[1].

h may be calculated from the balance of some prescribed ocean heat flux, and the conductive heat flux through the sea ice (Equation 1.3). There are several unknowns in the heat fluxes in the Roland von Glasow air-sea-ice chamber, such as the heat from instrumentation, the proportion of heat from outside heating pads that enters water, heat introduced by replacing sampled water and heat transfer between the under ice water and the relatively warm side tank. For this reason, when surface temperature is calculated or prescribed, the ocean heat flux, atmospheric downwelling longwave, or sea-ice emissivity, should be tuned to force a reasonable thickness.

A temperature profile may then calculated by linearly interpolating between T_s and T_b over h. This temperature profile is used to calculate the brine salinity, at the edges and midpoints of each model layer, *via* a user defined function to calculate

[1]The surface temperature is never computed in this thesis. It is always prescribed by a coldplate temperature, or using measured sea-ice temperatures.

the brine salinity (Equation 2.3).

The solid fraction is then calculated as

$$\phi = 1 - \frac{S_b}{S_{br}} \tag{3.18}$$

For GN13, RJW14 and VC10, ϕ is used to calculate the sea-ice permeability at each depth (Equation 1.7, Freitag, 1999). This local permeability, Π, is used to calculate the harmonic mean permeability, Π_{HM}, for each layer, as suggested by Rees Jones and Worster (2014)

$$\Pi_{HM}(z) = \Pi_0 \left(\frac{1}{h-z} \int_z^h \frac{1}{\Pi(z)} dz \right)^{-1} \tag{3.19}$$

where Π_0 is a reference permeability (10^{-8} m^2 (Rees Jones and Worster, 2014)).

A local Rayleigh number is then calculated using the formulation of Rees Jones and Worster (2014)

$$Ra(z) = \frac{c_l g \beta_c}{k_l \nu} (S_{br}(z) - S_{ocean})(h-z)\Pi_{HM} \tag{3.20}$$

where g is the acceleration due to gravity; β_c is a the concentration expansion coefficient; k_l is the thermal conductivity; and ν is the kinematic viscosity. Note that Equation 3.20 is simply a more detailed version of Equation 1.4.

For VC10, the local Rayleigh number is used to calculate χ and the effective diffusivity D_e according to Equation 3.4 and Equation 3.5, respectively. GN13 calculate a downwelling brine flux, for each depth, based on this local Rayleigh number (Equation 3.8). RJW14 calculate an effective Rayleigh number

$$Ra_e = max(Ra(z) - Ra_c) \tag{3.21}$$

which is used to calculate w according to Equation 3.6.

For CWconv, Equation 3.13 is used to calculate w using ϕ rather than a Rayleigh number.

I show in Section 3.3.1, that by using an appropriate formulation of w, RJW14, GN13, and CWconv can all be represented using Equation 3.7. I therefore discretise and solve all convective schemes using Equation 3.22.

$$\frac{\partial S_b}{\partial t} = -w \frac{S_{br,k+\frac{1}{2}} - S_{br,k-\frac{1}{2}}}{\Delta z} \tag{3.22}$$

The diffusive schemes are evolved by solving Equation 3.3. To maximise stability, Equation 3.3 is solved implicitly using a finite difference scheme. This scheme was used in Vancoppenolle et al. (2010), has been copied over from that model, and is not my own work.

Salt is then advected (Equation 3.22) or diffused (Equation 3.3), and an intermediate bulk salinity profile is calculated. This intermediate profile takes into account only the flux of salt from the chosen gravity drainage parameterisation.

The final bulk salinity profile must take into account the flux of salt to the sea ice from basal growth. To do this, an additional ice layer, $N+1$, is added to the intermediate bulk salinity profile. The thickness of this layer is given by the change in sea-ice depth for the current timestep, and the salinity is calculated using

$$S_b(N+1,i) = k_{eff} S_o(i-1) \tag{3.23}$$

Only when using CW88 would I set $k_{eff} \neq 1$. The salinity for this new salinity profile is then linearly remapped onto an evenly spaced grid with N layers.

To simulate the complete ocean plus sea ice system in the Roland von Glasow air-sea-ice chamber, a simple tank configuration has been added for the MatLab model. A well mixed mass of water is adjusted based on the mass of sea ice at any given timestep

$$m_o(i) = m_{sys} - m_{si}(i) \tag{3.24}$$

where m_o is the mass of the ocean, m_{si} is the mass of the sea ice, m_{sys} is the total system mass, and i denotes the timestep. The change in salt and tracer content of the sea ice after gravity drainage and growth is subtracted from the total salt and

tracer content to give the updated ocean salt and tracer mass

$$m_{s,o}(i) = m_{s,o}(i-1) - (m_{si,o}(i) - m_{si,o}(i-1)) \tag{3.25}$$

where $m_{s,o}$ and $m_{si,o}$ represent the mass of solute (tracer or salt) in the ocean and sea ice, respectively. The updated ocean concentration is then the mass of solute in the ocean divided by the mass of the ocean

$$S_o(i) = m_{s,o}(i)/m_o(i) \tag{3.26}$$

3.4.2 Forcing parameterisations

Where possible I force the model with temperature profiles and thicknesses derived from experimental data. This eliminates error from modelling the thermodynamics, leaving only measurement error and error from the representation of brine dynamics.

I have a direct measure of sea-ice thickness from the wireharps from the depth of the deepest wirepair with a non zero solid fraction. However, the resolution on this measure of thickness is only 1 cm, and is not sufficient to provide the model with smooth forcing. To increase the resolution of the forcing thickness, I either linearly interpolate between points in time when the thickness changes, or extrapolate the linear sea-ice temperature profile to T_b, for each model timestep.

I have no direct measurement of surface temperature, so to force the model using experimental temperatures, I linearly extrapolate the measured temperature profiles back to $z = 0$. This treatment relies on the linearity of the sea-ice temperature profile, which has been demonstrated in our own experiments and in previous laboratory studies (e.g. Cox and Weeks, 1975). Furthermore, when forcing the model with experimental temperatures, the surface temperature does not affect the internal sea-ice temperature, so the consequences of any inaccuracy in its representation are reduced.

I make clear what procedures were used to formulate T_b, T_s and h for each individual experimental run. No single procedure was used, as different tank set

Table 3.2: Original and re-tuned parameters for gravity drainage parameterisations. The derivation of the new parameters is described in Chapter 4.

Scheme	Original parameters	Re-tuned parameters
RJW14	$Ra_c = 40$ $\alpha = 0.03$	$Ra_c = 3.0$ $\alpha = 0.20$
GN13	$Ra_c = 4.89$ $\alpha = 5.84 \times 10^{-4}$ / kg m^{-3}s^{-1}	$Ra_c = 2.6$ $\alpha = 0.009$ / kg m^{-3}s^{-1}
CWconv	$\delta = 1.68 \times 10^{-7}$ / g m kg^{-1} s^{-1} ^{o}C^{-1}	$\delta = 7.1 \times 10^{-7}$ / g m kg^{-1} s^{-1} ^{o}C^{-1}
VC10	$D_{tur} = 1 \times 10^{-6}$ / m^{2}s^{-1} $Ra_c = 5$	$D_{tur} = 3.0 \times 10^{-7}$ / m^{2}s^{-1} $Ra_c = 6.3$

ups, thermistor failures, wireharp failures and sea ice growing beyond the final wirepair or thermistor, mean the optimal procedures differ between runs.

3.4.3 Tuning parameterisations

To achieve the goals of this study, I need to tune each of the parameterisations against salinity measurements. By doing so I can evaluate the optimal performance of each parameterisation for salinity (Goal 1). Tuning the schemes to best capture the salinity evolution is also important for addressing Goal 2, evaluating these schemes for general dissolved tracers. Any errors in the salt dynamics, the calculation of the brine velocity, for example, will cause errors in the tracer dynamics also. Furthermore, the salt dynamics also determine the solid fraction of the sea ice, and so have knock on effects on, for example, Rayleigh numbers later in the simulation. Errors in the prediction of tracer dynamics could then come from, in addition to errors in the parameterisations, errors in the physical sea-ice properties. These errors in physical sea-ice properties must be minimised.

I therefore tune, and describe the tuning of, the schemes in Chapter 4, where I present data from an experiment with both tracer and salinity measurements. I

use the tuning parameters calculated in Chapter 4 in this chapter for two reasons, 1) for some schemes the original parameters perform poorly when evaluated in this chapter, and 2) evaluating the revised tuning parameters against a second data set allows me to investigate how robust they are. The original and revised tuning parameters are shown in Table 3.2.

3.5 Preliminary evaluation of parameterisations

3.5.1 Performance predicting salinity profiles

In this section I perform a preliminary evaluation of each parameterisation against wireharp measurements from an experiment in the Roland von Glasow air-sea-ice chamber. I have chosen this particular experimental run because the atmospheric temperature was relatively low, around -30 ^{o}C. This low atmospheric temperature caused the sea ice to grow relatively quickly and to retain more salt, and have a higher porosity that most other experimental runs. As the wireharps function best at higher porosities, the range of usefulness of the wireharps is maximised in this run. The highest solid fraction measurement presented is 0.9, and most of the measurements are closer to the recommended 0.8. Also, the cold temperature of this run is as close as possible to the range of temperatures presented in Section 3.5.2, where I perform an evaluation of the schemes for tracer dynamics. Finally, these atmospheric temperatures are much lower than those in Chapter 4, where I derive tuning parameters for the schemes. Good performance against these data would be a good indication that the tuning parameters are robust over a range of conditions.

To model this experiment I have used the measured water temperature as the basal sea-ice temperature. I have used a surface temperature linearly extrapolated from the interior sea-ice temperature profile. In the brief period where only one temperature sensor was frozen, I have used the earliest possible calculated surface temperature (i.e. the first point in time when two thermistors were frozen in). To force the internal sea-ice temperature I have linearly interpolated measured sea-ice

Table 3.3: Mean absolute deviation of modelled vertical bulk salinity profiles as compared to wireharp measurements, as shown in Figures 3.3 and 3.4.

	Mean absolute deviation [g kg^{-1}] original parameters				Mean absolute deviation [g kg^{-1}] re-tuned parameters			
Profile	RJW14	GN13	CWconv	VC10	RJW14	GN13	CWconv	VC10
0.3 days	9.16	8.43	7.19	11.61	4.67	4.19	7.00	9.86
0.4 days	10.30	7.93	9.88	10.01	3.07	3.02	7.49	8.67
0.6 days	9.91	6.71	10.73	9.69	3.14	3.14	6.84	12.44

temperature onto a model grid. I have set the number of layers in the sea ice to 25, and the timestep to 1 minute. The initial seawater and bulk sea-ice salinity is set to 35.25 g kg^{-1} NaCl, as this was the initial water composition in this run. I have used Equations 2.3 and 3.17 to calculate the brine and ocean salinity during this run. I ran the model using each parameterisation.

The measurements in Figure 3.3 show a progressive desalination of the sea ice through time, a near homogeneous interior salinity, and an increase in salinity near the ocean. None of the schemes capture the measurements using the original tuning parameters (Figure 3.3). GN13 captures the shape of the measurements, but not the magnitude of the desalination. RJW14 looks similar to GN13, but desalinates even less. CWconv has several inflections that are not present in the measurements. VC10 undergoes extreme desalination in the early stages, especially near the surface, and never recovers. In the earliest panel the second deepest layer in VC10 has an unrealistically high salinity, and in the later panels this unrealistically high salinity moves to the lowest layer.

This model run was not a fair test for CWconv because sea ice is defined as the region all the way to $\phi = 0$, rather than cutting off the skeletal layer. The poor performance should therefore be interpreted with caution. VC10 looks to have become unstable, and a similar behaviour persisted over a range of lengths of time steps, and number of internal layers (not shown). The cold temperature and quick growth rate in this run is outside of what VC10 has been applied to in the past, and

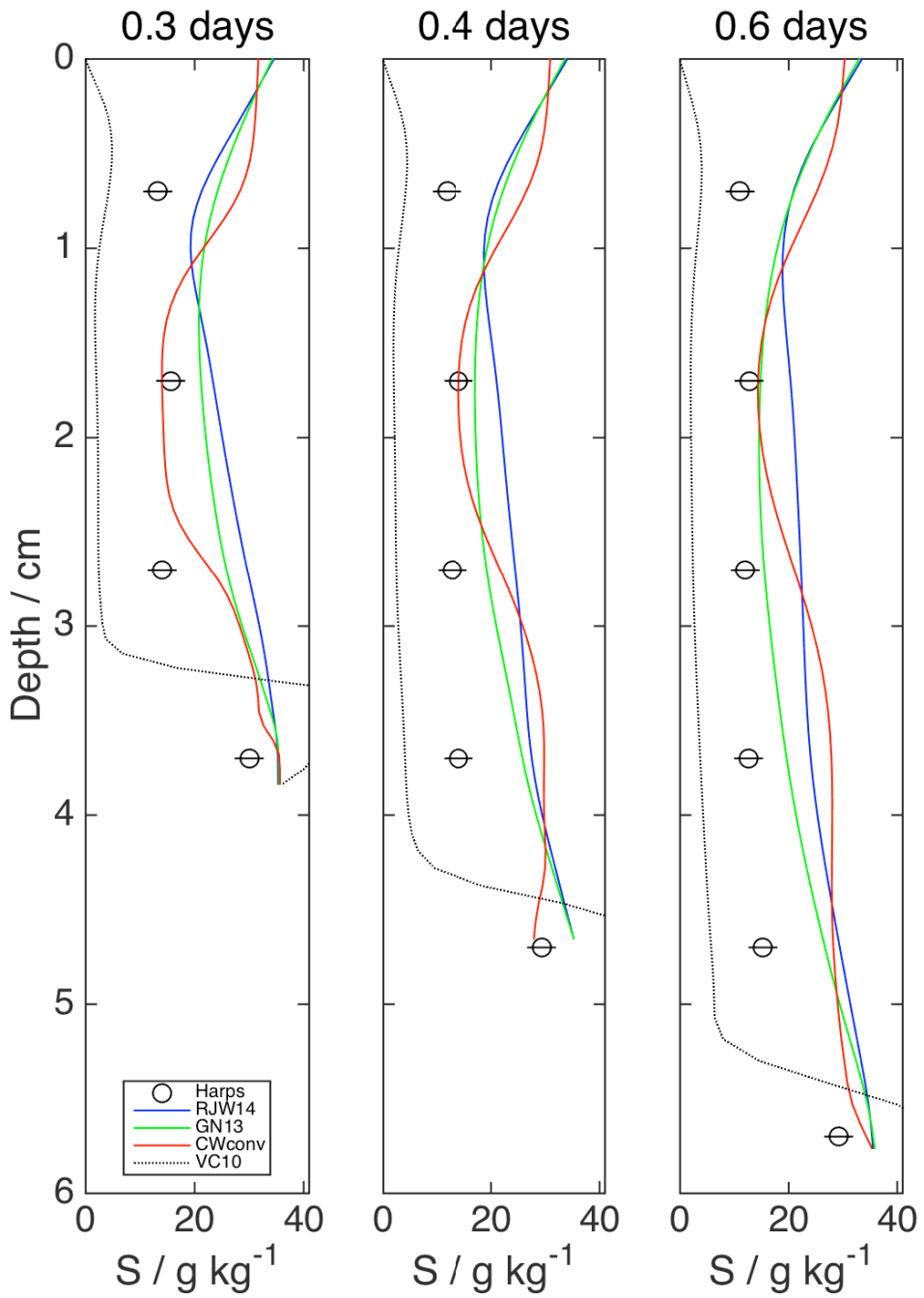

Figure 3.3: Modelled salinity against salinity as measured by wireharps during an experiment in the Roland von Glasow air-sea-ice chamber. The panels progress in time moving left to right. These model runs were performed using the tuning parameters given in the papers that present the parameterisations (Table 3.2).

this study may highlight a limit to the usefulness of VC10.

Using the tuning parameters derived in Chapter 4, RJW14 and GN13 are greatly improved (Table 3.3, Figure 3.4). Both capture the shape of the measurements and, for the most part, agree with the measurements to within experimental error. The mean absolute deviation (MAD) of the modelled bulk salinity compared to the model output shows this improvement quantitatively. The range of MAD for RJW14 for the three profiles improves from 9.16 to 10.30 g kg^{-1} (original tuning parameters) to 3.07 to 4.67 g kg^{-1} (revised tuning parameters). For GN13 the range of MAD for the three profiles improves from 6.71 to 8.43 g kg^{-1} (original tuning parameters) to 3.02 to 4.19 g kg^{-1} (revised tuning parameters). CWconv (which does not include initial segregation) also performs better, capturing the shape of the measurements, though it does not desalinate enough. The range of MAD for CWconv improves from 7.19 to 10.73 g kg^{-1} (original tuning parameters) to 6.48 to 7.49 g kg^{-1} (revised tuning parameters). VC10 continues to perform poorly. The underestimation of the interior and surface salinity is reduced, but the high salinities in the lower layers are higher and further from the measurements. With MADs ranging from 9.69 to 11.61 g kg^{-1} (original tuning parameters) to 8.67 to 12.44 g kg^{-1} (revised tuning parameters), VC10 is the only scheme not to perform consistently better with the revised tuning parameters.

This run shows that the interior desalination scheme proposed by Cox and Weeks (1988), reformulated in a convective framework, is capable of capturing some of the observed desalination. In Chapter 4, when I apply CWconv to a data set for which it was tuned, I will be able to show how well CWconv can perform for salinity measurements. VC10 is still unstable. The two convective schemes are capable of predicting salinity dynamics during this experiment, even with tuning parameters derived from a different experiment.

All of the models perform poorly against these experimental data when their original tuning parameters are used. With tuning, RJW14 and GN13 are greatly improved, perform similarly well, and are the best of the parameterisations. The average MADs for RJW14 and GN13 when re-tuned are 3.62 g kg^{-1} and 3.45

g kg^{-1}, respectively. CWconv is also improved, but does not desalinate enough, resulting in an average MAD of 5.16 g kg^{-1}, slightly worse than RJW14 and GN13. VC10 is struggling numerically and performs poorly, with a mean MAD of 10.33 g kg^{-1}.

3.5.2 Performance predicting the dynamics of a passive tracer

To date, only the experiments of Eide and Martin (1975) have isolated the upflow of caused by gravity drainage in sea ice. They grew laboratory sea ice from NaCl seawater in a thin cell so that they could visually observe the internal sea-ice structure. Two separate experiments were conducted, where dye was injected under sea ice and observed as the dye front rose up into the sea ice. In this section, I compare my model simulations to curves fit by Eide and Martin to the hight of the dye front above the initial injection point, z_d (Equation 3.27).

$$z_d = a(I - e^{-bt}) \tag{3.27}$$

The fit parameters a and b, and the sea-ice depth at the point of dye injection I, are different for each experiment and are given in Table 3.4. This experiment has never previously been modelled. However, making some simplifying assumptions, Rees Jones and Worster (2013) are able to show that the equations underpinning RJW14, when predicting dye height, are consistent with the functional form of Equation 3.27. They also ascribe physical meaning to the constants a, as the depth of the convecting layer, and b, as a function of the effective Rayleigh number.

Eide and Martin (1975) provide enough information to model their experiments, but not enough to tune the parameterisations to their experiments. I therefore perform a simulation with the original and revised tuning parameters for each parameterisation.

In the experiments of Eide and Martin (1975), the sea ice was cooled from above by a -17 ^{o}C coldplate, so I set the surface sea-ice temperature to this value throughout the run. Their tank was 0.3 x 35 x 50 cm, and the water had an initial salinity of 32 g kg^{-1} NaCl, and I have used these values to construct a salt and water

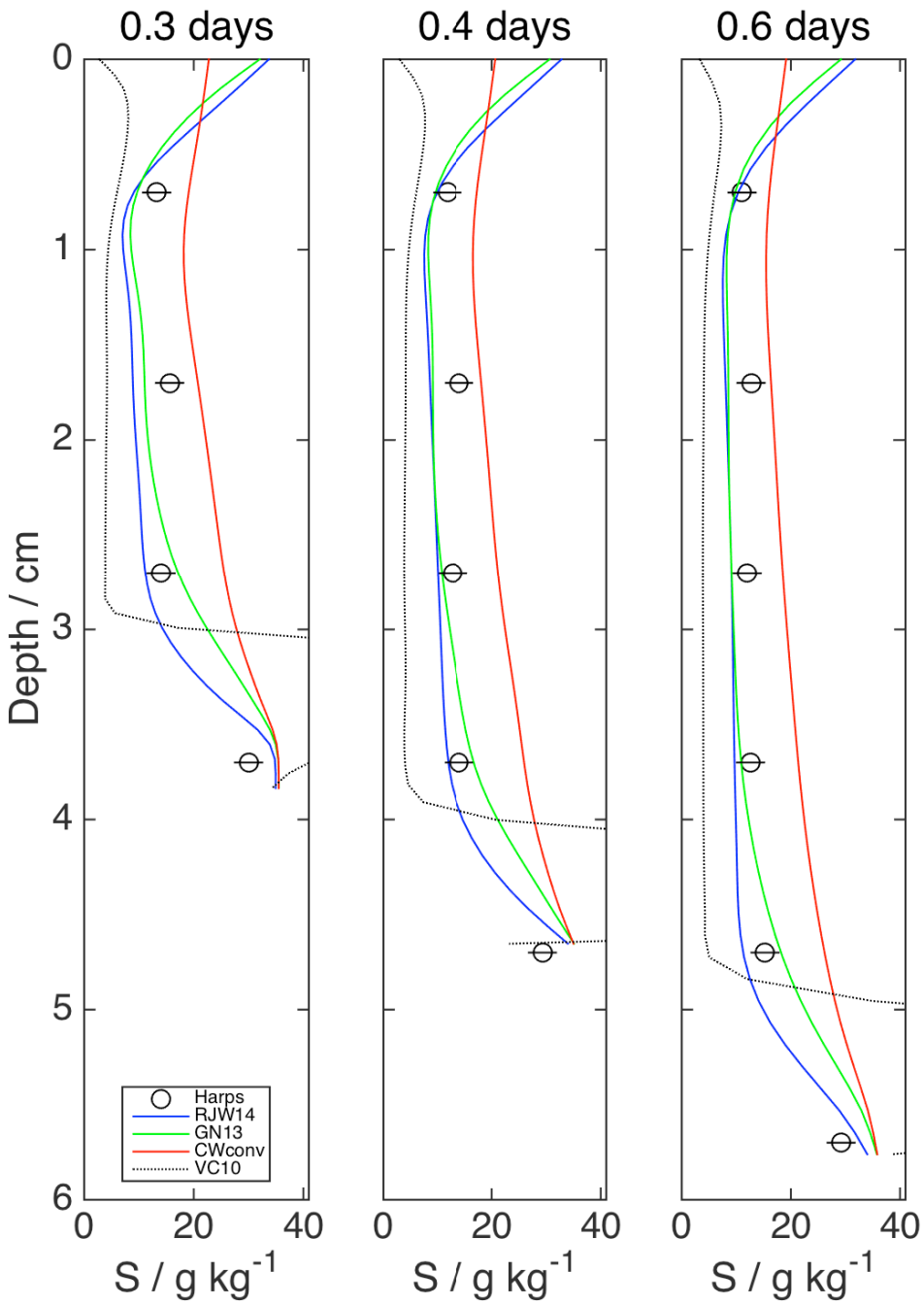

Figure 3.4: Modelled salinity against salinity as measured by wireharps during an experiment in the Roland von Glasow air-sea-ice chamber. The panels progress in time moving left to right. These model runs were performed using the tuning parameters that I calculated from the experiment presented in the next chapter (Table 3.2).

Table 3.4: Experimental runs in Eide and Martin (1975) and parameters fit to observed dye height.

Experiment	Time of dye injection / mins	Thickness at dye injection (I) / cm	Fit parameters
A	170^{+}	4.5*	$a = 1.8$ cm $b = 7.5 \times 10^{-5}$ s^{-1}
B	3600*	20^{+}	$a = 5.75$ cm $b = 7.5 \times 10^{-5}$ s^{-1}

* Modelled values
$^{+}$ Given in Eide and Martin (1975)

budget. The thickness, basal temperature and temperature profile of the sea ice are then calculated using the procedures presented in Section 3.4. Finally, they inject some unspecified mass of dye under the sea ice at two points during sea-ice growth, given as 170 minutes (experiment A), and 20 cm (experiment B). I have replicated these spikes by beginning each simulation with no tracer in the ocean, then injecting some tracer into the model ocean at an appropriate model timestep. This tracer is then incorporated into the sea ice as it forms, and transported by gravity drainage within the sea ice.

There are several caveats to this model simulation that limit the degree to which the results can be interpreted. First, Eide and Martin (1975) do not measure salinity, or dye concentration, after sea-ice growth begins. There are therefore no parameters with which to tune the model to the individual experiment. It is unclear which, if any, of the tuning parameters in Table 3.2 are applicable considering the sea ice was grown in this particular laboratory setting, in a thin cell. Second, the modelled dye concentration is not directly comparable to the measured dye height (Equation 3.27). The threshold concentration for when dye is visible may be significantly higher than zero. As this threshold is unquantified, the modelled dye height may be systematically higher than the observed dye height. Third, the injected dye is positively buoyant relative to the artificial sea water, which may cause it to rise faster than a tracer moving conservatively with salinity. Finally, the physical properties of the sea ice at the time of dye injection must be modelled,

so mismatch with measurements integrates discrepancies in the salt dynamics with errors in the representation of key physical properties, like brine salinity and sea ice permeability. In light of these caveats, comparison between measured and modelled dye height can therefore only be qualitative.

The simulation predicts around 25 cm of sea ice growth in 84 hours, with a larger growth rate at the start of the simulation (Figure 3.5). The dye heights observed by Eide and Martin do not overlap, so I plot both experiments on the same contour plot, though in reality they were separate runs under the same conditions. At the first dye injection the modelled sea ice thickness is 4.5 cm, which is consistent with the images presented in Eide and Martin (1975). The dye rise in experiment A is slower, and penetrates a smaller distance compared to experiment B. The eventual height of the dye front is determined by the parameter a, and the rate of rise by b, in Equation 3.27.

RJW14 and GN13 overestimate the rise of tracer into the sea ice during experiment A when using their original tuning parameters, both in terms of eventual height and rate of rise (Figure 3.5). CWconv captures the tracer rise in A well. VC10 performs poorly for experiments A and B, as almost all of the tracer is confined to the sea-ice/ocean interface in both cases. The bulk salinity and porosity profiles (not shown) during these runs suggest that rapid desalination in the interior has shut down convection in all but the lowest layers. This behaviour is similar to the performance of VC10 against salinity measurements. RJW14 captures the rate of rise in B. GN13 and CWconv underestimate the rate of rise during B and take up much less tracer than RJW14.

When the schemes are re-tuned (Figure 3.6) RJW14 and GN13 continue to overestimate the height and rate of rise of tracer in experiment A. CWconv performs worse with the new parameters for experiment A, but is now similar to the other convective schemes. VC10 performs similarly poorly with new tuning parameters, and for similar reasons, for experiments A and B. With new tuning parameters, all of the convective schemes capture the height and rate of rise in experiment B, with CWconv taking up slightly more tracer than the other schemes.

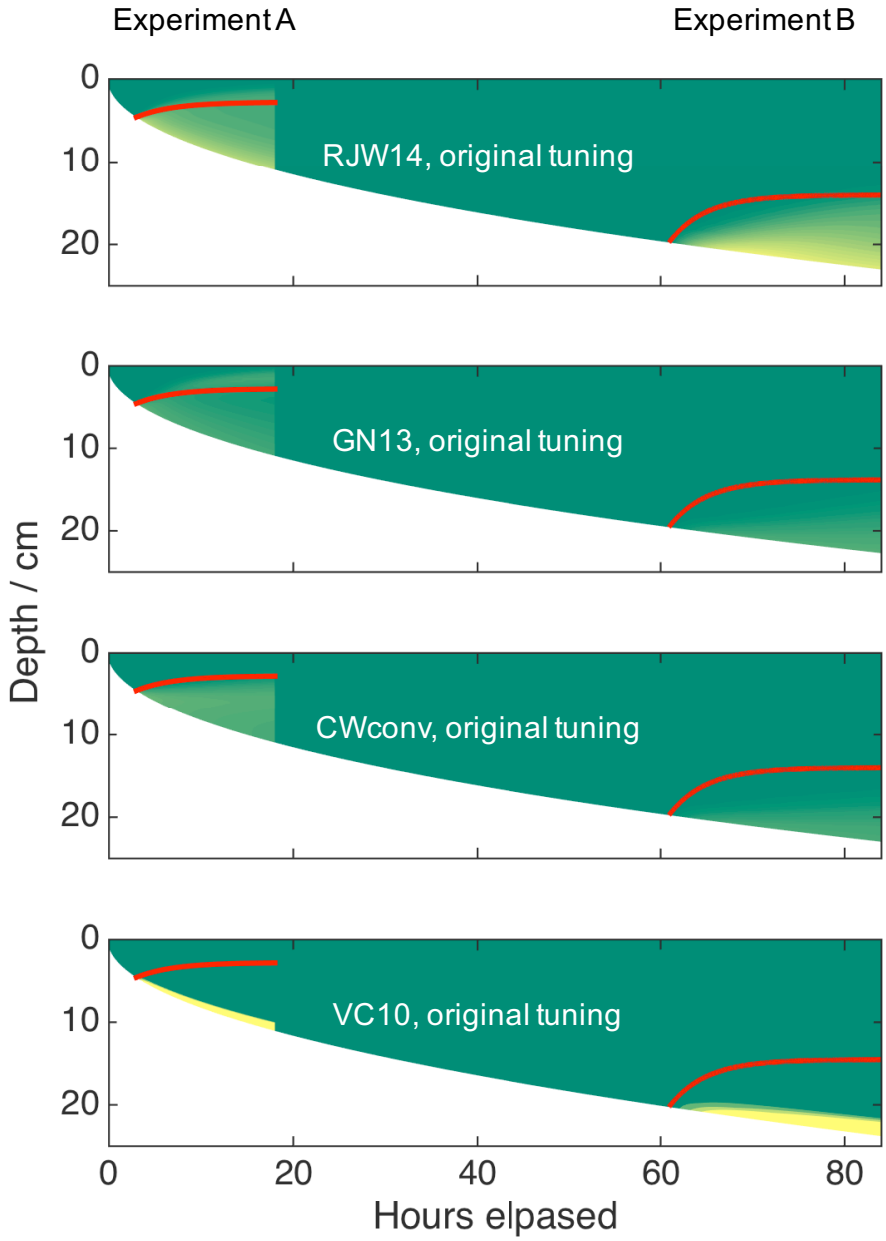

Figure 3.5: Simulations of tracer dynamics by each parameterisation during the two dye rise experiments presented in Eide and Martin (1975). More yellow colour indicates a higher tracer concentration. The colour scale is consistent across the figures but the absolute value is arbitrary. The red line shows the position of the dye front in the model of Eide and Martin (Equation 3.27). There is no overlap between the tracer in the two experiments so I have presented them on the same figure. These model runs were performed using the tuning parameters given in the papers that present the parameterisations (Table 3.2).

As with salinity, VC10 cannot be evaluated against the dye rise experiments of Eide and Martin (1975) because the scheme is unstable in the early stages.

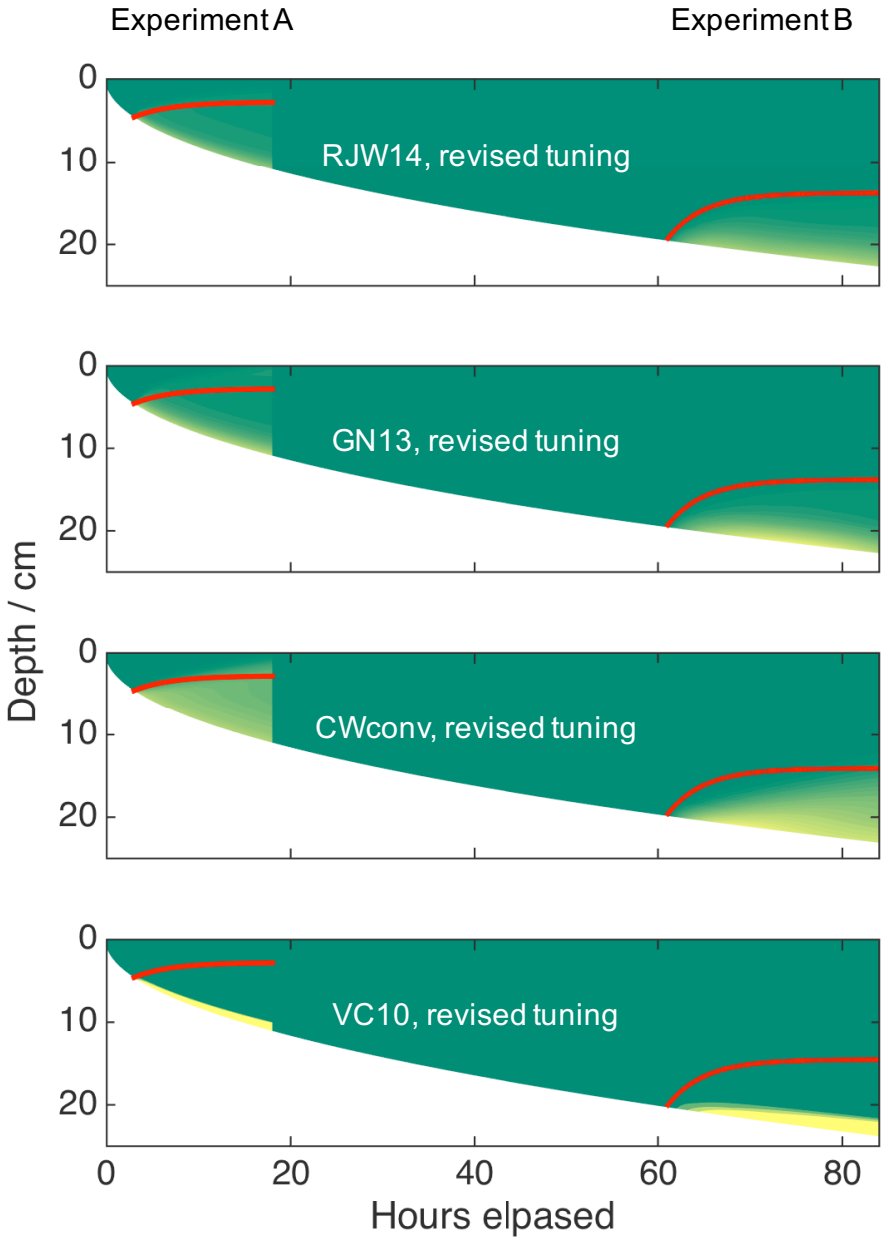

Figure 3.6: Simulations of tracer dynamics by each parameterisation during the two dye rise experiments presented in Eide and Martin (1975). More yellow colour indicates a higher tracer concentration. The colour scale is consistent across the figures but the absolute value is arbitrary. The red line shows the position of the dye front in the model of Eide and Martin (Equation 3.27). There is no overlap between the tracer in the two experiments so I have presented them on the same figure. These model runs were performed using the tuning parameters that I calculated from the experiment presented in the next chapter (Table 3.2).

Considering the difficulty in comparing the measured dye height to the modelled tracer, and the caveats of the model simulation, the convective schemes perform well

when re-tuned. For the convective schemes this is consistent with the conclusions of Rees Jones and Worster (2013), who show that convective models, when solved analytically, satisfy the functional form of Equation 3.27. The convective schemes all capture the rate of tracer rise, parameter b, reasonably well. The schemes also capture the confinement of the tracer near the sea-ice/ocean interface, parameter a, though the eventual height of the dye rise is overestimated for experiment A. The convective gravity drainage schemes show promise when predicting the dynamics of a general dissolved tracer, but a further, quantitative evaluation is needed.

3.6 Conclusions and next steps

In this chapter I described a model capable of simulating the evolution of salinity and general dissolved tracers using four important parameterisations. I am forced to re-cast CW88 in a convective form, CWconv, and to remove initial segregation, in order to include this often used scheme in this study. I then used this model to simulate salinity measured in an experiment in the Roland von Glasow air-sea-ice chamber, and the rise of a tracer into sea ice as measured by Eide and Martin (1975). VC10 could not cope with the conditions for these two data sets, and must be evaluated under conditions closer to its past uses. CWconv performs qualitatively well for salinity but underestimates desalination, performing quantitatively worse than RJW14 and GN13. RJW14 and GN13 perform well against salinity measurements, perform quantitatively and qualitatively similarly, and along with CWconv, within large uncertainties, perform adequately for tracer dynamics.

The caveats to my simulations of the experiments of Eide and Martin (1975), and the ambiguities in the comparison of modelled tracer concentrations to measured dye height, mean that I cannot address my second overarching goal for this work. Further experiments under different conditions are therefore required to quantitatively evaluate these schemes when predicting general dissolved tracer dynamics. In the next chapter, building on the work of Eide and Martin (1975), I

perform such an experiment.

Chapter 4

Evaluating gravity drainage parameterisations using tracer measurements

4.1 Summary

- I conduct an experiment to address the goals presented in Chapter 3. By injecting a dissolved tracer into water underlying an existing sea-ice cover, and sampling the sea ice after some time, I quantify the effects of gravity drainage on a general dissolved tracer, which is decoupled from salinity.
- Low concentration rhodamine 6G is used as the general dissolved tracer.
- I compare model output from four gravity drainage schemes to measurements of salinity and rhodamine.
- After tuning, all schemes perform well compared to salinity and tracer measurements in the sea ice, but the convective schemes outperform the empirical (recast as convective) scheme and the diffusive scheme.
- The error arising from the use of diffusive parameterisations in biogeochemical studies will be small in the sea-ice interior, but may become large near the surface, which could have implications for ice-atmosphere coupling.

- Only the convective schemes capture high near surface salinities and the shape of the final rhodamine profile, and these scheme have excellent predictive skill for both salt and rhodamine.

- Convective schemes, specifically Rees Jones and Worster (2014) and Griewank and Notz (2013) are powerful tools and should be used in future 1D modelling studies studies.

4.2 Objectives

In Chapter 3 I developed a numerical model to predict the evolution of salinity, and a general dissolved tracer, for growing sea ice using several gravity drainage parameterisations. I evaluated this model against measurements of salinity and a tracer, but those data were not sufficient to rigorously evaluate the schemes. In this chapter my objective is to rigorously evaluate the schemes using data from an experiment performed in the Roland von Glasow air-sea-ice chamber.

One issue in the previous chapter was that the parameterisation proposed by Vancoppenolle et al. (2010), VC10, was unstable, probably due to the extreme cold temperatures under which the data in the previous chapter was collected. I could conclude that there are limits to the usefulness of VC10, but could not evaluate VC10 in a scientific sense. The experiment in this chapter is performed under warmer, slower growth, conditions, similar to those VC10 have been applied to in the past.

Another issue was that the experiments of Eide and Martin (1975) could not be used to quantitatively evaluate the schemes for their performance for general dissolved tracers. There was ambiguity about what constituted good agreement with the model. In this chapter, rather than measuring the rate of rise of some tracer through time, I measure a final tracer profile, and perform a quantitative comparison.

Finally, Eide and Martin (1975) did not present salinity measurements, so I could not tune the schemes to their experiments. Poor model performance for tracer dynamics could therefore be driven by poor performance evolving the salinity. In this chapter I measure a tracer and salinity in the same samples. I am therefore able to tune the parameterisations to best match the salinity, and evaluate the parameterisations for tracer.

I address two scientific questions:

1. How well can the parameterisations of Rees Jones and Worster (2014) (RJW14), Griewank and Notz (2013) (GN13), a convective version of a scheme proposed by Cox and Weeks (1988) (CWconv), and VC10 perform

4. *Evaluating gravity drainage parameterisations using tracer measurements*

   for salinity?

2. When performing as well as possible for salt dynamics, how well do the above schemes perform for the transport of a general dissolved tracer?

First, in Section 4.3, I describe my experimental methodology and timeline. I then describe how I have simulated this experiment, and how I have tuned each scheme (Section 4.4). In Section 4.5 I compare model output to measurements of salinity and a tracer decoupled from the salinity. Model sensitivities and measurement biases are considered in Section 4.6 .The wider relevance of these results, including recommendations for future use of gravity drainage schemes, is presented in Section 4.7.

4.3 Experimental methodology

Figure 4.1 shows the set up of the instrumentation for this experiment. Thermistors (DS28EA00 and DS18B2OU) were deployed with $\approx$ 1 cm resolution, more than spanning the eventual sea-ice depth. Individual thermistors were calibrated against a weather station (WS600-UMB), and any offsets were identified and corrected during the period when all of the thermistors sat in the unfrozen, well mixed ocean. Wireharps (Notz et al., 2005) were deployed alongside the thermistors in a depth profile to measure the solid fraction. The CTD used in previous experiments (SBE-37 Microcat) was away for calibration, so I deployed two smaller CTDs (SeaStar DST CTD) in the main and side tank. These were used to calculate salinity (Chapter 2), but required offsetting against discreet salinity samples. Ice formed on the side tank CTD due to a lack of circulation and insufficient insulation, so these data are not presented.

In addition, novel light sensors engineered by Dirk Notz's group were deployed spanning 1 to 15 cm depth with 1 cm resolution (Figure 4.1). Glass rods are clad in a black casing, and allow light to pass into detectors (TCS3471) that sense light in four wavelength bands: unfiltered, red, green and blue. Rhodamine 6G absorbs strongly in the green region, and fluoresces in the red, so these sensors have the

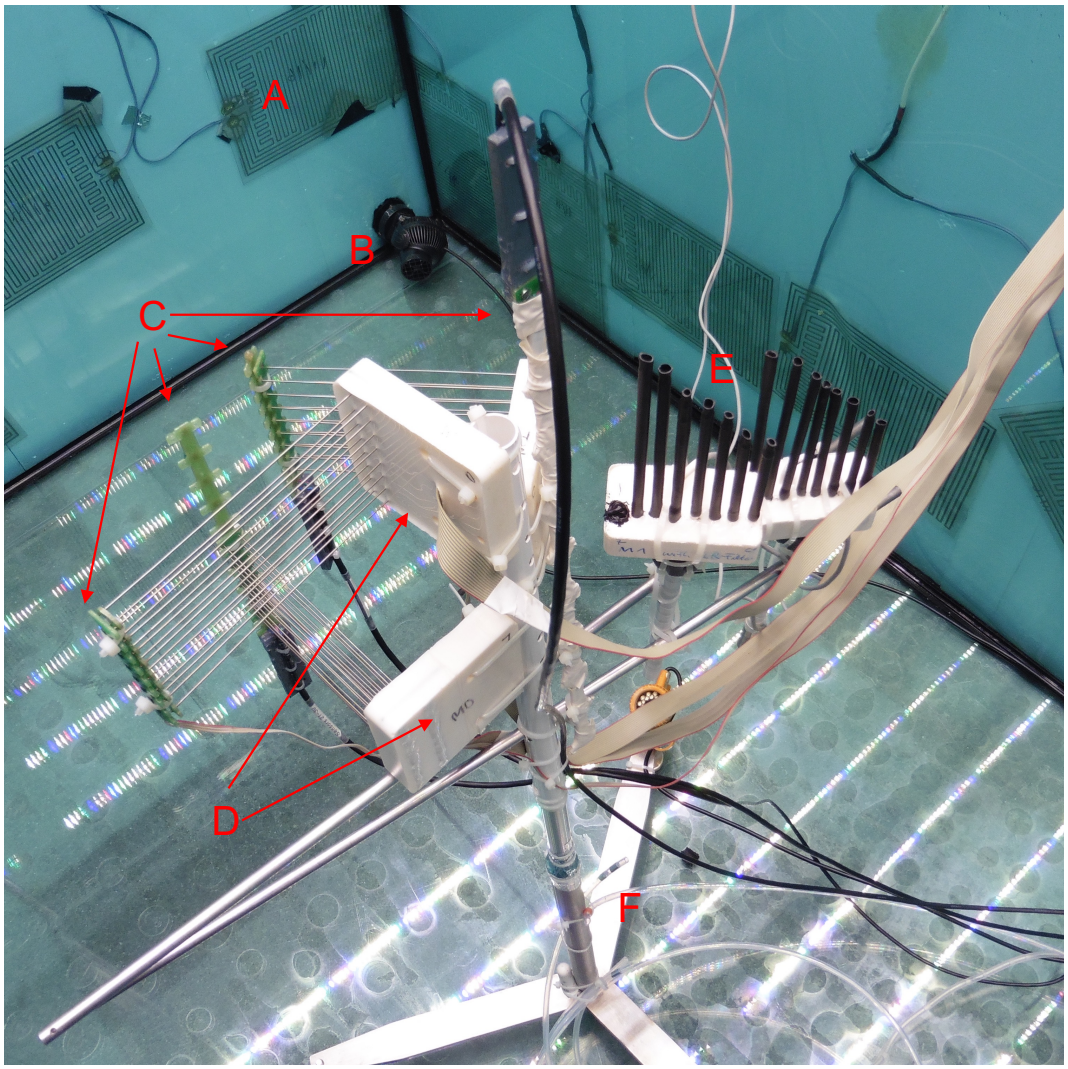

Figure 4.1: Picture of the central column supporting the instrumentation before the addition of water to the tank. A is one of several heating pads mounted on the outside of the glass. B is one of two pumps facing each other. C represents several thermistor strings, some of which are attached directly to wireharps (D). E shows the RGB light sensors, and F shows sample/spike lines. The central column is free to rise with the sea ice.

potential to detect signals caused by rhodamine in the path of the light leading to the detectors. They are in the early stages of development (the first results are presented here), and the results do not inform the conclusions of this study.

Four lengths of tubing were set up that ran from the tank into the outer lab (Figure 4.1). The purposes of these lines were to: sample water from the base of the main tank (5 cm height), sample water from the middle of the main tank (40 cm height), sample water from the side tank (5 cm height), and to spike rhodamine into the main tank (40 cm height). A dedicated spike line was used to prevent

contamination of samples. The three main tank lines ran through the side tank. Early on in the experiment the side tank line froze and could not be used. A heated wire, heating pads and insulation were wrapped around the lines once they left the water so they were never exposed to the cold atmosphere of the coldroom.

To minimise the artificial freeboard effects in this experiment, heating pads (THERM230V10W) were placed on the outside of the glass walls of the tank (Figure 4.1). This prevented sea ice from attaching to the tank walls. In addition, *in situ* instrumentation was mounted on a pole that was free to rise in the vertical. This configuration allowed the sea ice to float freely and maintain a natural position. I periodically checked that the sea ice was free by gently depressing one corner and noting that the slab bobbed.

The ocean for this experiment consisted of 109.8$\pm$0.1 kg of $>$ 99.5% NaCl (AksoNobel Sanal-P) dissolved in ultrapure water. The salinity of the well mixed ocean before sea ice formation was 33.9$\pm$1.1 g kg^{-1} (2σ). Using the mass of salt added, and the resulting salinity, I calculate the initial mass of water in the tank to be 3250$\pm$100 kg (2σ) if the mass of water in the side tank is omitted from the calculation. This is consistent with the water mass as calculated from the dimensions of the main tank (3170 kg). Mixing between the main and side tank is not well characterised. However, the mass of water in the side tank, calculated from its dimensions, is approximately 180 kg. As this is similar to the error derived from the calculation using the salinity, I consider the sensitivity of the modelled mass balance to the side tank volume rather than explicitly including the side tank in future budgets. Two pumps (TUNZE stream 6215) mixed the ocean throughout, and faced each other to minimise generated currents while maximising turbulence (Loose et al., 2011).

Sea-ice formation was initiated by turning the coldroom temperature to -20 ^{o}C. During the experiment I set the room temperature to -10 ^{o}C for a period, and then back to -20 ^{o}C, in order to give the model a complex forcing and robust test. After 5.1 days of elapsed experimental time, and $\approx$ 10 cm sea ice thickness, I added a spike of 0.2834 g rhodamine 6G (Arcos organics, Rhodamine 6G, 99%) dissolved

in 100 ml of ultrapure water to the ocean using the dedicated spike line. The experiment ran for 8.9 days from 1 cm sea-ice thickness to final sampling. Final sea ice thickness ranged from 15 to 17.5 cm, with the thickest sea ice nearest the fans, and the thinnest nearest the relatively warm side tank. Immediately before sampling, I drilled a hole in the sea ice and measured the position of the water line at 1.7 ± 0.1 cm below the sea ice surface, confirming that the freeboard was natural for the thickness of the experimental sea ice.

The experiment was run largely in the dark to prevent any photo-degredation of rhodamine. Overhead LED solar spectrum lighting was turned on for up to 10 minutes, once or twice a day, so that I could check the state of the sea ice surface, replace sampled volume, and so that I could measure a light intensity profile through the sea ice and ocean.

Ocean samples were extracted once or twice a day using a syringe connected to the sample lines from the main tank. The volume of a sample line was extracted once to flush the line, and a second time and used to rinse sample containers. Samples were then taken for salinity ($\approx$50 ml) and rhodamine ($\approx$50 ml into brown glass bottles). Salinity samples were stored in the fridge and measured within a month. Rhodamine samples were stored in the fridge for a week, then transferred to the freezer when analysis was delayed. Extracted volume was replaced manually into the side tank using ultrapure water. My original plan was to replace this volume through the sample lines, but when taking my first sample (with no ice cover) I found that I could not reliably do this without injecting some bubbles into the water. In addition, any ultrapure water left in the line may have frozen given the ocean temperature was below 0 ^{o}C during the experiment. Replacing fresh water directly into the side tank had the unexpected, but in hindsight predictable, consequence of forming a frozen subsurface layer. At the end of the experiment this layer completely isolated the surface side tank from the main tank, such that extracted volume was not being replaced into the main tank. However, in total less than 5 l, or 0.2%, of main tank water was extracted. Assuming, conservatively, that none of this was replaced, the water level in the tank would be decreased by less than 0.2

cm, and this did not disturb the freeboard as the sea ice was floating. The change in concentration in ocean salinity or rhodamine caused by sampling and replacement is insignificant in the context of analytical error.

Sea ice was sampled only once, at the end of the experiment. This is because sampling compromises the sea-ice surface, drives uneven growth, and may permit ocean water to infiltrate remaining sea ice laterally. Six sea-ice cores were taken using a 7.25 cm diameter Kovacs Mark III corer. Three of these were stored in a chest freezer for subsequent sectioning and analysis, but only the thickness of these cores informs this study as it appears significant brine was lost upon sampling. The remaining three cores were immediately cut in half and the top and bottom sections for each core were grouped together in separate sample bags in their *in situ* orientation. These were then left to melt slowly at 4 ^{o}C over a few days, and individual aliquots of the meltwater were collected (Fripiat et al., 2007). The cores covered the length of the tank to integrate as much variability as possible. Two sea ice slabs were taken using the methodology of Cottier et al. (1999), and from here these are referred to as slabs. A hole was cut into the sea ice that was big enough to comfortably submerge a plastic box. The boxes used had dimensions of $32 \times 22 \times 18$(deep) cm and $39 \times 28 \times 28$(deep) cm. A second ice section was then cut that was just smaller than the plastic box. This was the sample, and was carefully manoeuvred, floating freely, into position directly above the submerged box. The box was then lifted out of the water, such that the sample was extracted while still floating. This prevented brine drainage during the initial extraction of the sample. Ocean water was then drained from the box until the sample was just touching the bottom. The sample was then quickly stored in a -40 ^{o}C chest freezer to flash freeze it for later sectioning. I made three additions to this method. Firstly, before cutting had taken place, I froze a ring onto the surface of the eventual sample, and covered this tightly with a sample bag. This preserved the sea-ice surface, such that ocean accidentally washed over the sea-ice surface or sprayed ice from the cutting process did not contaminate the sample. Secondly, I used an ice climbing screw to manoeuvre the sample. Thirdly, once in the chest freezer, I placed plastic

sheets around the sides of the sea-ice slab to minimise infiltration of ocean water into the sample.

Within one month I cut all slabs and cores into 1 cm layers using a bandsaw with a pre cleaned blade. For the slabs, the now frozen ocean around the edges of the sample was cut away first, and then at least 3 cm of sample was removed from each edge to minimise ocean contamination. In between each sample, the bandsaw table top was cleaned, and the blade was run through frozen ultrapure water for a prolonged period. I always cut top to bottom through the sample, as I predicted the concentration of rhodamine was highest nearest the ocean. Individual layers were stored frozen at -40 ^{o}C in bags, and melted in the dark immediately before analysis.

Salinity and rhodamine concentrations were measured in ocean, melted bulk sea-ice samples, and aliquots from the slow melt. Samples were placed in a water bath alongside a sets of standards for salinity and rhodamine. Salinity was measured using a Hach HQd40 handheld logger with a CDC401 conductivity probe, and rhodamine was measured using a PerkinElmer LS45 fluorometer (500 nm excitation, 525 nm emission). Analytical errors were calculated using standard procedures (Taylor, 1997) and are reported with two standard deviation absolute error.

4.4 Model set up

4.4.1 Forcing

The forcing for this model run consists of measured and interpolated temperature profiles and the sea-ice thickness. Thickness was calculated by linearly extrapolating the interior sea-ice temperature profile to the measured water temperature, and smoothing the resulting thickness to remove high frequency thickness variations. I chose this method of determining the thickness because there are indications that ice has formed on some harp wirepairs ahead of the advancing sea-ice front, distorting the solid fraction measurement and giving erroneously high thicknesses. The thickness at the point of sea-ice sampling is 17.7 cm when calculated from the solid

fraction measured by the wireharps, which is greater than the range of thicknesses for the discrete samples even though the wireharps were in a region of intermediate thickness sea ice. Also, the temperature of the bottommost frozen wirepairs is similar to the ocean temperature suggesting that the co-located thermistors were not frozen in. Finally, there are occasional spikes in solid fraction well ahead of the advancing front that I was forced to remove during quality control of the final harp profiles. I used the calculated thickness to define which thermistors were frozen in for each timestep, and mapped temperature onto a model grid of 25 evenly spaced layers by interpolating between frozen thermistors, and extrapolating from interior thermistors to the surface and base of the sea ice. These temperatures were then used *in lieu* of a thermodynamic model component.

The model (described in Chapter 3) cannot simulate growth from open water, and I set 1 cm as the initial sea-ice thickness. The initial salinity in the ocean, and each model layer, is 33.9 g kg^{-1}. Tracer is added to the underlying water at the timestep nearest to the spike, which is accurate to within 10 minutes. The spike is assumed to mix instantly in the ocean. I use 0.2834 g as the mass of the tracer spike, and the resulting ocean concentration falls within the range of measured ocean rhodamine concentrations. No side tank volume is included in this simulation.

4.4.2 Tuning

I tune the model to the final salinity profile measured in each slab. I only tune against regions of the slabs where the salinity measurements agree well, and so exclude the shallowest and deepest layers from the tuning. I run the model using a wide range of tuning parameters for each scheme. For example, RJW14 was run using Ra_c ranging from 1 to 40, and α ranging from 0.01 to 0.5. Each parameter pairing was run individually, so to test three values of Ra_c and three values of α required 9 model runs. Initially I ran the model for widely spaced tuning parameters, then narrowed the range based on the schemes performance. To evaluate the schemes performance, I calculated the sum of the square of the difference between the

Table 4.1: Original and re-tuned parameters for gravity drainage parameterisations. This table is also displayed in Chapter 3, and is repeated here for ease of reading.

Scheme	Original parameters	Re-tuned parameters
RJW14	$Ra_c = 40$ $\alpha = 0.03$	$Ra_c = 3.0$ $\alpha = 0.20$
GN13	$Ra_c = 4.89$ $\alpha = 5.84 \times 10^{-4}$ / kg m^{-3}s^{-1}	$Ra_c = 2.6$ $\alpha = 0.009$ / kg m^{-3}s^{-1}
CWconv	$\delta = 1.68 \times 10^{-7}$ / g m kg^{-1} s^{-1} ^{o}C^{-1}	$\delta = 7.1 \times 10^{-7}$ / g m kg^{-1} s^{-1} ^{o}C^{-1}
VC10	$D_{tur} = 1 \times 10^{-6}$ / m^{2}s^{-1} $Ra_c = 5$	$D_{tur} = 3.0 \times 10^{-7}$ / m^{2}s^{-1} $Ra_c = 6.3$

model and measurements at each measured depth. I also used some common sense constraints on the range of tuning parameters. For example, for RJW14, values of α greater than 0.2 failed to capture the increase in near surface salinity, but performed well because the model was marginally closer to the interior measured salinity. I therefore excluded α values greater than 0.2. Using this methodology I tuned each parameter to two significant figures. The calculated tuning parameters for the two slabs always agreed within two significant figures.

Table 4.1 shows the tuning parameters used in this work, and the original tuning parameters presented in the papers detailing the schemes.

4.5 Results

4.5.1 Model performance against *in situ* salinity

Figure 4.2 shows how the bulk salinity predicted by each scheme compares to wireharp measurements. The measurements are from early timesteps so that the sea ice is still relatively porous, as the wireharps perform best at solid fractions below 0.8. No measurements are presented with a solid fraction higher than 0.9, and most of the measurements have a solid fraction closer to 0.8 or below. The measurements show a decrease through time in the bulk salinity, a fairly homogeneous bulk salinity

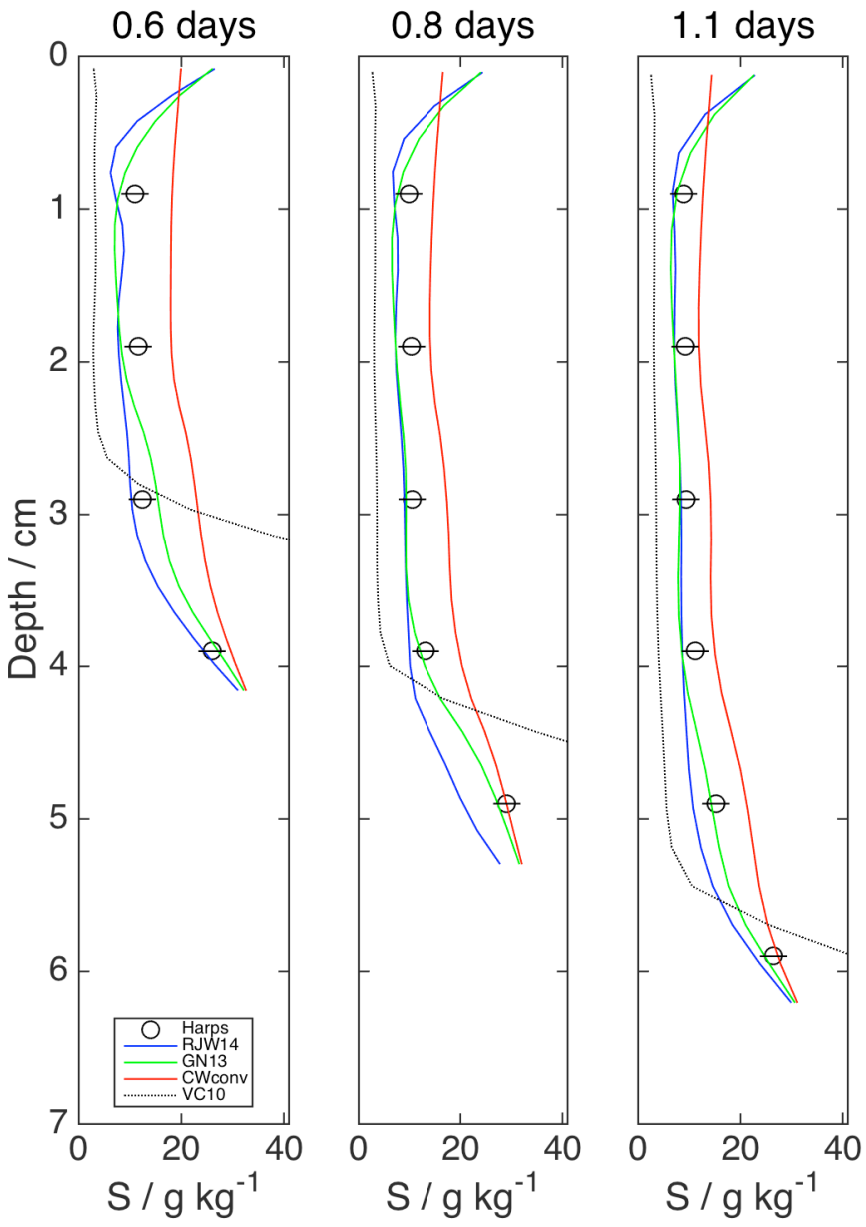

Figure 4.2: Bulk salinity measured using wireharps, and as predicted by four gravity drainage schemes.

away from the sea-ice/ocean interface, and an increase in bulk salinity in the sensor nearest the ocean.

I compare the performance of the schemes by calculating the mean absolute deviation (MAD) of the modelled bulk salinity from the measured bulk salinities

Table 4.2: Mean absolute deviation of modelled vertical bulk salinity profiles as compared to wireharp and slab measurements, as shown in Figures 4.3 and 4.2.

	Mean absolute deviation [g kg^{-1}]			
Profile	RJW14	GN13	CWconv	VC10
0.6 days	2.87	2.65	6.98	22.7
0.8 days	3.89	1.87	4.43	13.97
1.1 days	2.65	1.65	3.68	8.38
Slab 1	1.98	2.14	3.18	3.61
Slab 2	1.17	1.19	2.66	2.68

for the profiles shown in Figure 4.2 (Table 4.2). GN13 (mean MAD=2.06 g kg^{-1}), followed by RJW14 (mean MAD=3.13 g kg^{-1}), performs best, and both capture the measurements to within experimental precision for most timesteps. CWconv (mean MAD=4.14 g kg^{-1}) performs worse than GN13 and RJW14, capturing the shape of the bulk salinity profile but not the magnitude of the desalination. As time progresses CWconv comes closer to the measurements (MAD decreases from 6.98 to 3.68 g kg^{-1}). VC10 performs poorly (mean MAD=15.0 g kg^{-1}), overestimating the desalination early on and overestimating salinity near the base of the sea ice. The performance of the schemes for this experiment is similar to their performance against the data presented in Chapter 3.

4.5.2 Model performance against sea-ice samples

Figure 4.3 shows the predicted salinity and rhodamine concentration for each scheme, and the measured salinity and rhodamine concentration in the two slabs. Normalised depth is used because there was a $\approx$1 cm difference in thickness between the slabs. The data are consistent in shape and magnitude between the two slabs, especially away from the upper and lower interfaces.

Bulk salinity displays a typical 'C' shaped profile, with higher values near the surface, and highest values near the base of the sea ice. The salinity values in the

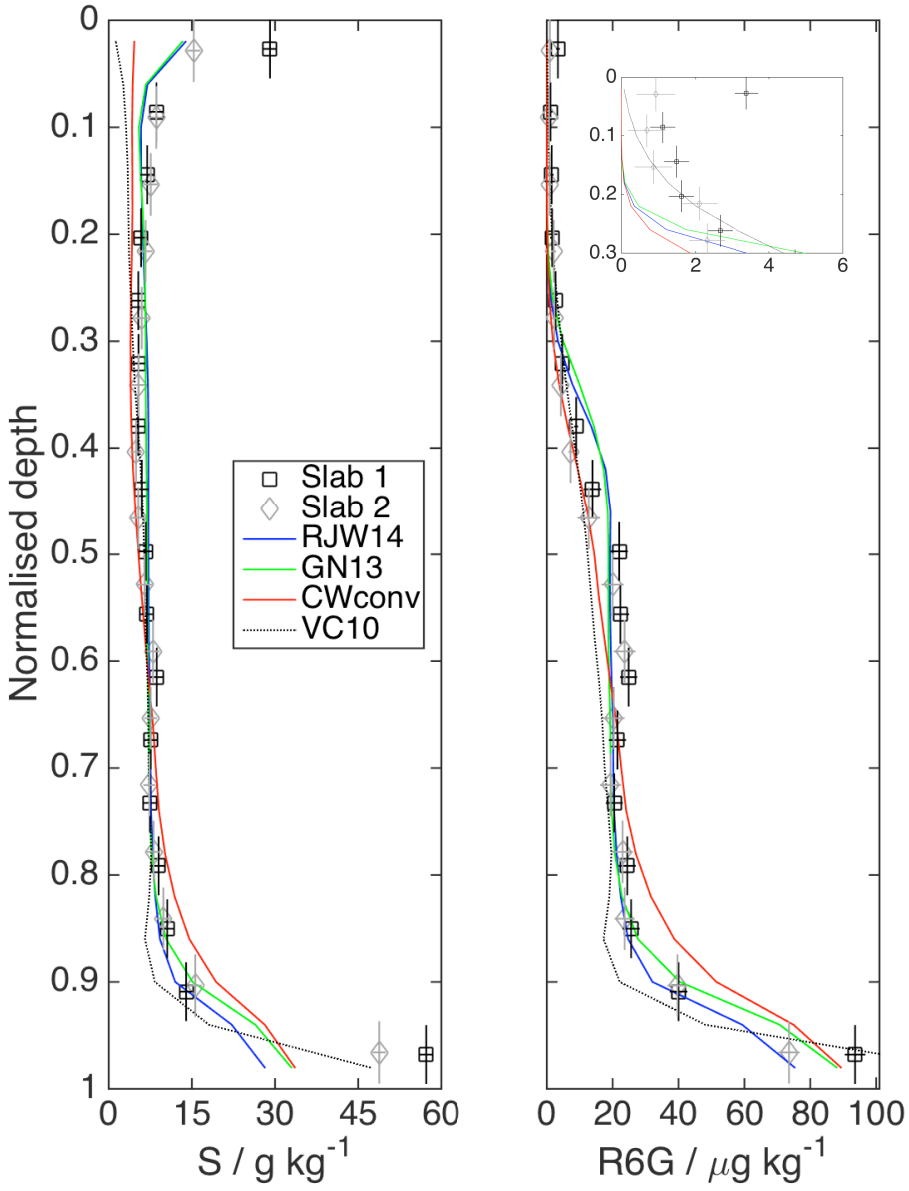

Figure 4.3: Salt (left) and rhodamine (right) concentration as measured in two sea-ice slabs and as predicted by four gravity drainage schemes at the end of the model runs as a function of depth in the sea ice, normalised to the total sea-ice thickness. The vertical bars on the measurements span the depth of each analysed layer, while the horizontal bars denote 2σ analytical error. The insert magnifies the rhodamine profiles near the surface.

bottom layer for both slabs is enriched relative to the ocean during sampling by 20-50%. This is likely an artefact caused by the sampling method (see Section 4.6.2). Slab 1 may have been contaminated at the surface, where there is a small increase

Table 4.3: Mean absolute deviation of modelled vertical bulk rhodamine profiles as compared to slab measurements, as shown in Figure 4.3.

	Mean absolute deviation [μg kg^{-1}]			
Profile	RJW14	GN13	CWconv	VC10
Slab 1	2.13	3.12	4.06	4.67
Slab 2	2.11	2.89	3.17	3.59

in rhodamine concentration, and high salinity relative to slab 2.

Only RJW14 and GN13 capture the full shape of the salinity profile because CWconv and VC10 do not reproduce the increase in near surface salinity. Depletion in near surface salinity is a persistent feature in VC10 due to the nature of diffusion. The RJW14 and GN13 schemes do a good job in the interior, but do not reproduce the finer structure. VC10 does an excellent job in the interior. All schemes capture the sharp increase in salinity near the base, though the increase is steeper for VC10 than the other three schemes.

Again, I compare the performance of the schemes by using the mean absolute deviation of the measured bulk slab salinities and the model predicted concentrations (Table 4.2). I have excluded the high basal bulk salinities in the bottommost slab samples from these calculations because they are artefacts. RJW14 performs best against bulk salinity in the slab profiles (MADs of 1.98 and 1.17 g kg^{-1}), followed by GN13 (2.14 and 1.19 g kg^{-1}). CWconv performs slightly worse (MADs of 3.18 and 2.66 g kg^{-1}), and VC10 performs worst (MADs of 3.61 and 2.68 g kg^{-1}). The difference in performance between the parameterisations is reduced for bulk salinity because the parameterisation performance is tuned to these profiles.

The highest rhodamine concentrations are nearest the ocean, and there is a steep concentration drop over the bottom 15% of the sea ice moving up into the interior. Rhodamine is then relatively constant in the sea ice interior, before dropping to very low values near the surface. At no point do near surface concentrations drop below 0.5 μg kg^{-1}.

All schemes capture the magnitude of the steep drop in rhodamine concentration near the base, but, as with salinity, VC10 predicts a steeper drop than the other three schemes. In the interior, RJW14 and GN13 capture the shape of the rhodamine profile, though both underestimate measured concentrations slightly at around 50% depth, and overshoot the beginning of the sharp decrease towards the surface by around 5% depth, or 1 cm. CWconv does not predict an area with relatively constant rhodamine, but does capture some change in regime and a drop towards the surface. Near the surface, VC10 captures the measurements well. The other schemes all predict near zero surface concentrations, which is at odds with the measurements, though the absolute error is small (Figure 4.3, insert). This discrepancy could be caused by brine expulsion, which is not included in the model. In RJW14, GN13 and CWconv the depth to which rhodamine penetrates significantly is determined by the position of the shallowest convecting layer, as predicted by Worster and Rees Jones (2015).

MADs are calculated for the rhodamine profiles, again excluding the bottom-most slab layer (Table 4.3). As with bulk salinity, RJW14 performs best against bulk bulk rhodamine concentrations in the slab profiles (MADs of 2.11 and 2.13 μg kg^{-1}), followed by GN13 (3.12 and 2.89 μg kg^{-1}). CWconv again performs slightly worse (MADs of 4.06 and 3.17 μg kg^{-1}), and VC10 performs worst (MADs of 4.67 and 3.59 μg kg^{-1}). The good performance of these parameterisations when predicting rhodamine concentrations is particularly impressive given that they were not tuned to these observations.

4.5.3 Model performance for ocean concentrations

Figure 4.4 shows how the schemes perform against measurements of water samples from the main tank ocean. The CTD salinity and all of the schemes are consistent with the measured salinity in the discrete samples. There appear to be some issues with the mixing and/or sampling procedure for rhodamine in the ocean, as the range in ocean concentrations for repeat samples is larger than analytical error. One sample in particular, during day 6, shows lower concentrations near the base of the tank relative to the middle, suggesting incomplete mixing, though this difference

does not persist.

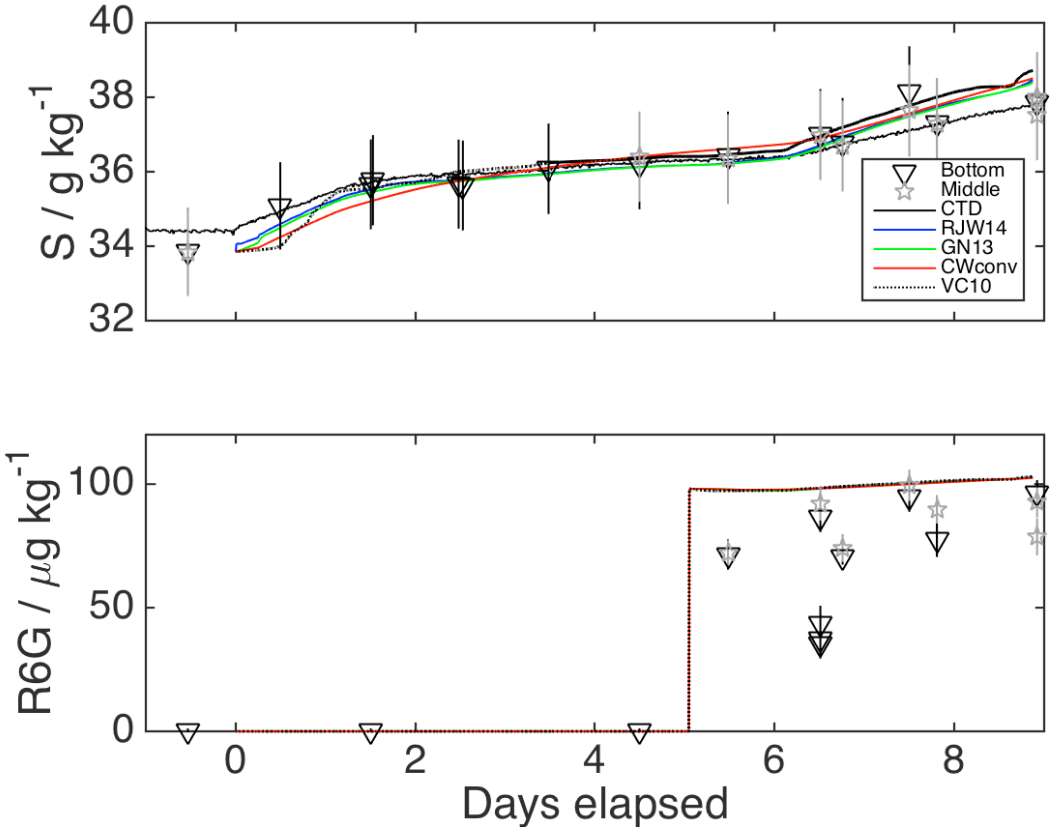

Figure 4.4: Salinity (top) and rhodamine concentration (bottom) as measured in the main tank ocean, and predicted by four gravity drainage schemes. Error bars represent 2σ analytical error. The markers for bottom (1 m depth) and middle measurements (40 cm depth) correspond to the sample lines described in Section 6.4. Note that rhodamine is spiked into the ocean at around 5.1 days elapsed.

4.5.4 Signals from RGB detectors

In its current state, data from the novel RGB light sensors cannot be used as a quantitive measure of rhodamine in the sea ice. However, using modelled rhodamine profiles, I have picked out signals that may be attributable to rhodamine in the sea ice. A change in the light field up to the surface sea ice was detectable immediately after spiking with rhodamine, when there was likely insignificant rhodamine in the sea ice. This shows that some of the light reaching the sensors had taken a path through the water column, and back into the sea ice, presumably reflecting of surfaces like the base of the tank. In order to remove the effect of this initial change in light field, I normalise all data to the first profile with rhodamine

only in the water. This is a crude method, considering the light field in the sea ice will change due to subsequent sea-ice growth.

The presence of rhodamine in the path of detected light should increase the value of normalised red intensity less the normalised green intensity (from here, red - green). Two regimes are discernible in the light profiles (Figure 4.5). Above around 7 cm depth, red - green roughly increases with time. Below 7 cm, red - green roughly decreases with time. The crossover point of these regimes is indicated by the left end of the double arrow. Noting that the RJW scheme captures the final rhodamine profile well, I assume that it is also performs well for previous timesteps. Figure 4.5 also shows rhodamine profiles, co-located in time with the light profiles. Two regimes are again discernible in the rhodamine profiles. Above the right end of the double arrow (around 7 cm depth), the rhodamine concentration increases through time for any depth as rhodamine is convected up into the sea ice. Below this depth the rhodamine concentration decreases through time, as rhodamine incorporated into newly forming sea ice is lost to the ocean *via* gravity drainage. The depth of the point of change in regime is similar to that for the red - green profiles. A reasonable explanation is that a build up of rhodamine above the depth of the regime change is driving an increase in red - green, and that a concurrent decrease below the depth of the regime change is driving a decrease in red - green. There are, however, areas that do not fit the pattern. At around 10 cm depth, for example, the decrease in rhodamine concentration is equal for 7.8 and 8.8 days elapsed, but there is a clear difference in the red - green at this depth.

While far from quantitative, this is a promising start for this instrumentation. It is also a confluent line of evidence that builds confidence in the measurements and modelling.

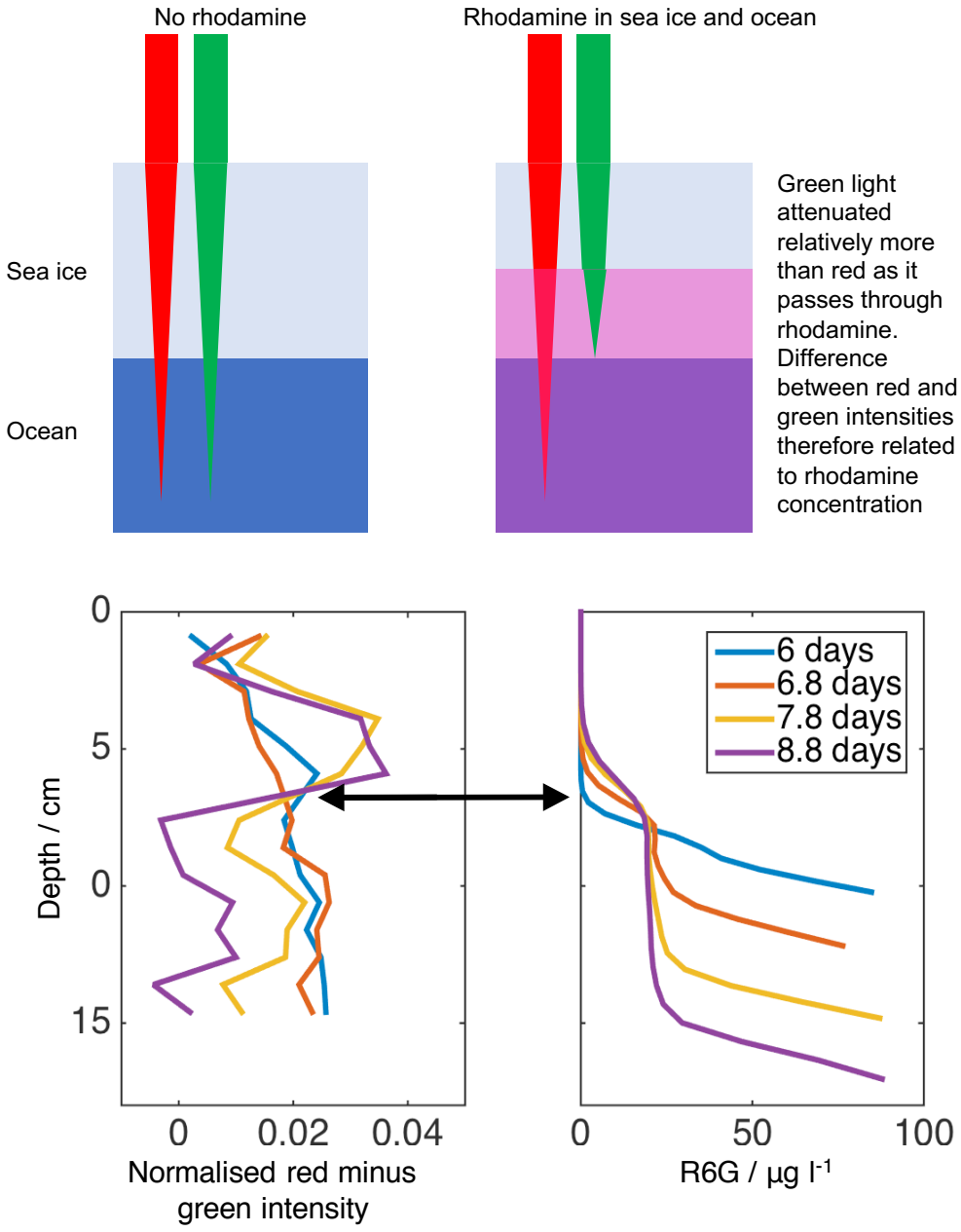

Figure 4.5: Top panels: Diagram of highly idealised behaviour of red and green light within sea ice (left) and sea ice containing rhodamine (right). **Bottom left:** Normalised red intensity less the normalised green intensity (red - green) for RGB light sensors. The data for each depth were normalised by dividing by the intensity for that depth in the profile immediately after spiking with rhodamine. **Bottom right:** Modelled rhodamine profiles (RJW14), co-located in time. The double arrow shows the position of the regime change described in the text.

4.6 Discussion

4.6.1 Model sensitivity

I choose RJW as the scheme for the sensitivity studies because it performs best against rhodamine concentration measurements. To analyse sensitivities, I have run the model over a range of ocean salinities, rhodamine spike masses, initial sea-ice thicknesses, and with an added side tank volume (Appendix, Table 4.4, Figure 4.7), and find that the model is relatively insensitive to these parameters. The addition of a side tank has a significant effect on ocean rhodamine concentrations, but would reduce the agreement between the modelled concentrations and the measurements. The bulk sea-ice salinity is sensitive to initial thickness, although an increase in surface salinity relative to the interior persists for a wide range of initial thicknesses. The predictive capacity of the model for the near surface bulk salinity is therefore reduced relative to the interior and near the base.

4.6.2 Post processing in sea-ice samples

Four factors may have influenced the distribution of salt and rhodamine in the slabs presented in Section 4.5.2: residual gravity drainage, brine expulsion, ocean infiltration and contamination. By consideration of each, I evaluate how representative the final measured slabs were compared to their *in situ* counterparts.

Gravity drainage is driven by the temperature profile in sea ice, with cooler temperatures near the surface, and as such likely plays a negligible role during the shock freezing where there should be only a weak, or even inverted, temperature profile. Brine expulsion, under environmental conditions, may redistribute salt within sea ice, but the effect is small (Notz and Worster, 2009). In the extreme environment of a -40^{o}C freezer brine expulsion may have a larger effect. As observed by Knight (1962), when brine pockets become isolated, further freezing will cause pressure to build in the pocket, stressing and eventually fracturing the surrounding ice and releasing some brine. However, in the interior of the sea ice, where brine volume fractions were around $\sim 5\%$, the $\approx 10\%$ volume expansion on

freezing likely caused only a small redistribution of salt. Near the base of the sea ice, brine expulsion may have been more significant, as the brine volume fraction was higher.

Ocean infiltration to the bulk ice *via* the sides should be at most $\approx 1\ \mu g\ kg^{-1}$ of the final rhodamine concentration, because the third shallowest layer of both slabs sat adjacent to well mixed ocean, but remained below this value. Ocean infiltration cannot have influenced the first layer as it sat above freeboard, and should have had a minimal effect on the second layer as it sat largely above freeboard. Ocean infiltration may have played a bigger role in the bottom layer, as brine drainage or expulsion from the freezing ocean could have infiltrated the base of the box, under the plastic sheets.

Finally, contamination could have occurred during sampling, or during the trimming of the frozen ocean from the sides of the sample, or from the bandsaw blade in between layers. The effect appears to be at least small, given that values below $1\ \mu g\ kg^{-1}$ of rhodamine were measured. In future, similar experiments, I would trim and cut an ultrapure water blank to asses this.

The lowest layer of each slab likely experienced the greatest post processing, given that it was most permeable at time of extraction. Also, the plastic dividers that I inserted around the sides of the sea ice effectively separate the interior sea ice from the re-freezing ocean, but likely do a worse job at the base of the box as they cannot form a water tight seal with the base of the box. Drained or expelled brine from the freezing ocean would affect the base layer much more than the interior layers.

Assuming the base of the sea ice was near ocean salinity at the time of sampling, I assume that a 20-50% change in salinity or rhodamine is a conservative upper limit for the level of post processing for any layer, and that shallower layers will experience less post processing. The profiles would be robust in the face of this given the regions of large concentration variations. The excellent match between slabs also builds confidence that the measured profiles are true to their *in situ* condition, because the two slabs were extracted in boxes with different sizes

and material, which would induce some randomness in the post processing. If they are a post processing effect, the low but measurable near surface rhodamine measurements conflict with RJW14, GN13 and CWconv, but may be caused by contamination during cutting, brine expulsion, or some combination of the two.

4.6.3 Impact of adsorption

Krembs et al. (2000) use rhodamine to measure the internal surface area of sea ice by exploiting its propensity to stick to icy surfaces. They derive two empirical relationships that I use to evaluate the impact of adsorption in this study. Equation 4.1 gives the adsorption of rhodamine per surface area, C_{SA} (μg cm^{-2}),

$$C_{SA} = C_{br} \times 11.413 - 1.7268 \times 10^{-4} \tag{4.1}$$

C_{br} is the rhodamine concentration in the brine, input in μg kg^{-1}. Krembs et al. (2000) also empirically parameterise the internal sea-ice surface area, A_i (cm^2 kg^{-1}), as a function of temperature (for columnar sea ice) using Equation 4.2,

$$A_i = e^{0.63T} \times 1.35 \times 10^5 \tag{4.2}$$

where T is the sea ice temperature (^{o}C).

To implement this adsorption scheme in the model, I first determine C_{SA} and A_i for each model layer. The product of C_{SA} and A_i is the rhodamine adsorbed to the internal surfaces of the sea ice, C_{ads} (μg kg^{-1}). Mass conservation dictates that C_{br} is reduced by C_{ads}. The adsorption scheme simply partitions the rhodamine, and does not alter the bulk concentration.

I also implement a simple adsorption scheme that partitions rhodamine using a constant between 0 and 1, where 1 indicates that 100% of rhodamine is adsorbed to the internal surfaces. The reduced C_{br} is then used in subsequent rhodamine dynamics, with C_{ads} assumed to be stationary. Rhodamine mass is conserved with both adsorption schemes.

Figure 4.6 shows the result of implementing the simple and Krembs adsorption

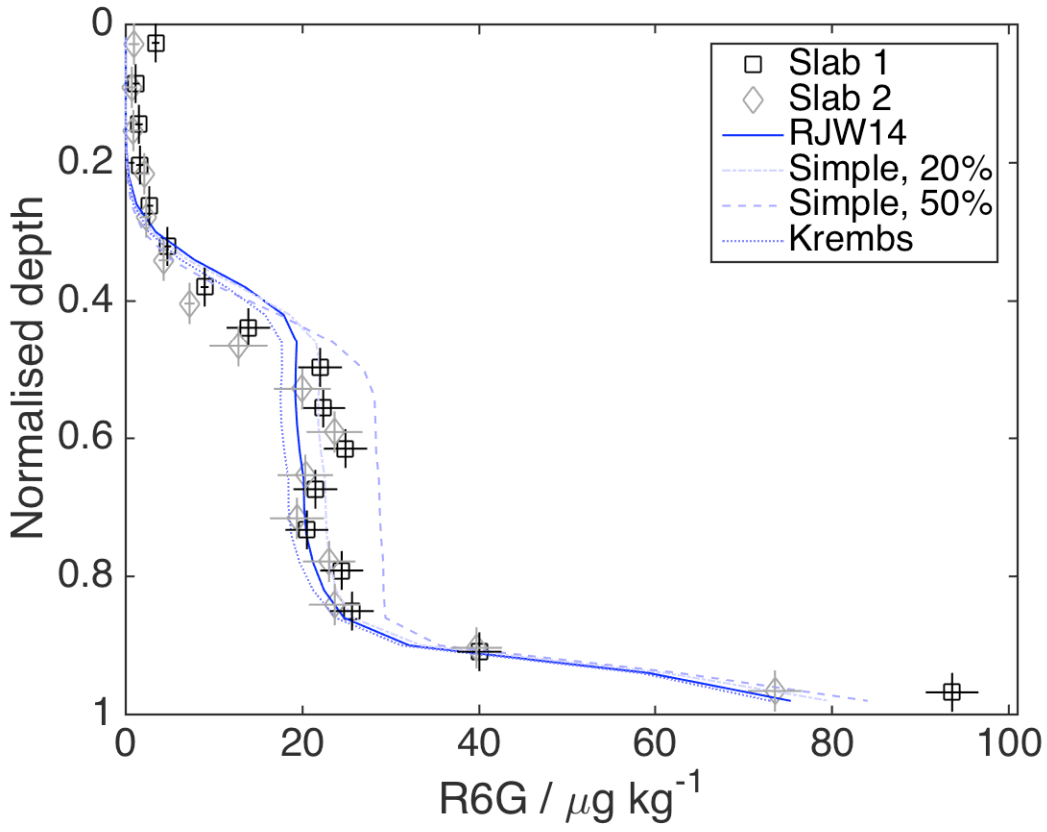

Figure 4.6: Bulk rhodamine concentration as measured in the slabs, and as predicted by RJW using different adsorption schemes, as a function of depth in the sea ice, normalised to the total sea-ice thickness. The vertical bars on the measurements span the depth of each analysed layer, while the horizontal bars denote 2σ analytical error. The simple and Krembs adsorption schemes are described in the text (Section 4.6.3), and 20% and 50% indicate that this percentage of dissolved rhodamine is adsorbed to the internal sea-ice surfaces.

schemes. I use RJW14 for these simulations (MADs of 2.13 and 2.11 μg kg^{-1}). The effect of the adsorption schemes is most dramatic between 0.4 and 0.8 normalised depth, in the region with relatively constant rhodamine. Krembs adsorption makes little difference to the profile relative to the model run without adsorption, making the fit slightly worse (MADs of 2.48 and 2.28 μg kg^{-1}). 20% simple adsorption also worsens the fit slightly (MADs of 2.89 and 2.86 μg kg^{-1}), and 50% simple adsorption is worst of all (MADs of 4.18 and 4.91 μg kg^{-1}).

However, in all adsorption schemes, surface area is the main driver of total adsorption, being 2 orders of magnitude lower near the surface of the sea ice relative to the base. The surface area parameterisation provided by Krembs et al. (2000) is derived from data with considerable scatter and so is poorly constrained, especially

at the high temperatures that occur near the base of the sea ice. It is therefore only prudent to use this parameterisation to qualitatively explore the effect of adsorption, and to examine sensitivity of the model to adsorption.

Two factors limit the impact of adsorption. Firstly, in the Krembs scheme, the highest brine concentrations in the upper layers of the sea ice, which will adsorb the most, coincide with very low surface areas, so little adsorption takes place. Secondly, for both the simple and Krembs adsorption schemes, there are competing effects from adsorption. As new sea ice forms, 100% of the rhodamine is entrained. Adsorption then lowers the concentration of rhodamine in the brine, which retards the loss of rhodamine back to the ocean, but also retards the upwelling of rhodamine into the sea ice. Quantitatively, the model is only weakly sensitive, and the shape of the profile is very insensitive, to adsorption. The assumption that rhodamine is acting as a dissolved tracer in order to evaluate the schemes is therefore appropriate. Further confirmation of this comes from analysis of the salt and rhodamine from the slow melt samples, where the highest rhodamine concentrations were released alongside the highest salinities, indicating rhodamine was highly associated with dissolved salt.

4.7 Conclusions

Combining convective gravity drainage schemes with measured temperature profiles as forcing has produced a model with minimal error from modelled thermodynamics. This is a powerful tool for future studies in controlled environments like the Roland von Glasow air-sea-ice chamber where model output can support other *in situ* or non-destructive measurements while preserving the integrity of the sea ice cover. It can also support wireharps as they become less accurate at very low liquid fractions.

There is good agreement between measured and modelled salinity and rhodamine profiles for all schemes, but particularly for the two schemes derived explicitly from consideration of brine convection, Rees Jones and Worster (2014)

and Griewank and Notz (2013). These schemes were designed as tools to predict sea-ice salt dynamics, and the results presented here build confidence that they can be applied to any dissolved tracer, whatever its distribution. While the sea ice grown in this experiment was thin relative to typical environmental sea ice, convective schemes act over a region of active convection that is often confined to some lower portion of sea ice. In this context, these results have a wider environmental relevance as they represent a convecting region in any sea-ice cover, rather than just convection in young sea ice. These results also show that error arising from the use of diffusive rather than convective gravity drainage schemes in previous studies modelling dissolved tracers in sea ice (Moreau et al., 2014; Zhou et al., 2014; Moreau et al., 2015) is likely small, but may be significant near the surface where the the diffusive scheme of Vancoppenolle et al. (2010) does not capture brine dynamics well.

Convective schemes should 1) be used in future; 2) can be used with high confidence to model salinity; and 3) can be used with high confidence to model any dissolved tracer.

4.8 Appendix

The model sensitivity to poorly constrained initial conditions (Table 4.4) is shown in Figure 4.7. The salinity and tracer profiles are robust to most changes in these conditions. Near surface salinity is affected by the initial sea-ice thickness. The addition of a side tank volume, which is likely an overestimate to the true contribution of the side tank, causes a drop in interior rhodamine concentrations of around 10%.

Table 4.4: Input parameters used in sensitivity analysis corresponding to Figure 4.7.

Run name	Initial Salinity / g kg^{-1}	Initial thickness / cm	180 kg side tank addition?	Mass rhodamine / g
Used configuration	33.85	1	No	0.2834
Low initial S	32.75	1	No	0.2834
High initial S	34.95	1	No	0.2834
1mm starting thickness	33.85	0.1	No	0.2834
2 cm starting thickness	33.85	2	No	0.2834
5 cm starting thickness	33.85	5	No	0.2834
180 kg sidetank	33.85	1	Yes	0.2834
0.2834 g R6G	33.85	1	No	0.26

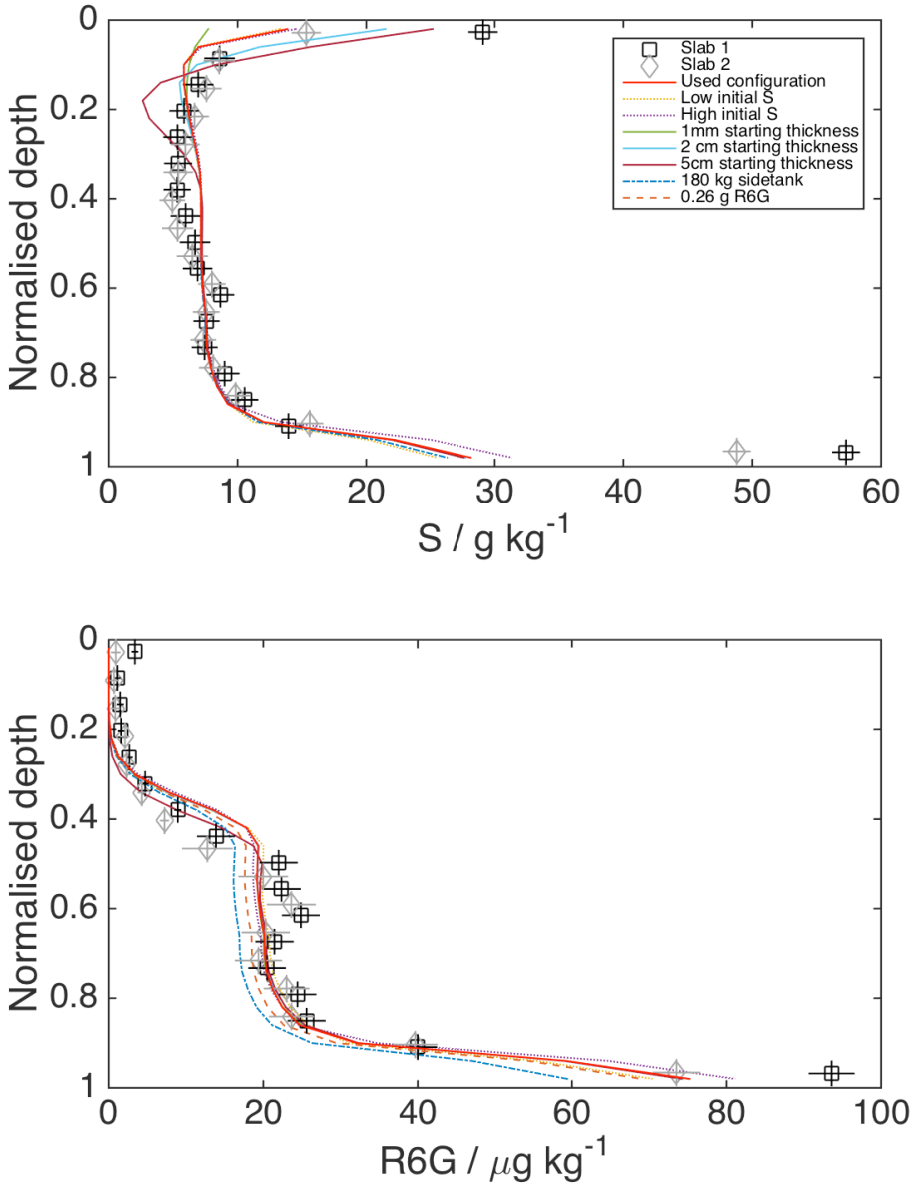

Figure 4.7: Performance of RJW for input parameters detailed in Table 4.4.

Chapter 5

Measurements of internal pressure in young sea ice

5.1 Summary

- Pressure is measured *in situ* in young sea ice with ≈2 cm vertical resolution.
- Pressure deviates from hydrostatic equilibrium pressure by up to 33 kPa, around 30%.
- Two modes of pressure build up and release are observed.
- In mode 1, near surface pressure increases (up to 25 kPa) and relaxes during the initial growth and cooling of the sea ice. The timescale of the increase is between one and three days, and the timescale of the decrease is on the order of days.
- In mode 2, near surface pressure increases (up to 33 kPa) and relaxes when the sea ice is warmed. The timescale of the increase is less than an hour, and the timescale of the decrease is on the order of days, similar to mode 1.
- Both modes are only observed in sea ice grown under quiescent conditions. When the water was pumped during initial growth neither mode was measured.

- Both modes are generated and sustained in sea ice with a low solid fraction (0.75), indicating that fluid within the sea ice was free to flow and so could not sustain a pressure. A significant component of both modes is therefore transferred to the sensor by the solid fraction of sea ice.
- An impermeable layer on the sea ice surface retards the relaxation of both modes.
- Mode 1 may be driven by thermal stresses within the sea ice, or by the volume expansion that occurs when sea ice solidifies.
- Mode 2 is very likely to be driven by thermal stresses.
- When brine and gas are free to flow, pressure build ups may result in the advection of fluid. For the measured pressures, brine flow will be negligible, but gas flow may be on the order of 10% of the total gas, which could be significant for gas dynamics in sea ice.

5.2 Background and objectives

Sea ice is a multiphase mixture of frozen water, liquid brine, gas bubbles, and precipitated salts. In the environment, changes in sea-ice temperature and salinity may significantly alter the proportion of these phases. For example, cooling sea ice causes some brine to freeze, increasing the solid fraction of the sea ice. The same cooling will also cause gases dissolved in brine to become less soluble (Tison et al., 2002), which may drive efflux of dissolved gases into bubbles, increasing the air volume fraction. Changes in the proportions of different phases vary widely over natural temperature and salinity ranges (Weeks, 2010).

Each phase change within sea ice is associated with a change in density. The density of frozen water is around 10% lower than that of liquid brine, for example. Therefore, as sea-ice solid fraction increase, the volume of that mass of sea ice increases. When brine is free to flow, one consequence of this is the advection of brine (Notz and Worster, 2009). However, when brine is immobilised, partial freezing of a brine pocket may result in a sustained pressure increase in the brine pocket, and eventual fracturing of the containing ice walls (Knight, 1962), or decreases in the size of bubbles (Light et al., 2003). Any change of phase in a region of immobile brine has the potential to alter the local pressure.

Biogeochemical processes in sea ice could be affected by pressure. Studies into climactically important volatile compounds in sea ice show that these compounds are partitioned between a dissolved and gaseous phase (Tison et al., 2002; Moreau et al., 2014, 2015; Zhou et al., 2014; Kotovitch et al., 2016; Crabeck et al., 2014). When the sum of the partial pressures in a brine pocket exceeds the local, hydrostatic pressure, bubbles may nucleate as gases efflux (Tison et al., 2002). However, modelling studies have yet to include any feedback between the volume occupied by nucleated bubbles and the local hydrostatic pressure (Moreau et al., 2014, 2015; Kotovitch et al., 2016). Instead, these studies parameterise bubble nucleation and growth as a linear function of the local gas supersaturation, that is tuneable *via* a bubble nucleation rate. The limitations of this approach are highlighted by Kotovitch et al. (2016), who are forced to use a bubble nucleation

rate that is orders of magnitude smaller than that used by Moreau et al. (2014), even though they use the same model. This is a symptom of a significant deficiency in the parameterisation of bubble nucleation, which may be remedied by the inclusion of pressure effects.

In Chapter 1 I show that the nucleation of bubbles within sea ice is always a controlling factor in sea-ice gas dynamics. Our poor understanding of the nucleation of bubbles hampers our ability to model gas dynamics in sea ice, and so hampers our ability to budget climactically important gases in the polar oceans. A critical step in improving our understanding of bubble nucleation is quantifying the magnitudes and drivers of pressure in sea ice.

I present high vertical resolution measurements of pressure in sea ice. I then use these measurements to address three questions:

1. What are the likely magnitudes of pressures in sea ice?

2. What processes control pressure in sea ice?

3. What are the potential biogeochemical implications of pressure in sea ice?

First, in Section 5.3, I describe the design, calibration, and deployment methodology of a novel *in situ* pressure sensor. Next, in Section 5.4, I define and describe two distinct signals observed using these sensors, referred to as 'mode 1' and 'mode 2'. The modes are distinct, because mode 1 occurs during cooling and growth, while mode 2 occurs during warming events. Then, in Section 5.5, I discuss the causes and implications of the observed signals.

5.3 Methodology

5.3.1 Design and calibration of pressure sensor

Pressure was measured using ten ceramic pressure sensors (ME506 piezo-resistive pressure sensor). The sensors are mounted in a PVC block to protect the electronics from sea water. Each sensor has a 1.2 cm face, and the vertical spacing of the

sensors is 1 cm (Figure 5.1). Closing a venting hole in each individual sensor sets the measurement to a differential pressure, which is relative to some sensor specific offset determined during the manufacture of the sensor. The dimensions of the main sensor body are $25 \times 4 \times 2.4$ cm.

The raw output voltage from the pressure sensors is related to the position of a diaphragm, which is set by pressure on the sensor face. The sensors are also weakly temperature dependant. I calibrated each individual sensor over a range of pressures (99 kPa to 114 kPa) and temperatures (-40 to +30 ^{o}C) using a combination of measured weather station atmospheric pressure (WS600-UMB) and overhead water depth. First, I placed the pressure sensor bar alongside the weather station in the coldroom. Natural atmospheric fluctuations in pressure ranged from 99 to 102 kPa, and I varied the temperature of the coldroom in 10 ^{o}C steps over the full temperature calibration range. I took the pressure bar temperature to be the measured weather station temperature, but excluded regions of rapid temperature change from the calibration because the temperature of the pressure sensor bar lagged slightly behind the air temperature. Next, I submerged the pressure sensor bar below 1 m of fresh water (exerting a constant 9.81 kPa of pressure), and took the true pressure to be sum of the overhead water and measured atmospheric pressure. The calculated true pressure ranged from 111 to 114 kPa. I measured the water temperature using a CTD (SBE-37 Microcat), and took this to be the temperature of the pressure sensor bar. For each sensor I then performed a multiple linear regression of true pressure, P, against pressure bar output voltage, V, and temperature, T (Equation 5.1).

$$P = x_0 + x_1 V + x_2 T + x_3 V T \tag{5.1}$$

Table 5.1 shows the coefficients derived for each sensor for this calibration procedure, and the coefficient of determination (R^2) of each model. The R^2 for sensor 5 is relatively poor because the sensor is noisier than the others, and data from sensor 5 are excluded from this study. The $x0$ coefficient gives the offset of a sensor for 0 V at 0 ^{o}C. $x1$ gives the pressure change for a given voltage change. $x2$ and $x3$ give the pressure change for a given temperature change, and the effect of

temperature on the response to pressure, respectively. The temperature dependant terms $x2$ and $x3$ are necessary for an accurate pressure reading, but the $x0$ and $x1$ coefficients contribute dominantly to the calculated pressure. For example, a 10 ^{o}C error in measured temperature would cause around a 1 kPa error in the measured pressure, which is small compared to the magnitude, and variability of, the signals observed in this report. The mean squared error between the true and calculated pressure during the calibration period is around 0.1 kPa for each sensor. I use Equation 5.1 with the corresponding coefficients (Table 5.1) to produce the pressure data in this thesis.

Although the calibrated pressure sensor tracks the true pressure well, the range of pressures achieved by this calibration procedure (99 to 114 kPa) is not sufficient to bracket the data presented in this report (up to 135 kPa). To verify the applicability of the coefficients in Table 5.1 over an extended range, I performed a second calibration over a wider pressure range (up to 130 kPa). To achieve this, I rested the pressure bar facing up, then attached a 3.2 m tube above each sensor face using a water tight sealant. I placed a thermistor within the tube, near the sensor face. I then filled the tube in four equal parts, allowing the sensor to stabilise between each fill, and calculated the water depth above the sensor for each fill. From this I calculated the true pressure in a similar way to the previous calibration, by summing the atmospheric pressure measured by the weather station and the calculated pressure from the overhead water. Due to time constraints I was only able to perform this validation for two sensors. Figure 5.2 shows a schematic of the calibration procedure, as well as the linear regressions of pressure sensor output of these sensors, calibrated using Table 5.1, against the true pressure. Agreement is excellent for the two sensors, with errors on the order of 1 kPa at the top end of the curves. This procedure verifies the calibrations described by Equation 5.1 and Table 5.1 over an extended pressure range but does not inform the final reported pressures as there is no temperature correction.

Finally, I offset the calibrated pressure before each experimental run to the expected pressure of each sensor below the water line. A sensor at depth z will

experience a hydrostatic equilibrium pressure of $P_a + (z \times \rho_o \times g)$ where ρ_o and g are the water density and acceleration due to gravity. Each sensor was offset based on its depth below the waterline and the measured atmospheric pressure such that it measured hydrostatic equilibrium pressure before any sea ice formed. This correction was typically less than 1 kPa, reflecting the error on the calibration. After offsetting the sensors at the start of each deployment the error on the pressure measurements will be less than 1 kPa.

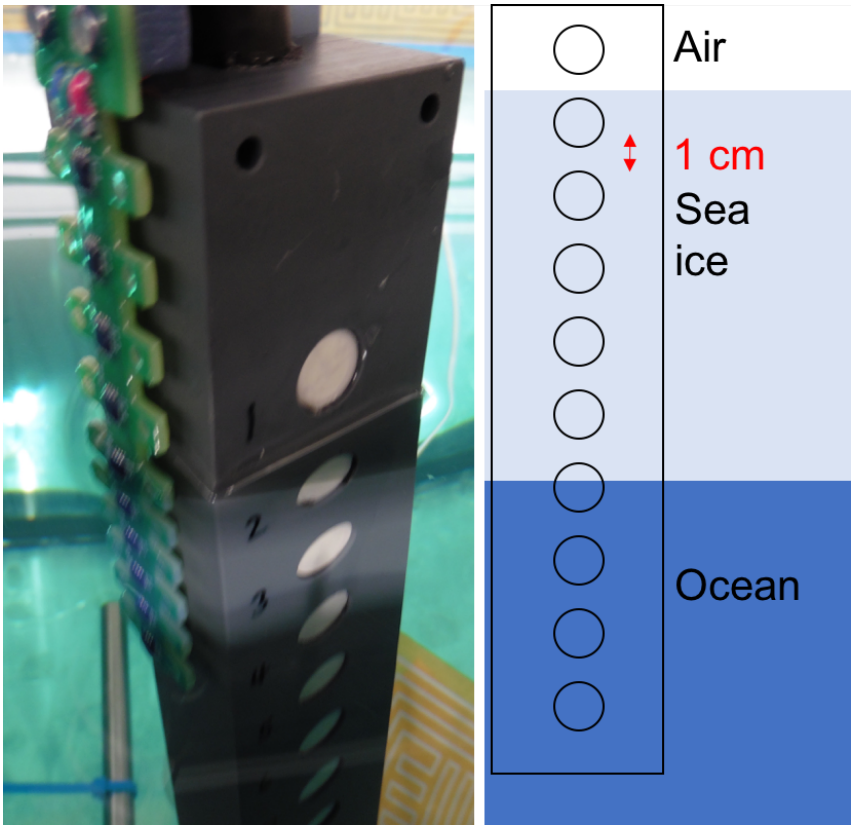

Figure 5.1: Left: Picture of pressure sensor bar with attached thermistors. Each white circle is the face of one piezo-resistive pressure sensor, and each black rectangle mounted on the green printed circuit board is one DS18B20U thermistor. **Right:** Schematic of pressure sensor bar, with sensors spanning the atmosphere, sea ice and ocean.

5.3.2 Deployment of pressure sensor

The pressure sensor was deployed vertically in open water, with at least one sensor above the water line, and left to freeze in (Figure 5.1). In this work depth is referenced in centimetres below the ocean/atmosphere interface, so atmospheric sensors have negative depths. I tried to position the shallowest submerged sensor so that it was as near to the surface as possible, but never exposed to the atmosphere.

Table 5.1: Coefficients and R^2 values for the multiple linear regressions used to calculate pressure from voltage (V) and temperature (T) for piezo-resistive pressure sensors using Equation 5.1. These coefficients were calculated using a calibration over 99 to 114 kPa, and -40 to +30 ^{o}C.

Sensor	x0 / kPa	x1 / kPa V^{-1}	x2 / kPa ^{o}C^{-1}	x3 / kPa (^{o}C V)$^{-1}$	R^2
1	128.1	5.9822	-0.027759	0.023873	0.9997
2	134.58	4.1806	-0.054611	0.026904	0.9998
3	144.02	2.7518	-0.10005	0.035616	0.9996
4	116.77	3.6868	-0.0087698	0.030204	0.9995
5	136.19	0.52709	-0.069067	0.039539	0.9977
6	149.68	7.0513	-0.11517	0.021416	0.9998
7	127.73	3.7296	-0.058396	0.031136	0.9996
8	132.21	6.3173	-0.098582	0.019084	0.9994
9	139.22	9.6626	-0.078337	0.0091770	0.9996
10	142.45	9.0569	-0.090743	0.010542	0.9995

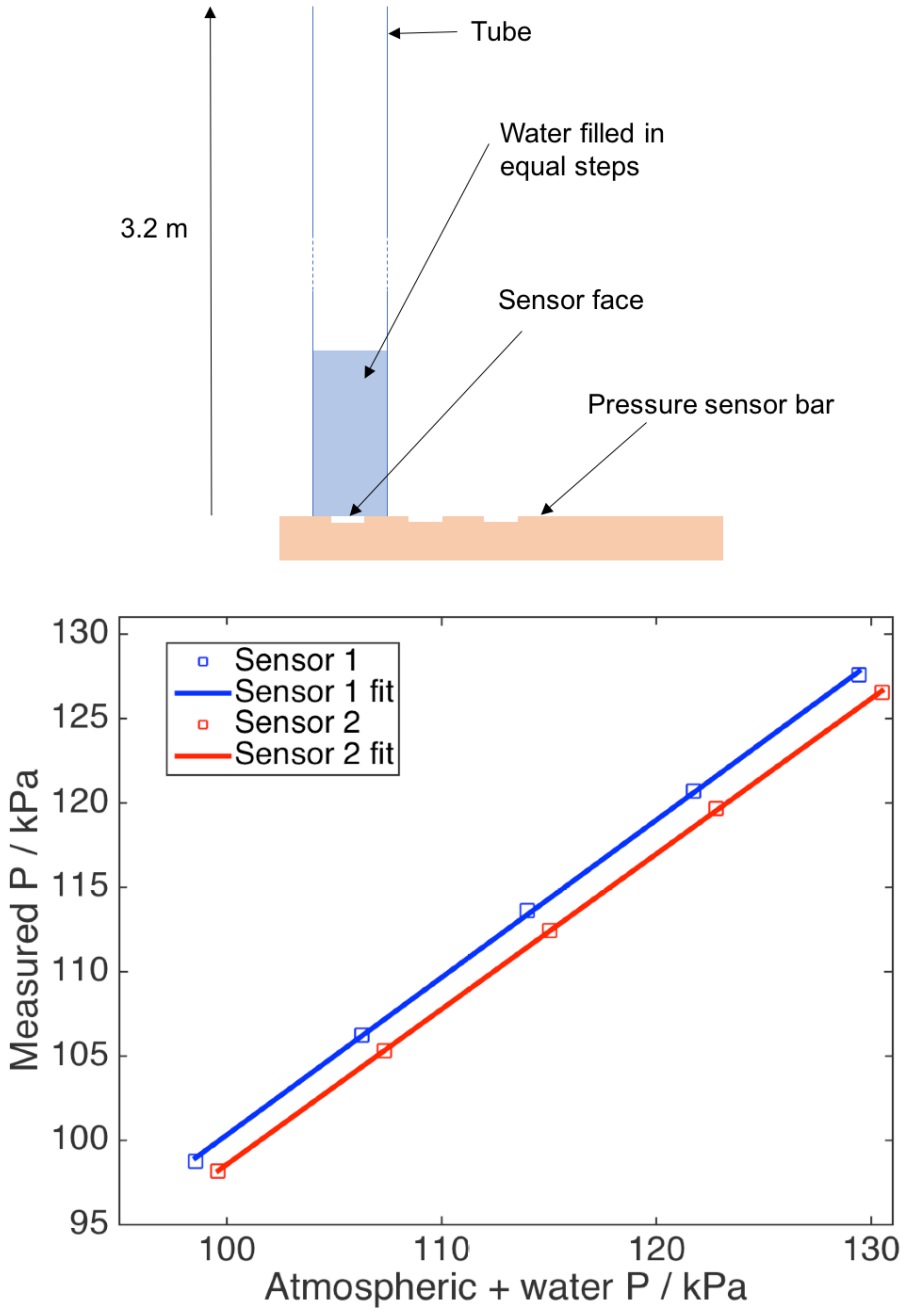

Figure 5.2: Top: Schematic of the set up used to generate high pressures above the sensor. **Bottom:** Pressure calculated from sensor output using the the coefficients in Table 5.1, against the pressure calculated from overhead water depth and atmospheric pressure.

In this work the state of sea ice at the sides of the tank can be fixed, free, or partially melted (Table 5.2). See Chapter 2 for the methodology used to achieve this. When sides were free the sea ice was floating with a natural freeboard, and when fixed was fast to the tank walls. Partially melted sides indicate that for much of the perimeter of the sea ice there was visible open water, but that the sea ice was fixed in place at various points. This situation arose during the development of methodology to maintain a free floating slab because heating pads maintained a gap around the tank sides, but ice fixed to the wires and connectors on the pads, and on small gaps between the pads. When my intention was to grow free floating sea ice, I mounted the pressure sensor bar from a metal support above the sea ice, then cut the bar free once the sea ice was a few centimetres thick so that it floated freely with the sea ice.

5.3.3 Instrumentation deployed alongside the pressure sensor

The core instrumentation deployed alongside the pressure bar were wireharps, thermistor strings and a weather station (Chapter 2). Much of this work was carried out during early facility testing and not all of these instruments were available for every experiment. Wireharps measure the sea-ice solid fraction, and so give an estimate of the level of connection between brine channels. They were deployed in depth profile with 1 cm vertical resolution. Thermistor strings were deployed alongside the pressure sensor bar and used to calibrate the pressure sensors. Both the wireharps and thermistors can be used to estimate the sea ice thickness. The weather station provided a calibrated reference pressure, which I used to verify the performance of the atmospheric pressure sensors.

5.4 Results

When the only factor contributing to the pressure at the face of a sensor is the weight of the overlying ocean, sea ice and atmosphere, the sensor is experiencing a hydrostatic equilibrium pressure, P_e. The weight of the overlying ocean and sea ice is, to a good approximation, constant, so deviations from measured atmospheric

pressure trends can be thought of as deviations from the hydrostatic equilibrium pressure, and as an indication that some process is occurring. To minimise error propagation, I consider the trend of each sensor relative to the atmospheric pressure trends rather than calculating the hydrostatic equilibrium pressure, and use the terms 'deviations from atmospheric trends' and 'deviations from hydrostatic equilibrium' interchangeably.

I use data from several experimental runs in this study, and some key features of the runs are summarised in Table 5.2. One common factor among all of the runs is that there was no turbulence in the ocean during initial sea ice formation. Deviations from atmospheric pressure trends (or hydrostatic equilibrium pressure) were greatly reduced or absent when sea ice grew from turbulent water. Several experimental runs have confirmed this, and these are not presented here due to the absence of signals in pressure. The role of turbulence is discussed further in Section 5.5.1. Brine skims, wet layers on the surface of sea ice, formed in some experiments and are discussed in Section 5.5.2.

A typical experimental run consists of some period of sea ice growth at constant atmospheric temperature, followed by one or more stepped atmospheric temperature changes. In this, and the next chapter I will discuss two distinct pressure signal, which I call 'mode 1' and 'mode 2'. Both of these modes of pressure build up and release are well illustrated by run 5.2 (Figure 5.3)[1]. Here, to orientate the reader, I describe modes 1 and 2 during this experimental run and identify the defining features of each.

In the first stage of run 5.2 sea ice forms from open water at a constant atmospheric temperature of -18 ^{o}C. During the initial period of cooling of the sea ice, near surface pressure increases over a day, deviating from atmospheric pressure by 13 kPa, before decreasing over around three days. *This is a mode 1 event, pressure build up and relaxation during cooling*. Spikes in near surface pressure also occur during the period of initial cooling, superimposed onto the mode 1 event.

[1] Unfortunately a thermistor failure for run 5.2 means that no *in situ* sea ice temperature data are available, so I have calibrated each pressure sensor using a reference temperature of -5 ^{o}C. The error from this crude approximation of temperature should be less than 1 kPa.

Table 5.2: Summary of key points from experimental runs contributing data to this chapter. Each run identifier is composed of two numbers in the form *x.y*, where *x* counts the number of fills of the tank, and *y* counts the melt/freeze cycles of that fill. The atmospheric temperature is the air temperature during the initial sea-ice growth period, before any stepped temperature changes. 'State of sides' indicates that the sea ice was freely floating, fixed to the tank walls, or fixed in places but with partial melting. 'Observed modes' indicates which of modes 1 and 2 were observed during a given run. 'Brine skim' indicates whether a noticeable liquid layer forms on the sea-ice surface. The 'magnitude of mode 1' is taken to be the maximum increase in pressure in the near surface sensor during the initial cooling and growth. The 'magnitude of mode 2' gives the magnitude of pressure spikes driven by sea ice temperature changes, relative to the size of the temperature change. 'ϕ start', 'Growth rate start', and 'Thickness start' refer to the solid fraction, growth rate, and thickness of the sea ice at the start of mode 1 events, respectively.

Run	Atmospheric temperature / ^{o}C	State of sides	Observed modes	Brine skim	Magnitude of mode 1 / kPa	Magnitude of mode 2 / kPa C^{-1}	ϕ start	Growth rate start / cm d^{-1}	Thickness start / cm
5.2	-18	Fixed	1 & 2	Yes	13	N/A*			
5.4	-28	Fixed	2	Yes	-	17 - 20			
6.2	-18	Partially melted	1 & 2	Yes	2	2	0.8 - 0.9	3.5	4
6.3	-18	Partially melted	1 & 2	Unknown	25	7.4 - 8.0	**	4	4
7.3	-18	Free	2	No	-	1			
8.3	-16	Fixed	1 & 2	Unknown	22	5.0	0.8 - 0.9	2.1	5

*Cannot calculate due to thermistor failure **No wireharp data

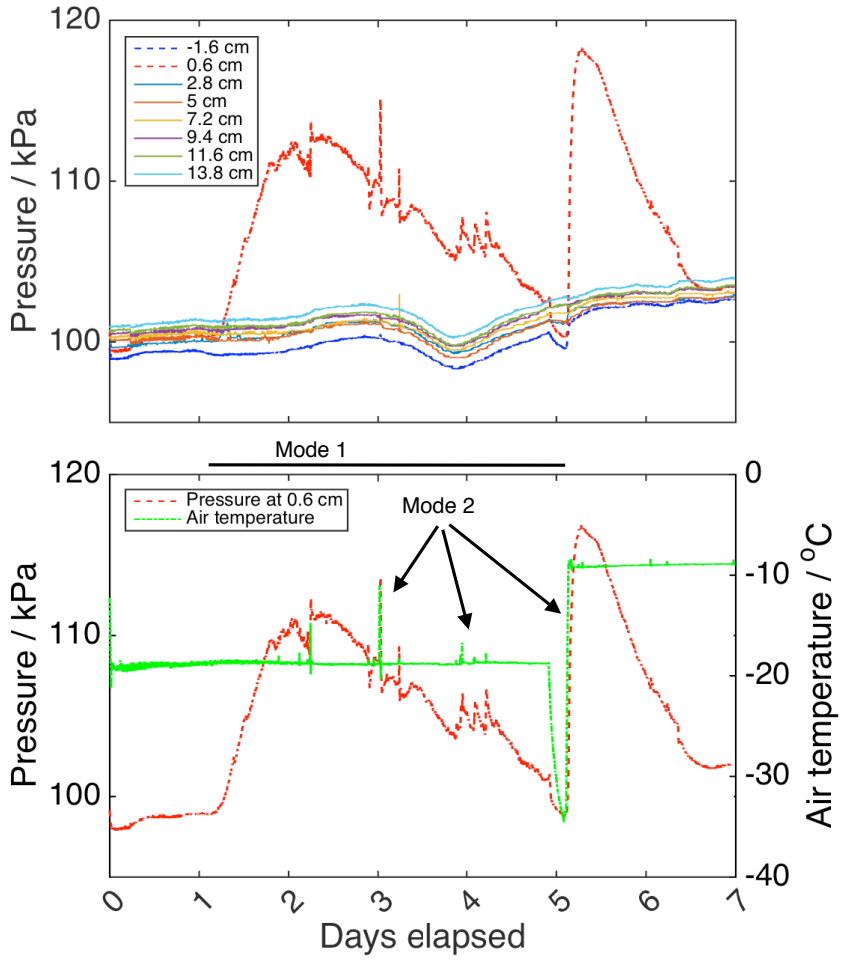

Figure 5.3: Data from run 5.2, where modes 1 and 2 are observed. Initial growth of sea ice took place at an atmospheric temperature of -18 ^{o}C, and a stepped temperature change follows this initial growth. Due to a thermistor failure all pressure sensors were calibrated to a constant temperature of -5 ^{o}C, which will cause an error on the order of 1 kPa. **Top:** Pressure for each sensor. The legend gives the depth of the midpoint of each sensor below the water line. **Bottom:** Near surface pressure (red) and atmospheric temperature (green).

These spikes are co-located in time with atmospheric temperature spikes, which were caused by experimenters entering the coldroom. Between day 2.5 and 5 there are at least six atmospheric temperature spikes that coincide with pressure increases. To investigate these spikes, I raised the atmospheric temperature on early on day 5 to warm the sea ice. As the temperature increases, near surface pressure increases, reaches a maximum in less than an hour, and then decreases over a period of days. Note that even after the atmospheric temperature has stabilised the sea ice will be warming. *This is a mode 2 event, pressure build up and release during warming*.

5.4.1 Pressure build up and relaxation during cooling (mode 1)

Mode 1 is a build up and subsequent relaxation of pressure in near surface sea ice, that occurs during the initial stages of growth and cooling. During a mode 1 event pressure builds in the near surface as sea ice cools and grows. Mode 1 events begin in nilas as it reaches around 4 cm thickness, and its near surface solid fraction increases above 0.8. After around a day, as the sea ice is still cooling and growing, the pressure begins to fall back towards hydrostatic equilibrium pressure, and this pressure relaxation occurs over around three days. The maximum pressure reached during mode 1 events ranges from around 2 kPa to 25 kPa. Mode 1 events have been observed in four experimental runs (Table 5.2). In this section I present results from the three experiments where mode 1 occurred, and where temperature data are available.

Figure 5.4 shows data from run 6.3, with a constant atmospheric temperature of around -18 ^{o}C followed by stepped temperature changes. The surface features observed in Figure 5.4 are similar to those in Figure 5.3, with build up of pressure over a day to a maximum, then a slower decrease over three days. The magnitude of the buildup in run 6.3 (25 kPa above atmospheric) is larger than in run 5.2 (13 kPa above atmospheric). Pressure build up is also observed in the sensors positioned at 2.8 and 5 cm depth, though the maximum pressure is smaller, and a smaller still buildup is observed at 7.2 cm. At around 3.5 days elapsed I begin stepped temperature changes to investigate mode 2, and I will discuss this section of the data in Section 5.4.2.

Pressure begins to build near the sea-ice surface at around 4 cm sea-ice thickness. During the initial build up of pressure at 0.6 cm depth, the sea ice at this depth is cooling at a rate of around 2 ^{o}C d^{-1}, and the the thickness of the ice slab is increasing at a rate of around 4 cm d^{-1}.

Figure 5.5 shows a mode 1 event observed during run 8.3, where initial growth occurred at a constant atmospheric temperature of -16 ^{o}C, and was followed by two stepped temperature increases[2]. A build up of pressure is again observed in the

[2]The data gap in is caused by a datalogger failure.

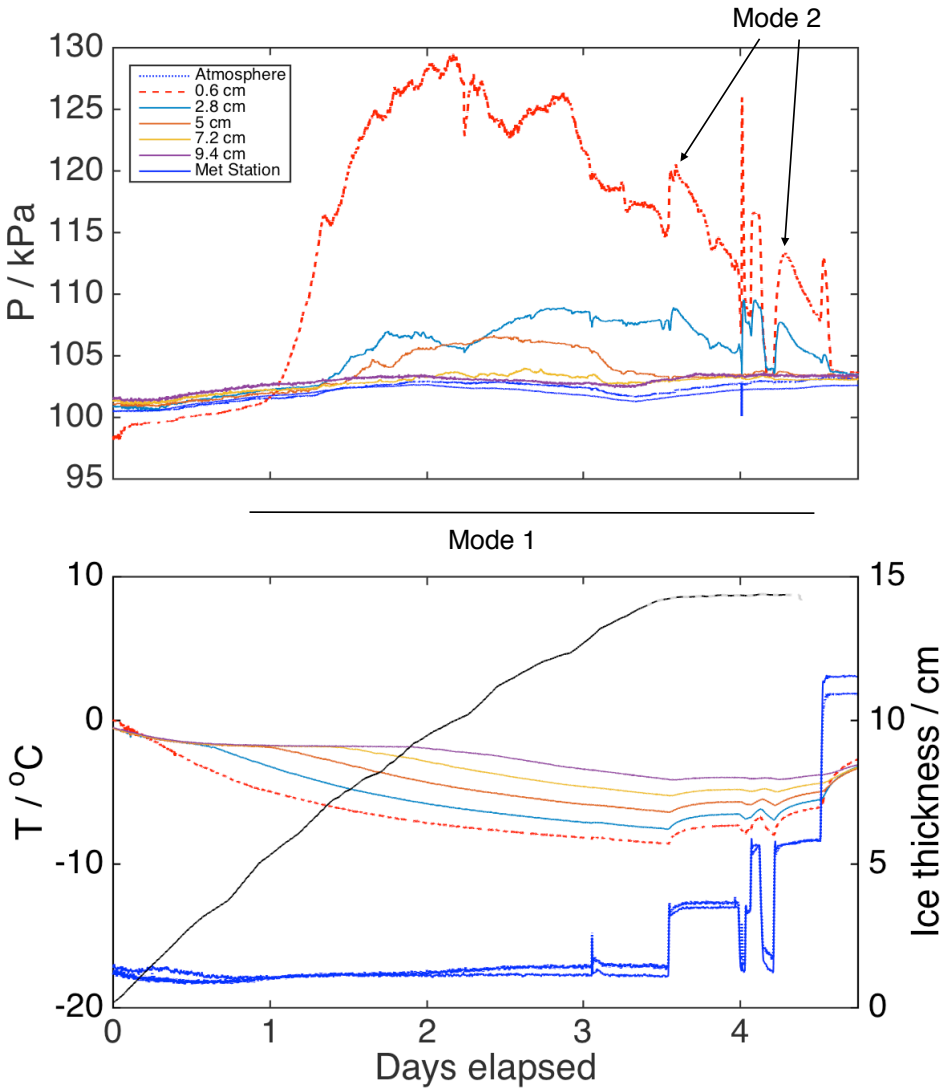

Figure 5.4: Data from run 6.3, where modes 1 and 2 were observed. Sea ice was grown initially at -18 ^{o}C, and was then subjected to several stepped temperature changes. **Top:** Pressure as measured by individual pressure sensors and the weather station. The legend shows the depth of sensors below the sea-ice surface. **Bottom:** Temperature co-located with pressure. Sea-ice thickness, as calculated from temperature profiles, is also shown (black line). The dashed portion in the sea-ice thickness shows minimum thickness, as the sea ice has grown past the deepest thermistor.

near surface sea ice, where the pressure increases over approximately three days, reaching 22 kPa. Due to time constraints I could not let the increased pressure relax, but the pressure increase has plateaued after around 5.7 days, when the melt phase was initiated. The pressure spikes at the end of the run are mode 2 events, and will be discussed in Section 5.4.2.

The growth rate[3] determined by the wireharps is around 2.9 cm d^{-1} over the

[3]During run 8.3 the wireharps were frozen in around 1 m away from the pressure sensor due to experimental constraints. The position of the pressure bar is further from the coldroom fans than the

growth period, and the growth rate determined by the thermistor chains is around 2.1 cm d^{-1}. The slower growth rate near the pressure sensors is likely due to the position of the sensors, and best represents the local environment of the pressure sensors. Both of these growth rates are lower than during run 6.3. At the beginning of the mode 1 event the sea ice thickness is around 5 cm and the near surface solid fraction is between 0.8 and 0.9.

During run 6.2, where initial sea ice growth took place at a constant atmospheric temperature of -18 ^{o}C, before three stepped temperature changes (Figure 5.5). A buildup in near surface pressure takes place over two days, and reaches around 2 kPa over atmospheric pressure. This buildup is small relative to other runs, and is similar in magnitude to potential errors from temperature and calibration artefacts, so the absolute magnitude of the pressure deviation is not well defined. However, the trend in near surface pressure differs from atmospheric and deeper sensors for the period between the 0.5 and 2.5 elapsed days. Also, early on day 3, near surface pressure begins to fall, in contrast to the trend in the atmospheric pressure and the trend in all other sensors. This observation could be the relaxation stage of a mode 1 event. A smaller buildup of pressure is measured by the next sensor down. The pressure spikes at the end of the run are mode 2 events, and will be discussed in Section 5.4.2.

From the wireharps I calculate the sea-ice growth rate in run 6.2 to be around 3.5 cm d^{-1} during the initial growth, and the thickness at the start of the mode 1 event to be around 4 cm. The solid fraction of the near surface sea ice at the start of the mode 1 event was between 0.8 and 0.9.

One common factor among mode 1 events is that they occur in runs with quiescent water during initial sea-ice growth. Another common factor is the sea-ice thickness and near surface solid fraction at which mode 1 events began, around 4 cm, and 0.8 to 0.9, respectively. The timescale of the pressure build up ranged from one day (5.2, 6.3) to three days (8.3), and the timescale of the relaxation was always

wireharps, and closer to the relatively warm side tank, and so the ice around the pressure bar should experience relatively less cooling. I have calibrated the pressure sensors using co-located thermistor chains so that changes in temperature are best represented.

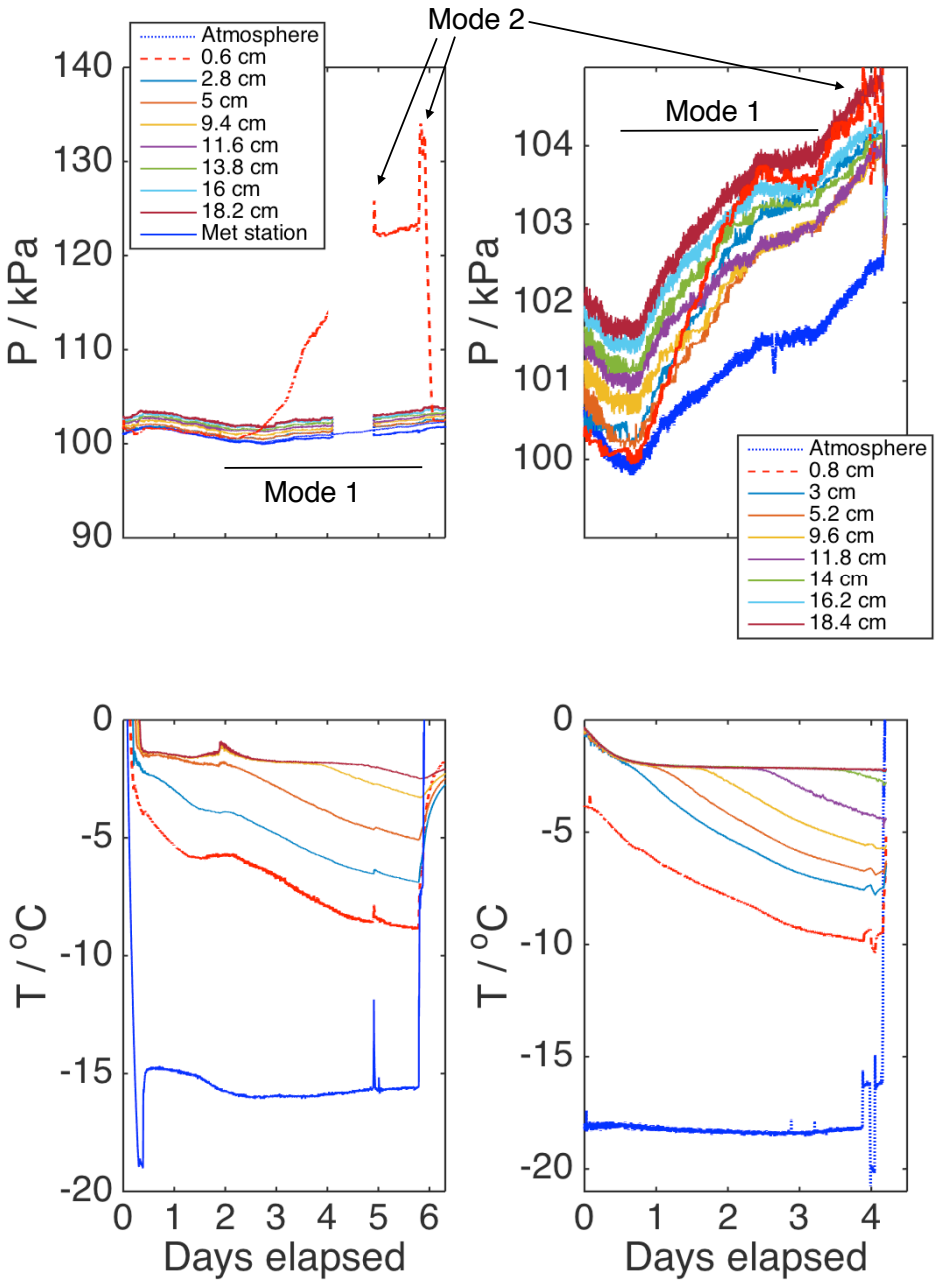

Figure 5.5: Data from runs 8.3 **(Left)** and 6.2 **(Right)** where modes 1 and 2 were observed. Pressure (top panels) was measured by piezo-resistive pressure sensors at various depths below the sea ice surface during both runs, and the meteorological station in the atmosphere during run 8.3. Temperature (bottom panels) is also shown for each run. The legend shows piezo-resistive sensor depth, and identifies the meteorological station. Stepped temperature changes cause the mode 2 events at the end of both runs. The data gap in run 8.3 is cause by a logging failure.

slower than the timescale of the build up. Higher growth rates may result in faster mode 1 build ups, with sea ice in run 6.3 growing at nearly double the rate of run 8.3. Mode 1 signals are generally confined to the top 3 cm of the sea ice, though

small deviations from atmospheric pressure trends are observed down to 7 cm in run 6.3. The magnitude of the pressure build up ranges from around 2 kPa (6.2) to 25 kPa (6.3). I have less confidence that the mode 1 event observed in run 6.2 is real due to its small magnitude, but even if it is an artefact it serves to highlight the large variability in observed mode 1 magnitudes for similar experimental conditions, because run 6.2 had a very similar set up to run 6.3. The higher end of the range of measured magnitudes is much too large to be driven by calibration or temperature artefacts. A 25 kPa increase is equivalent to over 2 m of overhead water, or put another way, is sufficient to make your ears pop while diving. I speculate on the causes of mode 1 events, and the variability between them, in Section 5.5.

5.4.2 Pressure build up and relaxation during warming (mode 2)

Mode 2 is a build up of pressure and subsequent relaxation in near surface sea ice caused by warming events. During a mode 2 event near surface pressure spikes in response to rapid increase in sea-ice temperature. These pressure spikes occur in less than an hour, after which the pressure relaxes back towards hydrostatic equilibrium pressure, on a timescale of several hours to days. The magnitude of the pressure spikes in mode 2 events ranges from around 1 kPa to 33 kPa. Mode 2 events have been observed in six experimental runs (Table 5.2). In this section I present data from the five runs where temperature data are available.

Figure 5.6 shows data from run 5.4, where sea ice is initially grown at -28 ^{o}C, before two stepped temperature increases cause pressure events in near surface sea ice. Deviations from atmospheric pressure trends are only observed in the near surface sensor, with all other sensors following atmospheric trends. The first pressure increase is highly correlated in time with a temperature increase in the sea ice, and a small overshoot in room temperature is reflected in both the near surface sea ice temperature and pressure. It takes around 45 minutes for pressure to peak, and it then begins to decrease, even as sea-ice temperature continues to rise. A second stepped temperature change causes the pressure to spike again, but

the magnitude of the pressure spike is less than that of the first spike, even though the temperature is greater. Relaxation then proceeds at a rate similar to relaxation from the first spike. The maximum pressure reached is 33 kPa above atmospheric pressure. Defining the start and end of each spike as the moment before sudden pressure change and the moment maximum pressure is obtained, respectively, I calculate that the change in pressure with temperature for the first and second spike to be 17 and 20 kPa C^{o-1}, respectively. The pressure appears to level off at a higher pressure than before the events started. The pressure events start while the solid fraction at 1 cm depth is around 0.9, and elevated pressures are sustained in sea ice with solid fractions as low as 0.75 towards the end of the run.

Mode 2 has also been observed superimposed onto mode 1 in 5.2, 6.2, 6.3, and 8.3. The rate of change of pressure with temperature varies between experiments, and between mode 2 events within them. In 6.2 the rate of change is around 2 kPa $^oC^{-1}$ for the stepped changes towards the end of the run (Figure 5.5). In 6.3 (Figure 5.4) mode 2 events at days 3.3 and 4 have rates of 8.0 and 7.4 kPa $^oC^{-1}$, respectively. In 8.3 (Figure 5.5) the rate for the spike just before day 6 has a rate of 5.0 kPa $^oC^{-1}$. However, pressure decreases sharply in 8.3, relative to other runs, and the near surface sea ice temperature quickly rises to around -2 ^{o}C. Together, these observations may indicate that the pressure sensor is decoupling from the sea ice, and that the measured pressure may be an underestimation. The time taken for the pressure to peak is around one hour for each run, and the pressure relaxes over several hours.

All of the data presented so far were collected in sea ice with walls fixed to the tank sides. As sea ice often exists in large floes, and is sometimes restricted by adjacent floes or the presence of land, fixed sides are often desirable for simulation of natural sea ice. However, sea ice may also exist in floes with dimensions on the order of centimetres, and to investigate pressure in these small floes, as well as the impact of edge effects in the tank, I performed run 7.3 with free floating sea ice.

Figure 5.7 shows data from run 7.3, where sea ice was grown at a constant atmospheric temperature of -18 ^{o}C, and then subjected to a set of stepped

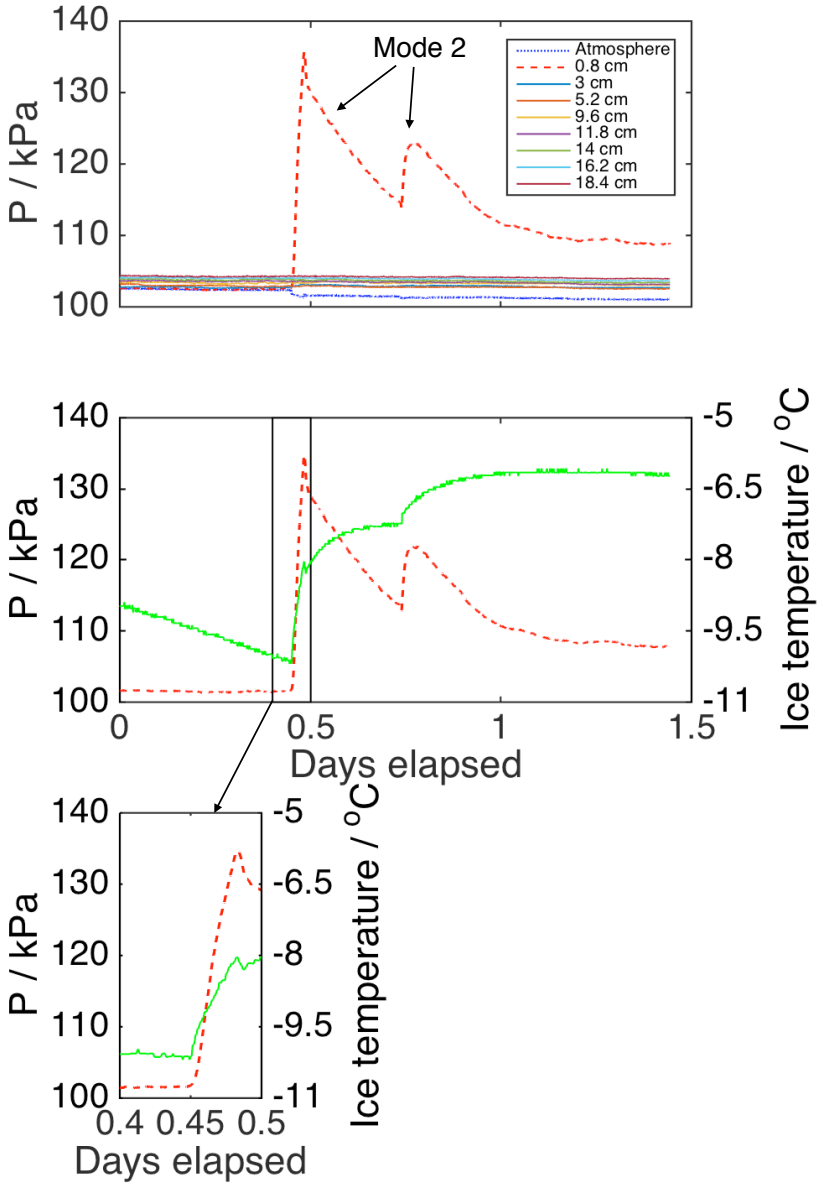

Figure 5.6: Data from run 5.4, where sea ice was grown at -28^{o}C, and is then subjected to two stepped temperature changes. **Top:** Pressure as measured by sensors. **Middle:** Near surface pressure (red) and temperature (green). **Bottom left:** Zoom in of first mode 2 event showing the co-location of the temperature increase and the pressure increase in time.

temperature changes. The first and largest increase in sea-ice temperature causes the near surface pressure to increase for around 45 minutes. This temperature increase also causes a smaller pressure increase at 2.8 cm, and a small decrease in measured atmospheric pressure, though the latter is likely a temperature artefact. Near surface pressure decreases after the initial spike over around six hours. Subsequent stepped temperature changes cause stepped pressure changes. The magnitude of the the

initial pressure spike is around 1 kPa $^{o}C^{-1}$, and the size of the subsequent spikes are a similar size.

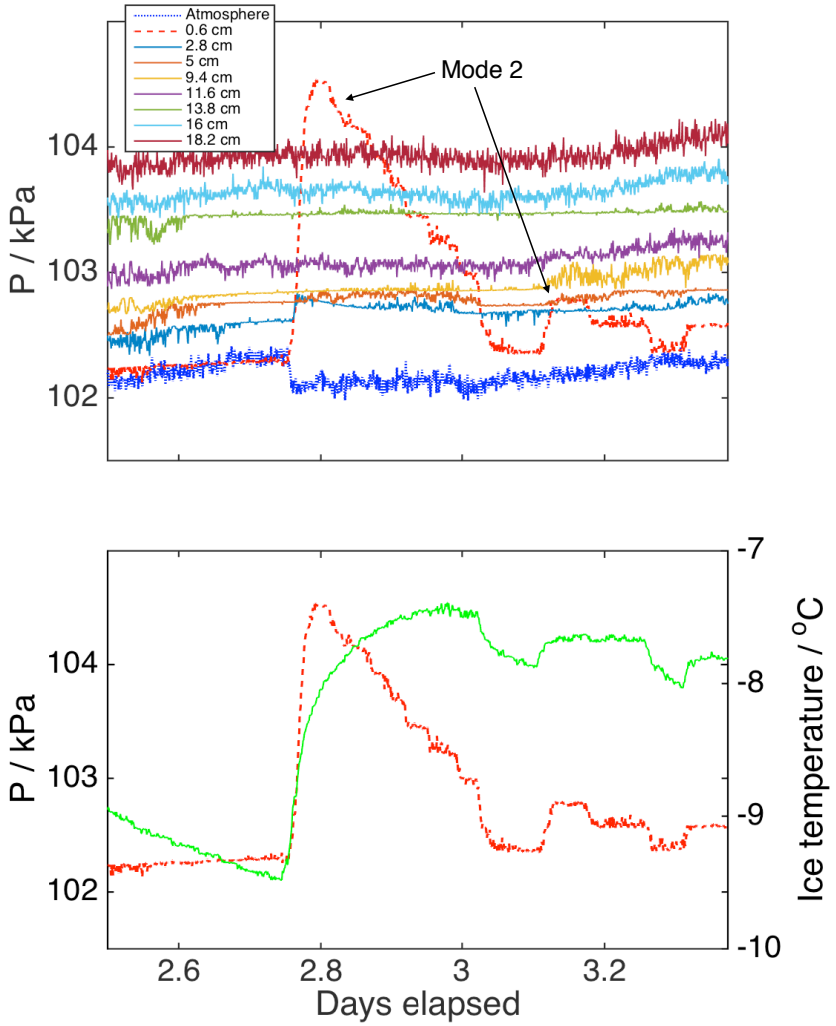

Figure 5.7: Data from run 7.3, where sea ice was grown at -18^{o}C, and was then subjected to several stepped temperature changes. The sea ice was free floating in run 7.3, in contrast to the other runs. **Top:** Pressure as measured by sensors. **Bottom:** Near surface pressure (red) and temperature (green).

Mode 2 events result in pressure increases with temperature increases, but in runs 5.4, 6.2, 6.3 and 7.3 temperature decreases drive pressure decreases. In run 5.4 this occurs at the height of the first spike, when the coldroom corrects an overshoot in the set point temperature, and in the other runs this occurs during the period of

stepped temperature changes. These pressure decreases with temperature decreases are distinct from mode 2 events because they only occur when the pressure is already elevated away from some baseline. In the near surface, pressure exerted on the sensor face by overlying sea ice is negligible relative to the atmospheric pressure, and I therefore define an 'absolute baseline' as the atmospheric pressure. Another useful definition of the baseline is the pressure at a given depth during a period of relatively stable temperature, and I call this the 'working baseline'. The working baseline may be elevated relative to the absolute baseline by a mode 1 or 2 event.

When these two baselines are considered, there is an asymmetry in the pressure changes with temperature, in that temperature increases may drive pressure increases above the absolute baseline, but temperature decreases may drive pressure below the working baseline, but not the absolute baseline. Take, for example, the period of stepped temperature changes in runs 6.3 and 6.2 (Figure 5.8). At some point during run 6.3 I lower the temperature (point labeled A5). This causes a rapid drop in pressure, that reaches a minimum before the temperature. This minimum is the absolute baseline, which is equal to the atmospheric pressure to within error. Cooling further does not decrease the pressure, and the pressure remains relatively constant. By contrast, in run 6.2 the pressure is elevated by a mode 1 event during the period of stepped temperature changes. I take the pressure before point B1 to be the working baseline. Lowering the temperature sufficiently drives the pressure below this working baseline (B2), before it begins to recover towards the working baseline, like a mirrored mode 2 event. Another temperature increase causes the pressure to rise (B3) before relaxing back towards the working baseline. The causes of pressure decreases with temperature decreases are discussed in Section 5.5.1.

As with mode 1 events, mode 2 events are observed only in sea ice grown from quiescent water. No mode 2 event is observed in other runs (not shown) with pumping during initial sea-ice growth. Mode 2 events do not fall below atmospheric pressures, but when pressures are elevated, temperature decreases cause pressure drops. Some experimental runs relax back to an unexcited pressure (6.3, 8.3),

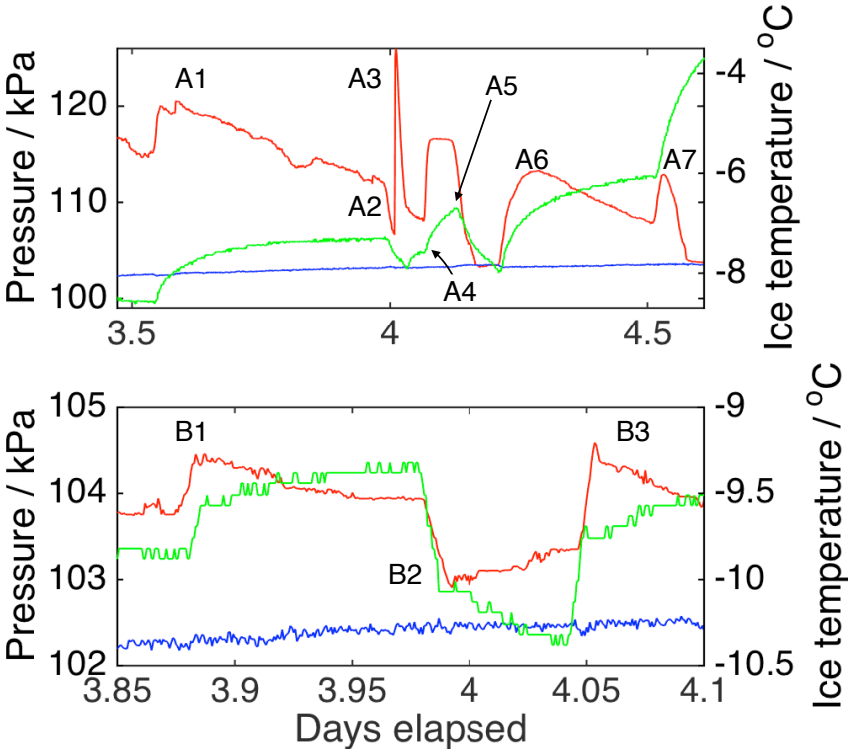

Figure 5.8: Data from run 6.3 **(Top)** and run 6.2 **(Bottom)** during the period of stepped temperature changes. The red and blue lines are the near surface pressure and the atmospheric pressure, respectively. The green line is the near surface temperature. The labels highlight key points in time that are discussed in the text. In Section 5.4.2 I use points A5, B1, B2, B3, B4, and B5 to show that pressure may never fall below an absolute baseline, but may fall below a working baseline. In Section 5.5.1 I use all of the A points to discuss the effect of an impermeable surface layer on the pressure.

whereas some runs relax back to an elevated pressure (5.2, 5.4). The magnitude of mode 2 events varies considerably between runs (Table 5.2). Run 7.3, with free floating sea ice, undergoes a 1 kPa C^{o-1} change, and for the runs with sea ice with fixed sides, the magnitude of the increase varies from 2 to 20 kPa C^{o-1}. For runs where both modes are observed, the relative magnitude of mode 1 and 2 events may be correlated, with 6.3 displaying the biggest, 6.2 the smallest, and 8.3 in the middle, for the magnitude of both modes. For all mode 2 events, the timescale of the pressure increase and relaxations are around an hour, and several hours, respectively. Mode 2 events are confined to the top 3 cm of sea ice. When the pressure is already elevated, temperature decreases cause drops in pressure. I speculate on the causes of mode 2 events, and drivers of variability between them, in Section 5.5.2.

5.5 Discussion

5.5.1 Factors influencing pressure signals

Drivers of variability in measured pressure

Turbulence in the water during initial sea ice growth precludes the measurement or generation of pressure signals. With no pumping I have observed mode 1 and 2 events on multiple occasions (Table 5.2), and over a range of growth rates. With pumping, signals are not observed. While I have observed a range of magnitudes for mode 1 and 2 events, the distinction between pumped and quiescent runs is clear.

A potential reason that pressure signals differ between runs depending on ocean turbulence is that the sea-ice structure is different between the runs. Nilas grows under quiescent conditions, and grease ice grows when there is turbulence in the ocean (Naumann et al., 2012). If indeed sea-ice structure is key for pressure signals to be observed, then there are differences between nilas and grease ice that may be important. Nilas is an elastic, consolidated layer, even at early stages of growth. This is in contrast to grease ice which will form an ice/brine slurry at the water surface (Weeks, 2010). It seems likely that a consolidated slab of sea ice is necessary to sustain pressure build ups, as pressure build up in grease ice may simply redistribute the ice and brine within the slurry.

Another factor that may influence the presence and magnitude of mode 1 and mode 2 signals is the state of the sea ice at the sides of the tank. The rate of change in pressure with temperature for mode 2 appears to be less when the sea ice is totally free floating (run 7.3) than when it is totally fixed (runs 5.4 and 8.3), though there are significant differences between these runs in other respects. In runs 6.2 and 6.3 the sea ice is partially fixed to the tank sides. The mode 2 magnitudes for runs 6.2 and 6.3 with partially fixed sides are greater than run 7.3, which was free floating, and less than run 5.4, which was totally fixed. The magnitude of mode 2 in run 8.3, with fixed sides, is between that of runs 6.2 and 6.3, but I believe this is an underestimate of the true pressure, as the rapid relaxation, which is far quicker than normally observed, indicates that the pressure sensor near the surface may be

mechanically decoupling from the ice in the rapidly warming surface sea ice. The state of the sides is not sufficient to explain the variability in magnitudes of the pressure increases, because both modes are greater in runs 6.3 than 6.2, which had similar experimental conditions and partially melted sides.

Heterogeneities in local sensor environment could be responsible for some of the variability in measured pressure. The 1.2 cm diameter sensor face may be in contact with several complete or partial ice crystals, brine pockets, or gas bubbles. Pressure may cause free brine and gas to flow rather than sustain and transmit a pressure to the sensor face, or a bubble may compress and transfer less pressure to the sensor. Crystal orientation may also play a role, as a crystal oriented parallel to the sensor face may transfer less pressure than one orientated perpendicular to it. In sea ice grown from quiescent water, the crystal orientation will be random, which could induce randomness in measured pressure. The fact that runs with large mode 1 events tended to have larger mode 2 events is evidence for local homogeneities driving some of the observed variability. If in one run the solid fraction at the sensor face was especially high, pressures may be transmitted more efficiently to the sensor in that case.

Drivers of mode 2

Temperature and pressure events are co-located in time for mode 2 events, and this strongly indicates a thermal process is driving mode 2 events. The thermal expansion of gas cannot be the cause, because it would lead to an order of magnitude smaller pressure response than is observed[4]. Measurement artefacts from temperature effects on the piezo-resistive temperature sensors are an order of magnitude too small to cause the observed pressure signals, evidenced by the reasonably accurate response of the atmospheric pressure sensors, which are subject to the greatest temperature changes. Also, pressure build ups must have at least one significant component that is not driven by brine or gas within the sea ice, because pressure signals are observed at solid fractions much lower than the

[4]Even a temperature change of 10 K, far in excess of what I have observed, causes only a $\approx$ 4% change in the absolute temperature. An isolated bubble, with a fixed volume, would therefore experience a $\approx 4\%$ pressure change, as pressure is linearly related to temperature through the ideal gas law. I observe pressure changes of around 30%. See also Section 5.5.2

typically assumed threshold for a well connected brine network, such that brine and gas would be free to advect to relieve pressure. For example, elevated pressures sustained in run 5.4 at a solid fraction as low as 0.75, were much higher than the 0.95 that is thought to be a rough threshold for a well connected brine network (Golden et al., 1998; Pringle et al., 2009), so the measured pressure must be delivered to the sensor by the solid fraction of the sea ice.

The likely driver of mode 2 events is thermal stress. This hypothesis is investigated in detail in Chapter 6, so I only provide a brief explanation here. A thermal stress is generated in a material when it is restricted from expanding or contracting freely when undergoing a temperature change (Noda, 2002). When sea ice is warmed it expands, and if this expansion is restricted compressive stress may be generated in the sea ice (Lewis et al., 1994). The converse is true for cooling. This mechanism accounts qualitatively for the initial pressure increases upon warming, and the pressure drops (from excited pressures) upon cooling. The restriction of expansion may come from the sides of the tank, or the mechanical linking of different depths in the sea ice undergoing different levels of expansion (Bogorodsky et al., 1972; Lewis, 1998). The magnitude of observed thermal stresses in field studies, 15 to 20 kPa ^{o}C (Richter-Menge and Elder, 1998), are similar to the mode 2 signals measured in this study.

The relaxation of excited pressures in mode 2 events can also be interpreted in terms of thermal stresses. Thermal stress models contain a relaxation term, whereby sea ice is driven to relax from excited stresses *via* a process call 'viscous creep' (Lewis, 1994). During viscous creep, a material deforms under stress, which reduces the stress. Viscous creep may also leave a material with residual stresses (Macosko, 1994), and residual pressures are observed in run 5.4 (Figure 5.6).

In the context of thermal stresses, sea ice growth conditions are important because the elastic properties of nilas may be required to transmit and sustain stresses in young, porous sea ice, while the state of the sea ice at the tank walls may affect the degree of restriction of expanding sea ice. Stresses could also be contained in the solid fraction of the sea ice, which would explain how pressures

are maintained in sea ice that is permeable enough for fluid to flow.

Drivers of mode 1

As sea ice thickens and solidifies, the total volume of the sea ice and ocean increases due to the expansion of water upon freezing. That this expansion is occurring in a tank environment is not a plausible explanation for the generation of mode 1 events for three reasons. First, the side tank is always liquid and open to the atmosphere, so volume is expanding into an open system and pressure is not generated. Second, even if some of this displaced volume rises above the sea-ice upper surface, the dimensions of the tank do not allow the $\approx$ 20 cm of water that would be required to drive even the lower end of mode 1 magnitudes (2 kPa). Third, pressure buildup due to the confinement of the system would be measured in the ocean and deeper sea ice as well as the surface, and this is not observed.

The volume expansion of water upon freezing within the sea-ice microstructure is a plausible driver of the build up of pressure in mode 1 events. Liquid freezing in the vicinity of the sensor expands into the sensor face, exerting a pressure. It is also possible that the relaxation in mode 1 events is driven by the flow of brine or gases to relieve pressure. Some difficulties remain with these hypotheses, however.

1. Mode 1 events begin at a solid fraction $>$0.9, above the threshold for the brine pocket network to be largely connected (Golden et al., 1998). Why doesn't solidification displace some of the remaining liquid to accommodate the new volume, rather than building pressure?

2. The relaxation of pressure takes place while the sea ice is still increasing in solid fraction, and proceeds towards an unexcited pressure. Why does the relief of pressure though fluid release start to outweigh the build up of pressure through volume expansion, even though volume expansion is still occurring?

3. Signals are generally observed the upper 2 cm sea ice. When signals occur deeper in the sea ice they are smaller. Why do mode 1 events often not occur deeper in the sea ice, where solidification is also occurring?

Some of these issues may be resolved by considering the local sensor environment. With regard to the first question, pressure may build up near the sensor in sea ice with well connected brine pockets if brine is trapped more easily near the sensor face. The total impermeability of the pressure sensors may cause brine to become isolated at the sensor face when the bulk solid fraction suggests the sea ice is permeable. In answer to the second question, solid fraction increases fastest during early sea-ice growth, when the total solid fraction is low. The relaxation may begin during solidification because the rate of solidification is decreasing. I cannot find an answer to the third question, because the internal sea ice generally reached solid fractions > 0.8 and is often more solid than the near surface sea ice, but deeper mode 1 events were only observed once, in run 6.3.

An alternative explanation for mode 1 events is provided, as with mode 2, by thermal stresses. For the build up of pressure, Lewis (1998), following Bogorodsky et al. (1972), propose that a mechanism that restricts the expansion of sea ice (and so generates thermal stresses) is the mechanical linking of different depths in the sea ice undergoing different levels of expansion. If near surface sea ice cools less than the layers below it, the surface will be contracted beyond its natural state, and experience compression. I observe greater cooling at depth in my experiments, as do Notz and Worster (2008) in a field study, and this is a phenomenon that is likely unique to young sea ice. The relaxation of pressure could occur *via* viscous creep. I explain this mechanism further, and investigate the hypothesis that mode 1 events are driven by thermal stresses in Chapter 6.

Neither of these hypotheses explain why mode 1 is not observed in runs 5.4 or 7.3, even though the mode 2 events in these runs show that the sea ice could transmit pressures to the sensor. I address possible reasons for the absence of mode 1 events from some runs in Chapter 6, once I have further considered the role of thermal stress.

Pressure relaxation with an impermeable surface layer

During the period of stepped temperature changes in run 6.3 (Figure 5.8), cold deionised water was poured onto the sea-ice surface around the pressure sensor. The

goal was to form a fresh, impermeable ice layer, a 'cap', on the surface, and to study the effect on pressure from capping the surface. Points A1 to A7 in Figure 5.8 are referenced in the following discussion.

During this discussion I take the working baseline of run 6.3 to be the extrapolation of the pressure trend between points A1 and A2, because during this period the temperature is stable relative to the subsequent stepped temperature changes. Just before the fresh water addition, there is a temperature drop that causes the pressure to drop below the working baseline (A2). During this period of decreasing temperature, the fresh water cap is added to the surface (A3). The first effect of the cap was to cause a pressure spike of around 20 kPa, likely due to the expansion of freezing water at the sensor face. The spike quickly falls, probably due to the continued cooling, because when the cooling slows, the pressure drop slows. The pressure reached is just below the working baseline and just above the pressure minimum before the spike. I interpret this observation as an offset from the working baseline driven by temperature, because the temperature is intermediate between the temperature of the baseline and the temperature at the pressure minimum.

When the temperature is raised the near surface sea ice experiences a mode 2 event (A4). However, the cap causes this mode 2 event to be atypical in two respects. First, the initial increase in pressure is faster, reaching a maximum in around 20 minutes, which is half the time of a typical mode 2 event. Second, there is no relaxation of the pressure. Both of these observations are consistent with the impermeable layer retarding the relaxation of pressure.

When the temperature is lowered to its minimum, the pressure drops and remains at the absolute baseline (A5). A second warming event causes the pressure to spike again, and the magnitude is similar to the first spike (A6). However, this is a typical mode 2, with an initial pressure increase over around 60 minutes, and a relaxation period over several hours. The effect of the cap is no longer observed. This is possibly due to erosion of the cap by the salt within the sea ice. Finally, a third temperature increase causes a third pressure spike, but the relatively small magnitude and steep drop in pressure indicate that the sensor is coming free from

the near surface sea ice (A7). The pressure returns to the absolute baseline.

An impermeable layer on the sea-ice surface retards the pressure decay, at least for mode 2 events. As all of the stepped temperature changes took place on a working baseline that was elevated due to a decaying mode 1 event, it is reasonable to assume that impermeable surface layers retard mode 1 relaxation also. Any hypothesis for the mechanism of relaxation should be consistent with this observation.

5.5.2 Biogeochemical implications of pressure signals

Deviations from hydrostatic equilibrium pressure are only observed in sea ice grown from calm conditions, and this observation indicates that nilas may generate and sustain pressures, but grease ice may not. As most sea ice in nature begins as grease ice (Weeks, 2010), the geographical relevance of these results is reduced. However, it is plausible that as sea ice thickens and solidifies it may become able to sustain pressures, regardless of its initial growth conditions.

The biogeochemical impact of increased pressure will depend crucially on the degree of connectedness of the local brine network. Pressurising a brine pocket that is connected to the atmosphere or ocean through a well connected network will result in the movement of fluid to relieve pressure, whereas pressuring an isolated brine pocket will result in a pressure build up in the brine inclusion. The movement of brine and gas will transport dissolved biogeochemical tracers. Pressure increases in a brine inclusion may affect biogeochemical processes, such as the nucleation of gas bubbles. When a brine inclusion is open, the question arises, how much fluid flows in response to the increase pressure? And when a brine inclusion is closed, what happens in the pressurised brine inclusion?

For the well connected brine network I use a theoretical framework from Gudmundsson (2012) to estimate the impact of the movement of brine. This theoretical framework does not account for the changes in brine and ice volume fraction as sea ice temperature changes, and so cannot be used to calculate the true brine displacement. This framework is useful however, as it gives the potential effect of pressure on brine displacement, which can be compared to the effect of

brine expulsion.

Gudmundsson (2012) considers the amount of magma displaced from a magma chamber under pressure (Equation 5.2). Replacing magma with brine, and rock with ice, all of which have very low compressibility, I use Equation 5.2 to calculate the fraction of volume of displaced brine, $\frac{\Delta V_{br}}{V_{br}}$, for a given excess brine pressure, P_e.

$$\frac{\Delta V_{br}}{V_{br}} = (K_i + K_{br})P_e \tag{5.2}$$

K_i and K_{br} are the compressibilities of ice (Feistel and Wagner, 2006) and water (Kell, 1970), respectively, and the sum of these compressibilities is $\sim 10^{-10}$ Pa^{-1}.

Taking a typical excess pressure measured in this study to be 25000 Pa, displaced brine volume is $<< 0.01\%$ of the total. The contribution of pressure effects to brine displacement is negligible relative to the displacement from processes such as brine expulsion, which redistribute around 1% of the salt in sea ice. This conclusion is not surprising, given that I show in Chapter 4 that the distribution of salt in sea ice can be accurately predicted with no consideration of the modes of pressure buildup observed in this study.

I also use Equation 5.2 to explore the possibility that pressure buildups drive the brine skims observed in many of these experiments (Table 5.2). Brine skims are obvious in person, appearing as a shiny and wet sea-ice surface, but are not easily discernible from the low resolution video that was used to observe the sea-ice surface in early experiments, and this is why the presence of a brine skim is unknown for several experimental runs. Brine skims were measured in several experiments to be around 1 mm deep. When observed, brine skims formed during the first day or two of sea-ice growth and persisted throughout the experiment, similar to field observations (Perovich and Richter-Menge, 1994). Mode 1 events provide a possible mechanism for the generation of brine skims. Pressure builds near the sea ice surface, either due to the volume expansion of freezing water or thermal stresses, and drives brine away from the surface, and brine that is expelled up forms a brine skim. To test this mechanism, I assume that the top 2 cm of sea ice contribute to brine skim formation (Perovich and Richter-Menge, 1994) and

that this layer of sea ice is around 25% liquid. Using Equation 5.2, I calculate that around 10^{-5} mm of brine is displaced by the excess pressures observed in this study. Pressure effects are therefore not the dominant drivers of the observed brine skims.

Gas may also flow to relieve pressure. The gas volume that will flow in response to a pressure increase is much larger than that of brine because of the higher compressibility of gas. I estimate the change in gas volume in a brine pocket in response to pressure changes in a well connected brine pocket using the ideal gas law

$$PV = nRT \tag{5.3}$$

where P and V are the pressure and volume of an individual gas bubble in a brine pocket, respectively. R is the universal gas constant, n is the moles of gas in the bubble, and T is the absolute temperature of the bubble.

T can be approximated as constant in this discussion, because typical changes in temperature of 2 ^{o}C correspond to a $< 1\%$ change in the absolute temperature, which is small compared to the observed pressure changes. I take V to be constant based on a simplifying assumption that the ice and brine are incompressible relative to the gas. Brine pocket pressure then equilibrates with its surroundings by releasing some fraction of the gas present in the bubble, n_r, according to,

$$n_r = \frac{P_{bub} - P_{sur}}{P_{bub}} \tag{5.4}$$

where P_{bub} and P_{sur} are the pressures of the pressurised bubble, and the pressure of the surroundings. For a 30% pressure excess in the bubble, Equation 5.4 predicts 23% of gas within the pocket will be released to surrounding pockets, or to the ocean or atmosphere.

Equations 5.2 and 5.4 give theoretical maxima for the amount of brine and gas displacement to relieve a given pressure change, respectively. The proportion of brine to gas that flows will depend on the resistance to the flow, which will depend on the permeability, and a quantitive assessment of the ratio of brine to gas flow is beyond the scope of this discussion. However, it is plausible that gas flow is stronger

when the upwards permeability is larger, given that bubbles reside at the top of brine pockets (Light et al., 2003). Ono and Kasai (1985) find that the upward permeability of sea ice is greater than than downward permeability, and so gas displacement may be favoured over brine displacement. Pressure increases in near surface sea ice may increase the rate of gas transfer between the sea ice and atmosphere by driving out gas.

When pressure increases in an isolated brine pocket some combination of five processes must occur:

1. gas inclusions are compressed
2. gas within gas inclusions dissolves
3. salts precipitate
4. brine is compressed
5. the surrounding ice fractures and releases fluid

Isolated brine pockets are rarely observed in my experiments, so I speculate only briefly on the possible effects of increases in pressure on the order of 10 kPa. Process 3) is likely to be negligible. Marion et al. (2005) find that the effect of pressure on salt precipitation is small even for pressures that are hundreds of times larger than the pressures measured in this study. With respect to 1) and 2), gas bubbles are always associated with brine inclusions in sea ice. When a gas bubble is pressurised in an isolated brine inclusion it may shrink (1) to occupy a new reduced volume, or some of the gas may dissolve in the brine (2) (Light et al., 2003). The compression or dissolution of gas may act as a buffer to fracturing the walls of the pocket (5). The pressures measured in this study would compress brine by a negligibly small amount (4).

5.6 Conclusions

In this chapter I presented high vertical resolution measurements of pressure in sea ice, and identified two modes where pressure deviates from hydrostatic equilibrium.

Both modes are confined to near surface sea ice, and are sustained significantly in the solid fraction of sea ice. During mode 1 events, near surface pressure builds (up to 25 kPa above hydrostatic equilibrium) and then relaxes during initial sea ice growth and cooling. During mode 2 events, increases in sea-ice temperature cause rapid pressure increases (up to 33 kPa above hydrostatic equilibrium) that then relax. The two modes can be superimposed to cause even higher pressures, and I expect the measured pressure to underestimate the true pressure because there is often free fluid at the sensor face. These experiments suggest pressure in young sea ice:

- may be elevated by several tens of kPa over hydrostatic equilibrium
- may increase from hydrostatic equilibrium on timescales of several hours (mode 1) or less than an hour (mode 2)
- is driven to relax back towards hydrostatic equilibrium over several hours
- is highly variable over vertical scales on the order of 1 cm

I am confident that mode 2 events are driven by thermal stresses. This is because of the co-location of mode 2 events with temperature increases, the reversibility of pressure changes with temperature, the generation and persistence of mode 2 events in permeable sea ice, and the similar magnitude of observed pressure increases to previously observed thermal stresses (Richter-Menge and Elder, 1998). Mode 1 events may also be driven by thermal stresses, or may be caused by the expansion of water upon freezing at the sensor face. A theoretical framework for thermal stresses in sea ice has been proposed by Bogorodsky et al. (1972) and Lewis (1993, 1998). In Chapter 6 I investigate whether thermal stress is driving the observed pressures by comparing measured pressure to output from a thermal stress model (Lewis, 1998).

If a pressurised brine pocket is closed, pressure is sustained. Any pressure effects are confined to the brine pocket until the brine pocket becomes open, at which point the pressure is relieved by fluid flow. If a pressurised brine pocket

is open, fluid flow is the only consequence of increased pressure on the brine and gas. The flow of brine is negligible but the flow of gas may be significant. As pressure increases occur in near surface sea ice, they have the potential to increase the gas transfer between the sea ice and atmosphere and thereby effect the cycling of volatile compounds in polar regions.

Chapter 6

Thermal stress in young sea ice

6.1 Summary

- To investigate to what extent thermal stresses drive the measured pressures described in Chapter 5, I model thermal stress (Lewis, 1998) and compare predicted stress to pressure measurements presented in Chapter 5.
- When simulating pressure build up and release during cooling and initial sea-ice growth (mode 1), the modelled thermal stress captures the timing, shape and frequent near surface localisation of pressure signals when mode 1 events are measured. However, the model often overestimates the magnitude, and predicts some mode 1 events that are not measured.
- When simulating pressure build up and release during warming events (mode 2), the modelled stress captures the timing, shape, and localisation near the surface of the sea-ice pressure signals, but often overestimates the magnitude.
- Mode 2 events are driven by thermal stresses.
- Mode 1 events cannot be driven exclusively by thermal stresses, so the expansion of water during sea-ice solidification likely plays an important role in mode 1 events.
- Sea-ice stress, thermal or dynamic, may be the dominant driver of pressure in sea ice, and in sea-ice brines. Future studies of sea-ice pressure should consider stress, and the effect of stress on brine and gas pressure.

6.2 Objectives

Two modes of pressure build up and release in young sea ice were measured and described in Chapter 5. These pressure signals were observed in sea ice where fluid was free to flow, and this observation suggests the solid fraction of sea ice is stressed. Differential cooling between the surface and deeper sea ice occurs during both modes, suggesting thermal stresses may play a role, and the reversible nature of mode 2 events strongly implies thermal stresses. In this chapter, I compare measured pressure to modelled thermal stress for several experimental runs to investigate the extent to which measured pressure is caused by thermal stress.

First, I provide an overview of sea-ice stress (Section 6.3). Next, I show how stress will be measured by the piezo-resistive sensors, and detail my formulation of the Lewis (1998) thermal stress model (Section 6.4). I then compare measured pressure to modelled stress for all of the runs from Chapter 5 where sufficient data are available (Section 6.5), and use the model performance to show that mode 2 is driven by thermal stress, and that at least a significant part of mode 1 is not driven by thermal stress (Section 6.6).

6.3 Background

6.3.1 Theory of stresses in sea ice

Stress is linked to the deformation (strain) of a body *via* the elastic modulus (Equation 6.1). A body may experience compressive or tensile stresses, depending on the sign of the strain. Compressive stresses are taken to be positive in this thesis.

$$\sigma_{ij} = E\varepsilon_{ij} \tag{6.1}$$

In Equation 6.1, σ, ε and E are the stress, strain and elastic modulus, respectively. The subscript i indicates one cartesian plane, while j indicates the direction in which the stress is acting.

Stress can be represented as a tensor, meaning stress has a magnitude,

direction, and acts upon a plane. The stress tensor has three normal stress components (on the diagonal) and six shear components (off the diagonal).

$$\sigma = \begin{bmatrix} \sigma_{xx} & \sigma_{xy} & \sigma_{xz} \\ \sigma_{yx} & \sigma_{yy} & \sigma_{yz} \\ \sigma_{xz} & \sigma_{zy} & \sigma_{zz} \end{bmatrix} \tag{6.2}$$

A set of axes can always be chosen such that the shear stress components are zero, and in this case Equation 6.2 reduces to Equation 6.3, and the three non-zero stress components (σ_{xx}, σ_{yy}, σ_{zz}) are known as 'principal stresses'.

$$\sigma = \begin{bmatrix} \sigma_{xx} & 0 & 0 \\ 0 & \sigma_{yy} & 0 \\ 0 & 0 & \sigma_{zz} \end{bmatrix} \tag{6.3}$$

I defined hydrostatic equilibrium in Section 5.4, and I can now re-define it using the stress tensor as the case where $\sigma_{xx} = \sigma_{yy} = \sigma_{zz} = P_h$ in Equation 6.3, where P_h is the hydrostatic equilibrium pressure. Under hydrostatic equilibrium, stress/pressure is an unexcited or resting state, and is simply the stress/pressure generated by the weight of the material above a point. Deviations from hydrostatic equilibrium indicate that some process is stressing the sea ice.

Thermal and dynamic processes act to stress sea ice. Thermal stress occurs when the expansion/contraction of sea ice undergoing a temperature change is restricted, such that the total strain is not equal to the strain from free thermal expansion. Because the temperature gradient in sea ice is generally vertical, thermal stresses in sea ice are usually isotropic in the horizontal plane (Richter-Menge and Elder, 1998), such that $\sigma_{xx} = \sigma_{yy}$ in Equation 6.3. Dynamic stresses are generated by the movement of sea-ice floes. Wind and wave action may act to compress floes to the point of ridging, or pull them apart, inducing fractures (Lewis et al., 1994). Dynamic stresses are highly anisotropic, as they are driven by directional atmosphere and ocean processes.

6.3.2 Studies of stresses in sea ice

Sea ice stress is of concern due to its impacts on sea-ice dynamics, and its role in fracturing and ridging. It is important for sea-ice dynamics modelling as internal stress is a term in the momentum conservation equation (Tucker and Perovich, 1992; Richter-Menge and Elder, 1998). Thermal stress is often the dominant stress component within sea ice (Richter-Menge and Elder, 1998), and has been investigated as a potential source of under ice noise as it may cause fracturing (Lewis et al., 1994).

Tucker and Perovich (1992) measure stress at three distances from the ice edge and at three depths in Arctic pack ice. They record compressive stresses of up to 400 kPa near the sea-ice surface, and tensile stresses with a magnitude up to 30 kPa deep in the sea ice. They find that both thermal and dynamic stresses contribute significantly to the stress state of the sea ice. Lewis et al. (1994) use a similar measurement technique to investigate thermal stresses in land-fast sea ice. They induce cooling at the sea-ice surface by removing snow, generating thermal stress, and skilfully reproduce some of the observed signals using a previously developed thermal stress model (Lewis, 1993). Richter-Menge and Elder (1998) measure stresses ranging from -50 to 300 kPa in multi year sea ice. They attempt to isolate the dynamic stress signal from their thermal stress signal by taking the dynamic stress to be the difference between the two principal stress axis. The rationale for this is that thermal stresses are horizontally isotropic and so affect both principal stress axes equally, and Hutchings et al. (2010) support this approach. However, Hata and Tremblay (2015b) find evidence for anisotropic thermal stresses driven by land-fast confinement of sea ice, so other approaches will be necessary to remove the thermal stress signal in some situations.

In addition to thermal and dynamic stresses, compressive stresses have been described during the process of freezing in stress sensors, presumably due to the volume expansion of water upon freezing. These were up to 300 kPa when using freshwater to freeze in the sensor (Tucker and Perovich, 1992), and 30 kPa when using seawater (Hata and Tremblay, 2015b). While these stresses were reported as

more of a methodological issue than a scientific result, they do provide some first order insight into the likely magnitude of compressive stresses that can be generated from the expansion of water upon freezing. Hata and Tremblay (2015b) find that compressive stresses switch from correlated to anti correlated with air temperature during the sea-ice melt phase, and they attribute this to meltwater re-freezing as it percolates through the sea-ice matrix. These stresses are an example of stress caused by phase changes in the internal sea ice.

6.3.3 Measurements of stresses in sea ice

Stress measurements in sea ice are often made using a measurement technique developed by Cox and Johnson (1983). This measurement technique has been deployed multiple times in the Arctic to investigate the stress state of Arctic sea ice, and was used in all studies described in Section 6.3.2. Stresses are resolved to within 20 kPa, though similar equipment is now commercially available with a 5 kPa resolution (Geokon Model 4350 Biaxial Streemeter (Hata and Tremblay, 2015b)). Three (or six) wires are mounted horizontally in a vertical steel tube. This tube is then frozen into a borehole in sea ice, and changes in the period of vibration of the wires can be related to deformation of the cylinder by stresses in the sea ice. The period of vibration is used to calculate the major and minor principal stress component in the horizontal plane. Stress measurements have also been made in ice using ice force panels (Frederking et al., 1986; Ulrich-Evers et al., 2015). Square panels are deployed vertically into holes cut into sea ice, and measure the force delivered by the sea ice to their face. Caline and Barrault (2008) measure stresses in sea ice using disks, filled with oil, connected to a transducer. The disks were 10.5 cm in diameter and measured stress with 0.1 kPa resolution. Tensile stresses could not be measured with their technique.

6.4 Methodology

6.4.1 Using piezo-resistive sensors to measure stress

The experimental methodology I have used to measure pressure in sea ice is described in detail in Chapter 5. In this section I describe how the output of the piezo-resistive pressure sensors relates to sea-ice stresses, and how the piezo-resistive sensors differ from previous methodologies used to measure stress in sea ice.

Stress is distinct from pressure, because stress is a tensor (acting on a plane, in a direction, and with a magnitude) while pressure is a scalar (having only a magnitude). The pressure sensors used in this work have a flat face, and this face defines the plane on which stress tensor acts. The output of the sensor relates to the position of a diaphragm, which is determined by the pressure on the sensor face. The movement of this diaphragm is perpendicular to the sensor face, so only stress acting perpendicular to the sensor can affect the sensor. As the sensors face the horizontal plane, only σ_{xx} and σ_{yy} in Equation 6.3 can be measured. If the position of the diaphragm is static, the pressure at the sensor face must be equal to the stress acting perpendicular to the sensor face. In the case of an isotropic thermal stress in the horizontal plane,

$$\sigma_{xx} = \sigma_{yy} = P \tag{6.4}$$

where P is the pressure experienced by the sensor. The pressure is at hydrostatic equilibrium when P is also equal to σ_{zz}.

Equation 6.4 is only strictly valid if the sensor is perfectly included in the sea ice, such that all stress acting perpendicular to the sensor face is transferred to the sensor face. The fraction of sea-ice stress transferred to the sensor is known as the 'inclusion factor' (Cox and Johnson, 1983). If the inclusion factor is less than unity, the pressure experienced by the sensor will be less than the true sea-ice stress.

The principle behind sensing stress using piezo-resistive sensors is therefore similar to the principle behind the Cox and Johnson (1983) sensor, where deformation of a cylinder, rather than depression of a diaphragm, is linked to

stress. However, there are several factors to consider when relating the measured pressure to the true sea-ice stress. Cox and Johnson (1983) give a list of important characteristics for a sea-ice stress sensor.

1. The sensor should not be affected by variations in the elastic modulus and non-elastic behaviour of the ice.

2. The sensor should have low temperature sensitivity and not be significantly affected by differential thermal expansion.

3. The sensor should not greatly overload the ice.

4. The sensor should be rugged and leakproof.

5. The sensor should be inexpensive, easily installed and monitored, and have a stable, repeatable response.

The sensor used in this work is much stiffer than sea ice, with the elastic modulus of Al_2O_3, which is the ceramic used to construct the sensor face, being an order of magnitude larger than typical sea ice values, and this satisfies the suggestions of Cox and Johnson (1983) for requirement 1. Temperature sensitivity is corrected for using multiple linear regressions outlined in Chapter 5, which satisfies the first part of requirement 2. The thermal expansion of Al_2O_3 is smaller than that of sea ice, and the sensor may therefore have a tendency to underestimate stress as the sensor will expand less upon warming than the surrounding ice. The pressure sensor bar is light when compared to the sea ice in accordance with requirement 3, and I have experienced no problems with leaking (requirement 4). With regard to requirement 5, the sensor bar was completed for less than £3000 including workshop time, and this figure could be reduced by bulk buying sensors. During my experimental work in the Roland von Glasow air-sea-ice chamber, the pressure sensors have sensibly tracked atmospheric pressure using a single calibration, displaying good stability. The repeatability of the pressure sensor response is excellent in air and water. However, the repeatability of the pressure sensor response in sea ice is not known. Put another way, the inclusion factor of

each sensor may not be constant between experimental runs, or between sensors within individual runs. Unquantified variability in the inclusion factor is a major limitation of the sensors used in this study.

The small size of the piezo-resistive sensors used in this work is their main advantage when compared to Cox and Johnson (1983) style sensors, and to previously deployed ice force panels (Frederking et al., 1986) and transducers (Caline and Barrault, 2008). The size of Cox and Johnson (1983) style stress sensors limits the maximum vertical resolution through sea ice to around 25 cm. For this reason, the Cox and Johnson (1983) technique for measuring stress in sea ice has been used to resolve a maximum of three depths in sea ice (Tucker and Perovich, 1992; Lewis et al., 1994), all of which were deeper than 25 cm. The size of Cox and Johnson (1983) sensors precludes studies of stress in young sea ice in general, or sea ice grown from open water, because the vertical resolution is too coarse and the heavy sensor would overload the sea ice. Previously deployed ice force panels have a 0.5 m $\times$ 0.5 m face, and so offer even lower resolution. The disc face connecting connecting to the transducer head in the measurement system of Caline and Barrault (2008) is 10.5 cm in diameter, smaller than Cox and Johnson (1983) style sensors and typical ice force panels, but an order of magnitude larger than the sensors deployed in this work.

Using small piezo-resistive sensors overcomes these issues. The diameter of the sensor face allows around 1 cm vertical resolution, though I achieve 2 cm in this thesis, and the low weight of the sensors means they can be deployed in open water and young sea ice without overloading the sea-ice slab. The signals observed in the Roland von Glasow air-sea-ice chamber could not have been observed without this fine resolution, or if the sensor was deployed in a consolidated sea-ice cover.

However, the small size of the piezo-resistive sensors is also likely to drive variability in the inclusion factor, which is their main disadvantage when compared to larger sensors. The 1.2 cm diameter of the pressure sensors is too small to consistently average over the various phases in sea ice. The relative proportion of ice, brine and gas may affect the inclusion factor of the sensor, and may do so

randomly. If, for example, a large brine fraction exists at a sensor face, and this brine is free to flow, then a large fraction of the material at the sensor face cannot sustain or transmit a pressure, which may cause measured pressure to be less than the true stress. Ice crystal orientation may also influence the inclusion factor in a random way. The length of an ice crystal perpendicular to the c-axis will generally be greater than the length parallel to the c-axis. The total strain of an ice crystal, for a given temperature change, will therefore be greater in the planes perpendicular to the c-axis. An ice crystal with a c-axis oriented perpendicular to the sensor face is therefore likely to transfer more stress than an ice crystal with a parallel orientation. The crystal orientation in these experiments is random, because there are no currents in the water. Larger sensors average over a larger area of sea ice which will minimise the effect of small scale heterogeneity.

It is also likely that tensile stresses cannot be measured in young sea ice using the current set up. As sea ice contracts it pulls away from the sensor face, and the sensor will likely revert to experiencing a hydrostatic equilibrium pressure, similar to the measurement technique of Caline and Barrault (2008) (Section 6.6.1). Cox and Johnson (1983) sensors are capable of measuring tensile stress, which is a significant advantage.

A disadvantage of the current configuration of piezo-resistive sensors is that it measures in only one direction. As thermal stresses are isotropic in the horizontal plane, except for special circumstances (Hata and Tremblay, 2015b), this is not a key issue for the determination of thermal stresses. However, for field deployment the current configuration must be extended to measure in at least three directions in the horizontal to allow the calculation of major and minor principal stresses. Multiple units, orientated in different directions, of other sensors (Caline and Barrault, 2008; Ulrich-Evers et al., 2015) can be deployed to capture anisotropic stresses using unidirectional sensors. Cox and Johnson (1983) sensors are able to measure in multiple directions, which is an advantage.

6.4.2 Using Lewis (1998) equations to model stress

Constructing the model

The thermal stress model presented by Lewis (1998) predicts depth-resolved thermal stress, as a deviation from hydrostatic equilibrium stress, in a one dimensional column of sea ice. The predicted stress is horizontal ($\sigma_{xx,yy}$), and the horizontal thermal stress is assumed to be isotropic. The model uses a visco-elastic rheology, which means the stress at a given depth and time is influenced by stress at a previous time (elastic), and that excited stresses are driven to reduce in magnitude through viscous creep (viscous). This rheological formulation extends the elastic formulation of Bogorodsky et al. (1972) to account for viscous creep. A similar model was used by Hata and Tremblay (2015a) to model anisotropic thermal stresses by assuming no strain in one horizontal direction.

Based on changes in the temperature and solid fraction at each timestep, the model first calculates three strain rates. A thermal strain rate calculates how much each layer would strain if it were free to expand under its new temperature. A viscous creep strain rate acts to relax deviations from hydrostatic equilibrium stress in each layer. And a mechanical strain rate is added to each layer that simulates the mechanical linking of the layers of sea ice to each other. The sum of these strain rates is then used to calculate a stress rate *via* a parameterisation of the elastic modulus of sea ice. This stress rate is then used to update the stress of each model layer. The rest of this section details the steps and equations used to calculate these terms, and to model thermal stress.

The model updates sea-ice stress by calculating the rate at which stress is changing at each model depth. The stress rate, σ_t (GPa s^{-1}) is related to the strain rate *via* an effective elastic modulus, $E^{'}$ (GPa),

$$\sigma_t = E^{'}(\varepsilon_t - \zeta_t - \gamma) \tag{6.5}$$

where ε_t, ζ_t and γ_t are thermal, mechanical and viscous creep strain rates (s^{-1}), respectively. Lewis (1993) parameterise $E^{'}$ as a fit to the data of Mellor (1986)

using Equation 6.6.

$$E^{'} = \omega log(STR+3) + 3.5GPa\Big((1-7.5472(1-\phi))(1-0.0714T)\Big) \qquad (6.6)$$

where $STR = |\varepsilon_t - \zeta_t - \gamma|$ is the magnitude of the overall strain rate (s^{-1}) at a given time and depth, T is the sea-ice temperature (^{o}C), $1-\phi$ is the porosity, and $\omega = 0.1$ per log(STR). The effective elastic modulus increases with increasing strain rate and solid fraction, and decreasing temperature. The porosity dependant term in Equation 6.6 tends to 0 as $(1-\phi)$ tends to 0.14, giving unphysical values for $E^{'}$ at low solid fractions. An additional condition is put in place that $E^{'}$ must never be less than 0.5 (Lewis, 1993) to prevent negative or very small values of $E^{'}$, which do not make physical sense. Further support for this constraint can be found in Weeks (2010) (and references therein), who note that while the elastic modulus of sea ice is a strong function of porosity (having a low elastic modulus at high porosities), it may become a much weaker function of porosity at when $1-\phi > 0.15$.

The strain rate from free expansion, ε_t, is calculated using Equation 6.7 for each model depth,

$$\varepsilon_t = \kappa \frac{dT}{dt} \qquad (6.7)$$

where $\kappa = 51 \times 10^{-6}\ ^o\mathrm{C}^{-1}$ is the coefficient of linear expansion of ice (Johnson and Metzner, 1990).

As with ε_t, a viscous creep strain rate is calculated for each depth. The viscous creep term relaxes stressed sea ice, back towards an unexcited stress. Three parameterisations of viscous creep are enabled: 1) Richter-Menge et al. (1995) (RMC95), 2) Lewis (1993) (Lew93a), and 3) Lewis (1993) (Lew93b). All of these parameterisations are fits to data collected in laboratory studies by Richter-Menge

et al. (1995). RMC95 is given by Equation 6.8,

$$\gamma = 1.86 \times 10^{-15}(1-T)^{-5.25}\left(\frac{\sigma}{(1-(1-\phi)^{0.5})^2}\right)^n + 3.63 \times 10^{-29}(1-T)^{-2.09}\left(\frac{\sigma}{(1-(1-\phi)^{0.5})^2}\right)^4 \quad (6.8)$$

σ is the stress of a layer (Pa), and $n = 1.36(1-T)^{0.19}$. Viscous creep parameterisations Lew93a and Lew93b are given by Equation 6.9, with the only difference being the set of constants used (Richter-Menge et al., 1995).

$$\gamma = B \times e^{(-Q/RT)} \times \left(\frac{\sigma}{(1-(1-\phi)^{0.5})^2}\right)^n \quad (6.9)$$

In Equation 6.9, Q (J mol^{-1}) and B (s^{-1}) are constants (values in Lewis (1993)), R is the gas constant (J mol^{-1} K^{-1}), T is the ice temperature (K) and σ is the stress (MPa).

The three viscous creep parameterisations behave qualitatively similar, increasing in magnitude with increased temperature or stress, and decreased solid fraction. Lew93a gives higher γ at the highest porosities. This deviation is possibly due to the extension of these parameterisations back to higher porosities than they were derived for, and all parameterisations are broadly similar when the porosity is less than approximately 0.2.

The mechanical strain rate is calculated using Equation 6.10. Each timestep is assigned a single value that is used for every layer. This parameterisation was first put forward by Lewis (1994), and improves on previous parameterisations (Bogorodsky et al., 1972) by including viscous creep. N is the fractional coverage of cracks, and is set to zero (see Section 6.4.2).

$$\zeta_t = \frac{\int_0^H E'(\varepsilon_t - \gamma_t)(1-2N)dz}{\int_0^H E' dz} \quad (6.10)$$

In the formulation of Equation 6.10 it is assumed that the modelled ice slab is sufficiently large that it cannot bend. This assumption constrains the sea ice such

that for any temperature change that is not uniform with depth, some ice depths will experience a thermal stress. Figure 6.1 illustrates the effect of this constraint in two idealised situations. In this case two identical bars are linked at both ends by some rigid material (Noda, 2002). Heating both bars by a different amount will drive one to expand more than the other. If the bars are allowed to bend, both expand freely and neither experiences a thermal stress. However, if we restrict the orientation of the bars, such that they cannot bend, we apply a global constraint that both bars must strain by the same amount. The difference between the final strain and the free strain in each bar is the strain that drives thermal stress to build. Equation 6.11 expresses this mathematically.

$$\varepsilon_i = \kappa \Delta T_i - \frac{\sigma_i}{E_i} \tag{6.11}$$

In Equation 6.11, ε_i is the total strain of bar i. The product of the coefficient of linear expansion, κ, and change in temperature, ΔT_i, is the free thermal expansion of the bar. The thermal stress developed in bar i, σ_i, divided by the elastic modulus gives the effective strain contributing to the thermal stress. By not allowing the bars to bend, we constrain Equation 6.11 such that $\varepsilon_1 = \varepsilon_2$. Assuming that the sum of the stresses of both bars is zero, because no external force is applied, and that the elastic modulus, cross sectional area (A) and coefficient of thermal expansion are the same for both bars, we can write

$$\varepsilon_1 = \varepsilon_2 = \varepsilon_i = \frac{\kappa}{2}(\Delta T_1 - \Delta T_2) \tag{6.12}$$

Substituting Equation 6.12 into Equation 6.11 allows calculation of the thermal stress in each bar

$$\sigma_1 = -\sigma_2 = \frac{\kappa E}{2}(\Delta T_1 - \Delta T_2) \tag{6.13}$$

It is clear from Equation 6.13 that σ_1 and σ_2 are equal and opposite, and that if $\Delta T_1 > \Delta T_2$, then $\sigma_1 > 0 > \sigma_2$, and vise versa.

In the model, sea ice behaves similarly if it is heated by a different amount at the surface than at depth (Figure 6.1). If warmed by more at the surface, and free

to expand naturally, Equation 6.7 dictates that the near surface sea ice would strain positively and more than the deeper sea ice, and the sea ice would curl downwards at its edges. However, Lewis (1998) assume that floes > 300m are sufficiently heavy/buoyant that the edges of the floe cannot be significantly lifted/submerged by thermal processes, which restricts the free thermal expansion and generates thermal stress.

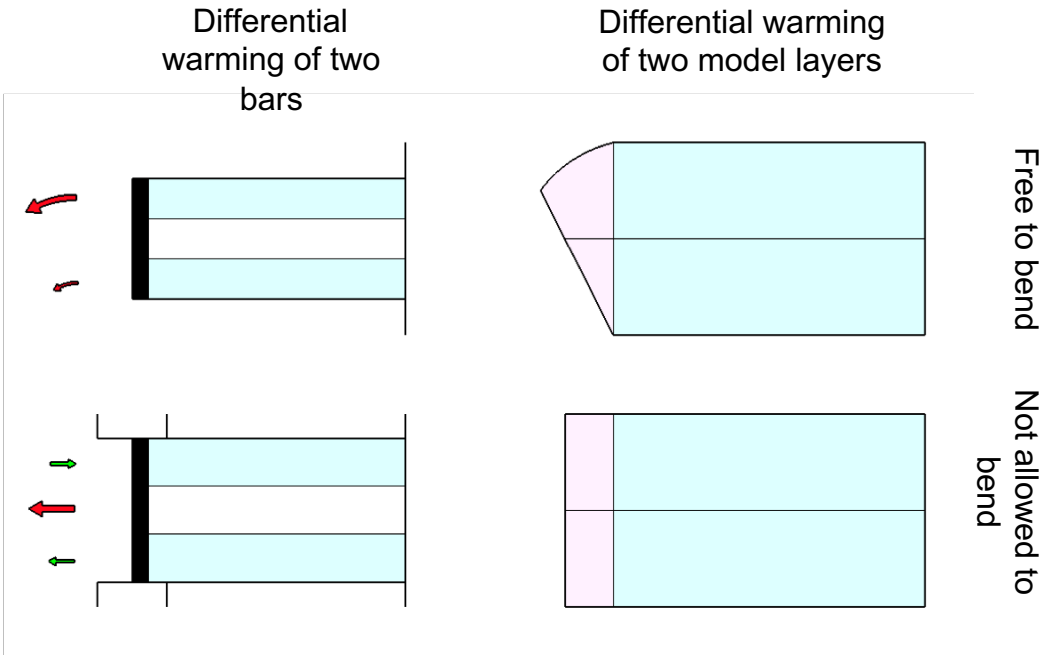

Figure 6.1: The left hand side of this figure shows the idealised behaviour of two expanding bars (Noda, 2002), which is analogous to the right hand side, which shows idealised behaviour for expanding sea ice. **Top left:** Two bars with equivalent rheological properties are linked by a rigid bar (black) that is free. The top bar is heated more than the bottom bar, which results in bending and no thermal stress. **Top right:** Equivalent situation to top left for sea ice if it was free to bend. Two levels in the sea ice (blue) are heated by differing amounts, causing the sea ice to curl at the edge (pink and blue). **Bottom left:** Same as top left, except that now the rigid bar cannot bend. Both bars must now strain by the same amount, so the resulting strain is less than free thermal expansion for the warmer (top) bar, and greater than free thermal expansion for the bottom bar, generating thermal stress. **Bottom right:** Equivalent situation to bottom left for sea ice if it cannot bend due to buoyant/gravitational constraints, as is assumed in the Lewis (1993, 1998) model. For clarity, the right hand side is fully constrained in all panels, but in the model it is assumed both sides are unconstrained. Red arrows indicate total deformation (strain) and green arrows indicate effective strain contributing to thermal stress, equivalent to ε_i and $\frac{\sigma_i}{E}$ in Equation 6.11, respectively. In all panels the upper is heated more than the lower section. The arrows apply to both the left and right hand panels.

Generalising Equation 6.12 to N bars, each with a varying elastic modulus, gives the mechanical strain term in the Bogorodsky et al. (1972) model, and including creep gives the same term for the Lewis (1993, 1998) model (Equation 6.10). To do this I note that $\sum_{i=1}^{N} \varepsilon_i / N = \varepsilon_i = \zeta_t$, and that $\sum_{i=1}^{N} \sigma_i = 0$, based on the assumption that the ice cannot bend and that no external force is applied,

respectively. The rheological formulation of (Lewis, 1993) is given by Equation 6.5, and can be re-written as Equation 6.14. The right hand side of Equation 6.14 gives the effective thermal strain as the strain from free expansion less the total strain at each depth. The left hand side partitions the effective thermal strain between a term containing the thermal stress, and a viscous creep term.

$$\frac{\sigma_i}{E_i} + \gamma_i = \kappa \Delta T_i - \zeta_t \tag{6.14}$$

Rearranging Equation 6.14 to isolate the thermal stress, and summing over all of the ice layers, gives

$$\sum_{i=1}^{N} \sigma_i = 0 = \sum_{i=1}^{N} E_i(\kappa \Delta T_i - \zeta_t - \gamma_i) \tag{6.15}$$

Expanding Equation 6.15 and rearranging gives

$$E_1\zeta_t + ...E_N\zeta_t = (E_1\kappa\Delta T_1 - E_1\gamma_1) + ...(E_N\kappa\Delta T_N - E_N\gamma_N) \tag{6.16}$$

From which the mechanical strain formulation from Lewis (1993) can be retrieved (Equation 6.17).

$$\zeta_t = \frac{\sum_{i=1}^{N} E_i(\kappa \Delta T_i - \gamma_i)}{\sum_{i=1}^{N} E_i} \tag{6.17}$$

With this set of equations thermal stresses can be calculated knowing just temperature and solid fraction. The behaviour of these equations can be understood qualitatively by examining Equation 6.5. As the elastic modulus is always positive, the sign of the change in stress in a given layer will depend on the relative size of the thermal, mechanical, and viscous creep strains. Figure 6.2 shows idealised behaviour of the model for two consecutive, idealised model time steps. In the top three panels the model responds to a sudden temperature increase by producing positive free expansion thermal strains, ε_t, at all depths. The increase is greatest near the surface because the basal temperature of the sea ice is defined by the freezing point of sea water, and temperature profiles in growing sea ice are linear to a good approximation. As the initial stress profile is unexcited there are no viscous creep

strains, and the mechanical strain term, ζ_t, is defined such that the integrated stress profile is zero (Equation 6.17). As ζ_t is subtracted from ε_t (Equation 6.5), the sign of the resulting stress rate is positive (compressive) near the surface and negative (tensile) deeper in the ice. In the next time step (Figure 6.2, bottom panels) there is a smaller temperature increase. Viscous creep, γ, acts to relax the stress at each depth, and the sum of strains leads to a relaxation of the stress profile at all depths. This is a typical response of the Lewis (1998) model to warming events (mode 2).

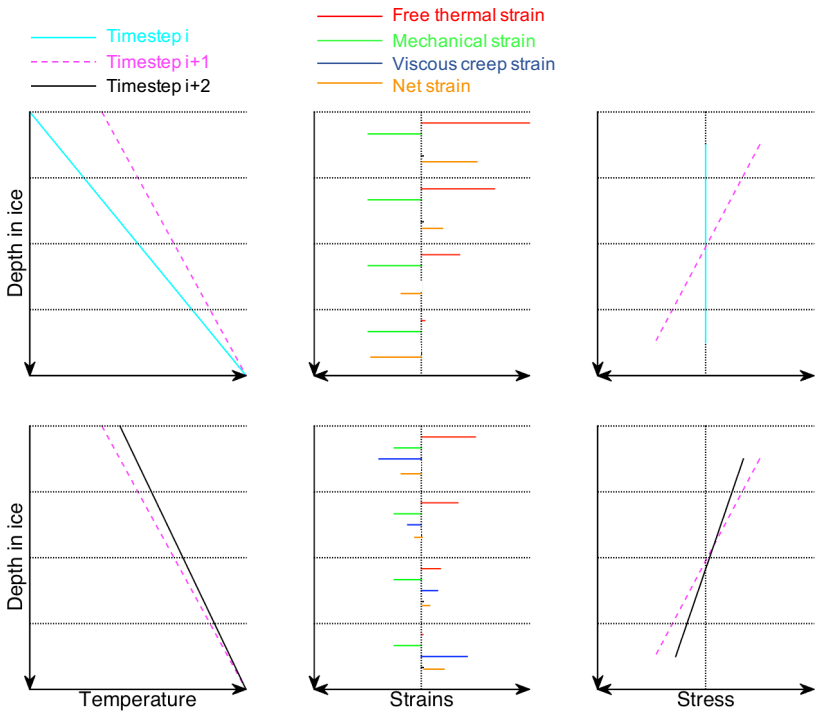

Figure 6.2: Conceptual model response for two consecutive time steps (i progressing to i+2) using a Lewis (1998) style thermal stress model. Horizontal dotted lines show the edges of the model layers, and the vertical dotted lines show the position of 0. The top three panels show the first time step, where a large warming even occurs. The bottom panels show the next time step, where a smaller warming event takes place. The leftmost panels show temperature profiles through the ice, with the blue, solid line showing the initial profile (i-1), purple dashed line showing the next step (i), and the black, solid line the i+1 step. The middle panels show the strains acting on each layer, with red, green, blue and orange representing thermal, mechanical, viscous creep and net strains, respectively. For clarity the signs of the mechanical and viscous creep strains are flipped. The rightmost panels show the stress profile at the midpoint of each layer, and are colour coded to match the temperature profile time steps. The idealised behaviour depicted is described in the text (Section 6.5.2).

Modifications to the model

One constraint I have added is a solid fraction cut off at which all strains, and hence changes in stress, are set to zero. Previous studies modelling stresses in sea ice (Lewis et al., 1994; Lewis, 1998) have all taken place on thicker sea ice, which generally had a higher solid fraction than I measure in this study, so these authors have not needed to consider at what liquid fraction their equations are no longer applicable. There must be some cut off, as very porous sea ice will have largely horizontally unconnected ice crystals that will be free to expand and curl into a well connected brine network. The skeletal layer of sea ice is defined as the bottom layer of sea ice, where the solid fraction is between 0 and 0.3 (Weeks, 2010), and is often thought of as a boundary layer between sea ice and liquid ocean. I have observed stresses persisting in sea ice with a solid fraction as low as 0.75. A reasonable solid fraction cut off should therefore be > 0.3 and < 0.75.

To investigate the impact of the imposed solid fraction cut off on the output from the thermal stress model I performed a sensitivity study. I ran the thermal stress model for run 5.4, using solid fraction cut offs ranging from 0 to 0.9 in increments of 0.1. I chose run 5.4 because there is a signal that is likely related to thermal stresses, and a simple temperature regime. Figure 6.3 shows results from this study at three model depths. Solid fraction cut offs smaller than 0.3 led to model instabilities and have not been plotted. Data from run 5.4 will be discussed in depth in Section 6.5.1, and here are used solely to investigate the effect of the solid fraction cut off. A cut off of 0.9 largely eradicates any stress signal, and 0.8 and 0.7 fail to follow the stresses predicted consistently by the model across the lower cut offs at all depths. For this reason I exclude solid fraction cut offs higher than 0.6 from consideration. All cut offs 0.6 or lower behave similarly in magnitude and timing, though there is some discrepancy between 0.6 and lower cut offs at 6 cm depth. Lower cut offs seem to generate larger stresses, but the difference between magnitudes of 0.3-0.5 is small across all depths. In this chapter the thermal stress model is run using a solid fraction cut off of 0.5. This is consistent with Jutras et al. (2016), who find sea ice consolidates at $\phi \approx 0.5$ in a laboratory study.

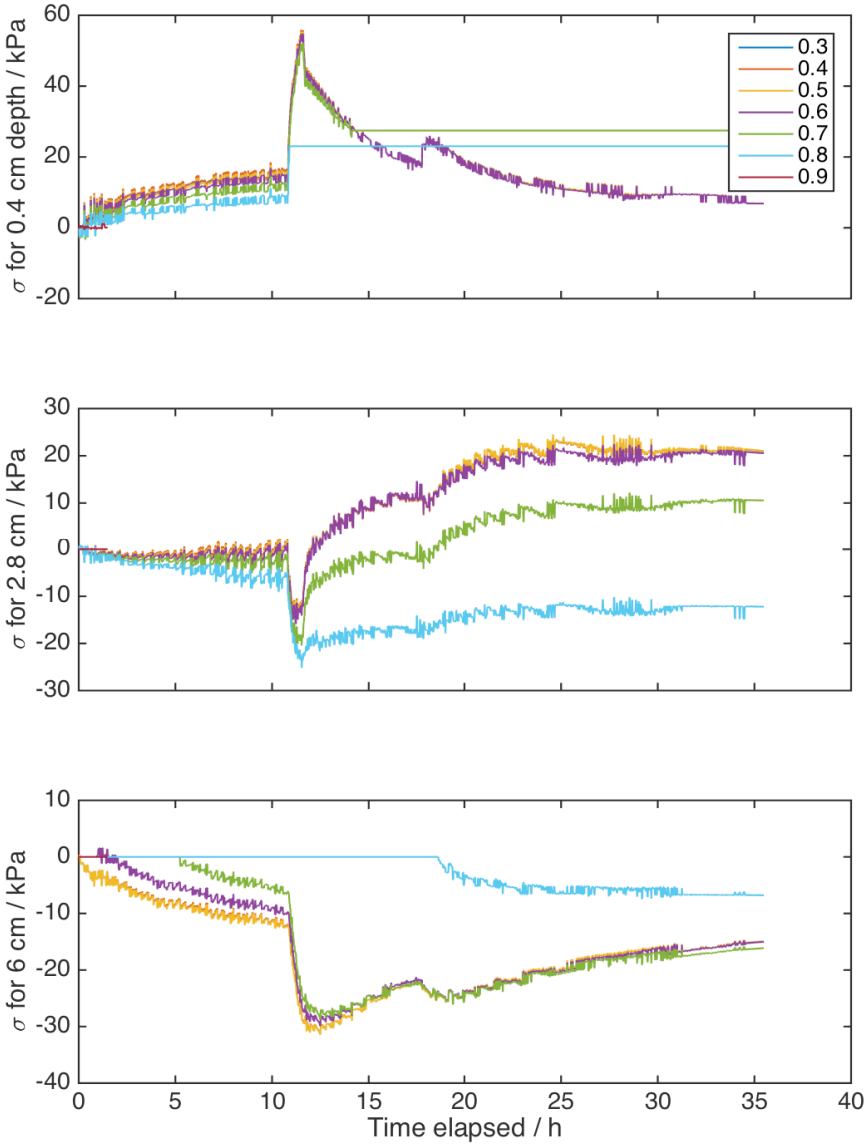

Figure 6.3: Sensitivity study into the effect of the solid fraction cut off on output from the thermal stress model. The model is run over wireharp data from run 5.4. Stress is displayed as a function of time as predicted by the thermal stress model at three model depths (top: 0.4 cm, middle: 2.8 cm, bottom: 6.0 cm) and for solid fractions ranging from 0.3 to 0.9 (legend). Where lines appear missing, their solid fraction has dropped below the cutoff. For a solid fraction cut off of 0.9, for example, stress is only plotted for the first hour, and only in the near surface sea ice.

Lewis (1998), based on the work of Lewis (1995), attempt to include the effect of cracks in their model. They did so by including a fractional crack coverage, N, in Equation 6.10 that is used as a tuning parameter. The gaps near the tank walls

(runs 6.2, 6.3) could be interpreted as cracks, as could brine channels within the sea ice, or interfaces at instrumentation, and it is not clear which interpretation, if any, is best. Given that in this study I use the model to investigate whether thermal stresses drive the measured pressures, and do not attempt to develop the model as a predictive tool, I see no value in tuning the model to a given crack coverage. In addition, no crack coverage could reconcile the variability in measured pressure, because the crack coverage would have to be similar for runs 6.2 and 6.3, where very different pressure magnitudes were observed.

Forcing the model

I have replaced the thermo/halo-dynamic component of the Lewis (1998) model with temperature and solid fraction data from the wireharps and thermistors for each experimental run. Temperature and solid fraction are sufficient to solve the equations presented in Section 6.4.2. Temperature and solid fraction are linearly interpolated onto a model grid with higher vertical resolution ($\approx$ 3 mm) than the measurements ($\approx$ 2 cm), and to a one minute timestep. These interpolated data are used to force the model. The model grid is evenly spaced vertically (50 layers) and in time (1 minute). In contrast to Chapter 4 the model grid is vertically static, so the depth of each layer does not change. The ice thickness at a given time step is defined as the depth of the deepest layer with a non-zero solid fraction. Prescribing the forcing minimises the error from the modelling of these parameters, and integrates the effect of all heat and salt fluxes. Discrepancies between modelled stress and measured pressure are therefore due to:

1. Deficiencies in the formulation of the rheological component in Lewis (1998).
2. Inconsistency between the tank setting and the model assumptions.
3. Errors in the measured pressure.
4. Error in the measurement of T and ϕ.

One disadvantage of using measured temperature profiles as forcing is that the modelled stress contains high frequency noise related to the resolution of the

thermistors. Nothing precludes coupling the rheological model with a thermo/halo-dynamic component, where the temperature and solid fraction are modelled, in future studies.

6.5 Results

The model predicts deviations in stress from hydrostatic equilibrium stress, rather than an absolute stress. To compare the model output to the measurements I subtract the atmospheric pressure from the measured pressure. This is valid because I compare the model to pressure measurements in the top few centimetres of sea ice, so the contribution of overlying sea ice to the measured pressure is negligible[1]. Also, subtracting the atmospheric pressure rather than calculating hydrostatic equilibrium pressure does not affect trends in pressure, only absolute values. Where possible, I took atmospheric pressure from the weather station, but in runs 5.4 and 6.2, the weather station was not deployed. In these runs I used atmospheric pressure as measured by a piezo-resistive sensor just above the ice-atmosphere interface. This causes small errors because the thermistors used to measure temperature near the pressure sensor bar responded quicker to temperature changes than the pressure sensor bar itself. Early on in runs, when the atmospheric temperature had recently decreased, the measured pressure bar temperature was underestimated, and this resulted in calculation of some negative near surface sea ice pressures, which are artefacts. Important features of the various runs are given in Table 6.1. A large and persistent discrepancy between measured pressure and modelled stress in all runs is that tensile stresses are always modelled, but sub hydrostatic equilibrium pressures are never measured. However, it is likely that the piezo-resistive sensors are not capable of measuring sub hydrostatic equilibrium pressures (Section 6.6.1), so I cannot compare the model to the measurements for regions of predicted tensile stress. To avoid repetition, in the following section I take disagreement between measured pressure and modelled stress to occur only when

[1] Assume the top 2 cm of sea ice have a density of around 930 kg m^{-3}. The hydrostatic equilibrium pressure will be 0.02 (m) $\times$930 (kg m^{-3}) $\times$ 9.8 (ms^{-2}) $\approx$ 0.2 kPa

Table 6.1: Key points from the runs presented in Chapter 5. The first column identifies the run. 'State of sides' indicates that the sea ice was freely floating, fixed to the tank walls, or fixed in places but with partial melting. 'Observed modes' indicates which of modes 1 and 2 were observed during a given run. 'Weather station' indicates if the weather station was present. If a run was modelled, 'Modelled?' gives the relevant figure number, or provides an explanation for why this run was not modelled. 'VC used' indicates which viscous creep parameterisation was used in the modelling. 'Magnitude of mode 1' gives the magnitude of the measured and, if applicable, modelled mode 1 events. 'Magnitude of mode 2' gives the magnitude of measured and, if applicable, modelled mode 2 events. Note that the units of the magnitude of mode 2 events are different from those in Chapter 5. Because I am now comparing measured pressure to modelled stress spikes, it is more appropriate to use the absolute size of the spike than their rate of change with temperature. The range of model values reflects the range of modelled stresses across the area of the sensor face.

Run	State of sides	Observed modes	Weather station	Modelled?	VC used	Magnitude of mode 1 / kPa Measured, *modelled*	Magnitude of mode 2 / kPa Measured, *modelled*
5.2	Fixed	1 & 2	No	No wireharp data	-	13, -	17, -
5.4	Fixed	2	No	Figure 6.7	Lew93a	-, -*	33 then 8**, *25 to 47, then 5 to 10*
6.2	Partially melted	1 & 2	No	Figure 6.6	Lew93a	2, *-3 to 40*	2, *30 to 70*
6.3	Partially melted	1 & 2	Yes	No wireharp data	-	25, -	5 then 13***, -
7.3	Free	2	Yes	Figure 6.8	Lew93a	-, $-^{+}$	1, *20 to 90*
8.3	Fixed	1 & 2	Yes	Figure 6.4	Lew93b	22, *10 to 25*	10, *100 to 110*

*Up to 35 kPa when simulation run from earlier point in time
**Mode 2 events on 0 and 7 elapsed hours, respectively
***Refers to the two mode 2 events discussed in Chapter 5

compressive stresses are predicted and pressures are not elevated above hydrostatic equilibrium.

There is significant variability in modelled stress over scales on the order of the diameter of an individual sensor face. In this study I chose to compare each measured pressure to three modelled stresses that lie near the top, middle and bottom of the sensor face. When the data are presented in this way, a meaningful indicator of good model performance is that the modelled stresses bound the measured pressure. However, given the potential for inclusion factors to be less than 1 (Section 6.4.1), and for inclusion factors to vary between runs, another useful indicator of model performance is that the modelled trends in stress at the depth of the sensor face bound the trend in the measured pressure of that sensor.

6.5.1 Model performance during cooling (mode 1)

If stresses are driving the measured pressures during mode 1 events, mode 1 can be defined as: A build up and subsequent relaxation of pressure/stress in near surface sea ice, that occurs during the initial stages of sea-ice growth and cooling. The timing, both in terms of the beginning of the build up in stress, and the beginning of the plateau and decline in stress, predicted by the model generally captures the pressure measurements well. The shape of modelled mode 1 events is also generally in good agreement with measured pressure during mode 1 events. Quantitive agreement between measured and modelled mode 1 events is achieved for one run, 8.3 (Figure 6.4), but the model significantly overestimates the magnitude of the mode 1 event for run 6.2 (Figure 6.6). In this section I present model results for these two experiments, and describe the mechanism that generates mode 1 events in the model.

The Lewis (1998) model accurately predicts the timing and magnitude of the mode 1 event observed in run 8.3 (Figure 6.4). Both the measured pressure and modelled stress begin to build after around 40 hours and 4 cm of sea-ice thickness, before levelling off sometime after 100 hours at around 20 kPa. The timing of the initial increase is not strongly affected by the start time of the simulation. When

Lew93b is used the modelled stress bounds the measured near surface pressure between 100 and 120 hours, displaying good agreement. When Lew93a or RMC95 are used the modelled stress between 100 and 120 hours is around 5 kPa lower than the measured pressure. Elevated pressures are not measured, and compressive stresses are not predicted, outside of the top two centimetres of sea ice, so the model is also consistent with the measurements away from the surface.[2]

The build up in near surface modelled stress is caused by deeper sea ice cooling more than the surface over a given period of time. Temperature profiles in growing sea ice are approximately linear, and the temperature at the base of the sea ice is constant to within around 0.2 ^{o}C because it is set by the freezing point of the underlying water (Notz and Worster, 2009; Weeks, 2010). Assuming a linear temperature profile is maintained, and the bottom temperature does not change, two competing effects determine the gradient of the temperature profile through sea ice. First, cooling the sea ice surface without significantly thickening the sea ice will cause the surface to cool more rapidly than deeper sea ice. Second, thickening the sea ice while holding a constant surface temperature will cause the deeper sea ice to cool more rapidly than the surface. In reality, neither effect is observed in complete isolation from the other, but in my experiments the effect of thickening the sea ice slightly outweighs the cooling of the surface, and is more dominant early in the runs. Greater cooling rates at depth can be observed in temperature profiles measured by Notz and Worster (2008) in young, Arctic sea ice, and is likely particular to young sea ice where the growth rate is high. In my experiments, and possibly in young sea ice in general, the surface temperature of sea ice is lower than the temperature nearer the base because that surface sea ice was formed earlier, and has been cooling for longer. The surface sea ice is colder, but is cooling more slowly than that deeper sea ice.

The effect of greater cooling at depth in the model is illustrated in Figure 6.5. The sea ice is driven to contract everywhere (Equation 6.7), and is driven

[2]Between 80 and 100 hours there is a gap in the measured pressure due to technical issues. There was no such gap in the forcing, so I continue to run the model through this period. A mode 2 event occurs at the end of the data gap, which causes an increase in modelled stress and measured pressure.

to contract most in deeper layers. The mechanical strain term (Equation 6.17) must be positive to ensure the resulting stress profile sums to zero, and this term drives reduced tensile stresses at depth and compressive stresses near the surface. The production of compressive near surface stresses *via* this mechanism is not specific to my formulation of the model, but mode 1 events were not noted by Lewis (1993, 1998) because young sea ice was not studied. For example, Lewis et al. (1994) induced sea-ice cooling by removing snow from the surface, but because their sea ice was thick the cooling of the surface outweighed the thickening of the sea ice, and tensile, rather than compressive, stresses were generated near the surface.

In general, the levelling off of modelled stress occurs when the action of viscous creep balances the action of the thermal and mechanical strains, and there are two effects that drive the stress build up during sea ice growth to plateau. First, the strength of the viscous creep increases with the magnitude of the stress deviations, and second, the level of differential cooling between the surface and deep sea ice decreases as the sea ice growth slows towards the end of the run. For run 8.3, viscous creep would eventually dominate and reduce the near surface stress, but this could not be observed in the model because the experimental run was ended early due to time constraints.

The model does not perform as well for run 6.2 (Figure 6.6) compared to run 8.3. The timing of the pressure build up is within the spread of the timing of the build up in the modelled stress, and in this way the model is consistent with the measurements. Also, the shape of the modelled stress near the middle of the sensor agrees well with the measured pressure. However, the measured pressure and modelled stress near the surface differ by an order of magnitude. A small pressure build up may be observed in the deeper sea ice (not shown), though this has potential to be a temperature artefact, and this build up is not consistent with the model which does not predict elevated stresses outside of the top 2 cm of sea ice. The build up of stress in the model is, like in run 8.3, driven by greater cooling rates at depth. Stepped temperature changes drive the mode 2 events near the end of the run, and these are discussed in Section 6.5.2.

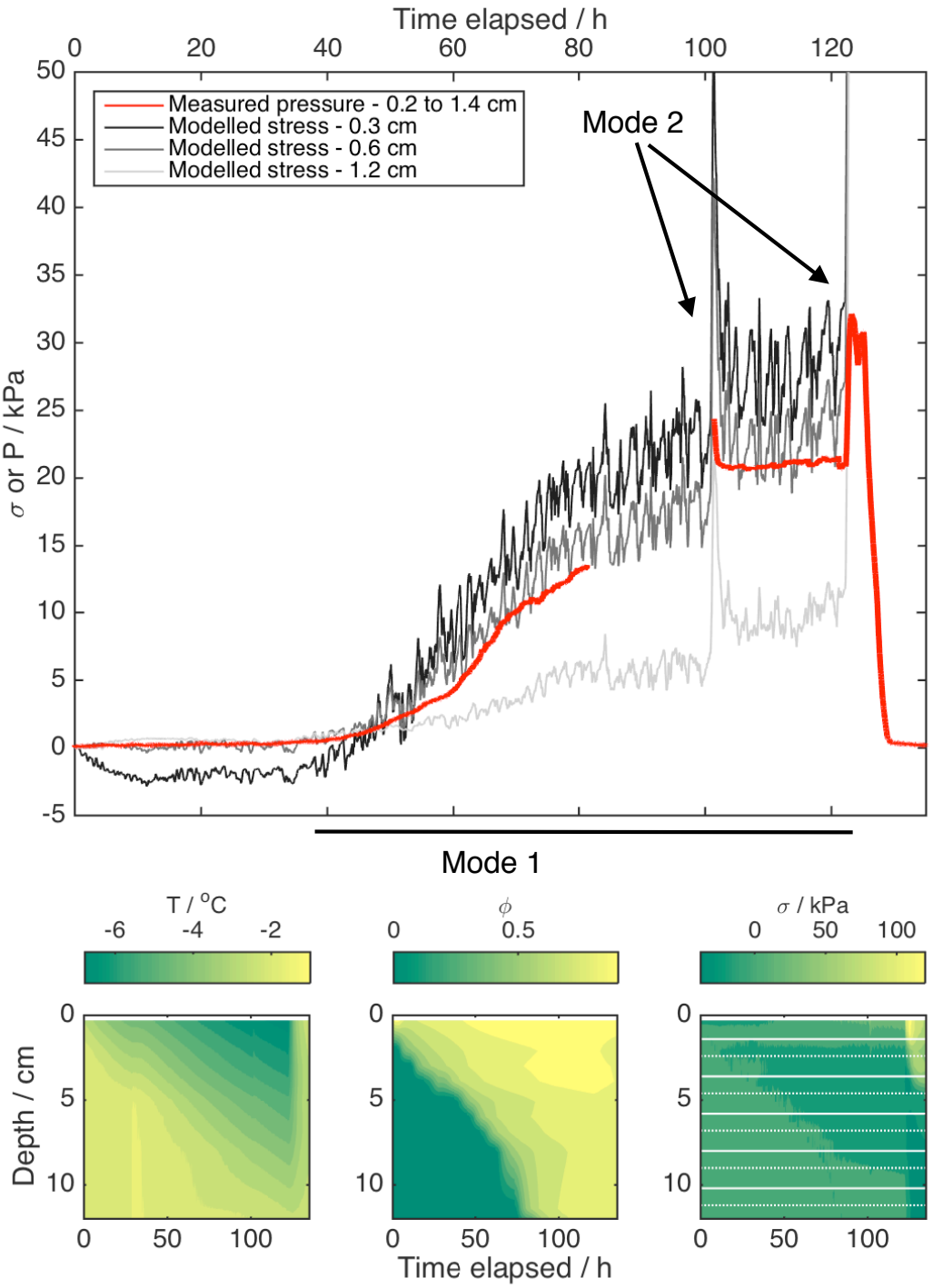

Figure 6.4: Measurements and model output from run 8.3, where modes 1 and 2 occurred. The mode 2 event at at around 100 hours is difficult to interpret due to a data gap cause by a logging failure. **Top:** Measured pressure (red) and modelled stress (grey) in near surface sea ice. **Bottom, left:** Temperature used to force the model. **Bottom, middle** Solid fraction used to force the model. **Bottom, right:** Modelled stress. The dashed and solid white lines denote the top and bottom of a piezo-resistive sensor, respectively.

In Chapter 5 I am unable to discern a pattern in the experimental conditions that can explain the variability between mode 1 events in runs 5.2, 6.2, 6.3 and 8.3.

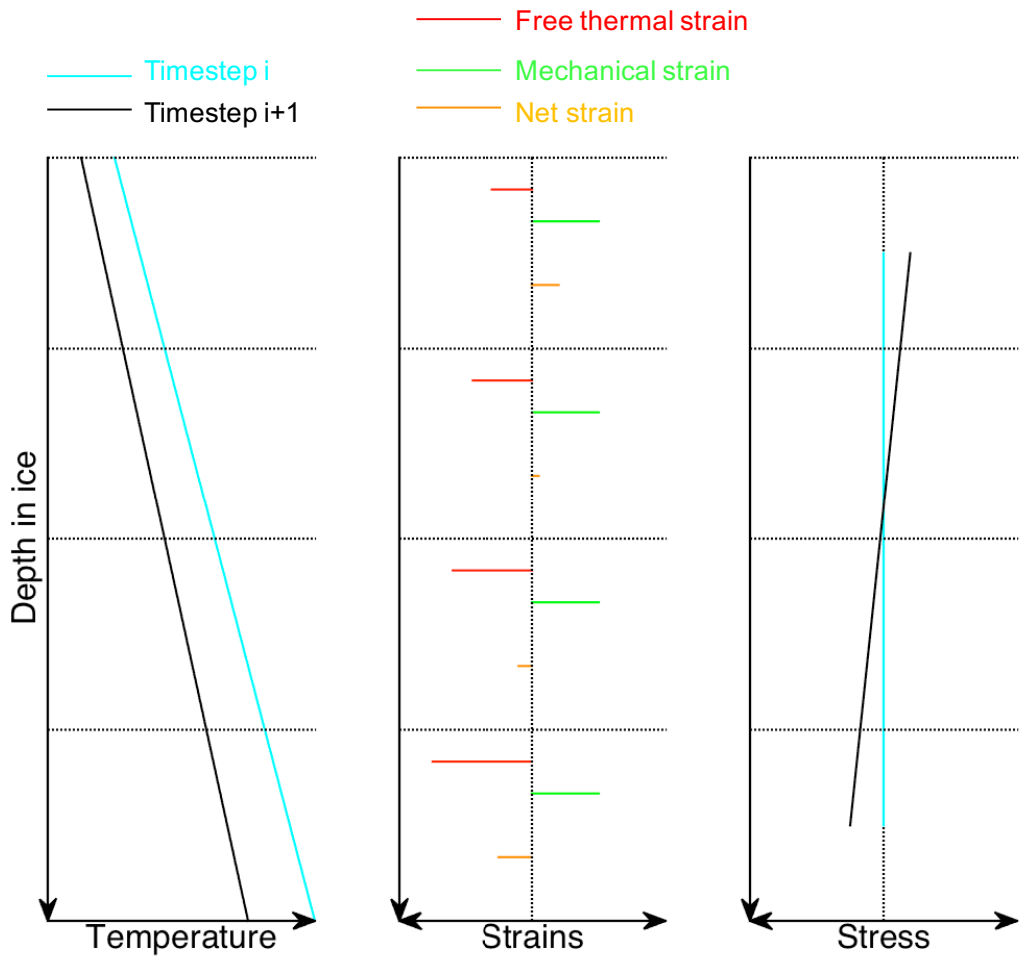

Figure 6.5: Conceptual model response for a mode 1 event. The model moves from some early timestep (blue) to a later timestep (black). As the model progresses, the sea ice cools everywhere, but cools more at depth (left panel). Negative free thermal expansion strains are induced at all depths, but are most negative in the deeper sea ice. To integrate the final stress profile to 0, the mechanical strain term acts to make strains more positive everywhere (middle panel). The result is compressive stresses near the surface, and tensile stresses at depth (right panel).

If thermal stresses are driving the pressure build ups, the model results presented in this section show that variability in the rate of change of temperature and solid fraction, which are the only inputs to the model, are not sufficient to explain the variability in the measurements. Either some important process is missing from the model, some model assumptions are violated, or there is significant randomness in the measurement or generation of pressure in these experiments.

In summary, modelled stress captures the timing and shape of measured pressure during mode 1 events. The model is quantitatively accurate for run 8.3 (Figure 6.4) but overestimates the measurements by an order of magnitude for run

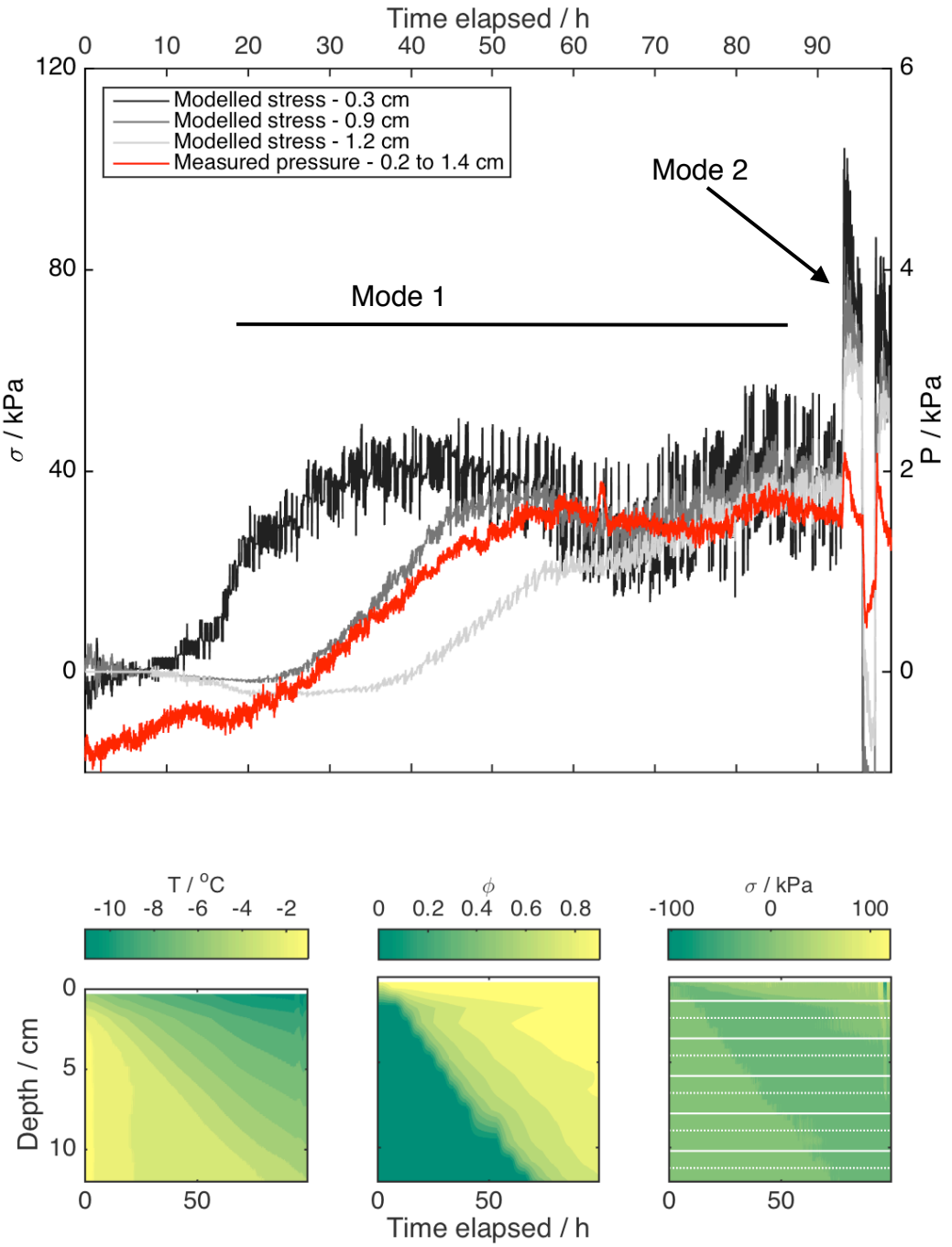

Figure 6.6: Measurements and model output from run 6.2, where a modes 1 and 2 occured. Mode 2 events occurred during the period of stepped temperature changes at the end of the run. **Top:** Measured pressure (red) and modelled stress (grey) in near surface sea ice. **Bottom, left:** Temperature used to force the model. **Bottom, middle** Solid fraction used to force the model. **Bottom, right:** Modelled stress. The dashed and solid white lines denote the top and bottom of a piezo-resistive sensor, respectively.

6.2 (Figure 6.6). Modelled mode 1 events are driven by a greater degree of cooling in deeper sea ice during growth.

6.5.2 Model performance during warming (mode 2)

If thermal stresses are driving the measured pressures during mode 2 events, mode 2 can be defined as: A build up and subsequent relaxation of pressure/stress in near surface sea ice, that occurs during sea ice warming events. The modelled stress consistently captures timing and duration of the near surface sea ice pressure spikes caused by increases in temperature. The model also captures the timing of the relaxation. The localisation of pressure in the near surface sea ice is also reproduced by the model. In one run, 5.4 (Figure 6.7), there is quantitative agreement between the measured pressure and modelled stress, but in all other runs the modelled stress overestimates the magnitude of the measured pressure spikes. In this section I describe the model performance for mode 2 events during four experiments (5.4 (Figure 6.7), 7.3 (Figure 6.8), 8.3 (Figure 6.4), and 6.2 (Figure 6.6)), and describe the mechanism that generates these events in the model.

The model captures the shape and magnitude of the mode 2 event in run 5.4 (Figure 6.7). Two warming events caused spikes in the measured pressure and modelled stress. After each spike the pressure/stress decreases, and levels off to an elevated pressure/stress rather than relaxing back completely. The magnitude of the initial pressure spike (33 kPa) is bounded by the modelled stresses. The shape of the subsequent relaxation of pressure is reasonable for any viscous creep parameterisation, though none produce sufficiently large strains to bound the measured pressure. Lew93a performs best as it gives higher values than the other schemes at high porosities. Measured pressure deviates from atmospheric trends only in the surface sea ice. The model predicts stresses of around 10 kPa in the region of the second sensor from the surface, but these are not observed. However, the model does capture the localisation of compressive stresses near the surface to within around 0.5 cm, which is similar to the vertical resolution of the model.

As with mode 1, thermal stresses are generated for mode 2 events by the differential heating of the near surface and deeper sea ice. However, with mode 2 events the surface warms more than the deeper sea ice (see Figure 6.2, which shows an idealised mode 2 event). The effect of warming on the sea ice temperature

gradient far outweighs any reduction in thickness, so the near surface warms more than the deeper sea ice. Sea ice in my experiments often becomes isothermal before a significant change in thickness is observed. The result of high surface warming is to generate compressive stresses near the surface and tensile stresses at depth.

The largest stresses predicted by the model are centred at 2 cm depth, in the gap between the top two sensors. A band of relatively high solid fraction in this region reduces the magnitude of the viscous creep, and increases the elastic modulus, causing higher stresses to build relative to the near surface even though the surface temperature change is greatest.

In run 7.3 the model is only able to capture the shape of the mode 2 events, but the change in stress for a given temperature rise is an order of magnitude larger than the measured pressure change (Figure 6.8). An initial warming event causes an increase in the near surface measured pressure and modelled stress. The pressure and stress then relax over around six hours, before a temperature drop causes a decrease in pressure and stress. Finally, stepped temperature changes cause stepped pressure and stress changes, and the run finishes at an elevated stress, but a pressure that is at hydrostatic equilibrium. The model is largely consistent with the measurements deeper in the sea ice, where negligible pressure deviations are measured, and only small ($\sim$ 1 kPa) stresses are predicted.

Mode 2 events were also measured and modelled for runs 8.3 (Figure 6.4) and 6.2 (Figure 6.6). Towards the end of run 6.2, several pressure spikes on the order of 1 kPa are superimposed onto a mode 1 event. While the two pressure increases are mode 2 events, the pressure decrease is not formally a mode 2 event. I justify the exclusion of pressure decreases from the mode 2 definition in Chapter 5. The model captures the shape and timing of the pressure spikes, but overestimates the magnitude[3]. As mentioned in Chapter 5, the mode 2 event towards the end of run 8.3 may be underestimated by the pressure measurements because the near surface sensor partially decouples from the sea ice. The modelled stress captures the shape and timing of the pressure reasonably well (off axis scale), but is much larger than

[3]I will not discuss the first mode 2 event in run 8.3, after around 100 hours, because it occurs partially during a data gap.

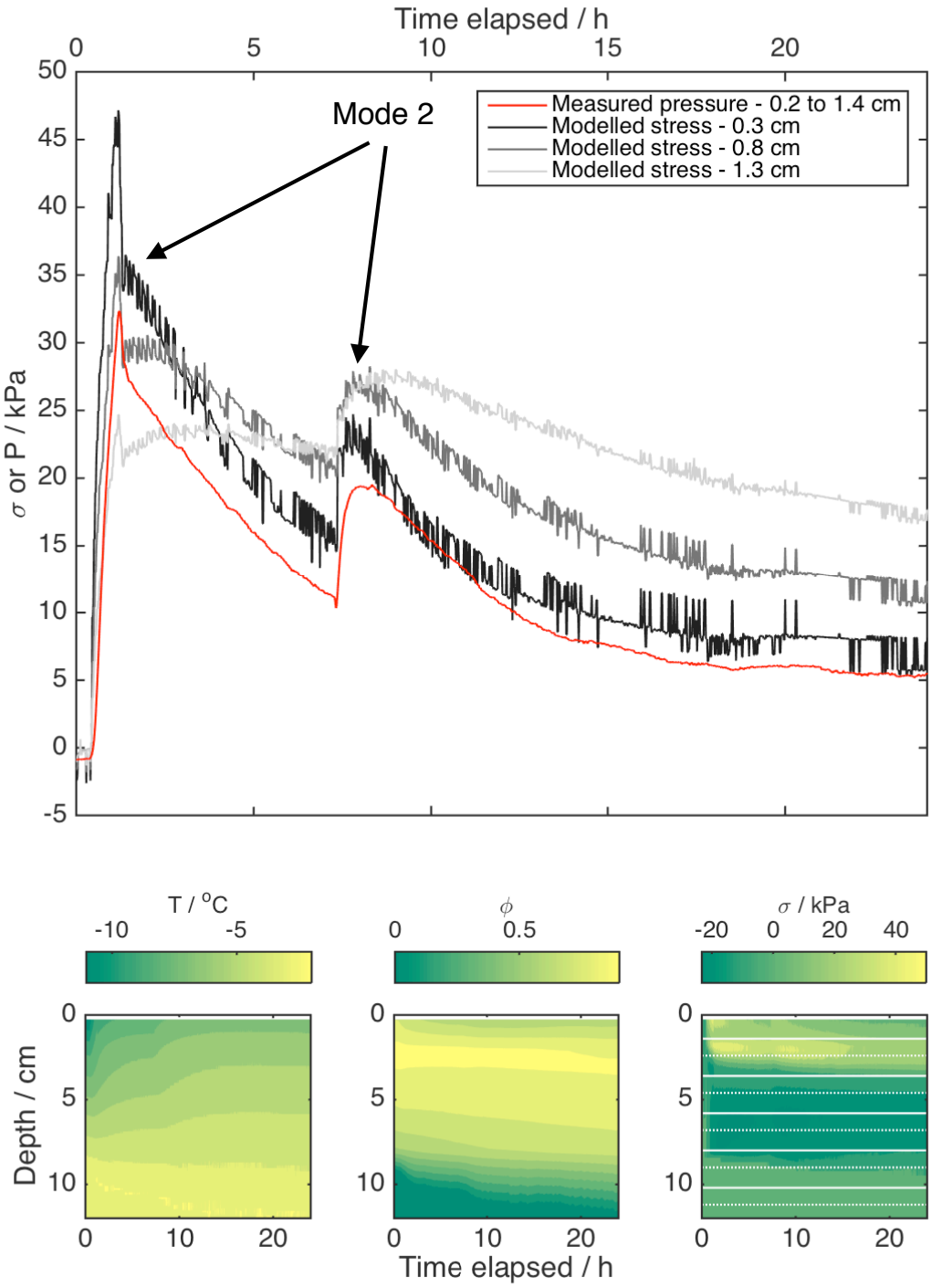

Figure 6.7: Measurements and model output from run 5.4, where two mode 2 events occurred. **Top:** Measured pressure (red) and modelled stress (grey) in near surface sea ice. **Bottom, left:** Temperature used to force the model. **Bottom, middle** Solid fraction used to force the model. **Bottom, right:** Modelled stress. The dashed and solid white lines denote the top and bottom of a piezo-resistive sensor, respectively.

the measured pressure for this event.

The timing and shape of mode 2 events is always similar for stress and pressure,

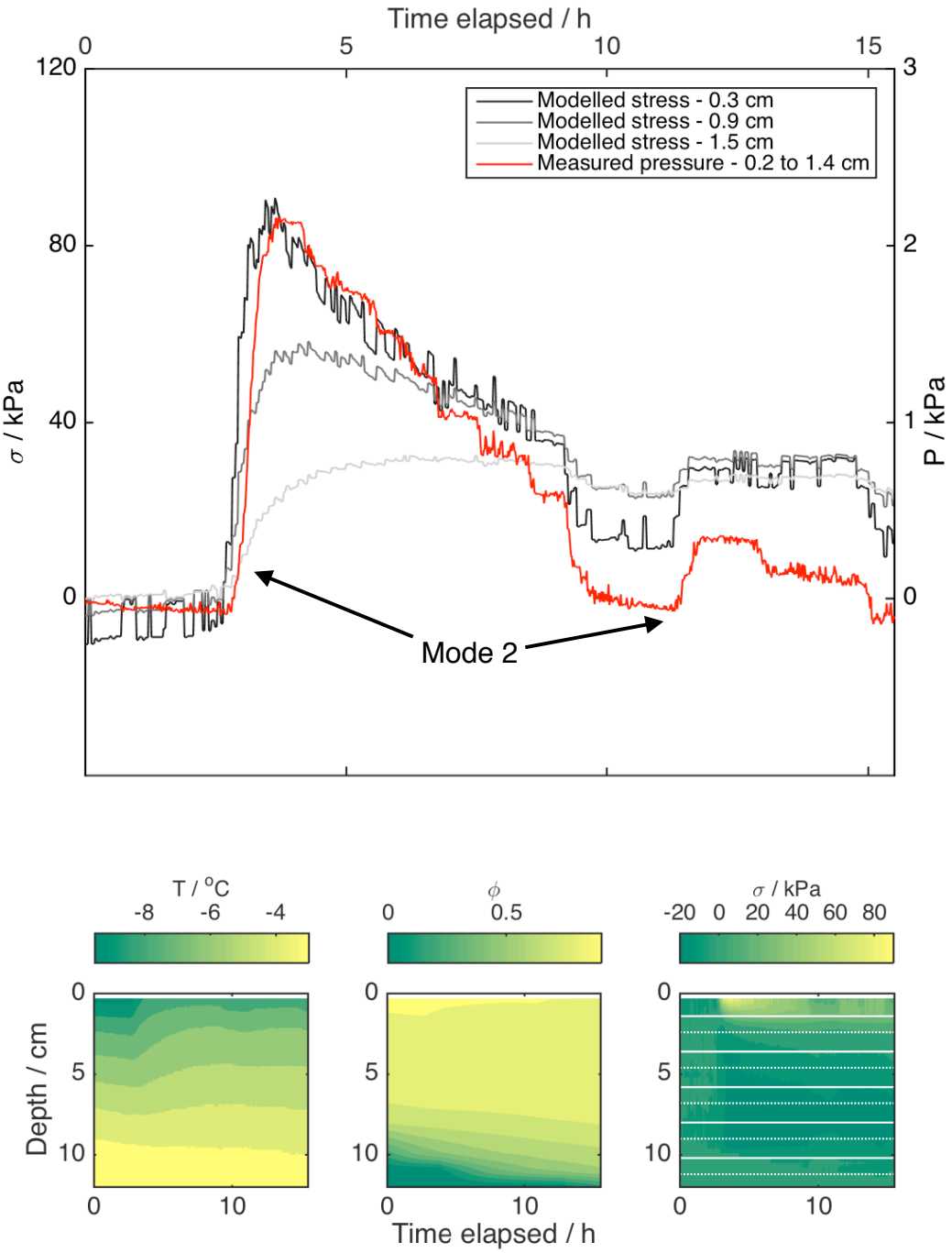

Figure 6.8: Measurements and model output from run 7.3, where several mode 2 events occurred. This run had free floating sea ice. **Top:** Measured pressure (red) and modelled stress (grey) in near surface sea ice. **Bottom, left:** Temperature used to force the model. **Bottom, middle:** Solid fraction used to force the model. **Bottom, right:** Modelled stress. The dashed and solid white lines denote the top and bottom of a piezo-resistive sensor, respectively.

but the model often overestimates the magnitude of the events. In this chapter I define the magnitude of the maximum pressure/stress build up for a given event[4].

[4]I choose this definition, rather than the rate of change of pressure/stress with temperature,

For run 5.4 (Figure 6.7) the magnitudes are similar, but for the other runs (6.2, 7.3, 8.3) the stress build up for mode 2 events is around ten times larger than the pressure build up for a given temperature change. The model appears to do a qualitatively good job for mode 2 events, but is not able to consistently reproduce the magnitude of measured pressure signals (Table 6.1).

6.6 Discussion

6.6.1 Sources of disagreement between measured pressure and modelled thermal stress

There are several areas of disagreement between the model and the measurements. The goal of this section is to identify important sources of disagreement and discuss their implications so that I can use the model performance in Section 6.6.2 to investigate whether the pressure signals presented in Chapter 5 are driven by thermal stresses. First, I discuss how the confined tank environment may affect the various parameters in the model, and the assumptions used to derive them. Next, I discuss the variability in the measured pressure and conclude that the magnitude of the stress signals cannot be expected to capture the variability in the measured pressure. I then justify my assertion that pressures below hydrostatic equilibrium cannot be measured by the piezo-resistive sensors. Finally, I discuss the absence of mode 1 signals from run 5.4, and show that this calls into question whether mode 1 events are driven solely by thermal stresses.

The overarching goal of this chapter is to investigate to what extent the pressures measured in Chapter 5 are driven by thermal stresses. While I do not assume that measured pressure is driven by thermal stress, for the sake of brevity I have written this section using wording that implies measured pressure is driven by thermally induced stresses.

---

because in this chapter I am comparing measured to modelled events, rather than different events.

Applying the model to a tank environment

A careful consideration of the applicability of the Lewis (1998) model to a tank environment is required, first because of the confined tank walls, and second because the model is being applied to young sea ice for the first time. Three strain rates and the elastic modulus are used to calculate the change in stress at a given depth in the sea ice (Equation 6.5), and I will consider how valid the formulation of each of these terms is.

The elastic modulus is a function of the temperature and solid fraction of the sea ice, and the strain rate. The parameterisation for the elastic modulus (Equation 6.6) was derived for colder, less porous sea ice (Lewis, 1993), and may not represent the true elastic modulus well for some warm and highly porous layers. However, Lewis (1998) find that the model is relatively insensitive to the formulation of the elastic modulus, and there is evidence that the elastic modulus is only weakly a function of solid fraction at very high porosities (Weeks, 2010), so the representation within the model is reasonable.

The free thermal strain term, ε_t, is a function of temperature, time and the linear thermal expansion coefficient of sea ice (Equation 6.7). None of these are significantly affected by the artificial tank environment.

The mechanical strain term requires the most serious consideration. It relies on the assumptions that 1) the sea ice cannot bend, and 2) there are no external forces acting on the sea ice (Figure 6.1). Assumption 1) is likely to be partially violated when the sea-ice slab is free floating, because the ice slab is so small that the buoyant/gravitational forces at its edges may not be sufficient to completely prevent flexing. While no lower limit is given in Lewis (1998) for the size of a floe that cannot bend, the free floating floes grown in the Roland von Glasow air-sea-ice chamber are an order of magnitude smaller in area, and much thinner, than floes studied in the field. Violation of assumption 1) would allow the sea ice to expand/contract freely, or more freely, and reduce the generated thermal stress (Figure 6.1). Assumption 2) is violated, or partially violated, when the sea ice is fixed to the tank sides. In this case, an external force is applied to the sea ice by

the tank walls, such that $\sum_{i=1}^{N} \sigma_i \neq 0$. However, the force exerted by the tank walls cannot completely prevent the sea ice from expanding in the horizontal because of the porous sea-ice microstructure. If 2) was completely violated, then not only could the ice not expand freely at the tank walls, but it could not expand into the porous microstructure either. If the brine within the sea ice is free to flow, I see no mechanism by which the side confinement can stop ice expanding into internal brine pockets, so assumption 2 cannot be completely violated.

Finally, the parameterisations for viscous creep (Equation 6.8 and 6.9) are functions of temperature, solid fraction and stress. The parameterisations were developed in laboratory experiments, albeit at lower porosities than are often found in young sea ice. They are the best available, and were derived at temperatures and porosities that are representative of the majority of the experimental conditions in Chapter 5. They do rely, however, on the sea ice being free to creep. A similar argument applies to γ as to ζ_t if the sea ice is fixed to the tank walls. The ice in contact with the glass cannot creep, but the internal ice can creep into brine pockets in permeable sea ice.

The parameterisations used for E, ε_t and γ were derived from experiments. They are not used as tuning parameters, and their magnitude and functional form should be reasonable, both in young sea ice and within the tank environment. The greatest caveat to applying the Lewis (1998) model to results from the Roland von Glasow air-sea-ice chamber is the method used to prevent the ice from bending (assumption 1) without applying an external force (assumption 2). Whether the ice is free or fixed, some compromise is made such that 1) and/or 2) are partially violated, and I take this into consideration when discussing the model performance in the rest of this section.

Variability in measured pressure

The pressure sensors have an accuracy of around 1 kPa (Section 5.3.1). However, due to high variability in measured pressure between experiments under similar conditions, I am less confident that the sea ice transmits pressure to the sensor face

in a repeatable way. For example, much larger pressures were measured during run 6.3 compared to 6.2, even though the experimental conditions were similar. Variables like the state of the sea ice at the tank edges, which could be interpreted as cracks in the context of the model, are therefore not sufficient to explain variability in observed pressures. It is likely that there is some randomness in the local sensor environment.

Some of this randomness could be caused by randomness in the inclusion factor of the sensor. The inclusion factor of the pressure sensor is not known, and may not be constant between experiments. The orientation of ice crystals at the sensor face, and the relative proportion of ice, brine and gas, are two factors that could randomly affect the pressure experienced by the pressure sensor. There is also potential for the inclusion factor for a given sensor to change during an experiment. A dramatic example of this occurs at the end of run 8.3, where the near surface sensor decouples from the sea ice. However, when mode 1 or 2 signals are observed during a run the solid fraction is generally greater than 0.8. Subsequent changes in the absolute amount of brine and gas are then relatively small. Also, crystal orientation should be preserved. Before significant melting occurs the inclusion factor should therefore be relatively constant during a run. Whatever the inclusion factor, measured pressure is unlikely to overestimate the true stress.

The high variability in measured pressure is one reason I cannot evaluate the model quantitatively against these data. Comparing the modelled stress to the absolute magnitude of the measured pressure gives an indication of the skill of the model for reproducing measured pressure signals. However, as the relationship between the true pressure and the measured pressure is not well known, it is reasonable to compare the model to the presence/absence, shape, and timing of pressure signals also.

Another factor that could cause disagreement between the modelled stress and the measured pressure is the co-location of model layers with pressure sensor depths. Modelled stress is highly variable over 1 cm scales, and this has two consequences for the co-location of model data with pressure data. First, the

pressure measured by the sensor will be some combination of the stresses on the sensor face. In the model there will generally be four simulated stresses within each depth bounded by the pressure sensor. I am unable to judge whether the measured pressure is affected equally by stresses at all points across its face, by some points more than others (for example, favouring those closest to the sensor centre), or if the measured pressure corresponds to the largest/smallest stress. The approach I have taken in this study is to plot pressure against stresses at depths that span the sensor face, and assume that the model is skilfully predicting the pressure if the stresses bound the measured pressure, considering magnitude and trends. A more robust assesment of the response of the pressure sensor could help to interpret the model results.

The second consequence of the large vertical variability in modelled stress is that millimetre errors in the position of the pressure sensor could cause the modelled stresses across the sensor face to change in timing and magnitude. For example, if in run 5.4 (Figure 6.7) the pressure sensor bar sat 3 mm deeper, the model would likely overestimate the measurements near the surface but better capture the absence of pressure measured by the next sensor down. The depth of a sensor below the waterline before all experimental runs was known to within 1 mm, but subsequent sea-ice growth and freeboard changes mean the position of each sensor is known to around 3 mm during each run, which is similar to the spacing between model layers. The uncertainty in the modelled stress when compared to the measured pressure is therefore at least as large as the variability between adjacent model layers.

Absence of tensile stresses in measurements

The model consistently predicts tensile stresses at depth, but pressure measurements never dip significantly below hydrostatic equilibrium pressure. When sub hydrostatic equilibrium pressures are measured they are small, and I attribute them to artefacts caused by temperature or calibration effects (Section 6.5). Also, during the calibration of the sensors, pressures were measured that were slightly lower than the hydrostatic equilibrium pressures in many experiments, so the sensors are not

reaching some limited minimum. I hypothesise that the pressure sensors used in this work cannot measure tensile stress, and that this is the source of disagreement between measurements and model.

To see why this might be the case I consider how sea ice interacts with the sensor face. To change the pressure measured by a sensor the sea ice must change the position of the sensor face. For compressive stresses the sea ice must depress the sensor face, and for tensile stresses the sea ice must extrude the sensor face. However, the sea ice is not mechanically linked to the sensor face, and this may result in an asymmetry in the capability of the sensor. I have measured pressures in highly porous sea ice, where the brine and gas are free to move (run 5.4, Section 6.5.1). It is reasonable to assume that the brine and gas remain at a hydrostatic equilibrium pressure in this situation, and that the pressure on the sensor face comes from the ice as it pushes the sensor face. However, there is no mechanism by which ice can pull the sensor, as it is not attached to the face. Instead, to generate pressures below hydrostatic equilibrium, the local environment at the sensor face must be at a lower than hydrostatic equilibrium pressure, which implies than no brine or gas can flow into the area to relieve the pressure. Put another way, the local sensor environment would have to exist at a vacuum relative to the atmosphere and ocean. In porous sea ice this is not possible. The sea ice in this study is always relatively porous and rarely falls below the approximate 5% permeability threshold. Also, tensile stresses are generally predicted in the deeper sea ice where the permeability is highest. I do not claim that tensile stresses are generated or not, just that they cannot be measured, and as such the absence of sub hydrostatic equilibrium pressures does not conflict with the model.

As noted in Chapter 5, while overall tensile stresses cannot be observed, reductions in compressive stress can be. For example, towards the end of run 6.2 (Figure 6.6 and Chapter 5) the pressure is elevated over hydrostatic equilibrium pressure because of a mode 1 event, and I take this elevated pressure to be a working baseline. Temperature drops can cause pressure to dip below this baseline, but not below the hydrostatic equilibrium pressure. This observation can be interpreted in

the context of thermal stresses. The sea ice is depressing the sensor diaphragm, causing measured pressure to be above hydrostatic equilibrium. Sudden decreases in the temperature cause the sea ice to contract, lowering the measured pressure. However, if the temperature drop causes the sea ice to contract away from the sensor face, the sensor reverts to measuring the hydrostatic equilibrium pressure.

Erroneous prediction of mode 1 events

Mode 1 events are predicted by the model for runs 5.4 (Figure 6.9) and 7.3 (not shown) if they are run from an earlier point in time (*i.e.* not just before the mode 2 signal), but are not observed in the measured pressure. For both runs, the mode 1 events are driven by greater cooling at depth, as described in Section 6.5.1. I focus on run 5.4 in this discussion, because run 7.3 was free floating and the potential for the sea ice to flex could preclude a mode 1 event in this instance. Figure 6.9 shows model output for run 5.4 if it is run for a day longer than Figure 6.7. Pressure builds to around 30 kPa before plateauing, and the subsequent mode 2 events are superimposed onto the mode 1 build up. Why does no mode 1 event occur in the pressure measurements, or why is an erroneous mode 1 event predicted by the model? The local sensor environment must be able to transmit stresses to the sensors because mode 2 events are observed, and this rules out poor inclusion of the sensor as an explanation. Either the measurements have failed to capture a mode 1 event, or some process is absent or poorly represented in the model.

The model could be deficient in two ways. First, the prediction of mode 1 events by the model could be spurious in general, or for the tank environment. In this case some process other than thermal stress drives mode 1 events in these experiments. If thermal stress driven mode 1 events never occur in nature the model should be modified somehow to preclude the generation of near surface compressive stress, or the model should not be applied to situations where sea ice cools more at depth. If the tank environment precludes the generation of thermal stress driven mode 1 events, then the model may be suitable for some natural conditions, but not for use in tank experiments. Second, the prediction of mode 1 events may be

reasonable for the given model assumptions, but some of these model assumptions are met only by experimental conditions where mode 1 events are observed. In this case, the relevant experimental condition should be identified and controlled in future studies.

Mode 1 events arise from the core rheology of the model, which can be broken down into four steps. 1) The lower model layers cool more than the surface layers; 2) the free thermal contraction of the lower layers is larger than the upper layers; 3) the layers must contract by the same amount because each is joined to the layer above and the sea ice cannot bend; 4) each layer contracts by an amount that is intermediate between the free thermal contraction of the upper and lower layers, so the upper layers are compressed.

Is the prediction of mode 1 events an error in the model in all situations? For this to be so, one of the four steps above must be violated. Step 1) is uncontroversial as it is a measured parameter. I have checked for biases arising from anomalous cooling of the near surface thermistor by linearising the temperature profile at each time step, and mode 1 events are still predicted (Figure 6.9). Step 2) corresponds to Equation 6.7, and it is a reasonable assumption that the thermal contraction of ice is constant over the relatively small temperature range in these experiments. Step 3) is likely not correct when sea ice is very porous. In the skeletal layer, for example, ice crystals dangle freely in the ocean, and may be able to flex in response to contraction. I have addressed this by setting a lower limit for the solid fraction that can sustain and transmit stress (Section 6.4.2). In essence, the solid fraction cut off removes some portion of the bottom of the model sea ice. However, even for high solid fraction cut offs mode 1 events are observed because the solid fraction in growing sea ice rapidly rises, reaching 0.8 or more in deeper sea ice while it is still cooling more than the surface (Figure 6.3). In nature, young sea ice may be able to bend if it is very thin, or exists in small floes, and this would violate 3). My data set is not sufficient to judge whether 3) is always violated in nature. To violate step 4) some external force would need to be applied to the sea ice (Section 6.4.2), and there are situations in nature where this is not the case. I therefore cannot conclude

that thermal stress induced mode 1 events do not occur in general.

Are there model assumptions that are violated in the tank that could preclude mode 1 events? If there are such violated assumptions, are they consistent between runs or can they explain variability between runs? If the growing sea ice pulls away from the tank sides as it contracts then the assumption that the sea ice cannot bend may be violated, because the now free slab is relatively small. However, if the sea ice did pull away from the tank sides, it would cause the sea ice to be free floating, and this was not observed during experiments other than run 7.3. When sea ice was attached to the tank sides the assumption that no external force is applied to the sea ice is violated because the tank sides would pull the sea ice edges. As discussed in Section 6.6.1, the sea ice would still be able to contract freely into the porous microstructure, but the effect of fixed sides would be to add tensile stresses to each sea ice depth, reducing the magnitude of mode 1 events. There is no consistent pattern between the violation of either assumption and the observation of mode 1 pressure events, but violation of either could act across all experiments to reduce thermal stress induced mode 1 stresses.

Could a mode 1 event have occurred and not been measured? There is large variability between measured pressures, but the generation of mode 2 events during run 5.4 suggests that the sea ice at the sensor face could sustain and transmit pressures. One difference between run 5.4 and other runs where a mode 1 event has occurred is that the atmospheric temperature was lower in 5.4. Over several runs in the Roland von Glasow air-sea-ice chamber I have observed that sea ice grown from atmospheric temperatures below -25^{o}C has a more irregular surface, and the sea ice surrounding the pressure sensor was uneven. Another difference between run 5.4 and other mode 1 runs was that the pressure sensor faces the bulk of the instrumentation in run 5.4, but faces the tank walls in other runs. It could be that breaks in the sea ice around the instrumentation disrupted the mode 1 event in the region around the face of the pressure sensor bar. The presence of instrumentation in the path of the sensor is a consistent difference between run 5.4 and other runs where mode 1 was observed, but it is not clear why the presence of instrumentation

in the sea ice at the sensor face would preclude mode 1 events, while allowing mode 2 events.

In summary, the rheology in the Lewis (1998) model predicts mode 1 events during run 5.4 that are not measured by the pressure sensors. This observation must be explained for me to conclude that mode 1 events are driven by thermal stress, because the local sensor environment was able to transmit pressure to the sensor. I cannot conclusively link the absence of a mode 1 event from run 5.4 to a deficiency in the model, a limitation of the model when applied to the tank, or to some experimental condition that prevented pressure from being measured. However, I have speculated on several potential causes. The presence of instrumentation in the immediate face of the sensor preventing the transfer of, or dissipating, pressure build up is a promising explanation, as this only occurs in run 5.4. It is also plausible that thermal stress driven mode 1 events do not occur or are reduced in magnitude in the tank, and that the measured mode 1 pressures are driven in part by the expansion of water upon freezing.

6.6.2 Thermal stress contribution to measured pressure

Is mode 2 driven by thermal stress?

Even without consideration of the thermal stress model, there are strong indications that thermal stress drives mode 2 events. First, pressures are generated and sustained in sea ice where fluid is free to flow, suggesting some portion of the pressure is delivered by the ice, and consequently that the ice must be stressed. Second, after a temperature increase causes a pressure increase, a temperature decrease can cause a pressure decrease. This reversible behaviour is consistent with a thermal stress. Third, the shape and magnitude of mode 2 events is consistent with thermal stresses generated by warming events observed in the field (Richter-Menge and Elder, 1998).

Comparison of measured pressure to modelled thermal stress provides further evidence that thermal stresses are driving mode 2 events. The model captures the

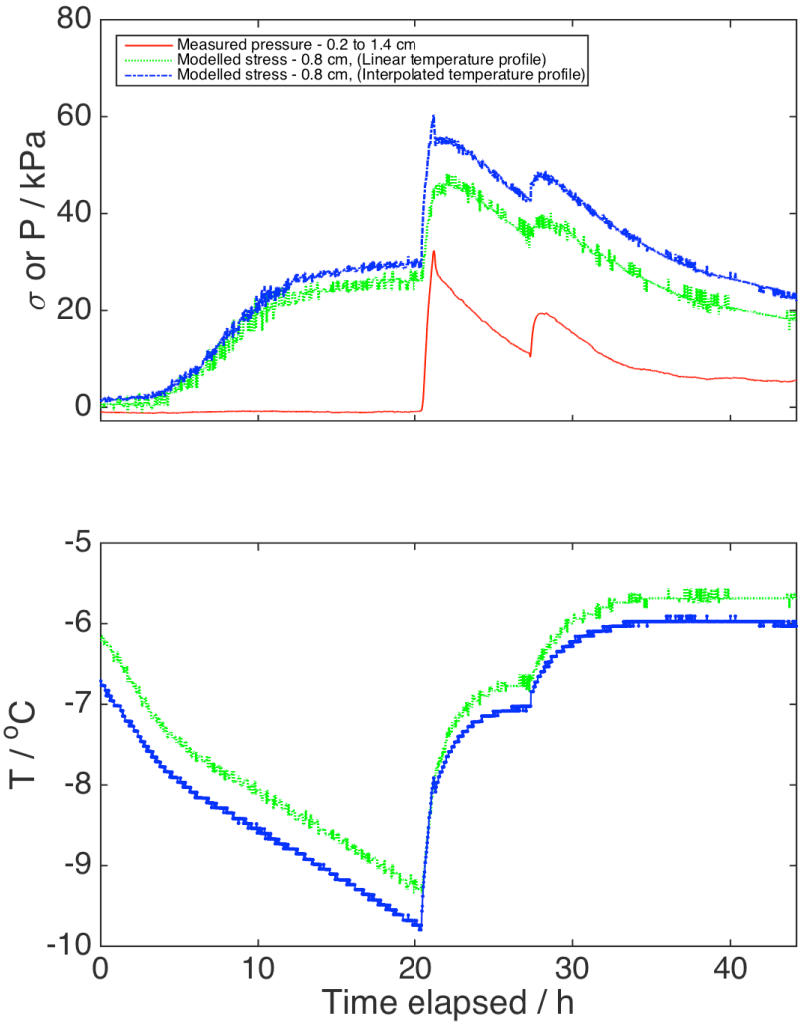

Figure 6.9: Measurements and model output from run 5.4, where two mode 2 events occurred. In this model run I have started the simulation at an earlier timestep than for Figure 6.7. **Top:** The red line shows pressure measured by a piezo-resistive sensor. The blue and green line show modelled stress for a run with uncorrected temperature as forcing, and for a run with a linearised temperature profile, respectively. **Bottom:** Uncorrected temperature forcing (blue) and linearised temperature forcing (green). To linearise the temperature profile, I first performed a linear regression of the sea ice temperature as a function of depth for each timestep. I then calculated mode forcing for each depth using this model, rather than interpolating between the measured temperatures.

timing, shape and localisation near the surface for each run. In addition, even if the confined sea ice edges critically violate the assumption that no external force is

applied to the sea ice, the model output will still be qualitatively accurate. The most extreme violation of this assumption results in the total strain for each depth in the sea ice being 0, and the consequence of this is simply to increase the compressive stress of each layer by the same amount, so the timing and shape of near surface compressive stresses would be preserved. Several lines of evidence suggest thermal stresses drive mode 2 events.

Given that mode 2 events are driven by thermal stresses, a more general definition of mode 2 is a rapid near surface pressure/stress change that is positively correlated with temperature. I have not included the relaxation term in this definition because I can differentiate the thermally induced stress from the viscous creep relaxation using the rheological formulation of Lewis (1998). An additional question that arises from this work is: does the rheological formulation of Lewis (1998) skilfully predict thermal stress in young sea ice? Qualitatively the model does have skill, but further studies in natural sea ice, with a better quantified inclusion factor, are needed to evaluate the model. Regardless, I can conclude with confidence that mode 2 is driven by thermal stress.

Is mode 1 driven by thermal stress?

When compared to mode 2 events, there are fewer indications that mode 1 events are caused by thermal stress, and there is a plausible alternative explanation in the expansion of water upon freezing. However, as with mode 2 events, mode 1 events occur in sea ice that is permeable enough that fluid is likely free to flow. The ice fraction of sea ice must therefore deliver some of the pressure to the sensors, and this suggests that the ice is stressed. Also, while mode 1 events are not as obviously linked to temperature as mode 2 events, both modes occur during a period of differential cooling between the surface and deeper sea ice.

The timing and shape of the modelled stresses capture the measured mode 1 pressures. The model also captures the localisation of mode 1 signals near the surface sea ice. However, in run 6.3 elevated pressures are observed in deeper sea ice (Chapter 5). While I cannot model run 6.3, there is no indication from any of the

model runs I have performed that suggest compressive stresses would be generated over the depths where elevated pressures were measured. This is evidence that some process other than thermal stress at least contributes to mode 1 events. The model also predicts signals that are not measured in run 5.4, even though the sensor is well included in the sea ice (Section 6.6.1). This may be due to violation of model assumptions in the tank, where, in contrast to mode 2, external forces on the sea ice counteract the compressive near surface stresses (Section 6.6.1).

I therefore conclude that measured mode 1 events are not driven entirely by thermal stresses in this study. There is likely to be some contribution to the measured pressures by the expansion of water upon freezing. This effect could be localised near the sensor face, or could create stresses that are transferred throughout the sea ice. I do not believe that the prediction of mode 1 events by the model is spurious in general, but either or both of the restriction of the contraction of sea ice by fixed sides, or the small floes grown, could preclude mode 1 events.

6.6.3 Viscous creep drives stress relaxation

Even if the pressure build up in mode 1 events is not driven by thermal stress, viscous creep is the likely driver of the relaxation. There are indications that mode 1 events are contained, in part at least, in the solid fraction of sea ice. This suggests that the ice is stressed, and viscous creep is the likely process driving stress relaxation in ice (Richter-Menge et al., 1995). Viscous creep also drives the relaxation in mode 2 events, which are driven by thermal stress. Furthermore, within the range of the available parameterisations, the representation of viscous creep within the model can skilfully predict the strength of viscous creep relaxation when the magnitude of the measured pressure is similar to the modelled stress. Not only does viscous creep drive the observed relaxation, but the current parameterisations are useful tools for predicting the relaxation of stress/pressure in young sea ice.

In Chapter 5 I show that an impermeable cap on the sea ice surface prevents relaxation of excited pressure. This fits with viscous creep as a mechanism for relaxation. If, by adding the cap, I isolated brine present near the pressure sensor,

such that brine was not free to flow, then the surrounding ice would not be able to deform into the porous microstructure of the sea ice, or at the tank sides. The relaxation by viscous creep deformation would not take place. This observation highlights the importance of the sea ice microstructure to sea ice stress.

6.7 Conclusions

6.7.1 Wider relevance of results

In my experiments, pressure deviations from hydrostatic equilibrium are only observed in sea ice grown in quiescent conditions. Sea ice in the environment grows most often under turbulent conditions, which may limit the frequency of mode 1 and 2 events. However, mode 2 events have been observed in a pack (Richter-Menge and Elder, 1998; Tucker and Perovich, 1992), landfast (Lewis et al., 1994; Hata and Tremblay, 2015b), first year (Lewis et al., 1994; Hutchings et al., 2010), and multiyear sea ice (Lewis, 1994), and it is very unlikely that initial growth conditions were calm for the sea ice in all of these studies. Turbulence during initial formation may therefore preclude pressure/stress signals only in young sea ice where the solid fraction is relatively low. Mode 2 events must occur frequently over a large geographical area.

The occurrences of mode 1 events may be more limited. To the extent that they are driven by thermal stress, rapid sea-ice growth is necessary to generate mode 1 events, so they can only occur in young sea ice. Another growth condition that may be necessary if mode 1 events are driven by thermal stress is constrained sea-ice edges. With unconstrained edges the thin sea ice that sustains mode 1 events is likely able to flex, which would greatly reduce the generated thermal stress. If thermal stresses drive mode 1 events then mode 1 events are likely confined to calm leads and laboratory sea ice. If the expansion of water upon freezing drives mode 1 events then they may be more widespread because all sea ice solidifies.

In their weakest form, the results and conclusions from this study are only applicable to tank experiments and specific environmental conditions. In this case

I can speculate that Kotovitch et al. (2016) would likely have had mode 1 events in their experimental sea ice, and that pressure effects could contribute to their observed gas fluxes. I have shown that thermal stresses drive mode 2 events in the Roland von Glasow air-sea-ice chamber, and that thermal stresses may play a role in mode 1 events.

In their strongest form, the results and conclusions from this study are applicable to nilas in general, and probably to more mature sea ice regardless of growth conditions. In this case, I have demonstrated that observed mode 2 events are caused by thermal stress, and that the Lewis (1998) thermal stress model has predictive skill for the timing and shape of warming events in young sea ice. This is a significant extension of the model. The model also shows predictive skill for mode 1 events. Though I cannot attribute mode 1 events solely to thermal stress in the tank environment, I predict that they will occur when the model assumptions are satisfied, and sea ice is growing rapidly. This may occur when large floes of young sea ice form in quiescent water.

The true relevance of these results lies somewhere between these two extremes. Better characterisation of the piezo-resistive pressure sensor response and variability, and deployment of the sensors alongside Cox and Johnson (1983) style sensors in the field are needed to place this work in a wider context, and to robustly evaluate the model. However, I can say with confidence that thermal stress drives mode 2 events in these experiments, and that thermal stress may partially drive mode 1 events.

6.7.2 Insights into sea-ice stress

Research into sea-ice stress often focusses on dynamic stresses, either neglecting thermal stress or attempting to subtract the thermal stress from measured signals (Richter-Menge and Elder, 1998). However, thermal stress is often the single largest contribution to the internal stress of sea ice (Hata and Tremblay, 2015b).

Furthermore, the response of sea ice to dynamic stresses will depend on the existing stress state of the sea ice, which is dependant on the thermal stress. For

example, during periods of warming the stresses in near surface sea ice may be large and compressive (mode 2). The collision of two sea ice floes will tend to generate compressive stress, and this compressive stress will be superimposed upon the pre-existing, thermally generated compressive stress. Floe collisions might therefore be more likely to damage surface sea ice at noon as opposed to midnight.

One aspect of thermal stress that is highlighted by these results, is that thermal stress is highly variable, and not necessarily monotonic in the vertical. Single depth measurements are therefore not sufficient to capture the internal stress state of sea ice if thermal stresses are a significant component of the stress. Higher vertical resolution measurements or additional modelling are required. The piezo-resistive sensors and Lewis (1998) model may prove to be powerful tools in future studies of sea-ice stress.

Chapter 7

Conclusions and future work

7.1 Achievements of this thesis

7.1.1 Scientific achievements

In this thesis I have used laboratory measurements and numerical modelling to address two broad scientific questions:

1. How well do gravity drainage parameterisations capture the dynamics of dissolved compounds in young sea ice?

2. What are the likely magnitudes, drivers, and implications of pressure in young sea ice?

Question 1) is important because the performance of gravity drainage schemes has only been evaluated against salinity, but these parameterisations are increasingly being applied to biogeochemical tracers that are decoupled from salinity. In Chapter 4 I investigated whether parameterisations that were derived from, tuned using, and evaluated against, measurements of salinity could be applied to general dissolved tracers.

I show that convective parameterisations (Griewank and Notz, 2013; Rees Jones and Worster, 2014), when tuned to best capture salinity, skilfully predict the dynamics of such a tracer. I also show that the diffusive (Vancoppenolle et al., 2010) and empirical (Cox and Weeks, 1988) parameterisation performs worse than the convective parameterisations for both salt and tracer dynamics.

The answer to question 1) is that we can model dissolved tracer dynamics with high confidence in young sea ice, and in convecting sea ice in general, using the parameterisations described in Rees Jones and Worster (2014) and Griewank and Notz (2013). In 1D sea-ice modelling, these convective schemes perform best for salt and tracer, should be used in future, and are a powerful tool.

Question 2) is important because even though several important processes in sea ice may be affected by pressure, the state of pressure in sea ice is poorly constrained. In Chapter 5 I investigate whether sea ice pressure deviates from atmospheric pressure trends and how large these deviations are. In Chapters 5 and 6 I speculate on the causes of pressure deviations and their implications.

I show that sea-ice pressure deviated from atmospheric pressure trends, and is highly variable in the vertical. Pressure deviated by up to 35 kPa during my experiments. There were two modes of pressure build up, both of which relaxed under viscous creep. One of these modes is caused by thermal stress. The other mode is caused by some combination of thermal stress and the expansion of water upon freezing. If pressures on the order of 10 kPa were experienced by gas in sea ice, on the order of 10% of the gas would be expelled.

The answer to question 2) in a sea-ice tank is summarised by the previous paragraph. But I take care when extrapolating these conclusions to natural sea ice because the confined tank environment may significantly affect pressure. The measurements and modelling of pressure and stress in this thesis are an early step to an adequate understanding of sea-ice pressure.

7.1.2 Technical achievements

Data collected in the Roland von Glasow air-sea-ice chamber underpin all of the work in this thesis. To collect these data I first had to achieve two broad technical goals:

1. To assist in the design and implementation of a facility capable of growing sea ice, and measuring important properties in the ocean, sea ice and atmosphere of that facility.

2. To develop methodology to grow sea ice in such a way that measurements of that sea ice are useful for addressing scientific questions.

The purpose of the Roland von Glasow air-sea-ice chamber is to bridge a gap between numerical modelling and the environment, and is most powerful when used in this way. Therefore, to maximise the relevance of the data I collected I wrote two numerical models that could be applied to my experiments. The need for these models created two more technical goals:

3. To write a model that simulates gravity drainage in sea ice using convective (Rees Jones and Worster, 2014; Griewank and Notz, 2013), diffusive (Vancoppenolle et al., 2010), and empirical (Cox and Weeks, 1988) gravity drainage parameterisations in a sea-ice tank; and to add a dissolved tracer that moves conservatively with salt.

4. To write a model that predicts thermal stress in sea ice using the equations of Lewis (1998).

In this thesis I achieve all four of these goals. Chapter 2 describes the realised facility (technical goal 1) and procedures for growing artificial sea ice (2). The development of the gravity drainage model (3) and the pressure model (4) are described in Chapters 3 and 6, respectively. Both of these models are available for use in future studies[1].

7.2 Next steps

7.2.1 Developing pressure work

A first step along developing the work presented in Chapter 5 would be to better characterise the repeatability of the pressure sensor response. Assessing how the local sensor environment affects the sensor response would allow future users to draw stronger conclusions from the sensors. Repeatability in sensor response could

[1] Contact myself or Jan Kaiser at the University of East Anglia.

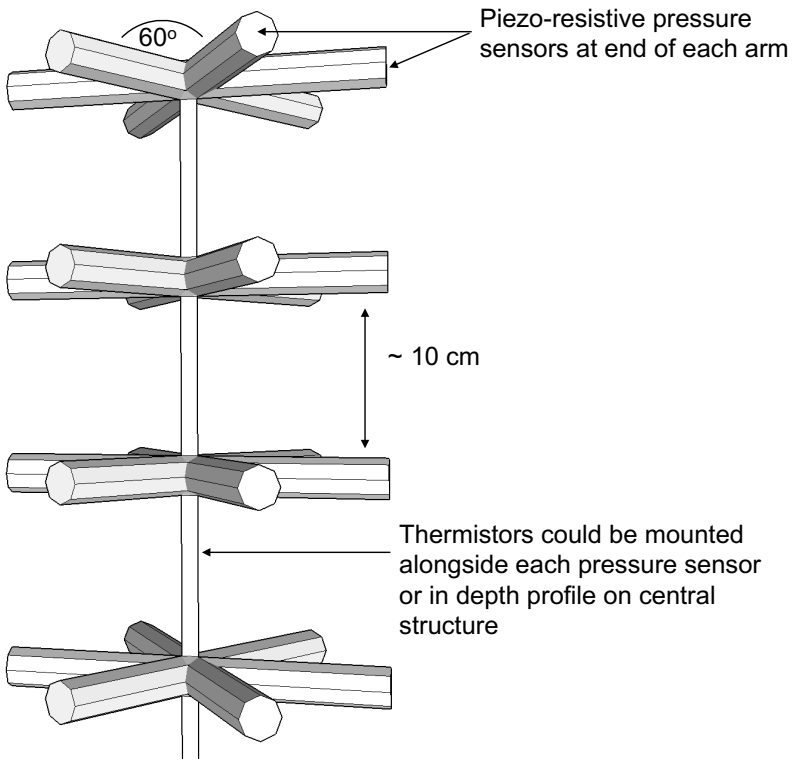

Figure 7.1: Sketch of a possible design for an improved pressure sensor, showing the top four measuring depths. The amount of measuring depths, and the spacing between them, would be tailored to the expected eventual sea-ice thickness. This design improves on the pressure sensor bar described in Chapter 5 by measuring pressure in 3 directions at each depth, and by integrating thermistors. This sensor could be deployed in open water, as in Chapter 5, or into a hole cut in an existing sea-ice cover, as is typical of Cox and Johnson (1983) style sensors.

be investigated by deploying multiple sensors at the same depth within the tank, freezing them into sea ice, then inducing a pressure signal.

The next step would be to construct an array of piezo-resistive pressure sensors that measure in multiple directions in the horizontal (Figure 7.1). Horizontally anisotropic pressures and stresses could then be measured. The repeatability would determine the number of sensors deployed at each depth, and in each direction. The number of measuring depths would be determined by the nature of future deployments. Completing these two technical steps would produce a novel and powerful sea-ice pressure sensor.

I see two scientific questions that could be addressed by such a sensor. The first question is, how does pressure within sea ice affect gas dynamics? In Chapter 5 I took a first step towards estimating the magnitudes of, and mechanisms behind, pressure build up in sea ice. I also showed that the pressures I measured could

significantly affect gas dynamics if the measured pressure were experienced by brine and bubbles. Further studies are needed to show that pressure is an important factor with regard to sea-ice gas dynamics. A key missing link is demonstrating that measured pressures are experienced by gases.

This question could be addressed by a combination of field and laboratory experiments. The Roland von Glasow air-sea-ice chamber could be used to freeze the sensor into sea ice, and to generate controlled pressure signals. Measuring gas concentrations above the sea ice during pressure events could provide evidence that sea-ice pressure and air/sea-ice gas exchange are linked. Deploying the sensor in natural sea ice and measuring pressure signals would show whether the pressures measured in the Roland von Glasow air-sea-ice chamber are representative of natural pressures.

The second question is, how important are thermal stresses to the stress state of sea ice? In Chapter 6 I infer thermal stresses from measured pressures. These stresses are highly variable in the vertical, and it may be important to consider vertical variation in stress when defining and measuring the stress state of sea ice. For example, a single thermal stress event may produce stresses of opposite signs at different depth in sea ice. In some contexts it may therefore not be useful to define a single value sea-ice stress. Future studies are needed to show the extent to which vertical stress variations need to be considered, and to define the best methodologies for taking these variations into account.

To address this question the new pressure sensor array would be deployed in sea ice in the field, ideally alongside a Cox and Johnson (1983) style stress sensor. The Cox and Johnson (1983) sensor could be used to calibrate the inclusion factor of the pressure sensors, and to confirm that measured pressures can be used to infer stress. Stress, as inferred from pressure, would be measured with a vertical resolution an order of magnitude greater than previous studies. Vertical variations in stress would be quantified, and sensitivity studies could be performed on the data to gauge how many depths are required to give a representative stress state, and whether a Lewis (1998) thermal stress model can be used to skilfully predict

thermal stresses throughout the sea ice. Best practise methodologies for defining the vertical stress profile of sea ice would be developed.

7.2.2 Developing gravity drainage work

The MatLab model used to predict salt and brine dynamics in Chapters 3 and 4 is already being used to support several studies. The model can accurately predict salinity and solid fraction when forced with measured temperature, and so can be used as an alternative to the wireharps. Indeed, the model outperforms the wireharps in two situations: when solid fractions are greater than around 0.8, or if an experiment requires minimal instrumentation in the tank. For these reasons, a recent study measuring sea-ice light profiles in the facility will use solid fraction predicted by the MatLab model.

The MatLab model will also be used to help interpret data collected as part of the POPSICLE project (persistent organic pollutants in sea ice in a controlled laboratory environment). In this study, performed in the facility, a suite of persistent organic pollutants was spiked into the ocean before sea-ice formation. The model was used to help investigate whether or not the pollutants behaved conservatively with salt.

As part of my PhD I also modified LIM1D, a one dimensional biogeochemical sea-ice model. My modifications include adding modules to simulate convective brine and tracer dynamics, as described in Chapter 3, and to construct a tank mass balance. Experiments in the facility never progressed to the stage where the additional processes in LIM1D were required, so results from LIM1D do not inform this thesis. However, the results in Chapter 4 allow future studies to use LIM1D with high confidence in the dynamics of dissolved tracers in growing sea ice.

7.3 Ideas for future studies

While working with the facility, and the scientists who came to use it, I had many ideas for experiments that could be conducted in the Roland von Glasow air-sea-ice

chamber. Indeed, the amount of control and instrumentation afforded by the facility means many of these experiments could only be performed in the facility. I could not conduct the vast majority of these experiments due to time constraints. In this section I describe six of the most promising of these ideas in the hope that some are performed in the future.

The level of detail I go into for each experiments depends on how well developed the idea is and my expertise in the topic. For some experiments the description approaches an experimental plan, while for others I only provide a general methodology. In each of the following sections I give a description of a scientific process to be investigated, what specific question would be investigated, my proposed experimental methodology, and my speculation on the outcomes. All of these ideas link to modelling because I believe the facility is best used in this way.

7.3.1 Tracer dynamics not driven by gravity drainage

In this section I describe two experiments to investigate the dynamics of compounds driven by mechanisms other than gravity drainage. The first experiment quantifies a convective process, distinct from gravity drainage, acting on dissolved compounds. The second experiment investigates the controls on particulate incorporation and rejection from sea ice.

Forced convection of dissolved compounds

By forced convection I refer to convection of sea-ice brine driven by something other than the brine density profile. One such driver may be the flow of ocean beneath sea ice (Feltham et al., 2002). In a modelling study, Feltham et al. (2002) show under ice currents can cause corrugations[2] to form at the ice/ocean interface. The pressure at the ice/ocean interface is greater in the troughs of the corrugations than at the crests. This pressure gradient drives brine convection, and is a mechanism distinct from gravity drainage.

I propose an experiment to address the question:

[2] A series of ridges and grooves

How important is forced convection, driven by ocean currents, to the dynamics of dissolved compounds in sea ice?

This question could be addressed by quantifying the difference in the uptake of a dissolved tracer injected under an existing sea-ice cover, with and without a current flowing under the sea ice (Figure 7.2). The experimental design would be similar to that presented in Chapter 4. However, in Chapter 4 I deliberately minimised ocean currents by aiming the ocean pumps at each other (Loose et al., 2011), so that I could disregard forced convection. In this experiment the tank would be divided up into two sections, both of which can be mixed without currents, with one section able to generate currents (Figure 7.2).

The sections would share an ocean of artificial NaCl sea water. Sea ice would then be grown to around 10 centimetres, in both sections, in the absence of currents. Then some tracer would be injected into the underlying ocean, and the pump configuration would be switched to generate currents under the sea ice in one section. After some period of time the sea ice would be sampled, and the tracer and salt concentrations would be measured in depth profile. It would also be important to quantify the under ice currents.

According to the model of Feltham et al. (2002), the sea ice undergoing forced convection should have higher tracer and lower salt concentrations than the sea ice with no currents. The magnitude of this effect would show how important forced convection is in certain cases. To generalise these results the model I present in Chapter 3 could be modified to include current driven forced convection using the equations of Feltham et al. (2002). The ocean salinity and tracer concentration would need to be measured and used to force the model. Data from this experiment could then be used to evaluate the model.

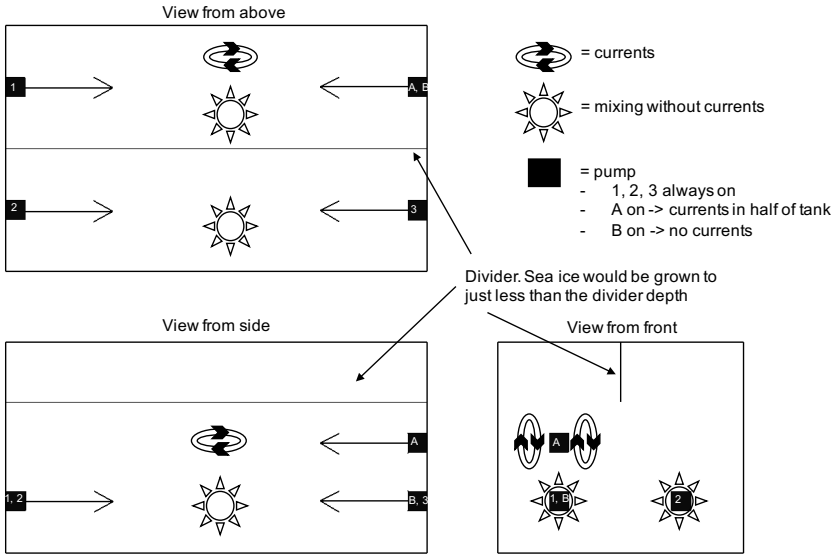

Figure 7.2: Schematic diagram of the main tank set up to simulate forced convection. A divider separates the top 30 or so centimetres of the tank. Pumps facing each other can be used to mix the water (Loose et al., 2011), and this is the situation for both sides of the divide when B is on. When A is switched on, and B off, a current would be generated on one side of the divider, with water flowing between pumps A and 1.

Incorporation and rejection of particulates

The concentrations of particulates, including sediments, organic matter, and microplastics (<5 mm pieces of plastic) (Pfirman et al., 1995; Obbard et al., 2014) are often orders of magnitude larger in sea ice than typical seawater concentrations, and so are enriched relative to salinity in sea ice. This enrichment may be due to scavenging of particles from the water column by rising frazil ice, freezing of river discharge at the sea-ice base, or preferential retention of large or sticky particles (Pfirman et al., 1995).

Also, pollutants may preferentially sorb to this particulate matter, and so become enriched in the sea ice. Sea-ice drift may then transport concentrated particulate and pollutants, and release them into the water column when sea ice melts. The marginal ice zones tend to be highly productive, so the concentration, transport, and release of particulates and pollutants by sea ice may affect ecosystems (Pfirman et al., 1995). In the case of microplastics, sea ice may be a significant global sink that is changing rapidly due to climate change (Obbard et al., 2014).

In this section I focus on incorporation of microplastics, which are poorly studied in sea ice (Obbard et al., 2014). The general methodology could be applied

to any particulate, however. I propose an experiment to address the question:

How do microplastics behave when freezing into sea ice, and how could we parameterise this?

This question could be addressed by quantifying the enrichment/depletion of different size and shaped microplastics during the freezing of seawater relative to salt. Two types of freezing experiments could be conducted: 1) congelation sea-ice growth (experiments in this thesis), and 2) growth from supercooled water, with frazil crystals nucleating and rising up (Chapter 2, Figure 2.8). The different size/shapes of the microplastics would show how important particle properties are to the freezing in process. Profiles of sea ice bulk microplastic concentration would be compared to salinity at the end of the experimental runs to quantify the level of enrichment.

The microplastics could be made by precisely scoring the top of a block of plastic, then shaving off a layer of known thickness using a microtome. I suggest making two shapes of microplatics, cubes and cuboids. These shapes could each be made into, say, three different sizes. Using different coloured versions of the same plastic for each size category of microplastic would allow for the microplastic concentration to be quantified by counting particles under a microscope.

Given that the cuboid particles would have a larger surface area to mass ratio than the cubes, I would expect the cuboid particles to be the stickiest, and therefore the most strongly retained in the sea ice. I would also expect that microplastic concentrations would be more enriched relative to salinity in runs with frazil ice rising up from supercooled water.

The data from this experiment could be used as an early step towards developing parameterisations for microplastic incorporation in sea ice. Likely leading order drivers of microplastic concentration could be identified. If microplastic concentrations are not enriched by orders of magnitude relative to salinity, it would be a strong indication that key drivers are missing from the

experimental system. Such drivers could be sorbing of microplastic to sediments and subsequent entrainment, or atmospheric deposition of microplastics.

7.3.2 Effects of calcium carbonate precipitation

The Roland von Glasow air-sea-ice chamber gives the user total control of the experimental water composition. I exploited this in Chapter 4 to decouple a dissolved tracer from salt, but future experiments could make use of the composition of the initial salt. By varying the composition of Ca^{2+}_{aq} experimenters could investigate the effect of calcium carbonate precipitation on two important biogeochemical cycles in sea ice, bromine explosions and the sea-ice carbon pump.

In both of the subsequent experiments, repeats (sequential or parallel) would be conducted with varying concentrations of Ca^{2+}_{aq}. In runs with no Ca^{2+}_{aq} no calcium carbonate could precipitate, and results could be compared with runs with normal Ca^{2+}_{aq}.

On bromine explosions

The term 'bromine explosion' is used to describe periods of high concentrations of reactive bromine in the tropospheric boundary layer. This reactive bromine drives chemistry that depletes tropospheric ozone and deposits atmospheric mercury (Simpson et al., 2007b). Bromine explosions occur frequently at high latitudes, and the initiation of these events has been linked to frost flowers (Sander et al., 2006) and first year sea ice (Simpson et al., 2007a).

One stage in the generation of reactive bromine is acid catalysed, but frost flowers and first year sea ice are formed from alkaline seawater. Some mechanism must therefore be employed that alters the ionic ratios in the brine on icy polar surfaces away from those in the original seawater. Sander et al. (2006) argue that this mechanism may be the precipitation of calcium carbonate. This hypothesis was refined by Sander and Morin (2010) to take into account the fact that ikaite is the likely form of the precipitated calcium carbonate. But significant uncertainties remain in the mechanism, partly caused by assumptions that must be made about

the relevant chemistry at low temperatures. I propose an experiment to address the question:

Is the precipitation of calcium carbonate, in whatever form, required to initiate bromine explosions over first year sea ice and/or frost flowers?

To answer this question, sea ice would be grown in a set of duplicate experimental runs, where the only difference between the runs is the presence/absence of calcium in the initial ocean. I suggest running sequential experiments, with $CaCl_2$ added to the water between the runs. Calcium carbonate precipitation would then only occur in the second run. The existing lights in the facility would be used to drive the photochemistry. Bromine explosions could be inferred, using only existing instrumentation, by measuring ozone over the sea ice, with drops in ozone suggesting the presence of reactive bromine.

If bromine explosions could be generated if and only if calcium was present in the initial seawater it would provide strong evidence that calcium carbonate precipitation was an important step in the bromine explosion mechanism. If bromine explosions occurred whether calcium was present or not it would provide strong evidence to the contrary.

This is the only experiment in this section where a general result is generated in the absence of a numerical model. However, the data generated would be ideal for developing and evaluating atmospheric chemistry models. One such model is MISTRA (e.g. von Glasow et al., 2002). This experiment is therefore an opportunity to link two of Roland's scientific legacies.

On the sea-ice carbon pump

The 'sea-ice carbon pump' was proposed by Rysgaard et al. (2007), and is a mechanism that increases the flux of carbon from the atmosphere to the polar oceans. One aspect of the sea-ice carbon pump is driven by calcium carbonate, specifically ikaite, precipitation in sea ice (Rysgaard et al., 2012, 2014). The role of

ikaite is summarised below:

1. Ikaite precipitates in sea-ice brines (Dieckmann et al., 2008, 2010). The precipitation of one mole of ikaite removes two moles of total alkalinity (TA) and one mole of dissolved inorganic carbon (DIC) from the brine. The resulting brine is therefore enriched in DIC relative to TA, and so has high fCO_2.

2. Some fraction of these high fCO_2 brines are transferred from the sea ice to the ocean *via* gravity drainage.

3. Some fraction of these rejected high fCO_2 brines are exported from the mixed layer to deeper waters.

4. When the sea ice melts the ikaite dissolves. The dissolving ikaite releases TA in excess over DIC, and so lowers the fCO_2 of the resulting meltwater.

Therefore, when CO_2 is transferred between the atmosphere and the ocean after sea-ice melt, more CO_2 is transferred to the ocean than would have been the case in the absence of steps 1-4. Ikaite therefore increases the size of the carbon sink in sea-ice covered oceans. Rysgaard et al. (2012) estimate that the presence of ikaite doubled the ocean carbon uptake around melting Arctic sea ice.

Subsequent modelling studies suggest that the sea-ice carbon pump is not a large driver of carbon uptake on global scales, partially because of inefficiencies in step 3, but may be important on regional scales (Moreau et al., 2016; Grimm et al., 2016). I propose an experiment that would allow steps 1 and 2 to be quantified. The data produced by this experiment, combined with 1D modelling, could address the question:

How well can we model the budget of TA and DIC in growing sea ice?

In this experiment sea ice would be grown in two or more separate mesocosms, with $CaCl_2$ added to some but not all. To prevent differences in the salinity of

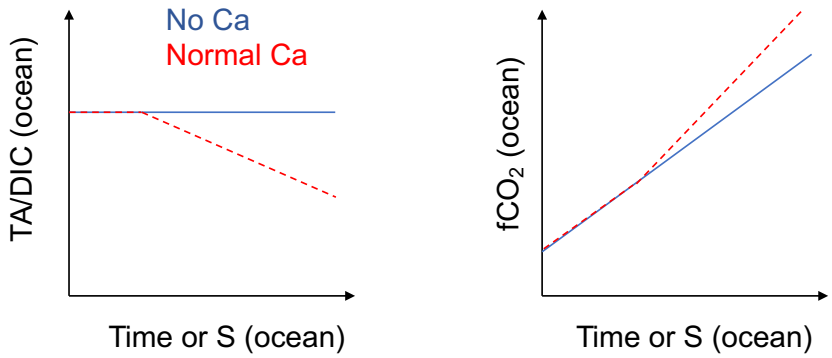

Figure 7.3: Possible effects of ikaite precipitation on carbonate system parameters in a proposed experiment. Both graphs show the growth phase of an experiment, where ocean salinity, total alkalinity (TA) and dissolved inorganic carbon (DIC) would all increase due to gravity drainage. **Left:** The ocean TA/DIC ratio would decrease as brines affected by ikaite precipitation drained and mixed into the ocean. I have drawn TA/DIC as constant in the run with no calcium for simplicity. Biology (which would ideally be minimal) and sea-ice/atmosphere gas exchange may affect TA/DIC but would have similar effects across both runs. **Right:** The resulting ocean fCO_2 would be higher in runs where ikaite precipitation occurred.

the mesocosms, $MgCl_2$ could be added to those with no calcium. The mesocosms without calcium would act as an ikaite 'blank' that integrate the effects of biology, gas exchange, and any other processes that affect the carbonate system in the absence of ikaite precipitation. The ocean of each mesocosm would be sampled through time. The experiment would end after the sea-ice growth phase because step 3 cannot be simulated in the tank environment. At the end of the experiment sea ice and ocean could be sampled in each mesocosm to make a budget of TA and DIC.

I would expect that the ocean concentrations would behave like Figure 7.3. I would also expect that the mesocosms where ikaite was present had less total carbon (sea ice and ocean) at the end of each experiment, because ikaite precipitation should increase carbon fluxes from sea-ice brines to the atmosphere. The magnitude of these differences between mesocosms would give a first order approximation of the importance of ikaite to the sea-ice carbon budgeting.

Stronger conclusions could be drawn by using these data alongside a numerical model with sea-ice carbonate system processes included, such as LIM1D with convective brine dynamics. The advantage of having an ikaite blank is that the other processes that affect the carbonate system, which generally are poorly constrained, can be tuned to the blank mesocosms. The function of the model for ikaite can

then be evaluated in isolation. The model could then be applied to other data sets, or sensitivity studies, with a better constrained uncertainty for parameterisations regarding ikaite.

7.3.3 Segregation of compounds by phase change

This section presents two studies that would investigate the effect of partitioning of chemicals between a dissolved and non-dissolved component, and the subsequent separation of the components. The first study is purely modelling, and seeks to build on the study of Butler et al. (2016) by considering the effects of convection on salt precipitation in sea-ice. The second study seeks to quantify, with experiments in the facility, gas specific processes in sea ice to aid in the development and evaluation of model parameterisations.

Salt precipitation

As sea-ice brines cool they become more saline, and some salts precipitate (Assur, 1958). One such salt is mirabillite ($NaSO_4.10H_2O$). As mirabilite precipitates, the remaining brine becomes depleted in sulfate and sodium relative to seawater. Mirabilite affects the optical properties of sea ice (Light et al., 2003), and so has implications for the Arctic energy budget. The ionic ratios of sea-ice derived aerosol is affected by mirabilite, which has implications for ice core sea-ice proxies (Rankin et al., 2000). Quantification of mirabilite is therefore an important problem.

Butler et al. (2016) predict mirabillite concentrations in sea ice through numerical modelling. They do this by combining two models. The first model is a parameterisation of the mirabillite concentration in a parcel of freezing seawater, M, as a function of temperature, T. This parameterisation is derived from measurements and modelling of the mirabilite concentration in a freezing parcel of standard sea water. The second model is the empirical desalination scheme of Cox and Weeks (1988). They use this model, forced by input data representative of the Arctic Ocean, to predict the temperature and bulk salinity, S_b, of growing sea ice. In this study, the original formulation of the Cox and Weeks (1988) model was

used, rather than the convective version that I formulate in Chapter 3. Finally, they use Equation 7.1 to predict the bulk mirabilite concentration in sea ice, M_i.

$$M_i(T) = M(T)\frac{S_b}{S_o} \tag{7.1}$$

Equation 7.1 states that the bulk mirabilite concentration is equal to the concentration of mirabilite in a parcel of standard sea water frozen to T, scaled by the reduction in sea ice salinity, due to desalination, from the ocean concentration, S_o.

But Equation 7.1 is not valid if mirabilite has precipitated and gravity drainage has subsequently occurred, because the convective overturning in sea ice will distort the ionic ratios in the brine away from that of standard sea water cooled to T. Figure 7.4 shows the contrasting behaviour of a one way desalination scheme and a convective scheme, with a detailed explanation. I summarise here that the return flow in convective schemes will tend to increase the proportion of ions that have precipitated relative to that of standard seawater cooled to T. Convective schemes would therefore tend to predict greater mirabilite concentrations than the one way desalination scheme used by Butler et al. (2016). By taking convection into account, future modelling could address, with improved accuracy relative to Butler et al. (2016), the question:

What are the likely mirabilite concentrations in sea ice?

I propose two modelling approaches. Both approaches would use FREZCHEM, or some similar model, to calculate ion precipitation/dilution concentrations in brine. The precipitation/dilution routine would be coupled to a model similar to that used in Chapter 4, where tracers (in this case dissolved ions) are transported conservatively with brine, but can have their concentration altered by other processes (in this case precipitation/dissolution of salts). Implementing varying dissolved salt ratios in a sea ice model would be a technical challenge, given that models generally calculate the total brine salinity as a function of temperature. The difference in the two models is the way this total brine salinity is calculated.

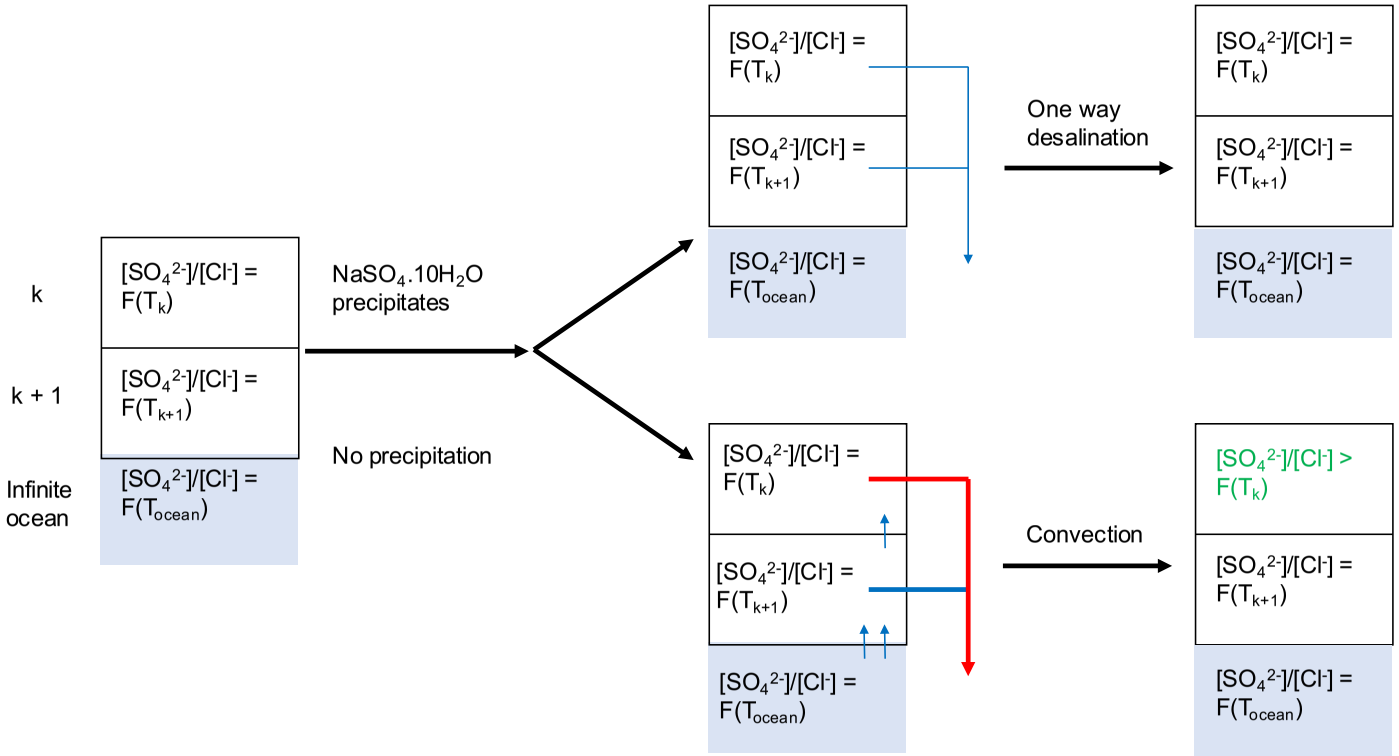

Figure 7.4: Schematic diagram of a two layer sea ice (white boxes) model, with an infinitely large ocean (blue boxes) underneath. In each layer the simulation starts with the sulphate to chloride to sulfate ratio of seawater cooled down to the temperature of the layer, F(T). I have chosen sulfate to chloride because sulfate would be depleted by mirabilite precipitation, but chloride would not. Blue arrows show brine movement where the ionic composition of the brine is the same as seawater. The red arrow shows brine that has a sulfate to chloride ratio smaller than that of seawater.

The top layer, k, is so cold that some mirabilite ($Na_2SO_4.10H_2O$) precipitates. There is no precipitation in layer k+1 or the ocean. In the one way desalination scheme (Cox and Weeks, 1988) employed by Butler et al. (2016) the salinities of the layers change. However, it is implicitly assumed that the transfer of salt is one way, and that the ionic ratios are always consistent with sea water cooled to T.

In the case of convection a return flow must be considered. After precipitation, gravity drainage moves brine from each sea-ice layer into the ocean layer, and from each layer to the layer above. The ionic ratio of this moving brine is consistent with seawater cooled to the temperature of the layer. But now consider the ionic ratios in the downward and return flow in layer k. Because mirabilite has precipitated in this layer the sulfate to chloride ratio is lower than that of k+1. Replacing some mass of brine in k with an equal mass from k+1 increases the sulfate to chloride ratio of k. The temperature of k may not have changed, so the sulfate to chloride ratio of k is no longer consistent with seawater cooled to the temperature of k. The increased sulfate in the convective model would tend to support more mirbilite precipitation.

M1: Given that sodium and chloride make up more than 97% of the ions in seawater, a liquidus could be used to calculate a good approximation of the brine salinity. This brine salinity could drive the brine dynamics in the scheme. Specific ions of interest, sodium and sulfate, could then be treated as individual compounds, moving with brine, but not contributing to the brine salinity. These compounds of interest would begin at natural seawater concentrations, and their concentration at a given time and depth would be calculated based on the temperature at a given time, and the concentration of ions at the previous timestep.

M2: Brine salinity would be taken to be the sum of several major ions, each with a concentration stored at each depth and time. The concentration of each major ion would be calculated from the precipitation/dissolution routine based on the concentrations at the previous timestep, and the new temperature. This brine salinity would drive the brine dynamics. These ions move together due to brine dynamics, and decouple due to precipitation/dissolution.

The second approach would be more versatile and elegant, though it would be difficult to implement in an established model (such as LIM1D or my MatLab code). To do so would require making a large change to a core model component, the definition of brine salinity. The first approach could only be used for specific salts, and would not be applicable if sodium or chloride were depleted significantly. For the study of mirabilite, the first approach is therefore only appropriate at warmer temperatures, where the sodium depletion cause by mirabilite precipitation is relatively small (Butler et al., 2016).

The improved model could then be run, in a similar fashion to Butler et al. (2016), using typical Arctic and Antarctic forcing. Concentrations of mirabilite, or any salt coded into FREZCHEM, could then be predicted with greater confidence. This modelling study is the only idea in this section that does not explicitly use the facility, but the facility could be used to evaluate the model.

I expect that greater mirabilite concentrations would be predicted by these proposed modelling approaches when compared to one way desalination schemes.

Mirabilite precipitation will be greatest at the coldest temperatures, where the sea ice is least permeable and convective overturning is weakest, which will tend to reduce differences between the schemes. But full depth convection of thick sea ice can occur (Griewank and Notz, 2013), and would resupply dissolved ions.

I focus on mirabilite for clarity, but other studies could be improved by explicitly considering convection. For example, Butler et al. (2017) investigate gypsum and hydrohalite dynamics using a similar methodology to Butler et al. (2016). Dugan and Lamoureux (2011) also use the Cox and Weeks (1988) gravity drainage scheme to investigate parameters other than salinity. They study oxygen isotopes rather than salt precipitation, but similar arguments apply to their study as to Butler et al. (2016). A convective scheme with chemicals of interest decoupled from salinity would be more accurate.

To the best of my knowledge, the only studies that allow for decoupling of ions from brine by precipitation are Moreau et al. (2015); Kotovitch et al. (2016) and use LIM1D. They use the parameterisations of Papadimitriou et al. (2013, 2014) to predict ikaite precipitation based on the concentration of calcium and carbonate ions in sea-ice brines. The concentration of carbonate is free to change in response to precipitation, but does not feed back on the brine salinity (M1). Brine, including the dissolved carbonate, is then transported *via* the diffusive gravity drainage scheme of Vancoppenolle et al. (2010). The approach of Moreau et al. (2015) would likely be the best approach to model the experiment presented in Section 7.3.2 investigating the sea-ice carbon pump, though a convective gravity drainage scheme should be used.

Bubble nucleation and rise

Analogous to salt precipitation, the partitioning of chemicals between a dissolved (in brine) and gaseous (in bubbles) phase in sea ice decouples chemicals in sea ice. The dynamics of some volatile compound are therefore partly controlled by processes that affect this partitioning, and the buoyant rise of bubbles (Zhou et al., 2014; Crabeck et al., 2014). Crabeck et al. (2014) propose a conceptual model that splits the controls on gas dynamics into three regimes, though I modified these

slightly in Chapter 1. The (modified) regimes are:

1. When sea ice is convecting and impermeable to bubbles, convection and bubble nucleation control gas dynamics.

2. When sea ice is convecting and permeable to bubbles, convection, and bubble nucleation and rise, control gas dynamics.

3. When sea ice is not convecting and is permeable to bubbles, bubble nucleation and rise control gas dynamics.

4. When sea ice is not convecting and is impermeable to bubbles, molecular diffusion and bubble nucleation control the gas dynamics.

Sea ice is taken to be convecting below the first super critical Rayleigh number (Rees Jones and Worster, 2013, 2014; Griewank and Notz, 2013), and a layer of sea ice is thought to be permeable to bubbles at brine volume fractions greater than around 7% (Zhou et al., 2014; Crabeck et al., 2014).

Though our conceptual understanding of gas dynamics in sea ice is developing, our quantitive understanding of specific processes remains poor. For example, to capture observations, two modelling studies simulating gas dynamics with LIM1D had to use bubble nucleation timescales that differed by an order of magnitude (Kotovitch et al., 2016; Moreau et al., 2015). This discrepancy is driven by missing processes in the parameterisation of bubble nucleation.

Normally several processes control gas dynamics at any one time, and this hampers our ability to develop and evaluate parameterisations for individual processes. The control afforded by the facility over water composition and sea-ice physical properties allows these processes to be quantified and partly isolated. I propose a set of experiments to address the question:

How well can we model gas specific processes in sea ice, and how can we improve this modelling?

The method I propose for quantifying gas specific processes is to spike a gas of interest into the ocean underlying some sea ice alongside a perfectly dissolved tracer. Spiking the gas alongside a perfectly dissolved tracer allows the experimenter to isolate the signal of the gas specific processes by subtracting the relative change in concentration of the non-volatile from the volatile compound. Spiking the chemicals under an existing sea-ice cover prevents decoupling of the chemicals *via* air-sea gas transfer. The tracer should be chosen such that it has no sources or sinks in the experimental system, and has a molecular diffusivity similar to the gas.

The method I propose for partly isolating the individual processes is to control the physical properties of the sea ice at and subsequent to the spike, such that one of the four regimes is dominant. The facility is capable of producing all of the regimes. For example, according to modelled brine volume fractions in Chapter 4 I simulated three of four regimes by chance in this experiment, and would likely have simulated the fourth had I continued the experiment another few days (Figure 7.5). Hypothetically, if I had spiked a gas alongside the rhodamine in this experiment I would expect to see differences in their final profiles because of the different regimes. Because the entire sea ice was permeable to bubbles for some period after the spike, I would expect to have lost some gas from the experimental system as bubbles formed, then floated up and out of the sea ice. I would also expect a gas build up between 2 and 4 cm depth because of the layer of sea ice that is impermeable to bubbles. Finally, I would expect gas concentrations in the ocean to be depleted relative to rhodamine because the gas partitioned to the bubbles would not be available for rejection back to the ocean.

Planning would allow sea ice to be grown with certain regimes dominant. Taking the experimental run in Chapter 4 as a starting point, an experimenter could grow the sea ice slower, or from lower salinity starting water, to decrease the resulting brine volume fraction. Regime 1 would then come about earlier and cover a large fraction of the sea ice. Regime 2 could have been studied in near isolation by simply spiking and sampling earlier. Quicker growth rates will also tend to generate

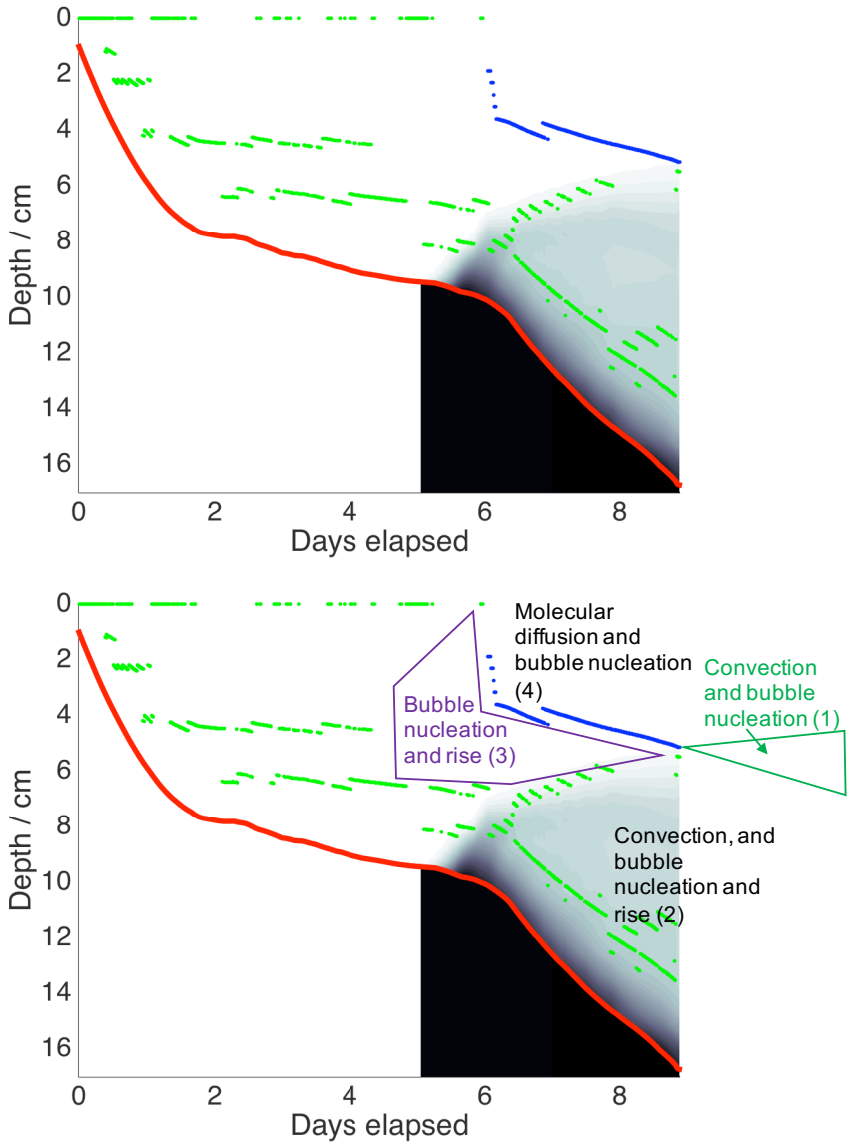

Figure 7.5: Top: Model output using Rees Jones and Worster (2014) gravity drainage parameterisation for bulk tracer concentration, after spiking the ocean with tracer at day 5.1. This is the experiment that forms the basis of Chapter 4. Darker contours represent more tracer. The red line shows the sea-ice thickness. The green and blue dots show the top of the convecting layer, and the deepest impermeable layer for bubbles, respectively. If there is no blue dot for a timestep, then the entire sea ice is permeable to bubbles. **Bottom:** Same as the top panel, but with rough gas dynamics regimes indicated. I have adapted the regimes from Crabeck et al. (2014), and the regimes are described in Section 7.3.3. The area of regime 1 is a rough extrapolation, by eye, of the eventual overlap between the convecting region and the sea ice above the impermeable layer.

regime 2. Regime 3 could be produced throughout an entire column of sea ice if it had a shallow temperature gradient. Regime 4 could be studied in low brine volume fraction sea ice with a shallow temperature gradient.

Model runs with gas dynamics parameterisations could then be evaluated against these idealised experiments. Simulating regimes 1 and 3 would be

particularly valuable because subtracting the signal of the dissolved tracer would quantify the effects of bubble nucleation, which is a particularly poorly constrained process.

7.4 Closing thoughts

The first strand of this thesis makes strong statements regarding the well studied process of gravity drainage. Several parameterisations are currently used in the literature. Using an experimental design inspired by Eide and Martin (1975), I compare the performance of empirical (Cox and Weeks, 1988), diffusive (Vancoppenolle et al., 2010), and convective parameterisations (Griewank and Notz, 2013; Rees Jones and Worster, 2013) for the dynamics of dissolved compounds. I conclude form this work that convective parameterisations are best, and that convective parameterisations can skilfully predict the dynamics of any dissolved compound in sea ice, whatever its distribution.

My results add a novel line of evidence that the physical mechanism driving gravity drainage is convective. The implications of this convection reach beyond the salinity of sea ice. Biogeochemically relevant chemical species are also transported by this convection. Future numerical and conceptual frameworks for sea-ice biogeochemical processes should account for both the loss of dissolved compounds from sea ice to, and their resupply from, the ocean. Gravity drainage is, at any time, active over vast areas of the world's oceans. My results show that we understand the underlying physics of gravity drainage, and that we can model this globally relevant process with high fidelity.

The second strand of this thesis takes early steps towards understanding pressure in sea ice. It is plausible that phase changes and stresses in sea ice could alter the pressure within brine pockets. It is certain that there are processes occurring in sea ice that would be affected by pressure. I show that sea-ice pressure deviates from atmospheric trends, is variable over centimetre scales in the vertical, and that pressure build ups may be large enough to significantly affect gas dynamics in sea ice. I also show that at least some of the pressure deviations are driven by thermal

stresses.

But large uncertainties remain, both in terms of the magnitudes of pressures within sea ice, and the impact of these pressures on gases. Further work is needed to 1) show whether the pressures measured in the tank are representative of natural sea-ice pressures, and 2) quantify how pressure measured over a sensor face relates to pressure experienced by gas and brine inclusions. Furthering our understanding of sea-ice pressure is a key next step in adequately parameterising gas dynamics in sea ice.

These two broad scientific strands tie together scientifically by furthering our understanding of the physics that underpins biogeochemical processes in sea ice. Future models of sea-ice biogeochemistry should use convective schemes (Griewank and Notz, 2013; Rees Jones and Worster, 2014) to transport dissolved compounds. They may also calculate a local pressure, potentially with a component driven by thermal stress (Lewis, 1998), and could use this pressure in calculations of gas partitioning and transport.

Experimental work on these two strands has built a strong methodological foundation for future studies using the facility. The procedures for growing and sampling sea ice are now well defined. Also, the numerical models I developed are available for future studies. The MatLab code simulating gravity drainage will be used to model the solid fraction and bulk salinity of sea ice in future experiments, and all future studies using LIM1D will be performed using gravity drainage modules that I helped to implement.

Several collaborative experiments, funded through EUROCHAMP project, have now been completed in the Roland von Glasow air-sea-ice chamber that build on this methodological foundation. Light profiles have been measured *in situ* (collaboration with Dirk Notz's group), extending the sea-ice physics work I have presented. Two experiments have been completed that measure the dynamics of environmentally relevant chemicals, methane (collaboration with Ellen Damm's group) and a suite of persistent organic pollutants (collaboration with Crispin Haspall's group). Excitingly, the first biological experiment has now been

completed in the facility (collaboration with Catherine Larosse's group).

And several further studies are planned. The BEPSII (biogeochemical processes at sea-ice interfaces) working community will soon run an instrument inter-calibration experiment. Karen Haywood's group are testing automated equipment for use in the southern ocean. The facility is part of a successful proposal, again looking at persistent organic pollutants, and is part of several submitted proposals.

The facility builds a bridge between numerical simulations and the environment. Subsequent to my experiments, several groups have brought scientific questions back from field campaigns, and exploited the controlled environment provided by the facility to address them. The facility can test certain unknowns raised by fieldwork in a systematic way. In turn, exciting results in the facility may be validated in the field. I believe that the future of the Roland von Glasow air-sea-ice chamber is to be used in this way, as one step in an iterative process linking field, modelling, and laboratory studies.

The experiments conducted by myself and others demonstrate the value of the Roland von Glasow air-sea-ice chamber, which I hope will be used for years to come to progress environmental research.

References

Aagaard, K., Coachman, L., Carmack, E., 1981. On the halocline of the arctic ocean. Deep Sea Research Part A. Oceanographic Research Papers 28, 529–545.

Assur, A., 1958. Composition of sea ice and its tensile strength. Arctic sea ice 598, 106–138.

Bogorodsky, V., Gavrilo, V., Gusev, A., Gudkovich, Z., Polyakov, A., 1972. Stressed ice cover state due to thermal wave and related underwater noise in the ocean, in: Proc. Ice Symposium 1972, pp. 28–33.

Budycko, M.I., 1969. The effect of solar radiation variations on the climate of the earth. Tellus 21, 611–619.

Butler, B.M., Papadimitriou, S., Day, S.J., Kennedy, H., 2017. Gypsum and hydrohalite dynamics in sea ice brines. Geochimica et Cosmochimica Acta 213, 17–34.

Butler, B.M., Papadimitriou, S., Santoro, A., Kennedy, H., 2016. Mirabilite solubility in equilibrium sea ice brines. Geochimica et Cosmochimica Acta 182, 40–54.

Caline, F., Barrault, S., 2008. Measurements of stresses in the coastal ice on both sides of a tidal crack. 19 th IAHR International Symposium on Ice .

Collins, M., Knutti, R., Arblaster, J., Dufresne, J.L., Fichefet, T., Friedlingstein, P., Gao, X., Gutowski, W., Johns, T., Krinner, G., Shongwe, M., Tebaldi, C., Weaver, A., Wehner, M., 2013. Long-term Climate Change: Projections, Commitments and Irreversibility. Cambridge University Press, Cambridge, United Kingdom and New York, NY, USA. book section 12. p. 1029–1136.

Cottier, F., Eicken, H., Wadhams, P., 1999. Linkages between salinity and brine

channel distribution in young sea ice. Journal of Geophysical Research: Oceans (1978–2012) 104, 15859–15871.

Cox, B.G.F.N., Weeks, W.F., 1986. Sea-ice samples during shipping and storage. Journal of Glaciology, 32, 371–375.

Cox, G.F., Johnson, J.B., 1983. Stress measurements in ice. CRREL Report 83-23, 1–27.

Cox, G.F., Weeks, W.F., 1975. Brine Drainage and Initial Salt Entrapment in Sodium Chloride Ice. Technical Report. DTIC Document.

Cox, G.F., Weeks, W.F., 1983. Equations for determining the gas and brine volumes in sea-ice samples. Journal of Glaciology 29, 306–316.

Cox, G.F.N., Weeks, W.F., 1988. Numerical simulations of the profile properties of undeformed first-year sea ice during the growth season. Journal of Geophysical Research 93, 12449–12460.

Crabeck, O., Delille, B., Rysgaard, S., Thomas, D., Geilfus, N.X., Else, B., Tison, J.L., 2014. First *in situ* determination of gas transport coefficients (DO_2, DAr, and DN_2) from bulk gas concentration measurements (O_2, Ar, N_2) in natural sea ice. Journal of Geophysical Research: Oceans 119, 6655–6668.

Dai, M., Shen, H.H., Hopkins, M.A., Ackley, S.F., 2004. Wave rafting and the equilibrium pancake ice cover thickness. Journal of Geophysical Research: Oceans (1978-2012) 109.

De La Rosa, S., Maus, S., Kern, S., 2011. Thermodynamic investigation of an evolving grease to pancake ice field. Annals of Glaciology 52, 206–214.

Delille, B., 2006. Inorganic carbon dynamics and air-ice-sea CO_2 fluxes in the open and coastal waters of the Southern Ocean. Ph.D. thesis. University of Liege.

Delille, B., Vancoppenolle, M., Geilfus, N.X., Tilbrook, B., Lannuzel, D., Schoemann, V., Becquevort, S., Carnat, G., Delille, D., Lancelot, C., et al.,

2014. Southern Ocean CO_2 sink: The contribution of the sea ice. Journal of Geophysical Research: Oceans 119, 6340–6355.

Dieckmann, G., Nehrke, G., Uhlig, C., Göttlicher, J., Gerland, S., Granskog, M., Thomas, D., 2010. Ikaite ($CaCO_3$. 6H2O) discovered in Arctic sea ice. The Cryosphere 4, 227–230.

Dieckmann, G.S., Nehrke, G., Papadimitriou, S., Göttlicher, J., Steininger, R., Kennedy, H., Wolf-Gladrow, D., Thomas, D.N., 2008. Calcium carbonate as ikaite crystals in Antarctic sea ice. Geophysical Research Letters 35.

Doble, M.J., Coon, M.D., Wadhams, P., 2003. Pancake ice formation in the Weddell Sea. Journal of Geophysical Research: Oceans 108.

Dugan, H.A., Lamoureux, S.F., 2011. The chemical development of a hypersaline coastal basin in the High Arctic. Limnology and Oceanography 56, 495–507.

Eicken, H., 1994. Structure of under-ice melt ponds in the central Arctic and their effect on, the sea-ice cover. Limnology and Oceanography 39, 682–693.

Eicken, H., Bock, C., Wittig, R., Miller, H., Poertner, H.O., 2000. Magnetic resonance imaging of sea-ice pore fluids: methods and thermal evolution of pore microstructure. Cold Regions Science and Technology 31, 207–225.

Eide, L., Martin, S., 1975. The formation of brine drainage features in young sea ice. Journal of Glaciology 14, 137–154.

Feistel, R., Wagner, W., 2006. A new equation of state for H_2O ice Ih. Journal of Physical and Chemical Reference Data 35, 1021–1047.

Feltham, D., Untersteiner, N., Wettlaufer, J., Worster, M., 2006. Sea ice is a mushy layer. Geophysical Research Letters 33.

Feltham, D.L., Worster, M.G., Wettlaufer, J., 2002. The influence of ocean flow on newly forming sea ice. Journal of Geophysical Research: Oceans (1978-2012) 107, 1—–9.

Fofonoff, N., Millard, R., 1978. Algorithms for computation of fundamental properties of seawater. UNESCO technical papers in marine science 44.

Frederking, R., Wessels, E., Maxwell, J., Prinsenberg, S., Sayed, M., 1986. Ice pressures and behaviour at adams island, winter 1983/1984. Canadian Journal of Civil Engineering 13, 140–149.

Freitag, J., 1999. Untersuchungen zur hydrologie des arktischen meereises: Konsequenzen für den kleinskaligen stofftransport (in german) the hydraulic properties of arctic sea-ice: Implications for the small scale particle transport. Reports on polar research 325.

Fripiat, F., Cardinal, D., Tison, J.L., Worby, A., André, L., 2007. Diatom-induced silicon isotopic fractionation in Antarctic sea ice. Journal of Geophysical Research: Biogeosciences 112.

Fritsen, C., Lytle, V., Ackley, S., Sullivan, C., 1994. Autumn bloom of Antarctic pack-ice algae. Science 266, 782–784.

Galley, R., Else, B., Geilfus, N.X., a.a. Hare, Isleifson, D., Barber, D., Rysgaard, S., 2015. Imaged brine inclusions in young sea ice—Shape, distribution and formation timing. Cold Regions Science and Technology 111, 39–48.

von Glasow, R., Sander, R., Bott, A., Crutzen, P.J., 2002. Modeling halogen chemistry in the marine boundary layer 1. cloud-free mbl. Journal of Geophysical Research: Atmospheres 107.

Golden, K., Ackley, S., Lytle, V., 1998. The percolation phase transition in sea ice. Science 282, 2238–2241.

Gosink, T.A., Pearson, J.G., Kelley, J.J., 1976. Gas movement through sea ice. Nature 263, 41.

Griewank, P.J., Notz, D., 2013. Insights into brine dynamics and sea ice desalination from a 1-D model study of gravity drainage. Journal of Geophysical Research: Oceans 118, 3370–3386.

Griewank, P.J., Notz, D., 2015. A 1-D modelling study of Arctic sea-ice salinity. The Cryosphere 9, 305–329.

Grimm, R., Notz, D., Glud, R.N., Rysgaard, S., Six, K.D., 2016. Assessment of the sea-ice carbon pump: Insights from a three-dimensional ocean-sea-ice-biogeochemical model (MPIOM/HAMOCC). Elementa Science of the Anthropocene 4.

Gudmundsson, A., 2012. Magma chambers: Formation, local stresses, excess pressures, and compartments. Journal of Volcanology and Geothermal Research 237, 19–41.

Hata, Y., Tremblay, L., 2015a. A 1.5-d anisotropic sigma-coordinate thermal stress model of landlocked sea ice in the canadian arctic archipelago. Journal of Geophysical Research: Oceans 120, 8251–8269.

Hata, Y., Tremblay, L., 2015b. Anisotropic internal thermal stress in sea ice from the Canadian Arctic Archipelago. Journal of Geophysical Research: Oceans 120, 5457–5472.

Hutchings, J.K., Geiger, C., Roberts, A., Richter-Menge, J., Elder, B., 2010. On the spatial and temporal characterization of motion induced sea ice internal stress, in: Proceedings from the International Conference and Exhibition on Performance of Ships and Structures in Ice, Anchorage, AK.

Jeffery, N., Hunke, E.C., Elliott, S.M., 2011. Modeling the transport of passive tracers in sea ice. Journal of Geophysical Research 116, 1–15.

Jeffries, M., Weeks, W., Shaw, R., Morris, K., 1993. Structural characteristics of congelation and platelet ice and their role in the development of antarctic land-fast sea ice. Journal of Glaciology 39, 223–238.

Johnson, J.B., Metzner, R.C., 1990. Thermal expansion coefficients for sea ice. Journal of Glaciology 36, 343–349.

Jutras, M., Vancoppenolle, M., Lourenço, A., Vivier, F., Carnat, G., Madec, G., Rousset, C., Tison, J.L., 2016. Thermodynamics of slush and snow-ice formation in the Antarctic sea-ice zone. Deep Sea Research Part II: Topical Studies in Oceanography 131, 75–83.

Kell, G.S., 1970. Isothermal compressibility of liquid water at 1 atm. Journal of Chemical and Engineering Data 15, 119–122.

Knight, C., 1962. Polygonization of aged sea ice. The Journal of Geology , 240–246.

Kotovitch, M., Moreau, S., Zhou, J., Vancoppenolle, M., Dieckmann, G.S., Evers, K.U., Van der Linden, F., Thomas, D.N., Tison, J.L., Delille, B., 2016. Air-ice carbon pathways inferred from a sea ice tank experiment. Elementa Science of the Anthropocene 4.

Krembs, C., Gradinger, R., Spindler, M., 2000. Implications of brine channel geometry and surface area for the interaction of sympagic organisms in Arctic sea ice. Journal of Experimental Marine Biology and Ecology 243, 55–80.

Lake, R., Lewis, E., 1970. Salt rejection by sea ice during growth. Journal of Geophysical Research 75, 583–597.

Lewis, J.K., 1993. A model for thermally-induced stresses in multi-year sea ice. Cold regions science and technology 21, 337–348.

Lewis, J.K., 1994. Relating Arctic ambient noise to thermally induced fracturing of the ice pack. The Journal of the Acoustical Society of America 95, 1378–1385.

Lewis, J.K., 1995. A conceptual model of the impact of flaws on the stress state of sea ice. Journal of Geophysical Research: Oceans 100, 8829–8835.

Lewis, J.K., 1998. Thermomechanics of pack ice. Journal of Geophysical Research 103, 21.

Lewis, J.K., Tucker, W.B., Stein, P.J., 1994. Observations and modeling of thermally induced stresses in first-year sea ice. Journal of Geophysical Research: Oceans 99, 16361–16371.

Light, B., Maykut, G., Grenfell, T., 2003. Effects of temperature on the microstructure of first-year Arctic sea ice. Journal of Geophysical Research: Oceans (1978-2012) 108.

Loose, B., Miller, L.A., Elliott, S., Papakyriakou, T., 2011. Sea ice biogeochemistry and material transport across the frozen interface. Oceanography 24, 202–218.

Macosko, C.W., 1994. Rheology: Principles, measurements and applications. Wiley.

Maksym, T., Jeffries, M.O., 2000. A one-dimensional percolation model of flooding and snow ice formation on Antarctic sea ice. Journal of Geophysical Research: Oceans (1978-2012) 105, 26313–26331.

Marion, G.M., Kargel, J.S., Catling, D.C., Jakubowski, S.D., 2005. Effects of pressure on aqueous chemical equilibria at subzero temperatures with applications to Europa. Geochimica et cosmochimica acta 69, 259–274.

Maykut, G.A., Untersteiner, N., 1971. Some results from a time-dependent thermodynamic model of sea ice. Journal of Geophysical Research 76, 1550–1575.

Meier, W., 2017. Losing arctic sea ice: observations of the recent decline in the long term context, in: Sea ice, John Wiley & Sons.

Mellor, M., 1986. Mechanical behaviour of sea ice, in: The geophysics of sea ice. Springer, pp. 165–281.

Meredith, M., Brandon, M., 2017. Oceanography and sea ice in the southern ocean, in: Sea ice, John Wiley & Sons.

Middleton, C., Thomas, C., De Wit, A., Tison, J.L., 2016. Visualizing brine channel development and convective processes during artificial sea-ice growth using Schlieren optical methods. Journal of Glaciology 62, 1–17.

Moreau, S., Vancoppenolle, M., Bopp, L., Aumont, O., Madec, G., Delille, B., Tison, J.L., Barriat, P.Y., Goosse, H., 2016. Assessment of the sea-ice carbon pump: Insights from a three-dimensional ocean-sea-ice biogeochemical model (NEMO-LIM-PISCES). Elementa Science of the Anthropocene 4.

Moreau, S., Vancoppenolle, M., Delille, B., Tison, J.L., Zhou, J., Kotovitch, M., Thomas, D.N., Geilfus, N.X., Goosse, H., 2015. Drivers of inorganic carbon dynamics in first-year sea ice: A model study. Journal of Geophysical Research: Oceans .

Moreau, S., Vancoppenolle, M., Zhou, J., Tison, J.L., Delille, B., Goosse, H., 2014. Modelling argon dynamics in first-year sea ice. Ocean Modelling 73, 1–18.

Nakawo, M., 1983. Measurements on air porosity of sea ice. Annals of Glaciology 4, 204–208.

Naumann, A., Notz, D., Håvik, L., Sirevaag, A., 2012. Laboratory study of initial sea-ice growth: properties of grease ice and nilas. The Cryosphere 6, 729–741.

Niedrauer, T.M., Martin, S., 1979. An experimental study of brine drainage and convection in young sea ice. Journal of Geophysical Research: Oceans (1978–2012) 84, 1176–1186.

Noda, N., 2002. Thermal stresses. CRC press.

Notz, D., 2005. Thermodynamic and fluid-dynamical processes in sea ice. Ph.D. thesis. University of Cambridge.

Notz, D., McPhee, M.G., Worster, M.G., Maykut, G.A., Schlünzen, K.H., Eicken, H., 2003. Impact of underwater-ice evolution on Arctic summer sea ice. Journal of Geophysical Research: Oceans (1978-2012) 108.

Notz, D., Stroeve, J., 2016. Observed Arctic sea-ice loss directly follows anthropogenic CO_2 emission. Science 354, 747–750.

Notz, D., Wettlaufer, J.S., Worster, M.G., 2005. A non-destructive method for measuring the salinity and solid fraction of growing sea ice in situ. Journal of Glaciology 51, 159–166.

Notz, D., Worster, M.G., 2008. In situ measurements of the evolution of young sea ice. Journal of Geophysical Research: Oceans (1978-2012) 113.

Notz, D., Worster, M.G., 2009. Desalination processes of sea ice revisited. Journal of Geophysical Research: Oceans (1978-2012) 114.

Obbard, R.W., Sadri, S., Wong, Y.Q., Khitun, A.A., Baker, I., Thompson, R.C., 2014. Global warming releases microplastic legacy frozen in Arctic sea ice. Earth's Future 2, 315–320.

Oertling, A.B., Watts, R.G., 2004. Growth of and brine drainage from NaCl-H_2O freezing: A simulation of young sea ice. Journal of Geophysical Research: Oceans (1978-2012) 109.

Ono, N., Kasai, T., 1985. Surface layer salinity of young sea ice. Ann. Glaciol 6, 57.

Papadimitriou, S., Kennedy, H., Kennedy, P., Thomas, D.N., 2013. Ikaite solubility in seawater-derived brines at 1 atm and sub-zero temperatures to 265 K. Geochimica et Cosmochimica Acta 109, 241–253.

Papadimitriou, S., Kennedy, H., Kennedy, P., Thomas, D.N., 2014. Kinetics of ikaite precipitation and dissolution in seawater-derived brines at sub-zero temperatures to 265 K. Geochimica et Cosmochimica Acta 140, 199–211.

Perovich, D.K., Richter-Menge, J.A., 1994. Surface characteristics of lead ice. Journal of Geophysical Research: Oceans 99, 16341–16350.

Pfirman, S., Eicken, H., Bauch, D., Weeks, W., 1995. The potential transport of pollutants by Arctic sea ice. Science of the Total Environment 159, 129–146.

Polashenski, C., Golden, K.M., Perovich, D.K., Skyllingstad, E., Arnsten, A., Stwertka, C., Wright, N., 2017. Percolation blockage: A process that enables melt pond formation on first year Arctic sea ice. Journal of Geophysical Research: Oceans 122, 413–440.

Pringle, D., Miner, J., Eicken, H., Golden, K., 2009. Pore space percolation in sea ice single crystals. Journal of Geophysical Research: Oceans (1978-2012) 114.

Rankin, A., Auld, V., Wolff, E., 2000. Frost flowers as a source of fractionated sea salt aerosol in the polar regions. Geophysical Research Letters 27, 3469–3472.

Rees Jones, D.W., Worster, M.G., 2013. A simple dynamical model for gravity drainage of brine from growing sea ice. Geophysical Research Letters 40, 307–311.

Rees Jones, D.W., Worster, M.G., 2014. A physically based parameterization of gravity drainage for sea-ice modeling. Journal of Geophysical Research: Oceans 119, 5599–5621.

Richter-Menge, J., Elder, B., 1998. Characteristics of pack ice stress in the Alaskan Beaufort Sea. Journal of Geophysical Research: Oceans 103, 21817–21829.

Richter-Menge, J.A., Cox, G.F., et al., 1995. The creep of saline ice at low stresses and high temperatures, in: The Fifth International Offshore and Polar Engineering Conference, International Society of Offshore and Polar Engineers.

Rysgaard, S., Bendtsen, J., Delille, B., Dieckmann, G.S., Glud, R.N., Kennedy, H., Mortensen, J., Papadimitriou, S., Thomas, D.N., Tison, J.L., 2011. Sea ice contribution to the air-sea CO_2 exchange in the Arctic and Southern Oceans. Tellus B 63, 823–830.

Rysgaard, S., Glud, R.N., Lennert, K., Cooper, M., Halden, N., Leakey, R., Hawthorne, F., Barber, D., 2012. Ikaite crystals in melting sea ice-implications

for pCO_2 and pH levels in Arctic surface waters. The Cryosphere Discussions 6, 1015–1035.

Rysgaard, S., Glud, R.N., Sejr, M., Bendtsen, J., Christensen, P., 2007. Inorganic carbon transport during sea ice growth and decay: A carbon pump in polar seas. Journal of Geophysical Research: Oceans (1978-2012) 112.

Rysgaard, S., Wang, F., Galley, R.J., Grimm, R., Notz, D., Lemes, M., Geilfus, N.X., Chaulk, a., Hare, a.a., Crabeck, O., Else, B.G.T., Campbell, K., Sø rensen, L.L., Sievers, J., Papakyriakou, T., 2014. Temporal dynamics of ikaite in experimental sea ice. The Cryosphere 8, 1469–1478.

Saenz, B.T., Arrigo, K.R., 2012. Simulation of a sea ice ecosystem using a hybrid model for slush layer desalination. Journal of Geophysical Research: Oceans 117.

Sander, R., Burrows, J., Kaleschke, L., 2006. Carbonate precipitation in brine – a potential trigger for tropospheric ozone depletion events. Atmospheric Chemistry and Physics 6, 4653–4658.

Sander, R., Morin, S., 2010. Introducing the bromide/alkalinity ratio for a follow-up discussion on "Precipitation of salts in freezing seawater and ozone depletion events: a status report", by Morin et al., published in Atmos. Chem. Phys., 8, 7317–7324, 2008. Atmospheric Chemistry and Physics 10, 7655–7658.

Schröder, D., Feltham, D.L., Flocco, D., Tsamados, M., 2014. September Arctic sea-ice minimum predicted by spring melt-pond fraction. Nature Climate Change 4, 353–357.

Shirtcliffe, T., Huppert, H.E., Worster, M.G., 1991. Measurement of the solid fraction in the crystallization of a binary melt. Journal of Crystal Growth 113, 566–574.

Simpson, W., Carlson, D., Hönninger, G., Douglas, T., Sturm, M., Perovich, D., Platt, U., 2007a. First-year sea-ice contact predicts bromine monoxide (BrO)

levels at Barrow, Alaska better than potential frost flower contact. Atmospheric Chemistry and Physics 7, 621–627.

Simpson, W., Glasow, R.v., Riedel, K., Anderson, P., Ariya, P., Bottenheim, J., Burrows, J., Carpenter, L., Frieß, U., Goodsite, M.E., et al., 2007b. Halogens and their role in polar boundary-layer ozone depletion. Atmospheric Chemistry and Physics 7, 4375–4418.

Stammerjohn, S., Maksym, T., 2017. Gaining (and losing) antarctic sea ice: variability, trends, and mechanisms, in: Sea ice, John Wiley & Sons.

Strove, J., Meier, W., 2017. Sea ice trends and climatologies from smmr and ssm/i-ssmis .

Taylor, J., 1997. Introduction to error analysis, the study of uncertainties in physical measurements. University Science Books.

Tison, J., Dellile, B., Papadimitriou, S., 2017. Gases in sea ice, in: Sea ice, John Wiley & Sons.

Tison, J.L., Haas, C., Gowing, M.M., Sleewaegen, S., Bernard, A., 2002. Tank study of physico-chemical controls on gas content and composition during growth of young sea ice. Journal of Glaciology 48, 177–191.

Tucker, W.B., Perovich, D.K., 1992. Stress measurements in drifting pack ice. Cold Regions Science and Technology 20, 119–139.

Turner, A.K., Hunke, E.C., Bitz, C.M., 2013. Two modes of sea-ice gravity drainage: A parameterization for large-scale modeling. Journal of Geophysical Research: Oceans 118, 2279–2294.

Ulrich-Evers, K., Jochmann, P., Wilkinson, J., Hinse, P., 2015. Design and fabrication of a lateral stress sensor and measuring lateral stresses in Arctic sea ice. Technical Report. Report for deliverable D2.51 on EU project 265863.

Vancoppenolle, M., Bitz, C.M., Fichefet, T., 2007. Summer landfast sea ice desalination at Point Barrow, Alaska: Modeling and observations. Journal of Geophysical Research: Oceans 112.

Vancoppenolle, M., Fichefet, T., Bitz, C.M., 2006. Modeling the salinity profile of undeformed Arctic sea ice. Geophysical Research Letters 33.

Vancoppenolle, M., Fichefet, T., Goosse, H., Bouillon, S., Madec, G., Maqueda, M.A.M., 2009. Simulating the mass balance and salinity of Arctic and Antarctic sea ice. 1. Model description and validation. Ocean Modelling 27, 33–53.

Vancoppenolle, M., Goosse, H., De Montety, A., Fichefet, T., Tremblay, B., Tison, J.L., 2010. Modeling brine and nutrient dynamics in Antarctic sea ice: The case of dissolved silica. Journal of Geophysical Research: Oceans 115.

Vancoppenolle, M., Meiners, K.M., Michel, C., Bopp, L., Brabant, F., Carnat, G., Delille, B., Lannuzel, D., Madec, G., Moreau, S., 2013. Role of sea ice in global biogeochemical cycles: emerging views and challenges. Quaternary science reviews 79, 207–230.

Weast, R.C., 1971. Handbook of Chemistry and Physics. 52 ed., Chemical Rubber Co.

Weeks, W., 2010. On sea ice. University of Alaska Press.

Weiss, R., 1974. Carbon dioxide in water and seawater: the solubility of a non-ideal gas. Marine Chemistry 2, 203–215.

Wells, A., Wettlaufer, J., Orszag, S., 2010. Maximal potential energy transport: A variational principle for solidification problems. Physical Review Letters 105, 254502.

Wells, A., Wettlaufer, J., Orszag, S., 2011. Brine fluxes from growing sea ice. Geophysical Research Letters 38.

Wells, A.J., Wettlaufer, J.S., Orszag, S.A., 2013. Nonlinear mushy-layer convection with chimneys: stability and optimal solute fluxes. Journal of Fluid Mechanics 716, 203–227.

Wettlaufer, J., Worster, M.G., Huppert, H.E., 1997. The phase evolution of young sea ice. Geophysical Research Letters 24, 1251–1254.

Worster, M.G., Rees Jones, D.W., 2015. Sea-ice thermodynamics and brine drainage. Philosophical Transactions Royal Society A 373, 20140166.

Zhou, J., Delille, B., Eicken, H., Vancoppenolle, M., Brabant, F., Carnat, G., Geilfus, N.X., Papakyriakou, T., Heinesch, B., Tison, J.L., 2013. Physical and biogeochemical properties in landfast sea ice (Barrow, Alaska): Insights on brine and gas dynamics across seasons. Journal of Geophysical Research: Oceans 118, 3172–3189.

Zhou, J., Tison, J.L., Carnat, G., Geilfus, N.X., Delille, B., 2014. Physical controls on the storage of methane in landfast sea ice. The Cryosphere 8, 1019–1029.